Multi-scale Modeling of the Lung Parenchyma

Mahdi Manoochehrtayebi

▶ **To cite this version:**

Mahdi Manoochehrtayebi. Multi-scale Modeling of the Lung Parenchyma. Solid mechanics [physics.class-ph]. Institut Polytechnique de Paris, 2024. English. NNT : 2024IPPAX002 . tel-04871647

HAL Id: tel-04871647

https://theses.hal.science/tel-04871647v1

Submitted on 7 Jan 2025

HAL is a multi-disciplinary open access archive for the deposit and dissemination of scientific research documents, whether they are published or not. The documents may come from teaching and research institutions in France or abroad, or from public or private research centers.

L'archive ouverte pluridisciplinaire **HAL**, est destinée au dépôt et à la diffusion de documents scientifiques de niveau recherche, publiés ou non, émanant des établissements d'enseignement et de recherche français ou étrangers, des laboratoires publics ou privés.

INSTITUT POLYTECHNIQUE DE PARIS

NNT : 2024IPPAX002

Thèse de doctorat

ÉCOLE POLYTECHNIQUE

IP PARIS

Multi-scale Modeling of the Lung Parenchyma

Thèse de doctorat de l'Institut Polytechnique de Paris
préparée à École Polytechnique/LMS

École doctorale n°626 de l'Institut Polytechnique de Paris (ED IP Paris)
Spécialité de doctorat : Mécanique des fluides et des solides, acoustique

Thèse présentée et soutenue à Palaiseau, le 05/03/2024, par

MAHDI MANOOCHEHRTAYEBI

Composition du Jury :

Céline Grandmont Inria Paris	Présidente
Emmanuel Baranger ENS Paris-Saclay	Rapporteur
Adrien Baldit Université de Lorraine	Rapporteur
Pauline Assemat Institut de Mécanique des Fluides de Toulouse	Examinatrice
Kostas Danas École Polytechnique	Examinateur
Martin Genet École Polytechnique	Directeur de thèse
Aline Bel-Brunon INSA-Lyon	Directrice de thèse
Dominique Chapelle Inria Saclay	Directeur de thèse

To my dear family

Acknowledgements

The story of my PhD has come to a conclusion after three years and a few months. Such an achievement could not be possible without the help and support of many kind people I met during this journey. I am definitely so lucky to have the chance to face such lovely angles.

First of all, I would like to thank my dear supervisors, Aline Bel-Brunon, Dominique Chapelle, and Martin Genet. What I have learned from you is way beyond science. Thanks, Aline, for always being available to meet, even though we had to meet online. I appreciate your positive mindset. You are always kind and supportive of me and make me feel optimistic each time I discuss with you. It was an excellent opportunity to work with you when you provided me with practical information from the LaMCoS/LBMC experiment. I appreciate Dominique for your discipline at work. I enjoy working with serious people and did my best to implement such an attitude at work. It was an absolute pleasure working around Martin. I remember that at the CMBE conference in Milan, some people told me that I was so lucky to have the opportunity to work with you, and it is true. I enjoyed all the conversations we had besides science, as you have a great attitude, and it was pleasant talking to you. I have definitely learned a lot from you regarding my personal life. Regarding science, the amount of science I learned from you from the beginning of my internship, is not comparable to what I have learned before. Thanks for always being available in an office with a door open. Thanks for supporting me in many different ways, from supporting me to learn French to writing support letters to me. I appreciate you all three for helping me grow in different aspects and being patient while allowing me to improve. I have already missed working with you, even though I am happy I had such a great chance in my life.

I appreciate Jean-François Bernaudin (who is always kind and supportive to me), Pierre-Yves Brillet, Thomas Gille, and Hilario Nunes, clinicians of APHP hospital of Avicenne de Bobigny, as well as Dr. Catalin Fetita for the fruitful discussions. The insight you gave me during multiple discussions was definitely practical in modeling the physiological characteristics of the lung parenchyma.

I appreciate the reviewers of my manuscript, Adrien Baldit, and Emmanuel Baranger, for their time and effort in reviewing my manuscript and providing me with constructive suggestions. Thanks to Céline Grandmont for accepting the position of president of the jury and Pauline Assemat for being my jury member. Thank you all for managing to be present at my defense session from far away. Moreover, I appreciate Kostas Danas attending the jury despite the time difference between Tokyo and Paris. We had a fruitful discussion session, thanks to your precise questions during the defense session. Such feedback will definitely be helpful for me in extending my research culture.

A great thanks to Jean-Marc Allain and Kostas Danas for supporting my Ph.D. journey, being the monitoring committee of my thesis, providing me support regarding administrative procedures, and providing me constructive insight to drive my scientific path. I

appreciate Andrei Constantinescu, the head of the Solid Mechanics department at École Polytechnique, for his support. I know you have signed many paperwork during my PhD. I appreciate Alexandra Joly, Anna Johnsson, and Valérie Jamet for their availability and all of their support regarding my administrative work. Thanks to Abdelfattah Halim for all the information support.

I am grateful that I had been hosted by the friendly MΞDISIM team with a lively spirit. Chouquette meetings on Monday mornings would always make my week. I appreciate Philippe Moireau for his discipline in managing the team while providing support to Ph.D. candidates and creating a fun atmosphere in the team. During my journey, I have met amazing people in our team. I appreciate Cécile Patte and Nicole Tueni, who helped me learn some technical subjects at the beginning of my Ph.D., even though they were busy at the end of their Ph.D. Thanks to Alexandre Daby-Seesaram, Alice Peyraut, Chloé Giraudet, Colin Laville, François Kimmig, Jérôme Diaz, and Kateřina Skardova for the fruitful discussions we had. I have definitely profited from your practical suggestions. We had an excellent environment in our office, with two nice office mates, Julien Bonnafé and Qian Wu, who would change my mood each time I met you at work. I am happy to meet amazing people on the team, namely, Sébastien Imperiale, Patrick Le Tallec, Mathieu Barré, Louis-Pierre Chaintron, Nagham Chibli, Tiphaine Delaunay, André Dalmora, Élise Grosjean, Maria Gusseva, Gaël Le Ruz, Jessica Manganotti, Zineb Ramiche, and Vincenzo Zarra. A special thanks to Bahar Carabetta, who was always kind to me and would change my mood every time I met her.

I had three years of experience teaching with two outstanding professors, Abdul Barakat and Sophie Ramananarivo, who were always super kind to me. I really enjoyed such an experience. Working beside such nice people helped me to learn while teaching.

I appreciate my lovely friends who have supported me even before I arrived at École Polytechnique, Zahra Hooshmand Ahoor, Iman Toghraei, and Saman Vafadar. Their help and support allowed me to survive at some points. I appreciate my best friends, Mohammadreza Mirafzal and Amin Yazdani, with whom I made a lot of stories, even though those are related to out-of-work activities, but for sure, passing the time with them would keep my mental health in a situation that would benefit my work substantially.

Finally, and most importantly, I appreciate my family. Standing up in this place is more your effort and dedication than mine. I don't remember any point in my life when I wanted to embark on a journey and I didn't have your support. This achievement definitely belongs to you, and I appreciate all of your support.

Contents

Introduction (English)

Context

The lungs function, and the interstitial lung diseases

The lungs are the primary organs of the respiratory system in the body of humans and many animals, responsible for molecular exchange between the inhaled air and the bloodstream through the respiration mechanism. During respiration, the deformation of the lung permits the air to enter the respiratory tract, at the end of which oxygen is exchanged with carbon dioxide between the air and the blood. The mechanical deformation of the lung happens within the respiratory system and in collaboration with other organs that support the lungs in inflation and deflation. However, different factors affect lungs function, leading to decreased efficiency of the body, reduced quality of life, and even death.

Interstitial Lung Diseases (ILD) are among the factors that affect the function of the lung, and investigating them provides challenges for clinical specialists. ILD is a group of diffuse parenchymal lung disorders associated with substantial mortalities [Antoniou et al., 2014]. ILD can be divided into two categories of lung diseases associated with systemic disease (such as connective tissue diseases) and disease confined to the lung, including idiopathic pulmonary fibrosis [Demedts et al., 2001].

Idiopathic Pulmonary Fibrosis (IPF) is a severe type of ILD that affects lung function by scarring the parenchyma tissue, the progression of which, leads to respiratory failure. The word "idiopathic" refers to the unknown apparition and evolution mechanisms of the disease. IPF accounts for 20% to half of all cases of interstitial lung disease (ILD) and represents the most frequent and severe type of the idiopathic interstitial pneumonias, a group of ILDs of unknown cause [Travis et al., 2013, Sauleda et al., 2018]. Patients with IPF appear to have similar impairments in health-related quality of life to those with chronic obstructive pulmonary disease [Swigris, 2005]. In Europe alone, approximately 40,000 new cases are diagnosed each year [Navaratnam et al., 2011, Sauleda et al., 2018]. Pirfenidone and nintedanib are the only effective treatments validated for IPF [Rogliani et al., 2016], which are mostly effective when they are taken at the early stages of the disease progression. Nevertheless, there is often a significant delay between the first manifestation of the disease (typically a combination of dyspnea on exertion and dry cough) and the diagnosis, pointing that the early phase of IPF is still poorly understood [Poletti et al., 2013]. After receiving the diagnosis, it is not uncommon for patients to live five years or more, and many patients die from progressive, chronic hypoxemic respiratory failure [Lederer and Martinez, 2018]. IPF causes reduced lung compliance, reduced gas diffusing capacity, chronic arterial hypoxemia, and increased airway volumes [Plantier et al., 2018].

Indeed, IPF affects the mechanical behavior of the lung by creating scar tissue and making the interstitium stiffer. The progression of IPF might be driven by mechanics, such that the scarred, stiffer tissue undergoes higher stress, leading to more fibrous tissue. This condition could create a vicious cycle leading to the progression of IPF [Hinz and Suki, 2016]. So, mechanics could be a driving factor for IPF.

Challenges in pulmonology

Different interstitial lung diseases may have similar primary symptoms, raising the need for more precise investigations for diagnosis in successive steps, such as Computed Tomography (CT)-scans and biopsies. Such sequential investigation costs a significant amount of time in comparison to the life expectancy of the patient. Moreover, the prognosis of such diseases is crucial, as a significant portion of them lead to respiratory failure in a few years. So, a challenge arises here about the early stage recognition of such diseases and being able to predict the progression of the disease. Interstitial Lung Abnormalities (ILA) is a recent

notion that relates to abnormalities found in CT images incidentally and may be related to early-stage ILDs.

ILA is a common finding in CT scans and is often progressive and associated with worsened clinical outcomes, and may progress subclinical or early pulmonary fibrosis [Hatabu et al., 2019, Hata et al., 2021]. ILA is present in CT of about 10% of the patients undergoing lung cancer screening [Iwasawa et al., 2019]. It is also prevalent for smokers (4%–9% vs. 2%–7% for non-smokers) [Hata et al., 2021]. Individuals with ILA experience symptoms such as chronic cough and shortness of breath, decreased total lung capacity, reduced exercise capacity, and increased all-cause mortality [Doyle et al., 2012]. Figure 2 shows CT scans of three different people, one concerning a healthy lung, one at the early stages of ILA, and the other progressed case of ILA, resulting in the generation of fibrosis ground-glass. Such an example shows how the progression of ILA can be harmful by generating fibrous tissue and the importance of addressing ILA at early stages.

Radiologists have a central role in clinical management and research on ILA [Hata et al., 2021]; nonetheless, ILA is often subtle and varied, which makes it challenging to differentiate ILA from the normal lung [Hata et al., 2021]. Among patients with ILA, imaging patterns can be used to quantify the risk of progression and early death [Putman et al., 2019]. On the other hand, not all of the interstitial lung abnormalities lead to pulmonary fibrosis or cancer [Miller et al., 2018], so follow-up examinations are needed to investigate the progression of the disease by clinicians. These complexities create challenges for clinicians in the diagnosis of ILA as well as the prognosis regarding the progression of the disease. Such challenges can be addressed using digital tools.

Digital tools for pulmonologists

Digital tools include a wide range of technologies to help clinicians, such as radiologists and pulmonologists, have a better diagnosis, prognosis, and treatment of pathologies and also answer the patients' needs more efficiently. The contribution of such tools in healthcare is helping pulmonologists to diagnose pulmonary diseases at a very early stage and estimate the progression of the disease, which are essential clinical challenges. Digital tools in healthcare systems can significantly decrease the time of recognition by bypassing some medical examinations, such as surgical lung biopsy for diagnosis of IPF [Walsh et al., 2018]. They may be helpful in different stages, such as image processing tools and identifying radiographic features associated with ILA [Ash et al., 2017] and automated analysis based on Artificial Intelligence (AI) [Hata et al., 2021], to even addressing cancer treatment [Kaul et al., 2023]. AI-based tools such as machine learning and digital twins are growing trends in healthcare [Lim et al., 2020], and have a significant impact on clinicians by providing rapid interpretation for health systems, improving workflow, the potential for reducing medical errors and for patients by enabling them to process their data to promote health [Topol, 2019].

Machine learning (ML) is an AI tool that focuses on using data and algorithms to simulate how humans learn and make decisions. The ML algorithms use data to be trained to make predictions or decisions. Deep learning is a subset of ML that is based on multi-layer neural networks and follows more advanced algorithms. Such AI tools can be employed for clinical applications, specifically in pulmonology, to help clinicians diagnose the diseased regions of the lung from the clinical data, above all, CT images. Remarkably, chest radiography is a natural application domain because of the large number of stored images and reports facilitating the training of deep learning algorithms [Chassagnon et al., 2021]. High-resolution CT evaluation by a deep learning algorithm might provide a low-cost, reproducible, near-instantaneous classification of fibrotic lung disease with human-level

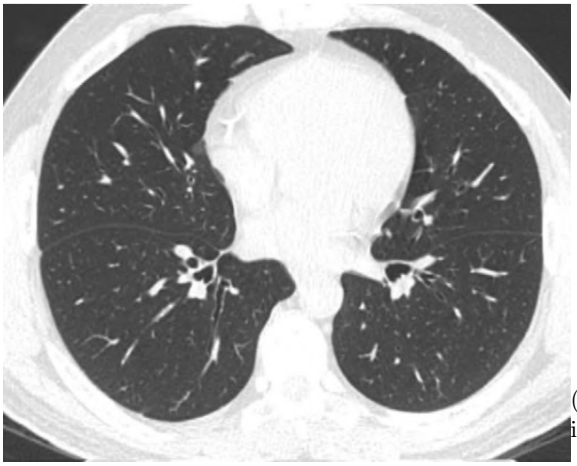

(a) CT-scan of a healthy lung, showing no evidence of ILA.

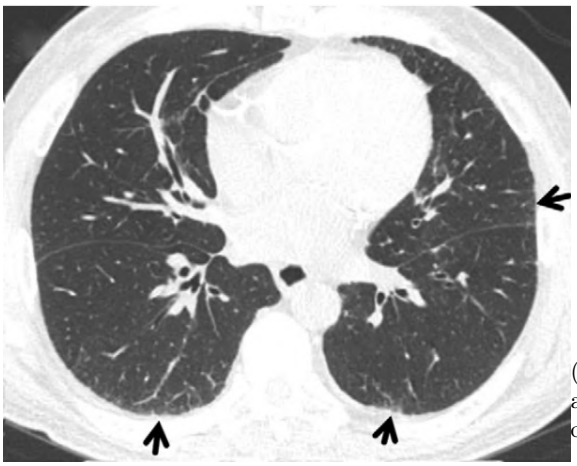

(b) Scan shows newly developed ground-glass abnormalities (arrows) in the subpleural area of bilateral lungs.

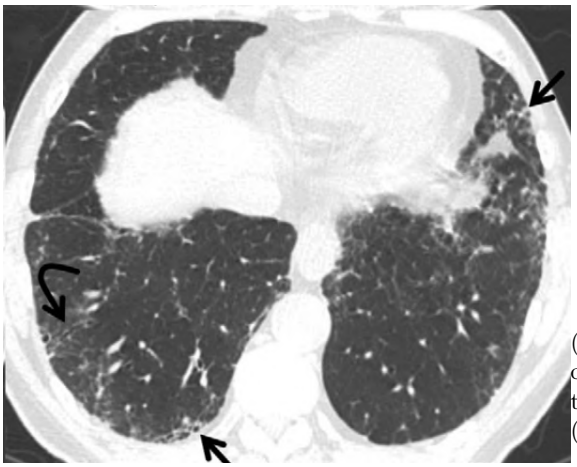

(c) Scan shows increased severity and extent of abnormalities (straight arrows) with new traction bronchiectasis indicating lung fibrosis (curved arrow).

Figure 1: CT-scan of three different people by [Hata et al., 2021], including a normal one, a case with an early stage of ILA, and a case with a severe ILA as well as IPF.

accuracy. These methods could be of benefit to centers in which thoracic imaging expertise is scarce, as well as for stratification of patients in clinical trials [Walsh et al., 2018]. So, ML and deep learning algorithms can assist radiologists with a number of tasks, such as the detection or characterization of radiological abnormalities or for prognostic purposes. For detection tasks, human validation by visual confirmation is possible to create annotated data for supervised machine learning [Chassagnon et al., 2021].

Application of data-based approaches in healthcare has been less beneficial, to date, with regard to personalization and transparency. These approaches are often criticized by patients for not providing patient-centered care and by clinicians for creating an opaque black box, resulting in thereby reducing transparency regarding decision support [Kaul et al., 2023]. On the other hand, the synergy between mechanistic and data-based models has shown value in aiding diagnosis, treatment, and prognosis evaluation [Corral-Acero et al., 2020]. Digital twins are of assistance in diagnosis, prognosis, and treatment of disease [Allen et al., 2021] in which the data is synced to its mechanistic model, which provides the physical explanations of the system, improving the plausibility of findings and increases their credibility [Corral-Acero et al., 2020]. This shows the importance of mechanistic modeling in digital tools, which can be used to provide a physical understanding of lung behavior.

Lung mechanical modeling

Lung mechanical modeling aims to describe the physical behavior of the lung based on a mechanical foundation. Such models establish a mathematical relation between the loading on the lung, such as the air pressure, and the deformation, which is aligned with the physiology of the lung. The lung parenchyma comprises different phases, such as air, blood, and interstitium tissue consisting of elastic and collagen fibers. Mechanical modeling of the lung aims to investigate the interaction between different phases under different loading and boundary conditions. Nonetheless, due to the complexity of the lung parenchyma and its behavior, different assumptions may be considered to simplify the mathematical models proposed to model lung behavior.

The lung is widely modeled from the organ scale to the alveoli scale. Modeling at the organ scale aims to investigate the behavior of the lung at the macroscopic scale in interaction with the lung surroundings and give structural estimations. Organ-scale models are relatively low-cost structural estimations of the lung parenchyma seen as a continuous material. However, they have limitations in showing the microscopic features and their contribution to the macroscopic scale. On the other hand, alveoli-scale models aim to investigate the behavior at the microscopic scale and can be employed for numerical analysis of stress distribution and septal deformation within the alveoli [Gefen et al., 1999].

At the organ/tissue scale, lung parenchyma is either considered as a compressible continuous, isotropic, and nonlinear material undergoing large strains [Tawhai et al., 2009, Bel-Brunon et al., 2014, Birzle et al., 2018], or as a porous material, where the interstitium tissue is considered as solid whose behavior can be studied in interaction with the air as the fluid. Poromechanics, fundamentally introduced by [Biot, 1941, Terzaghi, 1943, Biot and Temple, 1972], is employed to model the behavior of porous media at the macroscopic scale, based on the mixture theory [Bedford and Drumheller, 1979, Bowen, 1982, Coussy, 2004]. More precisely, it can be applied to model lung parenchyma as a porous hyperelastic material undergoing finite strains [Patte et al., 2022b]. Based on this approach, the behavior of the tissue needs to be described through a hyperelastic potential [Berger et al., 2016, Patte et al., 2022b]. Various nonlinear hyperelastic quasi-static models are proposed to study the behavior of the lung parenchyma [Rausch et al., 2011,

Bel-Brunon et al., 2014, Birzle et al., 2019, Jorba et al., 2019]. In addition, some take benefit from rheological models to capture the dynamic-mechanical behavior of the parenchyma [Romero, 1998].

To better understand the behavior of the lung at the microscopic scale and investigate the effect of interstitial-related lung diseases on the interstitium tissue and other microscopic properties, alveoli-scale models have been introduced, employing a micromechanical approach. Such an approach permits modeling more complex physiological phenomena occurring at the alveoli scale, such as surface tension [Wiechert et al., 2009, Coussy, 2010, Koshiyama et al., 2018] or tissue growth [Genet, 2019]. Moreover, micromechanical modeling allows us to investigate the stress and strain distribution under different loadings and boundary conditions [Concha et al., 2018, Álvarez-Barrientos et al., 2021] and also analyze the effective properties based on microscopic and morphological features [Zhu et al., 2017]. Micromechanical models require the definition of the microstructure geometry. There are different approaches to define the structure in alveoli-scale models.

The microstructure of the lung is either generated by segmenting X-ray-CT scans of the lung or using idealized geometries. Generating the microstructure of the lung through CT images concerns either the whole lung segmentation using multi-slide CT to reconstruct bronchial tree [Fetita et al., 2004], resulting in subject-specific computational meshes [Tawhai et al., 2004], or segmenting the alveoli walls. In the latter case, the microstructure of the acinus is extracted based on gray-scale binary images, employing a combination of image processing [Xiao et al., 2016, Koshiyama et al., 2018]. Nevertheless, such an approach to extract the exact geometry from CT images may be expensive, not only in the context of generation but also of computation. Alternatively, some researchers have used simplified geometrical elements to reconstruct the geometry of acinus, considering average polyhedral shapes of the alveoli to represent the representative geometry for alveoli [Dale et al., 1980, Denny and Schroter, 2000, Roth et al., 2017, Concha et al., 2018].

Adapting the models to physiological behavior of the lung

The developed mechanical models can be adapted to the physiological behavior of the lung parenchyma by assimilating experimental data. Such that the material properties include stiffness, density, viscoelasticity and porosity, and can be obtained from experimental testing of excised tissue [Neelakantan et al., 2022]. Various experiments have been conducted on the lung, based on different protocols. The experiments are conducted in vivo, where the measurements are performed in a living body, or ex vivo. In in vivo experiments, the deformation of the lung in spontaneous breathing or mechanical ventilation is measured using CT [Leclerc et al., 2009, Lovric et al., 2017], or Magnetic Resonance Imaging (MRI) [Boucneau et al., 2020] where deformation can be tracked through image registration at different time steps [Genet et al., 2018, Patte et al., 2022a, Genet, 2023, Laville et al., 2023]. On the other hand, ex vivo experiments allow a wider range of experiments, such as tensile test [Birzle et al., 2018, Arora et al., 2021], in addition to pressure-volume experiments [Schürch et al., 1976, Bachofen et al., 1987], where the deformation can be measured through digital image correlation [Mariano et al., 2020]. Noteworthy, such ex vivo experiments permit to investigate microscopic phenomena such as surface tension [Smith and Stamenovic, 1986, Bachofen and Schürch, 2001], which are modeled in micromechanical approaches as well [Karakaplan et al., 1980, Kowe et al., 1986].

The connection between the evolution of the microscopic mechanical and morphological features of the lung parenchyma due to IPF, which qualitatively is complicated to interpret, can be addressed through a mechanical model that is capable of studying the relationship

between microscopic properties and organ-scale behavior. Such a model is beneficial for two main reasons. On the one hand, it facilitates the diagnosis of idiopathic pulmonary fibrosis by quantifying CT images in a relatively short amount of time, enabling on-time intervention before the condition advances. On the other hand, it aids in prognosis by computing stress concentrations within the microstructure and comparing them to tissue limits.

Objectives: Lung parenchyma modeling: from microscopic to macroscopic scale

We aim to develop a multi-scale mechanical model that can simulate the behavior of the lung parenchyma and link the microscopic characteristics to the macroscopic behavior of the parenchyma. Such a model, which considers the microscopic physiological phenomena in the parenchyma, should bridge the gap between experimentally measured mechanical responses at tissue and organ scales. More precisely, the goal of this thesis branches out into two main objectives:

Objective 1 - Build a micro-poro-mechanical model

We aim to introduce a general microscopic poromechanical model that can simulate the behavior of compressible and incompressible porous materials at the microscopic scale and the contribution of the microscopic mechanical and morphological features to the macroscopic behavior. Such a model will be defined based on a geometrical microstructure and a constitutive behavior, and applied to finite strains. Moreover, it will allow to show not only the microscopic stress and strain distribution under various loadings such as macroscopic stress, macroscopic strain, and fluid pressure but also their average manifestations at the macroscopic scale.

Objective 2 - Adapting the model to the lung behavior

We aim to adapt the micro-mechanical model so that it can actually reproduce the lung behavior. We first introduce surface tension as a microscopic force applied at the air-tissue interface, secondly, the morphological and mechanical parameters of the model, along with the parameters of the surface tension model, are identified so that the response of the model matches the existing experimental data.

Overview of the work

Chapter 1 - Elements of lung physiology, modeling, and experiments

In the first chapter, we discuss the physiology of the pulmonary system, with a more precise focus on the lungs. The anatomy and function of the lung in the respiratory system during breathing are discussed. Then, we explain how the lung is mechanically modeled based on the elements of physiology. Models at two different scales, the alveoli scale and organ scale, and different elements of modeling, such as geometry, constitutive behavior, and boundary conditions, are discussed. In the end, we review different types of experiments conducted on the lung and measured data, which can be compared to the models.

Chapter 2 - Finite strain micro-poro-mechanics: formulation and compared analysis with macro-poro-mechanics

In the second chapter, we explain our approach to building a micro-poro-mechanical model. This approach proposes a general formulation that is applicable to any microstructure subjected to any macroscopic stress, strain, or internal pressure. Such a microscopic approach enables the study of the contribution of microscopic features to the macroscopic scale. The global response of the micro-poro-mechanical model is compared to a macroscopic model based upon the work of [Chapelle and Moireau, 2014] and [Patte et al., 2022b] to investigate the relevance of such models in capturing the behavior of porous media in finite strains and under different loading conditions, in addition to displaying the coupling between such quantities.

This chapter takes the form of a pre-print article co-authored by Mahdi Manoochehrtayebi, Aline Bel-Brunon, and Martin Genet, entitled *Finite strain micro-poro-mechanics: formulation and compared analysis with macro-poro-mechanics*, submitted to the Journal of the Mechanics and Physics of Solids.

Chapter 3 - Elements of microstructural modeling

In this chapter, we introduce a method to generate geometrical microstructures as an element of the micro-poro-mechanical model, which can be used to model biological tissues such as the lung parenchyma. This method employs an algorithm to generate irregular and random microstructures using seeds distributions. Periodic porous meshes are generated from a Voronoi tessellation of the seeds. Even though the seeds can be distributed based on any pattern, we defined a way of distribution of the seeds, leading to geometries with quantified level irregularity and porosity.

Chapter 4 - Toward a physiological micro-model: incorporating surface tension and fitting to experiments

This chapter expands on the generic micro-poro-mechanical model proposed in Chapter 2 for lung parenchyma modeling. First, an exponential constitutive behavior is proposed to capture the strain-induced stiffening behavior of the lung. Secondly, surface tensions are incorporated in the model as a physiological phenomenon inside the lung, benefiting from the micro-model to capture microstructural-based features. Finally, the model parameters are identified based on experimental data from the literature with and without the presence of surface tension.

Communications

Oral presentations

- **Oral presentation at X-UTC day.**
  Université de technologie de Compiègne, Compiègne, France - March, 2022.
- **Oral presentation at the Jean Mandel Symposium.**
  École Polytechnique, Palaiseau, France - June, 2022.
- **Oral presentation at CMBE conference.**
  Politecnico di Milano, Milan, Italy - June, 2022.
- **Oral presentation at GDR MécaBioSanté.**
  Sorbonne Université, Paris, France - November, 2022.

- **Oral presentation at CMBBE conference.**
  Arts et Métiers Institute of Technology, Paris, France - May, 2023.

Preprint

- **Micro-poro-mechanics: formulation and compared analysis with macro-poro-mechanics**
  M. Manoochehrtayebi, A. Bel-Brunon and M. Genet
  Submitted.

Bibliography

[Allen et al., 2021] Allen, A., Siefkas, A., Pellegrini, E., Burdick, H., Barnes, G., Calvert, J., Mao, Q., and Das, R. (2021). A Digital Twins Machine Learning Model for Forecasting Disease Progression in Stroke Patients. *Applied Sciences*, 11(12):5576.

[Álvarez-Barrientos et al., 2021] Álvarez-Barrientos, F., Hurtado, D. E., and Genet, M. (2021). Pressure-driven micro-poro-mechanics: A variational framework for modeling the response of porous materials. *International Journal of Engineering Science*, 169:103586.

[Antoniou et al., 2014] Antoniou, K. M., Margaritopoulos, G. A., Tomassetti, S., Bonella, F., Costabel, U., and Poletti, V. (2014). Interstitial lung disease. *European Respiratory Review*, 23(131):40–54. 150 citations (Crossref) [2023-12-18].

[Arora et al., 2021] Arora, H., Mitchell, R., Johnston, R., Manolesos, M., Howells, D., Sherwood, J., Bodey, A., and Wanelik, K. (2021). Correlating Local Volumetric Tissue Strains with Global Lung Mechanics Measurements. *Materials*, 14(2):439.

[Ash et al., 2017] Ash, S. Y., Harmouche, R., Ross, J. C., Diaz, A. A., Hunninghake, G. M., Putman, R. K., Onieva, J., Martinez, F. J., Choi, A. M., Lynch, D. A., Hatabu, H., Rosas, I. O., Estepar, R. S. J., and Washko, G. R. (2017). The Objective Identification and Quantification of Interstitial Lung Abnormalities in Smokers. *Academic Radiology*, 24(8):941–946.

[Bachofen et al., 1987] Bachofen, H., Schurch, S., Urbinelli, M., and Weibel, E. R. (1987). Relations among alveolar surface tension, surface area, volume, and recoil pressure. *Journal of Applied Physiology*, 62(5):1878–1887.

[Bachofen and Schürch, 2001] Bachofen, H. and Schürch, S. (2001). Alveolar surface forces and lung architecture. *Comparative Biochemistry and Physiology Part A: Molecular & Integrative Physiology*, 129(1):183–193.

[Bedford and Drumheller, 1979] Bedford, A. and Drumheller, D. (1979). A variational theory of porous media. *International Journal of Solids and Structures*, 15(12):967–980.

[Bel-Brunon et al., 2014] Bel-Brunon, A., Kehl, S., Martin, C., Uhlig, S., and Wall, W. (2014). Numerical identification method for the non-linear viscoelastic compressible behavior of soft tissue using uniaxial tensile tests and image registration – Application to rat lung parenchyma. *Journal of the Mechanical Behavior of Biomedical Materials*, 29:360–374.

[Berger et al., 2016] Berger, L., Bordas, R., Burrowes, K., Grau, V., Tavener, S., and Kay, D. (2016). A poroelastic model coupled to a fluid network with applications in lung

modelling. *International Journal for Numerical Methods in Biomedical Engineering*, 32(1).

[Biot, 1941] Biot, M. A. (1941). General Theory of Three-Dimensional Consolidation. *Journal of Applied Physics*, 12(2):155–164.

[Biot and Temple, 1972] Biot, M. A. and Temple, G. (1972). Theory of Finite Deformations of Porous Solids. *Indiana University Mathematics Journal*, 21(7):597–620. Publisher: Indiana University Mathematics Department.

[Birzle et al., 2019] Birzle, A. M., Martin, C., Uhlig, S., and Wall, W. A. (2019). A coupled approach for identification of nonlinear and compressible material models for soft tissue based on different experimental setups – Exemplified and detailed for lung parenchyma. *Journal of the Mechanical Behavior of Biomedical Materials*, 94:126–143.

[Birzle et al., 2018] Birzle, A. M., Martin, C., Yoshihara, L., Uhlig, S., and Wall, W. A. (2018). Experimental characterization and model identification of the nonlinear compressible material behavior of lung parenchyma. *Journal of the Mechanical Behavior of Biomedical Materials*, 77:754–763.

[Boucneau et al., 2020] Boucneau, T., Fernandez, B., Larson, P., Darrasse, L., and Maître, X. (2020). 3D Magnetic Resonance Spirometry. *Scientific Reports*, 10(1):9649.

[Bowen, 1982] Bowen, R. M. (1982). Compressible porous media models by use of the theory of mixtures. *International Journal of Engineering Science*, 20(6):697–735.

[Chapelle and Moireau, 2014] Chapelle, D. and Moireau, P. (2014). General coupling of porous flows and hyperelastic formulations—From thermodynamics principles to energy balance and compatible time schemes. *European Journal of Mechanics - B/Fluids*, 46:82–96.

[Chassagnon et al., 2021] Chassagnon, G., Vakalopoulou, M., Régent, A., Sahasrabudhe, M., Marini, R., Hoang-Thi, T.-N., Dinh-Xuan, A.-T., Dunogué, B., Mouthon, L., Paragios, N., and Revel, M.-P. (2021). Elastic Registration–driven Deep Learning for Longitudinal Assessment of Systemic Sclerosis Interstitial Lung Disease at CT. *Radiology*, 298(1):189–198.

[Concha et al., 2018] Concha, F., Sarabia-Vallejos, M., and Hurtado, D. E. (2018). Micromechanical model of lung parenchyma hyperelasticity. *Journal of the Mechanics and Physics of Solids*, 112:126–144.

[Corral-Acero et al., 2020] Corral-Acero, J., Margara, F., Marciniak, M., Rodero, C., Loncaric, F., Feng, Y., Gilbert, A., Fernandes, J. F., Bukhari, H. A., Wajdan, A., Martinez, M. V., Santos, M. S., Shamohammdi, M., Luo, H., Westphal, P., Leeson, P., DiAchille, P., Gurev, V., Mayr, M., Geris, L., Pathmanathan, P., Morrison, T., Cornelussen, R., Prinzen, F., Delhaas, T., Doltra, A., Sitges, M., Vigmond, E. J., Zacur, E., Grau, V., Rodriguez, B., Remme, E. W., Niederer, S., Mortier, P., McLeod, K., Potse, M., Pueyo, E., Bueno-Orovio, A., and Lamata, P. (2020). The 'Digital Twin' to enable the vision of precision cardiology. *European Heart Journal*, 41(48):4556–4564.

[Coussy, 2004] Coussy, O. (2004). *Poromechanics*. John Wiley & Sons.

[Coussy, 2010] Coussy, O. (2010). Mechanics and Physics of Porous Solids.

[Dale et al., 1980] Dale, P., Matthews, F. L., and Schroter, R. C. (1980). Finite element analysis of lung alveolus. *Journal of Biomechanics*, 13(10):865–873.

[Demedts et al., 2001] Demedts, M., Wells, A. U., Anto, J. M., Costabel, U., Hubbard, R., Cullinan, P., Slabbynck, H., Rizzato, G., Poletti, V., Verbeken, E. K., Thomeer, M. J., Kokkarinen, J., Dalphin, J. C., and Taylor, A. N. (2001). Interstitial lung diseases: an epidemiological overview.

[Denny and Schroter, 2000] Denny, E. and Schroter, R. C. (2000). Viscoelastic Behavior of a Lung Alveolar Duct Model. *Journal of Biomechanical Engineering*, 122(2):143–151.

[Doyle et al., 2012] Doyle, T. J., Washko, G. R., Fernandez, I. E., Nishino, M., Okajima, Y., Yamashiro, T., Divo, M. J., Celli, B. R., Sciurba, F. C., Silverman, E. K., Hatabu, H., Rosas, I. O., and Hunninghake, G. M. (2012). Interstitial Lung Abnormalities and Reduced Exercise Capacity. *American Journal of Respiratory and Critical Care Medicine*, 185(7):756–762. 98 citations (Crossref) [2023-11-09].

[Fetita et al., 2004] Fetita, C., Preteux, F., Beigelman-Aubry, C., and Grenier, P. (2004). Pulmonary Airways: 3-D Reconstruction From Multislice CT and Clinical Investigation. *IEEE Transactions on Medical Imaging*, 23(11):1353–1364.

[Gefen et al., 1999] Gefen, A., Elad, D., and Shiner, R. (1999). Analysis of stress distribution in the alveolar septa of normal and simulated emphysematic lungs. *Journal of Biomechanics*, 32(9):891–897.

[Genet, 2019] Genet, M. (2019). A relaxed growth modeling framework for controlling growth-induced residual stresses. *Clinical Biomechanics*, 70:270–277.

[Genet, 2023] Genet, M. (2023). Finite strain formulation of the discrete equilibrium gap principle: application to mechanically consistent regularization for large motion tracking. *Comptes Rendus. Mécanique*, 351(G2):429–458.

[Genet et al., 2018] Genet, M., Stoeck, C., Von Deuster, C., Lee, L., and Kozerke, S. (2018). Equilibrated warping: Finite element image registration with finite strain equilibrium gap regularization. *Medical Image Analysis*, 50:1–22.

[Hata et al., 2021] Hata, A., Schiebler, M. L., Lynch, D. A., and Hatabu, H. (2021). Interstitial Lung Abnormalities: State of the Art. *Radiology*, 301(1):19–34.

[Hatabu et al., 2019] Hatabu, H., Hunninghake, G. M., and Lynch, D. A. (2019). Interstitial Lung Abnormality: Recognition and Perspectives. *Radiology*, 291(1):1–3.

[Hinz and Suki, 2016] Hinz, B. and Suki, B. (2016). Does Breathing Amplify Fibrosis?

[Iwasawa et al., 2019] Iwasawa, T., Okudela, K., Takemura, T., Fukuda, T., Matsushita, S., Baba, T., Ogura, T., Tajiri, M., and Yoshizawa, A. (2019). Computer-aided Quantification of Pulmonary Fibrosis in Patients with Lung Cancer: Relationship to Disease-free Survival. *Radiology*, 292(2):489–498.

[Jorba et al., 2019] Jorba, I., Beltrán, G., Falcones, B., Suki, B., Farré, R., García-Aznar, J. M., and Navajas, D. (2019). Nonlinear elasticity of the lung extracellular microenvironment is regulated by macroscale tissue strain. *Acta Biomaterialia*, 92:265–276.

[Karakaplan et al., 1980] Karakaplan, A. D., Bieniek, M. P., and Skalak, R. (1980). A Mathematical Model of Lung Parenchyma. *Journal of Biomechanical Engineering*, 102(2):124–136.

[Kaul et al., 2023] Kaul, R., Ossai, C., Forkan, A. R. M., Jayaraman, P. P., Zelcer, J., Vaughan, S., and Wickramasinghe, N. (2023). The role of AI for developing digital twins in healthcare: The case of cancer care. *WIREs Data Mining and Knowledge Discovery*, 13(1):e1480.

[Koshiyama et al., 2018] Koshiyama, K., Nishimoto, K., Ii, S., Sera, T., and Wada, S. (2018). Heterogeneous structure and surface tension effects on mechanical response in pulmonary acinus: A finite element analysis. *Clinical Biomechanics*.

[Kowe et al., 1986] Kowe, R., Schroter, R., Matthews, F., and Hitchings, D. (1986). Analysis of elastic and surface tension effects in the lung alveolus using finite element methods. *Journal of Biomechanics*, 19(7):541–549.

[Laville et al., 2023] Laville, C., Fetita, C., Gille, T., Brillet, P.-Y., Nunes, H., Bernaudin, J.-F., and Genet, M. (2023). Comparison of optimization parametrizations for regional lung compliance estimation using personalized pulmonary poromechanical modeling. *Biomechanics and Modeling in Mechanobiology*.

[Leclerc et al., 2009] Leclerc, H., Périé, J.-N., Roux, S., and Hild, F. (2009). Integrated Digital Image Correlation for the Identification of Mechanical Properties. In Gagalowicz, A. and Philips, W., editors, *Computer Vision/Computer Graphics CollaborationTechniques*, volume 5496, pages 161–171. Springer Berlin Heidelberg, Berlin, Heidelberg.

[Lederer and Martinez, 2018] Lederer, D. J. and Martinez, F. J. (2018). Idiopathic Pulmonary Fibrosis. *New England Journal of Medicine*, 378(19):1811–1823. 1001 citations (Crossref) [2023-10-23].

[Lim et al., 2020] Lim, K. Y. H., Zheng, P., and Chen, C.-H. (2020). A state-of-the-art survey of Digital Twin: techniques, engineering product lifecycle management and business innovation perspectives. *Journal of Intelligent Manufacturing*, 31(6):1313–1337.

[Lovric et al., 2017] Lovric, G., Mokso, R., Arcadu, F., Vogiatzis Oikonomidis, I., Schittny, J. C., Roth-Kleiner, M., and Stampanoni, M. (2017). Tomographic in vivo microscopy for the study of lung physiology at the alveolar level. *Scientific Reports*, 7(1):12545.

[Mariano et al., 2020] Mariano, C. A., Sattari, S., Maghsoudi-Ganjeh, M., Tartibi, M., Lo, D. D., and Eskandari, M. (2020). Novel Mechanical Strain Characterization of Ventilated ex vivo Porcine and Murine Lung using Digital Image Correlation. *Frontiers in Physiology*, 11:600492.

[Miller et al., 2018] Miller, E. R., Putman, R. K., Vivero, M., Hung, Y., Araki, T., Nishino, M., Washko, G. R., Rosas, I. O., Hatabu, H., Sholl, L. M., and Hunninghake, G. M. (2018). Histopathology of Interstitial Lung Abnormalities in the Context of Lung Nodule Resections. *American Journal of Respiratory and Critical Care Medicine*, 197(7):955–958.

[Navaratnam et al., 2011] Navaratnam, V., Fleming, K. M., West, J., Smith, C. J. P., Jenkins, R. G., Fogarty, A., and Hubbard, R. B. (2011). The rising incidence of idiopathic pulmonary fibrosis in the UK. *Thorax*, 66(6):462–467.

[Neelakantan et al., 2022] Neelakantan, S., Xin, Y., Gaver, D. P., Cereda, M., Rizi, R., Smith, B. J., and Avazmohammadi, R. (2022). Computational lung modelling in respiratory medicine. *Journal of The Royal Society Interface*, 19(191):20220062.

[Patte et al., 2022a] Patte, C., Brillet, P.-Y., Fetita, C., Bernaudin, J.-F., Gille, T., Nunes, H., Chapelle, D., and Genet, M. (2022a). Estimation of Regional Pulmonary Compliance in Idiopathic Pulmonary Fibrosis Based on Personalized Lung Poromechanical Modeling. *Journal of Biomechanical Engineering*, 144(9):091008.

[Patte et al., 2022b] Patte, C., Genet, M., and Chapelle, D. (2022b). A quasi-static poromechanical model of the lungs. *Biomechanics and Modeling in Mechanobiology*.

[Plantier et al., 2018] Plantier, L., Cazes, A., Dinh-Xuan, A.-T., Bancal, C., Marchand-Adam, S., and Crestani, B. (2018). Physiology of the lung in idiopathic pulmonary fibrosis. *European Respiratory Review*, 27(147):170062.

[Poletti et al., 2013] Poletti, V., Ravaglia, C., Buccioli, M., Tantalocco, P., Piciucchi, S., Dubini, A., Carloni, A., Chilosi, M., and Tomassetti, S. (2013). Idiopathic Pulmonary Fibrosis: Diagnosis and Prognostic Evaluation. *Respiration*, 86(1):5–12.

[Putman et al., 2019] Putman, R. K., Gudmundsson, G., Axelsson, G. T., Hida, T., Honda, O., Araki, T., Yanagawa, M., Nishino, M., Miller, E. R., Eiriksdottir, G., Gudmundsson, E. F., Tomiyama, N., Honda, H., Rosas, I. O., Washko, G. R., Cho, M. H., Schwartz, D. A., Gudnason, V., Hatabu, H., and Hunninghake, G. M. (2019). Imaging Patterns Are Associated with Interstitial Lung Abnormality Progression and Mortality. *American Journal of Respiratory and Critical Care Medicine*, 200(2):175–183.

[Rausch et al., 2011] Rausch, S., Martin, C., Bornemann, P., Uhlig, S., and Wall, W. (2011). Material model of lung parenchyma based on living precision-cut lung slice testing. *Journal of the Mechanical Behavior of Biomedical Materials*, 4(4):583–592.

[Rogliani et al., 2016] Rogliani, P., Calzetta, L., Cavalli, F., Matera, M. G., and Cazzola, M. (2016). Pirfenidone, nintedanib and N-acetylcysteine for the treatment of idiopathic pulmonary fibrosis: A systematic review and meta-analysis. *Pulmonary Pharmacology & Therapeutics*, 40:95–103.

[Romero, 1998] Romero, F. (1998). A recruitment-based rheological model for mechanical behavior of soft tissues. *Biorheology*, 35(1):17–35.

[Roth et al., 2017] Roth, C. J., Yoshihara, L., and Wall, W. A. (2017). A simplified parametrised model for lung microstructures capable of mimicking realistic geometrical and mechanical properties. *Computers in Biology and Medicine*, 89:104–114.

[Sauleda et al., 2018] Sauleda, J., Núñez, B., Sala, E., and Soriano, J. (2018). Idiopathic Pulmonary Fibrosis: Epidemiology, Natural History, Phenotypes. *Medical Sciences*, 6(4):110.

[Schürch et al., 1976] Schürch, S., Goerke, J., and Clements, J. A. (1976). Direct determination of surface tension in the lung. *Proceedings of the National Academy of Sciences*, 73(12):4698–4702.

[Smith and Stamenovic, 1986] Smith, J. C. and Stamenovic, D. (1986). Surface forces in lungs. I. Alveolar surface tension-lung volume relationships. *Journal of Applied Physiology*, 60(4):1341–1350.

[Swigris, 2005] Swigris, J. J. (2005). Health-related quality of life in patients with idiopathic pulmonary fibrosis: a systematic review. *Thorax*, 60(7):588–594.

[Tawhai et al., 2004] Tawhai, M. H., Hunter, P., Tschirren, J., Reinhardt, J., McLennan, G., and Hoffman, E. A. (2004). CT-based geometry analysis and finite element models of the human and ovine bronchial tree. *Journal of Applied Physiology*, 97(6):2310–2321.

[Tawhai et al., 2009] Tawhai, M. H., Nash, M. P., Lin, C.-L., and Hoffman, E. A. (2009). Supine and prone differences in regional lung density and pleural pressure gradients in the human lung with constant shape. *Journal of Applied Physiology*, 107(3):912–920.

[Terzaghi, 1943] Terzaghi, K. (1943). *Theoretical Soil Mechanics*. John Wiley & Sons, Inc., Hoboken, NJ, USA.

[Topol, 2019] Topol, E. J. (2019). High-performance medicine: the convergence of human and artificial intelligence. *Nature Medicine*, 25(1):44–56.

[Travis et al., 2013] Travis, W. D., Costabel, U., Hansell, D. M., King, T. E., Lynch, D. A., Nicholson, A. G., Ryerson, C. J., Ryu, J. H., Selman, M., Wells, A. U., Behr, J., Bouros, D., Brown, K. K., Colby, T. V., Collard, H. R., Cordeiro, C. R., Cottin, V., Crestani, B., Drent, M., Dudden, R. F., Egan, J., Flaherty, K., Hogaboam, C., Inoue, Y., Johkoh, T., Kim, D. S., Kitaichi, M., Loyd, J., Martinez, F. J., Myers, J., Protzko, S., Raghu, G., Richeldi, L., Sverzellati, N., Swigris, J., and Valeyre, D. (2013). An Official American Thoracic Society/European Respiratory Society Statement: Update of the International Multidisciplinary Classification of the Idiopathic Interstitial Pneumonias. *American Journal of Respiratory and Critical Care Medicine*, 188(6):733–748.

[Walsh et al., 2018] Walsh, S. L. F., Calandriello, L., Silva, M., and Sverzellati, N. (2018). Deep learning for classifying fibrotic lung disease on high-resolution computed tomography: a case-cohort study. *The Lancet Respiratory Medicine*, 6(11):837–845.

[Wiechert et al., 2009] Wiechert, L., Metzke, R., and Wall, W. A. (2009). Modeling the Mechanical Behavior of Lung Tissue at the Microlevel. *Journal of Engineering Mechanics*, 135(5):434–438.

[Xiao et al., 2016] Xiao, L., Sera, T., Koshiyama, K., and Wada, S. (2016). Morphological Characterization of Acinar Cluster in Mouse Lung Using a Multiscale-based Segmentation Algorithm on Synchrotron Micro-CT Images. *The Anatomical Record*, 299(10):1424–1434.

[Zhu et al., 2017] Zhu, W., Blal, N., Cunsolo, S., and Baillis, D. (2017). Micromechanical modeling of effective elastic properties of open-cell foam. *International Journal of Solids and Structures*, 115-116:61–72.

Introduction (Français)

Contexte

La fonction pulmonaire et les maladies pulmonaires interstitielles

Les poumons sont les principaux organes du système respiratoire de l'homme et de nombreux animaux. Ils sont responsables des échanges moléculaires entre l'air inspiré et la circulation sanguine par le biais du mécanisme de respiration. Au cours de la respiration, la déformation du poumon permet à l'air de pénétrer dans les voies respiratoires, à la fin desquelles l'oxygène est échangé avec le dioxyde de carbone entre l'air et le sang. La déformation mécanique des poumons se produit au sein du système respiratoire et en collaboration avec d'autres organes qui soutiennent les poumons lors de l'inflation et de la déflation. Cependant, différents facteurs affectent la fonction pulmonaire, entraînant une diminution de l'efficacité de l'organisme, une baisse de la qualité de vie, voire la mort.

Les maladies pulmonaires interstitielles (MPI) font partie des facteurs qui affectent la fonction pulmonaire, et leur étude représente un défi pour les spécialistes cliniques. Les MPI sont un groupe de maladies pulmonaires parenchymateuses diffuses associées à une mortalité importante [Antoniou et al., 2014]. Les MPI peut être divisée en deux catégories : les maladies pulmonaires associées à des maladies systémiques (telles que les maladies du tissu conjonctif) ou bien les maladies limitées aux poumons, y compris la fibrose pulmonaire idiopathique [Demedts et al., 2001].

La fibrose pulmonaire idiopathique (FPI) est une forme sévère de la maladie pulmonaire idiopathique qui affecte la fonction pulmonaire en endommageant du tissu parenchymateux, dont la progression conduit à l'insuffisance respiratoire. Le terme "idiopathique" fait référence aux mécanismes inconnus d'apparition et d'évolution de la maladie. La FPI représente 20% à la moitié de tous les cas de pneumopathie interstitielle (PI) et constitue le type le plus fréquent et le plus grave des pneumonies interstitielles idiopathiques, un groupe de PI de cause inconnue [Travis et al., 2013, Sauleda et al., 2018]. Les patients atteints de FPI semblent présenter des altérations de la qualité de vie liées à la santé similaires à celles des patients atteints de bronchopneumopathie chronique obstructive [Swigris, 2005]. Rien qu'en Europe, environ 40 000 nouveaux cas sont diagnostiqués chaque année [Navaratnam et al., 2011, Sauleda et al., 2018]. La pirfénidone et le nintedanib sont les seuls traitements efficaces validés pour la FPI [Rogliani et al., 2016], qui sont surtout efficaces lorsqu'ils sont pris aux premiers stades de l'évolution de la maladie. Néanmoins, il y a souvent un délai important entre la première manifestation de la maladie (typiquement une combinaison de dyspnée à l'effort et de toux sèche) et le diagnostic, ce qui montre que la phase précoce de la FPI est encore mal comprise [Poletti et al., 2013]. Après avoir reçu le diagnostic, il n'est pas rare que les patients vivent cinq ans ou plus, et de nombreux patients meurent d'une insuffisance respiratoire hypoxémique chronique progressive [Lederer and Martinez, 2018]. La FPI entraîne une réduction de la compliance pulmonaire, une réduction de la capacité de diffusion des gaz, une hypoxémie artérielle chronique et une augmentation du volume des voies respiratoires [Plantier et al., 2018].

En effet, la FPI affecte le comportement mécanique du poumon en créant du tissu cicatriciel et en rendant l'interstitium plus rigide. La progression de la FPI pourrait être dictée par la mécanique, de sorte que le tissu cicatriciel et plus rigide subit un stress plus important, ce qui entraîne la formation d'un tissu plus fibreux. Cette situation pourrait créer un cercle vicieux conduisant à la progression de la FPI [Hinz and Suki, 2016]. La mécanique pourrait donc être un facteur déterminant de la FPI.

Défis en pneumologie

Différentes maladies pulmonaires interstitielles peuvent présenter des symptômes primaires similaires, ce qui rend nécessaire des examens plus précis pour le diagnostic par étapes successives, comme la tomodensitométrie (CT) et les biopsies. Ces examens séquentiels coûtent beaucoup de temps par rapport à l'espérance de vie du patient. En outre, le pronostic de ces maladies est crucial, car une grande partie d'entre elles conduisent à une insuffisance respiratoire en quelques années. Le défi consiste donc à reconnaître ces maladies à un stade précoce et à pouvoir prédire leur évolution. Les anomalies pulmonaires interstitielles (ILA) sont une notion récente qui se rapporte à des anomalies trouvées fortuitement sur des images de tomodensitométrie et qui peuvent être liées à des maladies pulmonaires interstitielles à un stade précoce.

L'ILA est une découverte courante dans les tomodensitogrammes, elle est souvent progressive et associée à une aggravation des résultats cliniques, et elle peut évoluer vers une fibrose pulmonaire subclinique ou précoce [Hatabu et al., 2019, Hata et al., 2021]. L'ILA est présente dans le scanner d'environ 10% des patients qui subissent un dépistage du cancer du poumon [Iwasawa et al., 2019]. Il est également prévalent chez les fumeurs (4%-9% contre 2%-7% chez les non-fumeurs) [Hata et al., 2021]. Les personnes atteintes d'ILA présentent des symptômes tels qu'une toux chronique et un essoufflement, une diminution de la capacité pulmonaire totale, une réduction de la capacité d'exercice et une augmentation de la mortalité toutes causes confondues [Doyle et al., 2012]. La figure 2 montre des tomodensitogrammes de trois personnes différentes, l'une avec un poumon sain, la deuxième aux premiers stades de l'ILA, et la troisième avec une progression de l'ILA, entraînant la formation d'un verre dépoli de fibrose. Cet exemple montre comment la progression de l'ILA peut être néfaste en générant du tissu fibreux et l'importance de traiter l'ILA dès les premiers stades.

Les radiologues jouent un rôle central dans la gestion clinique et la recherche sur la LIA [Hata et al., 2021] ; néanmoins, la LIA est souvent subtile et variée, ce qui rend difficile la différenciation de la LIA du poumon normal [Hata et al., 2021]. Parmi les patients atteints d'ILA, les modèles d'imagerie peuvent être utilisés pour quantifier le risque de progression et de décès précoce [Putman et al., 2019]. D'autre part, toutes les anomalies du poumon interstitiel ne conduisent pas à une fibrose pulmonaire ou à un cancer [Miller et al., 2018], de sorte que les examens de suivi sont nécessaires pour étudier la progression de la maladie par les cliniciens. Ces complexités créent des défis pour les cliniciens dans le diagnostic de l'ILA ainsi que le pronostic concernant la progression de la maladie. Ces défis peuvent être relevés à l'aide d'outils numériques.

Outils numériques pour les pneumologues

Les outils numériques comprennent un large éventail de technologies qui aident les cliniciens, tels que les radiologues et les pneumologues, à améliorer le diagnostic, le pronostic et le traitement des pathologies et à répondre plus efficacement aux besoins des patients. L'apport de ces outils dans les soins de santé est d'aider les pneumologues à diagnostiquer les maladies pulmonaires à un stade très précoce et à estimer la progression de la maladie, qui sont des défis cliniques essentiels. Les outils numériques dans les systèmes de santé peuvent considérablement réduire le temps de reconnaissance en contournant certains examens médicaux, comme la biopsie pulmonaire chirurgicale pour le diagnostic de la FPI [Walsh et al., 2018]. Ils peuvent être utiles à différentes étapes, comme les outils de traitement d'images et l'identification des caractéristiques radiographiques associées à la FPI [Ash et al., 2017] et l'analyse automatisée basée sur l'intelligence artificielle (IA) [Hata et al., 2021], jusqu'au traitement du cancer [Kaul et al., 2023]. Les outils basés

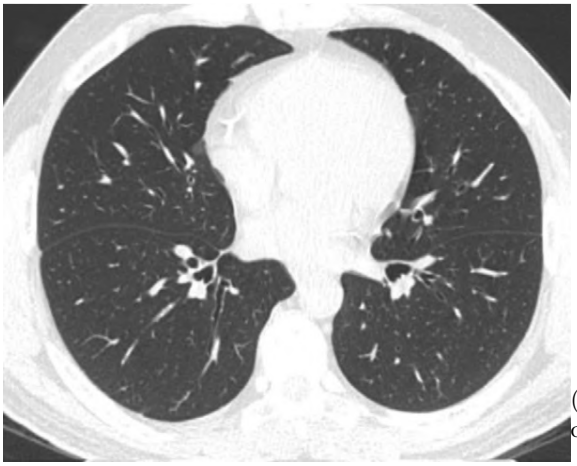

(a) TDM d'un poumon sain, ne montrant aucun signe d'ILA.

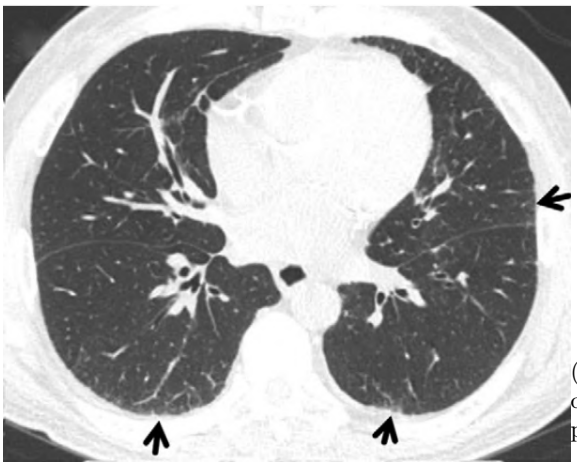

(b) Le scanner montre de nouvelles anomalies du verre dépoli (flèches) dans la zone sous-pleurale des poumons bilatéraux.

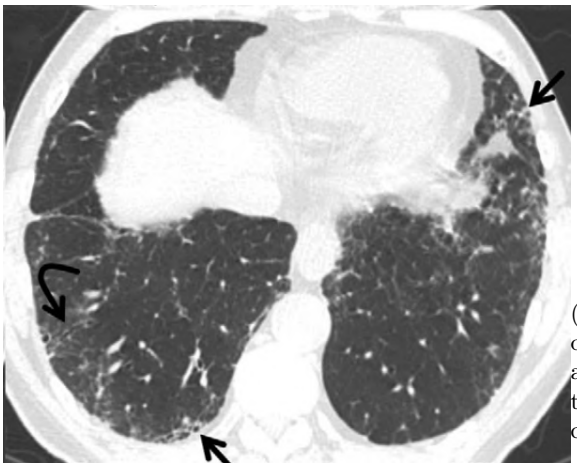

(c) Le scanner montre une gravité et une étendue accrues des anomalies (flèches droites) avec une nouvelle bronchectasie de traction indiquant une fibrose pulmonaire (flèche courbe).

FIGURE 2 : TDM de trois personnes différentes par [Hata et al., 2021], dont une normale, un cas avec un stade précoce d'ILA et un cas avec une ILA sévère ainsi qu'une FPI.

sur l'IA tels que l'apprentissage automatique et les jumeaux numériques sont des tendances croissantes dans les soins de santé [Lim et al., 2020], et ont un impact significatif sur les cliniciens en fournissant une interprétation rapide pour les systèmes de santé, en améliorant le flux de travail, le potentiel de réduction des erreurs médicales et pour les patients en leur permettant de traiter leurs données afin de promouvoir la santé [Topol, 2019].

L'apprentissage automatique est un outil d'IA qui utilise des données et des algorithmes pour simuler la façon dont les humains apprennent et prennent des décisions. Les algorithmes d'apprentissage automatique utilisent des données pour être entraînés à faire des prédictions ou à prendre des décisions. L'apprentissage profond est un sous-ensemble de l'intelligence artificielle qui repose sur des réseaux neuronaux multicouches et suit des algorithmes plus avancés. Ces outils d'IA peuvent être utilisés pour des applications cliniques, notamment en pneumologie, afin d'aider les cliniciens à diagnostiquer les régions malades du poumon à partir des données cliniques, en particulier des images de tomodensitométrie. Remarquablement, la radiologie thoracique est un domaine d'application naturel en raison du grand nombre d'images et de rapports stockés qui facilitent l'apprentissage des algorithmes d'apprentissage profond [Chassagnon et al., 2021]. L'évaluation de la tomodensitométrie à haute résolution par un algorithme d'apprentissage profond pourrait fournir une classification peu coûteuse, reproductible et quasi instantanée de la maladie pulmonaire fibrotique avec une précision de niveau humain. Ces méthodes pourraient être utiles aux centres dans lesquels l'expertise en imagerie thoracique est rare, ainsi que pour la stratification des patients dans les essais cliniques [Walsh et al., 2018]. Ainsi, les algorithmes de ML et d'apprentissage profond peuvent aider les radiologues dans un certain nombre de tâches, telles que la détection ou la caractérisation d'anomalies radiologiques ou à des fins pronostiques. Pour les tâches de détection, la validation humaine par confirmation visuelle est possible pour créer des données annotées pour l'apprentissage automatique supervisé [Chassagnon et al., 2021].

L'application d'approches basées sur les données dans les soins de santé a été moins bénéfique, jusqu'à présent, en ce qui concerne la personnalisation et la transparence. Les patients reprochent souvent à ces approches de ne pas fournir des soins centrés sur le patient et les cliniciens de créer une boîte noire opaque, ce qui réduit la transparence en matière d'aide à la décision [Kaul et al., 2023]. D'un autre côté, la synergie entre les modèles mécanistiques et les modèles basés sur les données s'est révélée utile pour faciliter le diagnostic, le traitement et l'évaluation du pronostic [Corral-Acero et al., 2020]. Les jumeaux numériques sont utiles pour le diagnostic, le pronostic et le traitement des maladies [Allen et al., 2021] dans la mesure où les données sont synchronisées avec leur modèle mécanistiques, qui fournit les explications physiques du système, améliorant la plausibilité des résultats et augmentant leur crédibilité [Corral-Acero et al., 2020]. Cela montre l'importance de la modélisation mécanistiques dans les outils numériques, qui peuvent être utilisés pour fournir une compréhension physique du comportement des poumons.

Modélisation mécanique du poumon

La modélisation mécanique du poumon vise à décrire le comportement physique du poumon sur une base mécanique. Ces modèles établissent une relation mathématique entre la charge exercée sur le poumon, telle que la pression atmosphérique, et la déformation, qui correspond à la physiologie du poumon. Le parenchyme pulmonaire comprend différentes phases, telles que l'air, le sang et le tissu interstitiel composé de fibres élastiques et de collagène. La modélisation mécanique du poumon vise à étudier l'interaction entre les différentes phases sous différentes charges et conditions limites. Néanmoins, en raison de la complexité du parenchyme pulmonaire et de son comportement, différentes hypo-

thèses peuvent être envisagées pour simplifier les modèles mathématiques proposés pour modéliser le comportement du poumon.

Le poumon est largement modélisé, de l'échelle de l'organe à l'échelle de l'alvéole. La modélisation à l'échelle de l'organe vise à étudier le comportement du poumon à l'échelle macroscopique en interaction avec son environnement et à fournir des estimations structurelles. Les modèles à l'échelle de l'organe sont des estimations structurelles relativement peu coûteuses du parenchyme pulmonaire considéré comme un matériau continu. Cependant, ils présentent des limites en ce qui concerne la représentation des caractéristiques microscopiques et leur contribution à l'échelle macroscopique. D'autre part, les modèles à l'échelle de l'alvéole visent à étudier le comportement à l'échelle microscopique et peuvent être utilisés pour l'analyse numérique de la distribution des contraintes et de la déformation septale au sein de l'alvéole.

À l'échelle de l'organe ou du tissu, le parenchyme pulmonaire est soit considéré comme un matériau compressible continu, isotrope et non linéaire subissant de grandes déformations [Tawhai et al., 2009, Bel-Brunon et al., 2014, Birzle et al., 2018], soit comme un matériau poreux, où le tissu de l'interstitium est considéré comme un solide dont le comportement peut être étudié en interaction avec l'air en tant que fluide. La poromécanique, introduite fondamentalement par [Biot, 1941, Terzaghi, 1943, Biot and Temple, 1972], est employée pour modéliser le comportement des milieux poreux à l'échelle macroscopique, sur la base de la théorie des mélanges [Bedford and Drumheller, 1979, Bowen, 1982, Coussy, 2004]. Plus précisément, elle peut être appliquée pour modéliser le parenchyme pulmonaire comme un matériau hyperélastique poreux soumis à des déformations finies [Patte et al., 2022b]. Selon cette approche, le comportement du tissu doit être décrit par un potentiel hyperélastique [Berger et al., 2016, Patte et al., 2022b]. Divers modèles hyperélastiques non linéaires quasi-statiques sont proposés pour étudier le comportement du parenchyme pulmonaire [Rausch et al., 2011, Bel-Brunon et al., 2014, Birzle et al., 2019, Jorba et al., 2019]. En outre, certains modèles rhéologiques permettent de saisir le comportement dynamique et mécanique du parenchyme [Romero, 1998].

Pour mieux comprendre le comportement du poumon à l'échelle microscopique et étudier l'effet des maladies pulmonaires liées à l'interstitium sur le tissu interstitiel et d'autres propriétés microscopiques, des modèles à l'échelle de l'alvéole ont été introduits, en utilisant une approche micromécanique. Une telle approche permet de modéliser des phénomènes physiologiques plus complexes se produisant à l'échelle de l'alvéole, tels que la tension superficielle [Wiechert et al., 2009, Coussy, 2010, Koshiyama et al., 2018] ou la croissance tissulaire [Genet, 2019]. En outre, la modélisation micromécanique nous permet d'étudier la distribution des contraintes et des déformations sous différentes charges et conditions limites [Concha et al., 2018, Álvarez-Barrientos et al., 2021] et d'analyser les propriétés effectives sur la base des caractéristiques microscopiques et morphologiques [Zhu et al., 2017]. Les modèles micromécaniques nécessitent la définition de la géométrie de la microstructure. Il existe différentes approches pour définir la structure dans les modèles à l'échelle de l'alvéole.

La microstructure du poumon est générée soit par segmentation des scans CT-RX du poumon, soit en utilisant des géométries idéalisées. La génération de la microstructure du poumon à partir d'images tomodensitométriques concerne soit la segmentation du poumon entier à l'aide d'une tomodensitométrie multi-lames pour reconstruire l'arbre bronchique [Fetita et al., 2004], ce qui permet d'obtenir des maillages informatiques spécifiques au sujet [Tawhai et al., 2004], soit la segmentation des parois des alvéoles. Dans ce dernier cas, la microstructure de l'acinus est extraite à partir d'images binaires en niveaux de gris, en utilisant une combinaison des traitements d'images [Xiao et al., 2016, Koshiyama et al., 2018]. Néanmoins, une telle approche pour

extraire la géométrie exacte à partir d'images CT peut être coûteuse, non seulement dans le contexte de la génération, mais aussi du calcul. Par ailleurs, certains chercheurs ont utilisé des éléments géométriques simplifiés pour reconstruire la géométrie de l'acinus, en considérant les formes polyédriques moyennes des alvéoles comme représentant la géométrie représentative des alvéoles [Dale et al., 1980, Denny and Schroter, 2000, Roth et al., 2017, Concha et al., 2018].

Adapter les modèles au comportement physiologique du poumon

Les modèles mécaniques développés peuvent être adaptés au comportement physiologique du parenchyme pulmonaire en assimilant des données expérimentales. Ainsi, les propriétés matérielles comprennent la rigidité, la densité, la viscoélasticité et la porosité, et peuvent être obtenues à partir d'essais expérimentaux sur des tissus excisés [Neelakantan et al., 2022]. Diverses expériences ont été menées sur le poumon, sur la base de différents protocoles. Les expériences sont menées in vivo, lorsque les mesures sont effectuées dans un corps vivant, ou ex vivo. Dans les expériences in vivo, la déformation du poumon lors de la respiration spontanée ou de la ventilation mécanique est mesurée à l'aide de la tomodensitométrie [Leclerc et al., 2009, Lovric et al., 2017], ou l'imagerie par résonance magnétique (IRM) [Boucneau et al., 2020] où la déformation peut être suivie grâce à l'enregistrement des images à différents pas de temps [Genet et al., 2018, Patte et al., 2022a, Genet, 2023, Laville et al., 2023]. D'autre part, les expériences ex vivo permettent un plus large éventail d'expériences, telles que l'essai de traction [Birzle et al., 2018, Arora et al., 2021], en plus des expériences pression-volume [Schürch et al., 1976, Bachofen et al., 1987], où la déformation peut être mesurée par corrélation d'image numérique [Mariano et al., 2020]. Il convient de noter que ces expériences ex vivo permettent d'étudier des phénomènes microscopiques tels que la tension superficielle [Smith and Stamenovic, 1986, Bachofen and Schürch, 2001], qui sont également modélisés dans les approches micromécaniques [Karakaplan et al., 1980, Kowe et al., 1986].

Le lien entre l'évolution des caractéristiques mécaniques et morphologiques microscopiques du parenchyme pulmonaire due à la FPI, qui est qualitativement compliqué à interpréter, peut être abordé à l'aide d'un modèle mécanique capable d'étudier la relation entre les propriétés microscopiques et le comportement à l'échelle de l'organe. Un tel modèle est bénéfique pour deux raisons principales. D'une part, il facilite le diagnostic de la fibrose pulmonaire idiopathique en quantifiant les images tomodensitométriques dans un délai relativement court, ce qui permet d'intervenir à temps avant que la maladie ne progresse. D'autre part, il facilite le pronostic en calculant les concentrations de contraintes dans la microstructure et en les comparant aux limites tissulaires.

Objectifs : Modélisation du parenchyme pulmonaire : de l'échelle microscopique à l'échelle macroscopique

Nous visons à développer un modèle mécanique multi-échelle capable de simuler le comportement du parenchyme pulmonaire et de relier les caractéristiques microscopiques au comportement macroscopique du parenchyme. Un tel modèle, qui prend en compte les phénomènes physiologiques microscopiques dans le parenchyme, devrait combler le fossé entre les réponses mécaniques mesurées expérimentalement à l'échelle du tissu et de l'organe. Plus précisément, le but de cette thèse s'articule autour de deux objectifs principaux :

Objectif 1 - Construire un modèle micro-poro-mécanique

Nous visons à introduire un modèle poromécanique microscopique général qui peut simuler le comportement des matériaux poreux compressibles et incompressibles à l'échelle microscopique et la contribution des caractéristiques mécaniques et morphologiques microscopiques au comportement macroscopique. Un tel modèle sera défini sur la base d'une microstructure géométrique et d'un comportement constitutif, et appliqué à des déformations finies. En outre, il permettra de montrer non seulement la distribution des contraintes et des déformations microscopiques sous diverses charges telles que les contraintes macroscopiques, les déformations macroscopiques et la pression des fluides, mais aussi leurs manifestations moyennes à l'échelle macroscopique.

Objectif 2 - Adapter le modèle au comportement du poumon

Nous visons à adapter le modèle micromécanique de manière à ce qu'il puisse réellement reproduire le comportement du poumon. Nous introduisons tout d'abord la tension superficielle en tant que force microscopique appliquée à l'interface air-tissu. Ensuite, les paramètres morphologiques et mécaniques du modèle, ainsi que les paramètres du modèle de tension superficielle, sont ajustés de manière à ce que la réponse du modèle corresponde aux données expérimentales existantes.

Aperçu du travail

Chapitre 1 - Éléments de physiologie pulmonaire, modélisation et expériences

Dans le premier chapitre, nous abordons la physiologie du système pulmonaire, avec un accent plus précis sur les poumons. L'anatomie et la fonction du poumon dans le système respiratoire pendant la respiration sont discutées. Ensuite, nous expliquons comment le poumon est modélisé mécaniquement à partir d'éléments de physiologie. Des modèles à deux échelles différentes, l'échelle des alvéoles et l'échelle des organes, ainsi que différents éléments de modélisation, tels que la géométrie, le comportement constitutif et les conditions aux limites, sont discutés. Au final, nous passons en revue différents types d'expériences menées sur le poumon et les données mesurées, qui peuvent être comparées aux modèles.

Chapitre 2 - Micro-poro-mécanique à déformations finies : formulation et analyse comparée avec la macro-poro-mécanique

Dans le deuxième chapitre, nous expliquons notre approche pour construire un modèle micro-poro-mécanique. Cette approche propose une formulation générale applicable à toute microstructure soumise à toute contrainte, déformation ou pression interne macroscopique. Une telle approche microscopique permet d'étudier la contribution des caractéristiques microscopiques à l'échelle macroscopique. La réponse globale du modèle micro-poro-mécanique est comparée à un modèle macroscopique basé sur les travaux de [Chapelle and Moireau, 2014] et [Patte et al., 2022b] afin d'étudier la pertinence de tels modèles pour capturer le comportement de milieux poreux sous des déformations finies et sous différentes conditions de chargement, en plus d'afficher le couplage entre ces quantités.

Ce chapitre prend la forme d'un article pré-print co-écrit par Mahdi Manoochehrtayebi, Aline Bel-Brunon et Martin Genet, intitulé *Micro-poro-mécanique à déformations finies :*

formulation et analyse comparée avec la macro-poro-mécanique , soumis au Journal of the Mechanics and Physics of Solids.

Chapitre 3 - Eléments de modélisation microstructurale

Dans ce chapitre, nous introduisons une méthode pour générer des microstructures géométriques en tant qu'élément du modèle micro-poro-mécanique, qui peut être utilisée pour modéliser des tissus biologiques tels que le parenchyme pulmonaire. Cette méthode utilise un algorithme pour générer des microstructures irrégulières et aléatoires à l'aide de distributions de seeds. Des maillages poreux périodiques sont générés à partir d'un pavage de Voronoi des seeds. Même si les seeds peuvent être distribuées selon n'importe quel motif, nous avons défini un mode de distribution des seeds, conduisant à des géométries avec une irrégularité de niveau et une porosité quantifiées.

Chapitre 4 - Vers un micro-modèle physiologique : intégration de la tension superficielle et ajustement aux expériences

Ce chapitre développe le modèle micro-poro-mécanique générique proposé dans le chapitre 2 pour la modélisation du parenchyme pulmonaire. Premièrement, un loi de comportement exponentielle est proposée pour capturer le comportement de raidissement du poumon induit par la contrainte. Deuxièmement, les tensions superficielles sont incorporées dans le modèle en tant que phénomène physiologique à l'intérieur du poumon, bénéficiant du micromodèle pour capturer les caractéristiques microstructurales. Enfin, les paramètres du modèle sont identifiés sur la base de données expérimentales de la littérature avec et sans présence de tension superficielle.

Communications

Présentations orales

- **Présentation orale lors de la journée X-UTC.**
  Université de technologie de Compiègne, Compiègne, France - mars 2022.
- **Présentation orale au Symposium Jean Mandel.**
  École Polytechnique, Palaiseau, France - juin 2022.
- **Présentation orale à la conférence CMBE.**
  Politecnico di Milano, Milan, Italie - juin 2022.
- **Présentation orale au GDR MécaBioSanté.**
  Sorbonne Université, Paris, France - novembre 2022.
- **Présentation orale à la conférence CMBBE.**
  Institut Polytechnique des Arts et Métiers, Paris, France - mai 2023.

Pré-publication

- **Micro-poro-mécanique : formulation et analyse comparée avec la macro-poro-mécanique**
  M. Manoochehrtayebi, A. Bel-Brunon et M. Genet
  Soumis.

Bibliographie

[Allen et al., 2021] Allen, A., Siefkas, A., Pellegrini, E., Burdick, H., Barnes, G., Calvert, J., Mao, Q., and Das, R. (2021). A Digital Twins Machine Learning Model for Forecasting Disease Progression in Stroke Patients. *Applied Sciences*, 11(12) :5576.

[Álvarez-Barrientos et al., 2021] Álvarez-Barrientos, F., Hurtado, D. E., and Genet, M. (2021). Pressure-driven micro-poro-mechanics : A variational framework for modeling the response of porous materials. *International Journal of Engineering Science*, 169 :103586.

[Antoniou et al., 2014] Antoniou, K. M., Margaritopoulos, G. A., Tomassetti, S., Bonella, F., Costabel, U., and Poletti, V. (2014). Interstitial lung disease. *European Respiratory Review*, 23(131) :40–54. 150 citations (Crossref) [2023-12-18].

[Arora et al., 2021] Arora, H., Mitchell, R., Johnston, R., Manolesos, M., Howells, D., Sherwood, J., Bodey, A., and Wanelik, K. (2021). Correlating Local Volumetric Tissue Strains with Global Lung Mechanics Measurements. *Materials*, 14(2) :439.

[Ash et al., 2017] Ash, S. Y., Harmouche, R., Ross, J. C., Diaz, A. A., Hunninghake, G. M., Putman, R. K., Onieva, J., Martinez, F. J., Choi, A. M., Lynch, D. A., Hatabu, H., Rosas, I. O., Estepar, R. S. J., and Washko, G. R. (2017). The Objective Identification and Quantification of Interstitial Lung Abnormalities in Smokers. *Academic Radiology*, 24(8) :941–946.

[Bachofen et al., 1987] Bachofen, H., Schurch, S., Urbinelli, M., and Weibel, E. R. (1987). Relations among alveolar surface tension, surface area, volume, and recoil pressure. *Journal of Applied Physiology*, 62(5) :1878–1887.

[Bachofen and Schürch, 2001] Bachofen, H. and Schürch, S. (2001). Alveolar surface forces and lung architecture. *Comparative Biochemistry and Physiology Part A : Molecular & Integrative Physiology*, 129(1) :183–193.

[Bedford and Drumheller, 1979] Bedford, A. and Drumheller, D. (1979). A variational theory of porous media. *International Journal of Solids and Structures*, 15(12) :967–980.

[Bel-Brunon et al., 2014] Bel-Brunon, A., Kehl, S., Martin, C., Uhlig, S., and Wall, W. (2014). Numerical identification method for the non-linear viscoelastic compressible behavior of soft tissue using uniaxial tensile tests and image registration – Application to rat lung parenchyma. *Journal of the Mechanical Behavior of Biomedical Materials*, 29 :360–374.

[Berger et al., 2016] Berger, L., Bordas, R., Burrowes, K., Grau, V., Tavener, S., and Kay, D. (2016). A poroelastic model coupled to a fluid network with applications in lung modelling. *International Journal for Numerical Methods in Biomedical Engineering*, 32(1).

[Biot, 1941] Biot, M. A. (1941). General Theory of Three-Dimensional Consolidation. *Journal of Applied Physics*, 12(2) :155–164.

[Biot and Temple, 1972] Biot, M. A. and Temple, G. (1972). Theory of Finite Deformations of Porous Solids. *Indiana University Mathematics Journal*, 21(7) :597–620. Publisher : Indiana University Mathematics Department.

[Birzle et al., 2019] Birzle, A. M., Martin, C., Uhlig, S., and Wall, W. A. (2019). A coupled approach for identification of nonlinear and compressible material models for soft tissue based on different experimental setups – Exemplified and detailed for lung parenchyma. *Journal of the Mechanical Behavior of Biomedical Materials*, 94 :126–143.

[Birzle et al., 2018] Birzle, A. M., Martin, C., Yoshihara, L., Uhlig, S., and Wall, W. A. (2018). Experimental characterization and model identification of the nonlinear compressible material behavior of lung parenchyma. *Journal of the Mechanical Behavior of Biomedical Materials*, 77 :754–763.

[Boucneau et al., 2020] Boucneau, T., Fernandez, B., Larson, P., Darrasse, L., and Maître, X. (2020). 3D Magnetic Resonance Spirometry. *Scientific Reports*, 10(1) :9649.

[Bowen, 1982] Bowen, R. M. (1982). Compressible porous media models by use of the theory of mixtures. *International Journal of Engineering Science*, 20(6) :697–735.

[Chapelle and Moireau, 2014] Chapelle, D. and Moireau, P. (2014). General coupling of porous flows and hyperelastic formulations—From thermodynamics principles to energy balance and compatible time schemes. *European Journal of Mechanics - B/Fluids*, 46 :82–96.

[Chassagnon et al., 2021] Chassagnon, G., Vakalopoulou, M., Régent, A., Sahasrabudhe, M., Marini, R., Hoang-Thi, T.-N., Dinh-Xuan, A.-T., Dunogué, B., Mouthon, L., Paragios, N., and Revel, M.-P. (2021). Elastic Registration–driven Deep Learning for Longitudinal Assessment of Systemic Sclerosis Interstitial Lung Disease at CT. *Radiology*, 298(1) :189–198.

[Concha et al., 2018] Concha, F., Sarabia-Vallejos, M., and Hurtado, D. E. (2018). Micromechanical model of lung parenchyma hyperelasticity. *Journal of the Mechanics and Physics of Solids*, 112 :126–144.

[Corral-Acero et al., 2020] Corral-Acero, J., Margara, F., Marciniak, M., Rodero, C., Loncaric, F., Feng, Y., Gilbert, A., Fernandes, J. F., Bukhari, H. A., Wajdan, A., Martinez, M. V., Santos, M. S., Shamohammdi, M., Luo, H., Westphal, P., Leeson, P., DiAchille, P., Gurev, V., Mayr, M., Geris, L., Pathmanathan, P., Morrison, T., Cornelussen, R., Prinzen, F., Delhaas, T., Doltra, A., Sitges, M., Vigmond, E. J., Zacur, E., Grau, V., Rodriguez, B., Remme, E. W., Niederer, S., Mortier, P., McLeod, K., Potse, M., Pueyo, E., Bueno-Orovio, A., and Lamata, P. (2020). The 'Digital Twin' to enable the vision of precision cardiology. *European Heart Journal*, 41(48) :4556–4564.

[Coussy, 2004] Coussy, O. (2004). *Poromechanics*. John Wiley & Sons.

[Coussy, 2010] Coussy, O. (2010). Mechanics and Physics of Porous Solids.

[Dale et al., 1980] Dale, P., Matthews, F. L., and Schroter, R. C. (1980). Finite element analysis of lung alveolus. *Journal of Biomechanics*, 13(10) :865–873.

[Demedts et al., 2001] Demedts, M., Wells, A. U., Anto, J. M., Costabel, U., Hubbard, R., Cullinan, P., Slabbynck, H., Rizzato, G., Poletti, V., Verbeken, E. K., Thomeer, M. J., Kokkarinen, J., Dalphin, J. C., and Taylor, A. N. (2001). Interstitial lung diseases : an epidemiological overview.

[Denny and Schroter, 2000] Denny, E. and Schroter, R. C. (2000). Viscoelastic Behavior of a Lung Alveolar Duct Model. *Journal of Biomechanical Engineering*, 122(2) :143–151.

[Doyle et al., 2012] Doyle, T. J., Washko, G. R., Fernandez, I. E., Nishino, M., Okajima, Y., Yamashiro, T., Divo, M. J., Celli, B. R., Sciurba, F. C., Silverman, E. K., Hatabu, H., Rosas, I. O., and Hunninghake, G. M. (2012). Interstitial Lung Abnormalities and Reduced Exercise Capacity. *American Journal of Respiratory and Critical Care Medicine*, 185(7) :756–762. 98 citations (Crossref) [2023-11-09].

[Fetita et al., 2004] Fetita, C., Preteux, F., Beigelman-Aubry, C., and Grenier, P. (2004). Pulmonary Airways : 3-D Reconstruction From Multislice CT and Clinical Investigation. *IEEE Transactions on Medical Imaging*, 23(11) :1353–1364.

[Genet, 2019] Genet, M. (2019). A relaxed growth modeling framework for controlling growth-induced residual stresses. *Clinical Biomechanics*, 70 :270–277.

[Genet, 2023] Genet, M. (2023). Finite strain formulation of the discrete equilibrium gap principle : application to mechanically consistent regularization for large motion tracking. *Comptes Rendus. Mécanique*, 351(G2) :429–458.

[Genet et al., 2018] Genet, M., Stoeck, C., Von Deuster, C., Lee, L., and Kozerke, S. (2018). Equilibrated warping : Finite element image registration with finite strain equilibrium gap regularization. *Medical Image Analysis*, 50 :1–22.

[Hata et al., 2021] Hata, A., Schiebler, M. L., Lynch, D. A., and Hatabu, H. (2021). Interstitial Lung Abnormalities : State of the Art. *Radiology*, 301(1) :19–34.

[Hatabu et al., 2019] Hatabu, H., Hunninghake, G. M., and Lynch, D. A. (2019). Interstitial Lung Abnormality : Recognition and Perspectives. *Radiology*, 291(1) :1–3.

[Hinz and Suki, 2016] Hinz, B. and Suki, B. (2016). Does Breathing Amplify Fibrosis ?

[Iwasawa et al., 2019] Iwasawa, T., Okudela, K., Takemura, T., Fukuda, T., Matsushita, S., Baba, T., Ogura, T., Tajiri, M., and Yoshizawa, A. (2019). Computer-aided Quantification of Pulmonary Fibrosis in Patients with Lung Cancer : Relationship to Disease-free Survival. *Radiology*, 292(2) :489–498.

[Jorba et al., 2019] Jorba, I., Beltrán, G., Falcones, B., Suki, B., Farré, R., García-Aznar, J. M., and Navajas, D. (2019). Nonlinear elasticity of the lung extracellular microenvironment is regulated by macroscale tissue strain. *Acta Biomaterialia*, 92 :265–276.

[Karakaplan et al., 1980] Karakaplan, A. D., Bieniek, M. P., and Skalak, R. (1980). A Mathematical Model of Lung Parenchyma. *Journal of Biomechanical Engineering*, 102(2) :124–136.

[Kaul et al., 2023] Kaul, R., Ossai, C., Forkan, A. R. M., Jayaraman, P. P., Zelcer, J., Vaughan, S., and Wickramasinghe, N. (2023). The role of AI for developing digital twins in healthcare : The case of cancer care. *WIREs Data Mining and Knowledge Discovery*, 13(1) :e1480.

[Koshiyama et al., 2018] Koshiyama, K., Nishimoto, K., Ii, S., Sera, T., and Wada, S. (2018). Heterogeneous structure and surface tension effects on mechanical response in pulmonary acinus : A finite element analysis. *Clinical Biomechanics*.

[Kowe et al., 1986] Kowe, R., Schroter, R., Matthews, F., and Hitchings, D. (1986). Analysis of elastic and surface tension effects in the lung alveolus using finite element methods. *Journal of Biomechanics*, 19(7) :541–549.

[Laville et al., 2023] Laville, C., Fetita, C., Gille, T., Brillet, P.-Y., Nunes, H., Bernaudin, J.-F., and Genet, M. (2023). Comparison of optimization parametrizations for regional lung compliance estimation using personalized pulmonary poromechanical modeling. *Biomechanics and Modeling in Mechanobiology*.

[Leclerc et al., 2009] Leclerc, H., Périé, J.-N., Roux, S., and Hild, F. (2009). Integrated Digital Image Correlation for the Identification of Mechanical Properties. In Gagalowicz, A. and Philips, W., editors, *Computer Vision/Computer Graphics CollaborationTechniques*, volume 5496, pages 161–171. Springer Berlin Heidelberg, Berlin, Heidelberg.

[Lederer and Martinez, 2018] Lederer, D. J. and Martinez, F. J. (2018). Idiopathic Pulmonary Fibrosis. *New England Journal of Medicine*, 378(19) :1811–1823. 1001 citations (Crossref) [2023-10-23].

[Lim et al., 2020] Lim, K. Y. H., Zheng, P., and Chen, C.-H. (2020). A state-of-the-art survey of Digital Twin : techniques, engineering product lifecycle management and business innovation perspectives. *Journal of Intelligent Manufacturing*, 31(6) :1313–1337.

[Lovric et al., 2017] Lovric, G., Mokso, R., Arcadu, F., Vogiatzis Oikonomidis, I., Schittny, J. C., Roth-Kleiner, M., and Stampanoni, M. (2017). Tomographic in vivo microscopy for the study of lung physiology at the alveolar level. *Scientific Reports*, 7(1) :12545.

[Mariano et al., 2020] Mariano, C. A., Sattari, S., Maghsoudi-Ganjeh, M., Tartibi, M., Lo, D. D., and Eskandari, M. (2020). Novel Mechanical Strain Characterization of Ventilated ex vivo Porcine and Murine Lung using Digital Image Correlation. *Frontiers in Physiology*, 11 :600492.

[Miller et al., 2018] Miller, E. R., Putman, R. K., Vivero, M., Hung, Y., Araki, T., Nishino, M., Washko, G. R., Rosas, I. O., Hatabu, H., Sholl, L. M., and Hunninghake, G. M. (2018). Histopathology of Interstitial Lung Abnormalities in the Context of Lung Nodule Resections. *American Journal of Respiratory and Critical Care Medicine*, 197(7) :955–958.

[Navaratnam et al., 2011] Navaratnam, V., Fleming, K. M., West, J., Smith, C. J. P., Jenkins, R. G., Fogarty, A., and Hubbard, R. B. (2011). The rising incidence of idiopathic pulmonary fibrosis in the UK. *Thorax*, 66(6) :462–467.

[Neelakantan et al., 2022] Neelakantan, S., Xin, Y., Gaver, D. P., Cereda, M., Rizi, R., Smith, B. J., and Avazmohammadi, R. (2022). Computational lung modelling in respiratory medicine. *Journal of The Royal Society Interface*, 19(191) :20220062.

[Patte et al., 2022a] Patte, C., Brillet, P.-Y., Fetita, C., Bernaudin, J.-F., Gille, T., Nunes, H., Chapelle, D., and Genet, M. (2022a). Estimation of Regional Pulmonary Compliance in Idiopathic Pulmonary Fibrosis Based on Personalized Lung Poromechanical Modeling. *Journal of Biomechanical Engineering*, 144(9) :091008.

[Patte et al., 2022b] Patte, C., Genet, M., and Chapelle, D. (2022b). A quasi-static poromechanical model of the lungs. *Biomechanics and Modeling in Mechanobiology*.

[Plantier et al., 2018] Plantier, L., Cazes, A., Dinh-Xuan, A.-T., Bancal, C., Marchand-Adam, S., and Crestani, B. (2018). Physiology of the lung in idiopathic pulmonary fibrosis. *European Respiratory Review*, 27(147) :170062.

[Poletti et al., 2013] Poletti, V., Ravaglia, C., Buccioli, M., Tantalocco, P., Piciucchi, S., Dubini, A., Carloni, A., Chilosi, M., and Tomassetti, S. (2013). Idiopathic Pulmonary Fibrosis : Diagnosis and Prognostic Evaluation. *Respiration*, 86(1) :5–12.

[Putman et al., 2019] Putman, R. K., Gudmundsson, G., Axelsson, G. T., Hida, T., Honda, O., Araki, T., Yanagawa, M., Nishino, M., Miller, E. R., Eiriksdottir, G., Gudmundsson, E. F., Tomiyama, N., Honda, H., Rosas, I. O., Washko, G. R., Cho, M. H., Schwartz, D. A., Gudnason, V., Hatabu, H., and Hunninghake, G. M. (2019). Imaging Patterns Are Associated with Interstitial Lung Abnormality Progression and Mortality. *American Journal of Respiratory and Critical Care Medicine*, 200(2) :175–183.

[Rausch et al., 2011] Rausch, S., Martin, C., Bornemann, P., Uhlig, S., and Wall, W. (2011). Material model of lung parenchyma based on living precision-cut lung slice testing. *Journal of the Mechanical Behavior of Biomedical Materials*, 4(4) :583–592.

[Rogliani et al., 2016] Rogliani, P., Calzetta, L., Cavalli, F., Matera, M. G., and Cazzola, M. (2016). Pirfenidone, nintedanib and N-acetylcysteine for the treatment of idiopathic pulmonary fibrosis : A systematic review and meta-analysis. *Pulmonary Pharmacology & Therapeutics*, 40 :95–103.

[Romero, 1998] Romero, F. (1998). A recruitment-based rheological model for mechanical behavior of soft tissues. *Biorheology*, 35(1) :17–35.

[Roth et al., 2017] Roth, C. J., Yoshihara, L., and Wall, W. A. (2017). A simplified parametrised model for lung microstructures capable of mimicking realistic geometrical and mechanical properties. *Computers in Biology and Medicine*, 89 :104–114.

[Sauleda et al., 2018] Sauleda, J., Núñez, B., Sala, E., and Soriano, J. (2018). Idiopathic Pulmonary Fibrosis : Epidemiology, Natural History, Phenotypes. *Medical Sciences*, 6(4) :110.

[Schürch et al., 1976] Schürch, S., Goerke, J., and Clements, J. A. (1976). Direct determination of surface tension in the lung. *Proceedings of the National Academy of Sciences*, 73(12) :4698–4702.

[Smith and Stamenovic, 1986] Smith, J. C. and Stamenovic, D. (1986). Surface forces in lungs. I. Alveolar surface tension-lung volume relationships. *Journal of Applied Physiology*, 60(4) :1341–1350.

[Swigris, 2005] Swigris, J. J. (2005). Health-related quality of life in patients with idiopathic pulmonary fibrosis : a systematic review. *Thorax*, 60(7) :588–594.

[Tawhai et al., 2004] Tawhai, M. H., Hunter, P., Tschirren, J., Reinhardt, J., McLennan, G., and Hoffman, E. A. (2004). CT-based geometry analysis and finite element models of the human and ovine bronchial tree. *Journal of Applied Physiology*, 97(6) :2310–2321.

[Tawhai et al., 2009] Tawhai, M. H., Nash, M. P., Lin, C.-L., and Hoffman, E. A. (2009). Supine and prone differences in regional lung density and pleural pressure gradients in the human lung with constant shape. *Journal of Applied Physiology*, 107(3) :912–920.

[Terzaghi, 1943] Terzaghi, K. (1943). *Theoretical Soil Mechanics*. John Wiley & Sons, Inc., Hoboken, NJ, USA.

[Topol, 2019] Topol, E. J. (2019). High-performance medicine : the convergence of human and artificial intelligence. *Nature Medicine*, 25(1) :44–56.

[Travis et al., 2013] Travis, W. D., Costabel, U., Hansell, D. M., King, T. E., Lynch, D. A., Nicholson, A. G., Ryerson, C. J., Ryu, J. H., Selman, M., Wells, A. U., Behr, J., Bouros, D., Brown, K. K., Colby, T. V., Collard, H. R., Cordeiro, C. R., Cottin, V., Crestani, B., Drent, M., Dudden, R. F., Egan, J., Flaherty, K., Hogaboam, C., Inoue, Y., Johkoh, T., Kim, D. S., Kitaichi, M., Loyd, J., Martinez, F. J., Myers, J., Protzko, S., Raghu, G., Richeldi, L., Sverzellati, N., Swigris, J., and Valeyre, D. (2013). An Official American Thoracic Society/European Respiratory Society Statement : Update of the International Multidisciplinary Classification of the Idiopathic Interstitial Pneumonias. *American Journal of Respiratory and Critical Care Medicine*, 188(6) :733–748.

[Walsh et al., 2018] Walsh, S. L. F., Calandriello, L., Silva, M., and Sverzellati, N. (2018). Deep learning for classifying fibrotic lung disease on high-resolution computed tomography : a case-cohort study. *The Lancet Respiratory Medicine*, 6(11) :837–845.

[Wiechert et al., 2009] Wiechert, L., Metzke, R., and Wall, W. A. (2009). Modeling the Mechanical Behavior of Lung Tissue at the Microlevel. *Journal of Engineering Mechanics*, 135(5) :434–438.

[Xiao et al., 2016] Xiao, L., Sera, T., Koshiyama, K., and Wada, S. (2016). Morphological Characterization of Acinar Cluster in Mouse Lung Using a Multiscale-based Segmentation Algorithm on Synchrotron Micro-CT Images. *The Anatomical Record*, 299(10) :1424–1434.

[Zhu et al., 2017] Zhu, W., Blal, N., Cunsolo, S., and Baillis, D. (2017). Micromechanical modeling of effective elastic properties of open-cell foam. *International Journal of Solids and Structures*, 115-116 :61–72.

CHAPTER 1

Elements of lung physiology, modeling, and experiments

This chapter is composed of three parts. In the first part, some elements of lung physiology are discussed, including the lung function in the respiratory system, the lung anatomy, the breathing mechanisms, and the physiological phenomena inside the lung that affect the lung behavior. The second part reviews lung mechanical modeling on different scales and homogenization methods, which connect the models behavior in different scales. In the last part, different experiments are reviewed.

Contents

1.1 Elements of lung physiology

The lungs play a key role in providing oxygen (O_2) to the body and removing carbon dioxide (CO_2) waste (as schematically shown in Figure 1.1). The lungs perform this function inside the respiratory system, including other organs that help the lungs function properly. The following section details the anatomy of the respiratory system and the function of its components.

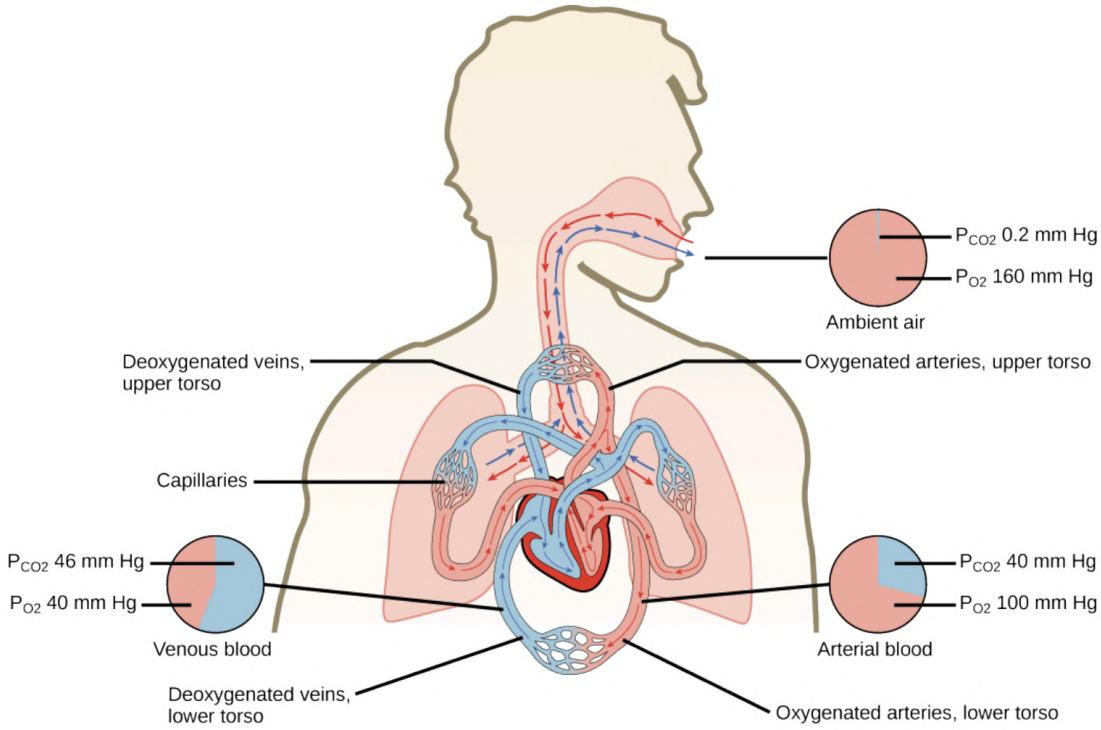

Figure 1.1: Oxygenating body through the respiratory system, Figure from OpenStax College Biology, licensed under CC BY 3.0.

1.1.1 Respiratory system anatomy

The respiratory system comprises the lungs, surrounding organs, and the respiratory tract, a pathway through which the air travels in and out of the body.

1.1.1.1 Lungs

There normally exist two lungs inside the body; the left lung and the right one. Each lung comprises several **lobes**, separated from each other by **fissures**. The right lung has three lobes (superior, middle, and inferior), and the left lung has only two lobes (superior and inferior), leaving more space for the heart.

1.1.1.2 Respiratory tract

The respiratory tract includes various parts, each of which plays a crucial role in breathing mechanics and gas exchange. The respiratory tract is divided into the upper and lower respiratory tracts. It begins from the nose and the mouth as the air entry point and continues into the lungs.

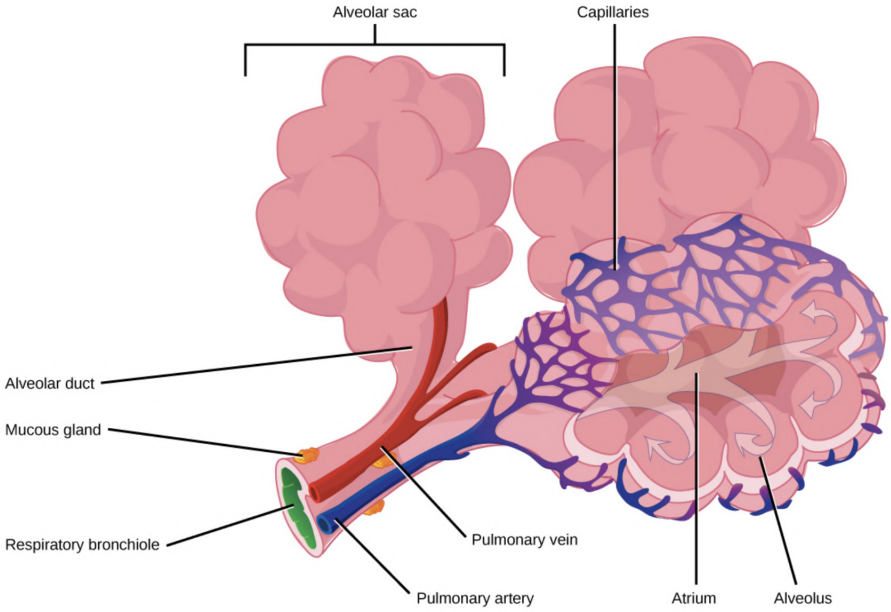

Figure 1.2: Alveolar sacs at the end of bronchioles. Figure from OpenStax College Biology, licensed under CC BY 3.0.

Upper respiratory tract

The upper respiratory tract begins at **the nose and nasal cavity**, where the air enters the respiratory system. The nose filters the incoming air and makes it warmer and more humid. The inlet air passes from the nasal cavity into the **pharynx**, located behind the mouth and nasal cavity. The pharynx is a common pathway for both the air and the food, which directs the air to the lowest component of the upper respiratory tract, called **larynx**, located at the top of the trachea. It contains vocal cords and prevents the entry of foods and liquids into the lower respiratory tract.

Lower respiratory tract

The lower respiratory tract begins from the **trachea**, which has a tube-like structure and connects the larynx to the **bronchi**. The bronchi bring the air from the trachea to the lungs. The trachea is divided into the left and right bronchi, and each bronchus branches out to smaller and narrower airways, called **bronchioles**. The bronchioles divide into smaller airways called terminal bronchioles and end up in respiratory bronchioles. At the end of respiratory bronchioles are tiny sacs called **alveoli**, shown schematically in Figure 1.2. Gas exchange occurs between the alveoli and the capillaries, which are tiny blood vessels wrapping around the alveoli. The alveoli walls are extremely thin, and are the field where the O_2 - CO_2 exchange occurs between the lung and the blood-stream. The lungs contain millions of alveoli which facilitate gas diffusion. The total surface area of the alveoli is estimated to be approximately as big as the area of a tennis court [Ananda Rao and Johncy, 2022].

1.1.1.3 Surrounding organs

There are multiple different organs around the lungs to help them deform in the breathing cycle, namely the **diaphram**, **intercostal muscles**, **chest wall**, and **pleural membrane** which are schematically shown in Figure 1.3.

Diaphragm The diaphragm is a large dome-shaped muscle beneath the lungs and at the bottom of the thoracic cavity. The diaphragm expands the thoracic cavity vertically during inhalation as it contracts and moves downward. This action expands the lungs and decreases pressure, allowing airflow into the lungs. During normal exhalation, the elastic diaphragm returns to its resting position. Additionally, the elastic recoil of the lung and of the chest wall reduces the lung volume and pushes the air out. On the other hand, during forced exhalation, for example, in intense physical activities or expelling the air forcefully, the diaphragm plays an important role in forcing upward and pushing the air out.

Intercostal muscles Intercostal muscles are located between the ribs and help them to move during breathing. There are the external and internal intercostal muscles. The contraction of the external intercostal muscles helps the ribcage lift and expand the thoracic cavity. Overall, it helps the expansion of the lung. Conversely, the contraction of the intercostal muscles during exhalation pushes the ribcage and assists in ejecting the air from the lungs.

Chest wall The chest wall forms the outer boundary of the thoracic cavity, which includes the ribs, sternum, and associated muscles. The chest wall supports the lungs and collaborates in breathing, expanding and creating negative pressure within the thoracic cavity during inhalation. This expansion which coincides with the contraction of the intercostal muscles and the diaphragm creates a negative pressure that facilitates air intake.

Pleural membrane The pleural membrane lines the inner surface of the chest cavity. It covers the lungs and consists of two layers: the visceral pleura, attached to the surface of the lungs, and the parietal pleura, which lines the diaphragm and the chest wall. The space between these two layers that contains pleural fluid is called the pleural cavity. This pleural fluid reduces friction during breathing by lubricating the pleural surfaces.

In addition to the organs surrounding the lungs that facilitate breathing, microscopic physiological phenomena affect lung behavior. One of these phenomena is related to a substance called **surfactant**, which is present on the alveolar walls. Surfactant plays an essential role in the behavior of the lungs, and its impact is discussed in detail in the following section.

1.1.2 Surfactant

Surfactant is a thin-layer fluid on the alveolar wall that affects the surface tension at the alveolar wall and air interface. This layer is extremely thin and does not interfere with pulmonary gas exchange, while it decreases the surface tension between the tissue and the air.

There is a dependency between the surface tension and the interfacial surface area or volume. Nonetheless, at lung volumes of 80% total lung capacity or more, the alveolar surface area-volume relation is mainly independent of surface tension [Bachofen and Schürch, 2001]. Surface tension acts at the tissue interface, while the value of this force depends on the fluid with which the tissue is in contact. Figure 1.4 shows scanning electron micrographs of the alveolar ducts, illustrating the presence of surface tension while the lung is filled with air and its absence when filled with saline. In the case of saline-filled, there is no surface tension between the tissue and saline, while the surface tension is evident between the tissue and air-filled lung, increasing the diameters of the alveolar ducts [Bachofen and Schürch, 2001]. Conversely, in the case of detergent-rinsed

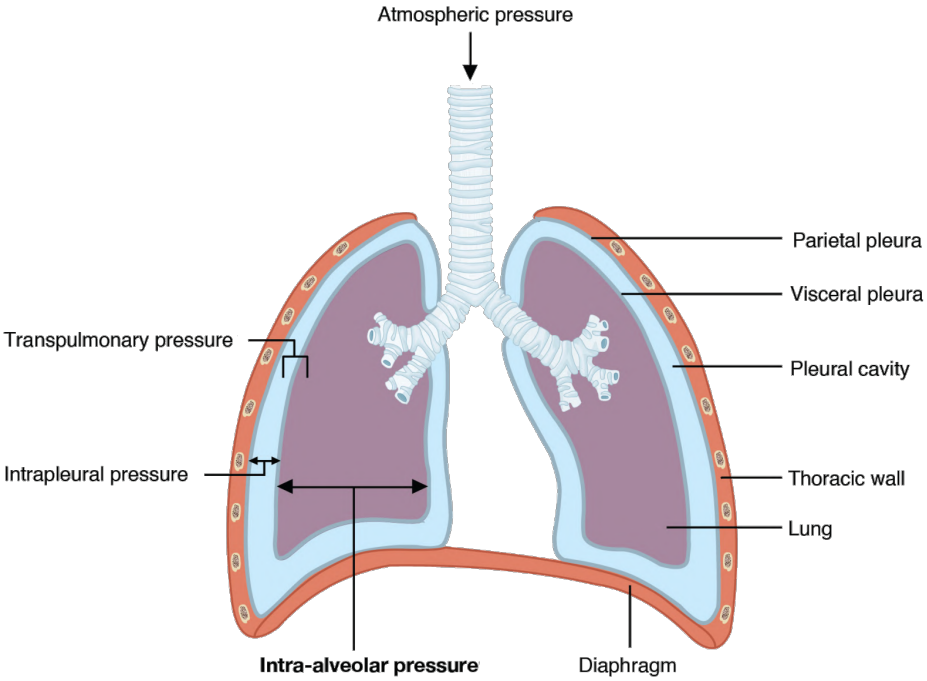

Figure 1.3: Schematic of lungs surrounding. Figures from OpenStax College Anatomy & Physiology, licensed under CC BY 3.0.

lungs, there is no surfactant to counteract surface tension, resulting in a higher value of surface tension. This demonstrates the crucial role of surfactant in decreasing the surface tension between the lung tissue and the air, facilitating the expansion of the alveoli during the breathing cycle.

1.1.3 Breathing mechanisms

In breathing, not only the lung but also the surrounding organs are involved. Each breathing cycle comprises an inhalation when the air enters the lungs and an exhalation when the air exits.

During inhalation, the diaphragm contracts and moves downward, and external intercostal muscles contract and lift the rib cage, pulling the lungs outward and creating a decreased air pressure inside the lungs compared to the atmospheric pressure. This makes the air rush into the lungs through the airways. On the contrary, during exhalation, the diaphragm moves upward, and the internal intercostal muscles allow the ribcage to move inward, which reduces the space in the chest cavity and pushes the air outside.

The mechanics of breathing is impacted by various factors, namely the compliance of the lungs as the central organ. Compliance refers to the lung ability to expand and recoil during breathing. Lung compliance may change due to pulmonary diseases, which impact the whole breathing mechanics.

The impact of pulmonary disease on the behavior of the lung

Various pulmonary diseases such as asthma, pneumonia, chronic obstructive pulmonary diseases (COPD), and interstitial lung diseases (ILD) impact lung function. Some of these diseases affect the lung microstructure. For instance, interstitial lung diseases affect the pulmonary tissue and the organ structure, consequently causing the lung tis-

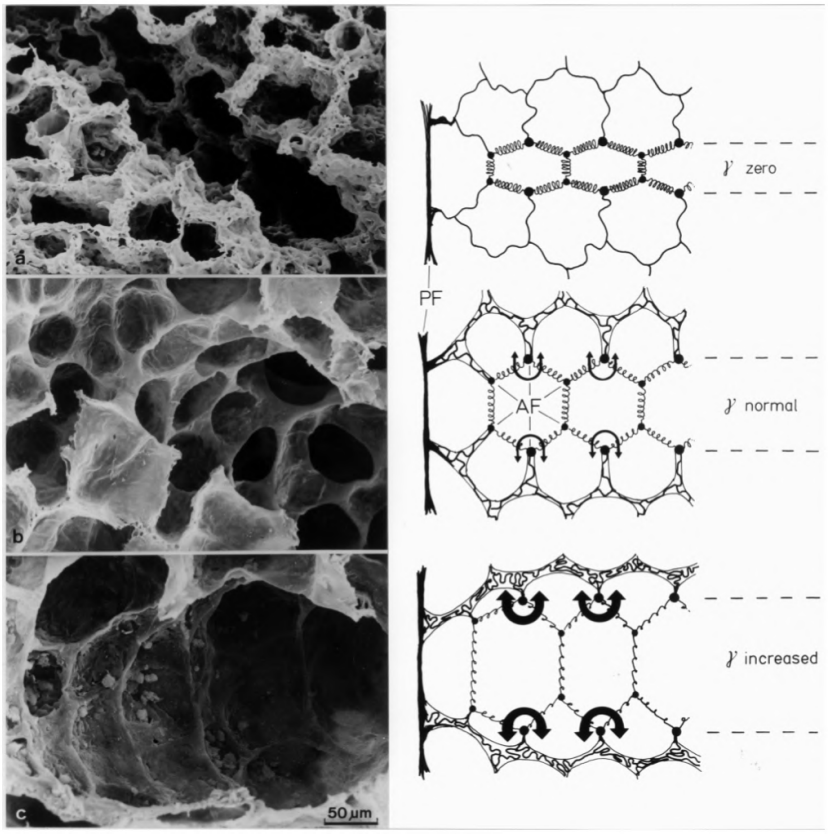

Figure 1.4: Left side: scanning electron micrographs of alveolar ducts of (a) saline-filled, (b) air-filled, and (c) detergent-rinsed rabbit lungs. Right side: mechanical schematic of the corresponding tension in alveoli. (γ, surface tension; PF, fibers of peripheral connective tissue system; AF, elements of axial fiber system that form alveolar entrance rings.) [Bachofen and Schürch, 2001].

sue to get thicker and stiffer, leading to functional impairments and respiratory symptoms [Patte et al., 2022b]. ILD may significantly affect lung compliance, impacting lung mechanical behavior.

Idiopathic pulmonary fibrosis (IPF) is a progressive form of ILD in which the lung tissue typical elastic properties are compromised due to the accumulation of collagen and other fibrous components. This leads to increased lung stiffness, i.e., reduced compliance, making it difficult for the lungs to expand and adequately fill with air during inhalation. As a result, IPF patients may experience reduced lung volumes and increased breathing effort. Progressive scarring and stiffening of the lung tissue can lead to airway narrowing and increased airway resistance, resulting in airflow limitation and a feeling of breathlessness during physical activities. Reduced lung compliance and increased airway resistance contribute to poor respiratory function and decreased exercise tolerance in IPF patients.

1.2 Lung mechanical modeling

The behavior of the lung can be modeled mathematically and computationally to perform simulations under different loading conditions and physiological processes. Lung mechanical modeling has received significant attention as a tool to study pulmonary diseases which affect the mechanical behavior of the lung. On the other hand, mechanics may play a role in the progression of some diseases, as excessive deformation may lead to parenchyma injury. Mechanical modeling can be an asset to healthcare professionals to diagnose and prognosis pulmonary disease by becoming personalized based on different pathologies [Patte et al., 2022a].

Lung has been mechanically modeled at different scales. Modeling at each scale includes specific elements. This section reviews elements of the lung mechanical modeling at the alveolar/microscopic and tissue/macroscopic scales, such as poromechanical framework, microstructural and micromechanical modeling, and upscaling methods to create a bridge between the models at different scales.

1.2.1 Tissue-scale modeling

We begin this Section by recalling some basics of continuum mechanics and poromechanics prior to tissue-scale models proposed to model the lung parenchyma behavior.

1.2.1.1 Basic continuum mechanics

Kinematics

Suppose a deformable continuum body occupies the domain Ω_0 in the reference configuration and ω in the deformed configuration. The displacement $\underline{U}$ is defined as the difference between the position of the body points in the deformed configuration $\underline{x} \in \omega$ and reference configuration $\underline{X} \in \Omega_0$, through the mapping $\underline{\chi} : \Omega_0 \to \omega$:

$$\underline{U}\left(\underline{X}\right) = \underline{\chi}\left(\underline{X}\right) - \underline{X} = \underline{x}\left(\underline{X}\right) - \underline{X}. \tag{1.1}$$

The deformation gradient $\underline{\underline{F}}$ is defined as

$$\underline{\underline{F}} = \underline{\mathrm{Grad}}\left(\underline{\chi}\right) = \underline{\underline{1}} + \underline{\mathrm{Grad}}\left(\underline{U}\right). \tag{1.2}$$

The relative volume change of the mixture J is defined as the determinant of the deformation gradient $\underline{\underline{F}}$:

$$J = \mathrm{Det}\left(\underline{\underline{F}}\right). \tag{1.3}$$

The right Cauchy-Green deformation tensor

$$\underline{\underline{C}} = \underline{\underline{F}}^T \cdot \underline{\underline{F}}, \tag{1.4}$$

and the Green-Lagrange strain tensor

$$\underline{\underline{E}} = \frac{1}{2}\left(\underline{\underline{C}} - \underline{\underline{1}}\right) = \frac{1}{2}\left(\underline{\underline{\text{Grad}}}\ (\underline{U}) + \left(\underline{\underline{\text{Grad}}}\ (\underline{U})\right)^T + \left(\underline{\underline{\text{Grad}}}\ (\bar{\underline{U}})\right)^T \cdot \underline{\underline{\text{Grad}}}\ (\underline{U})\right). \tag{1.5}$$

The first and second invariants of the right Cauchy-Green deformation tensor, as well as its first reduced invariant, are defined as:

$$I_1 = \text{Tr}\left(\underline{\underline{C}}\right), \qquad I_2 = \frac{1}{2}\left(\text{Tr}^2\left(\underline{\underline{C}}\right) - \text{Tr}\left(\underline{\underline{C}}^2\right)\right), \qquad J_1 = J^{-2/3} I_1. \tag{1.6}$$

Macroscopic stress

Based on the second principle of thermodynamics, the second Piola-Kirchhoff stress tensor, in reversible transformation, derives from the free energy density potential:

$$\underline{\underline{\Sigma}} = \frac{\partial \Psi}{\partial \underline{\underline{E}}}, \tag{1.7}$$

based on which, the Cauchy stress tensor is defined as:

$$\underline{\underline{\sigma}} = \frac{1}{J}\, \underline{\underline{F}}\, \underline{\underline{\Sigma}}\, \underline{\underline{F}}^T. \tag{1.8}$$

1.2.1.2 Poromechanics

The lung parenchyma is a porous medium that can be treated as a two-phase material with the interstitium tissue as *solid* and air as *fluid*. The interaction between these two phases can be studied through a poromechanical framework, which incorporates the principles of solid mechanics and fluid dynamics.

Porous media

Porous media refer to materials containing void spaces which can be filled with fluid, for instance, air. Porous materials are found widely in nature, for instance, soil, sponge, and biological tissue, such as the lung parenchyma. Understanding the mechanics of porous materials is essential to study their behavior under different loadings and boundary conditions. Considering their mechanical behavior, the porous materials discussed here contain two phases, i.e., solid and fluid.

Solid mechanics The solid structure of a porous material can be studied regarding the stress and deformation and the relation between them resulting from the constitutive choice. The solid can be assumed compressible or incompressible, and the behavior can be studied in linear elasticity or, in some cases, nonlinear hyperelasticity. Moreover, viscoelastic behavior can be considered for the solid as well.

Fluid mechanics The behavior of the fluid can be studied based on the principle of fluid mechanics. Knowing that the pores can be connected or disconnected in a porous medium. The fluid flow between the pores can be considered in the case of interconnected pores.

Poromechanics brings a macroscopic approach to porous media based on **mixture theory**, which treats a porous medium as a superposition of solid and fluid phases at each point where an average quantity is attributed. This theory is widely reviewed in [Bedford and Drumheller, 1979, Bowen, 1982, Coussy, 2004]. Works of [Biot, 1941, Terzaghi, 1943, Biot and Temple, 1972] are the foundation of poromechanics to study the porous media models employing volume fraction concept [De Boer and Ehlers, 1988]. The volume fraction concept aligned with the mixture theory, which establishes a connection between the average bulk quantities and average effective quantities, is practical, assuming that the volume and surface elements chosen are large enough to provide a representation of all the statistical properties of the pore space [Kubik, 1986, De Boer and Ehlers, 1988].

Poromechanics is widely used for different applications, such as environmental engineering, reservoir engineering, geomechanics, or civil engineering in studying soil mechanics [Siddique et al., 2017]. Moreover, poromechanics is used to describe the behavior of biological tissue such as cardiac perfusion [Chapelle et al., 2010] or lung parenchyma as a two-phased porous medium [Kowalczyk, 1993]. A general poromechanical formulation is proposed by [Chapelle and Moireau, 2014], coupling general solid and fluid models, based on [Coussy, 2004], which satisfies the fundamental physical principles, namely essential conservation and thermodynamics laws. Biological tissues, such as the lung parenchyma, can be modeled employing a poromechanical framework, considering large deformation for the mixture [Almeida and Spilker, 1998, Li et al., 2004].

Poromechanical framework

In this Section, some main elements of Biot's formulation of poromechanics [Biot, 1941, Biot and Temple, 1972], and the general poromechanical formulation of [Chapelle and Moireau, 2014] are reviewed, which can be found more detailed in [Patte et al., 2022b].

The quantities related to the solid are noted with the subscript "s" and those related to the fluid with the subscript "f". Moreover, a *bar* shows the quantities related to the mixture. In this formulation, the transformation is supposed to be quasi-static and isothermal. The quasi-static hypothesis and the assumption of interconnected pores result in homogeneous fluid pressure. In addition, the fluid is considered to be incompressible, and the solid is quasi-incompressible.

The domain occupied by the mixture is denoted by $\bar{\Omega}_0$, with boundary $\partial\bar{\Omega}_0$ in the reference configuration and $\bar{\omega}$, with boundary $\partial\bar{\omega}$ in the deformed configuration. Note that the quantities defined in the reference configuration are denoted in uppercase and those in the deformed configuration in lowercase. Furthermore, the quantities that characterize the reference configuration are denoted with a subscript "0".

Mixture variables

The infinitesimal domain in the reference and deformed configurations, denoted by $d\bar{\Omega}_0$ and $d\bar{\omega}$ respectively, each of which is decomposed into a solid and fluid phase such that $d\bar{\Omega}_0 = d\bar{\Omega}_{f0} \cup d\bar{\Omega}_{s0}$, and $d\bar{\omega} = d\bar{\omega}_f \cup d\bar{\omega}_s$. Based on this decomposition, the mixture variables as the volume fraction of fluid (also known as porosity) and the volume fraction of solid in the reference and deformed configuration are introduced:

$$\begin{cases} \bar{\Phi}_{f0} = \dfrac{|d\Omega_{f0}|}{|d\bar{\Omega}_0|}, & \bar{\phi}_f = \dfrac{|d\omega_f|}{|d\bar{\omega}|} \\ \bar{\Phi}_{s0} = \dfrac{|d\Omega_{s0}|}{|d\bar{\Omega}_0|}, & \bar{\phi}_s = \dfrac{|d\omega_s|}{|d\bar{\omega}|} \end{cases}, \tag{1.9}$$

such that $\bar{\Phi}_{f0} + \bar{\Phi}_{s0} = \bar{\phi}_f + \bar{\phi}_s = 1$. Additionally, the deformed volume fractions of fluid and solid pulled back into the reference configuration are introduced:

$$\begin{cases} \bar{\Phi}_f = \dfrac{|d\omega_f|}{|d\bar{\Omega}_0|} \\ \bar{\Phi}_s = \dfrac{|d\omega_s|}{|d\bar{\Omega}_0|} \end{cases}, \tag{1.10}$$

such that $\bar{\Phi}_f + \bar{\Phi}_s = \bar{J}$.

State laws

The constitutive behavior of the mixture can be characterized through its Helmholtz free energy density per unit reference mixture volume, denoted by $\bar{\Psi}$. Based on one of the fundamental principles of poromechanics, the free energy density is additively decomposed into solid and fluid parts [Coussy, 2004, Chapelle and Moireau, 2014]:

$$\bar{\Psi} = \bar{\Psi}_s\left(\underline{\underline{\bar{E}}}, \bar{\Phi}_s\right) + \bar{\Psi}_f\left(\bar{\Phi}_f\right), \tag{1.11}$$

where $\bar{\Psi}_s$ and $\bar{\Psi}_f$ are the free energies of the solid and fluid phases, respectively. Based on the assumptions of fluid incompressibility and isothermal condition, the fluid free energy density can be expressed as:

$$\bar{\Psi}_f(\bar{\Phi}_f) = -\bar{p}_{f0}\bar{\Phi}_f, \tag{1.12}$$

where $\bar{p}_{f0}$ is a reference pressure [Chapelle and Moireau, 2014].

Under the assumption of hyperelastic behavior for the skeleton and fundamental principle of the equality of the solid hydrostatic pressure with the fluid pressure [Chapelle and Moireau, 2014], and also using Equation 1.7 for the mixture, it concludes

$$\underline{\underline{\bar{\Sigma}}} = \frac{\partial \bar{\Psi}_s\left(\underline{\underline{\bar{E}}}, \bar{\Phi}_s\right)}{\partial \underline{\underline{\bar{E}}}} - \bar{p}_s \bar{J} \underline{\underline{\bar{C}}}^{-1}, \tag{1.13}$$

where $\bar{p}_s = -\frac{\partial \bar{\Psi}_s\left(\underline{\underline{\bar{E}}}, \bar{\Phi}_s\right)}{\partial \bar{\Phi}_s}$ represents the solid hydrostatic pressure associated to solid volume fraction change. Based on a fundamental principle of poromechanics, the solid hydrostatic pressure requires to be equal to the fluid pressure [Chapelle and Moireau, 2014]:

$$\bar{p}_s = \bar{p}_f, \tag{1.14}$$

which imposes the internal equilibrium of the mixture [Coussy, 2004, Chapelle and Moireau, 2014]. The internal equilibrium induces a coupling between the fluid and solid states in the mixture response, resulting in the following expression of the states laws:

$$\begin{cases} \underline{\underline{\bar{\Sigma}}} = \dfrac{\partial \bar{\Psi}_s\left(\underline{\underline{\bar{E}}}, \bar{\Phi}_s\right)}{\partial \underline{\underline{\bar{E}}}} - \bar{p}_f \bar{J} \underline{\underline{\bar{C}}}^{-1} \\ \bar{p}_f = -\dfrac{\partial \bar{\Psi}_s\left(\underline{\underline{\bar{E}}}, \bar{\Phi}_s\right)}{\partial \bar{\Phi}_s} \end{cases}. \tag{1.15}$$

The solid Helmholtz free energy $\bar{\Psi}_s$ can be constructed to be additively split into the skeleton energy $\overline{W}_{skel}$, which corresponds to the constitutive behavior of the skeleton, and the bulk free energy $\overline{W}_{bulk}$, that describes the dependency of the energy on the solid phase volume change:

$$\bar{\Psi}_s\left(\underline{\underline{\bar{E}}}, \bar{\Phi}_s\right) = \overline{W}_{skel}\left(\underline{\underline{\bar{E}}}\right) + \overline{W}_{bulk}\left(\bar{\Phi}_s\right). \tag{1.16}$$

The skeleton free energy characterizes the behavior of the solid matrix. It defines the relation between the macroscopic stress and the macroscopic strain, while the bulk free energy defines the relation between the pore pressure and the volume fraction of the solid.

Such a poromechanical framework can be employed in mechanical modeling of the lung parenchyma as a two phases porous material, including the interstitium tissue as the solid and the air as the fluid. In such case, the choice of the constitutive behavior defines the behavior of the porous lung, where the skeleton free energy characterizes the behavior of the interstitium tissue under deformation, and the bulk free energy characterizes the added air into the lung under the internal (air) pressure. Notably, characteristic behaviors, such as compressibility of interstitium tissue, permeability, and stiffness, can be tuned based on the constitutive parameters.

1.2.1.3 Constitutive behavior

The mechanical behavior of the lung parenchyma can be modeled mathematically to analyze its behavior at the tissue scale, considering the lung as a homogeneous continuum. This Section reviews the elastic and hyperelastic tissue-scale models proposed to represent lung behavior. A tissue-scale mechanical model is formulated based on **constitutive behavior**, which defines the relationship between stress and strain and how the system responds to a specific loading. Choice of the constitutive behavior results in how close or far the model is to the behavior of the lung at the tissue scale. Experimental data can lead us to have a better understanding of the parenchyma behavior considering some characteristics of the lung as:

- Nonlinearity: Lung tissue exhibits nonlinear mechanical behavior, indicating that its response to applied forces or strains is not proportional or linear. The nonlinear behavior of the lung arises from various factors, namely the presence of surfactant or elastin and collagen fibers within the tissue, which undergo stretching and reorientation as the lung deforms.

- Hyperelasticity: Hyperelastic materials can store and recover energy upon deformation without permanent deformation or dissipation. Similarly, lung tissue shows hyperelastic behavior due to elastin and collagen fibers. These fibers can undergo large deformation and return to their original shape after deformation without losing their elastic behavior.

- Isotropy: Isotropic materials exhibit similar behavior in different directions. In the literature, the lung parenchyma behavior is mainly assumed to be isotropic [Hoppin et al., 1975, Tai and Lee, 1981] due to the random distribution of collagen and elastin fibers [Sobin et al., 1988].

- Compressibility: The lung parenchyma shows a compressible behavior containing air as the fluid. On the other hand, the tissue itself is generally considered to be quasi-incompressible.

Considering the unique characteristic of the lung tissue, a constitutive model can be developed to capture the behavior of the lung parenchyma closely. Constitutive behavior of biological materials is nonlinear within the physiological ranges of stress and strain [Suki et al., 2011]. Nonetheless, some mechanical models employ a linear elastic model [Baudet et al., 2003, Zhang et al., 2004, Brock et al., 2005, Werner et al., 2009, Fuerst et al., 2015]. Conversely, there are nonlinear hyperelastic models proposed to study the behavior of the parenchyma at the macroscopic scale [Rausch et al., 2011, Birzle et al., 2019, Jorba et al., 2019]. Some authors take into account other characteristics of the lung parenchyma, such as viscoelastic behavior of the tissue [Bel-Brunon et al., 2014], by employing a rheological model that can capture dynamic-mechanical behavior of the lung [Romero, 1998].

Table 1.1: Material models and corresponding parameters proposed in the literature to describe the behavior of the lung parenchyma. ($\bar{I}_i$ and $\bar{J}_i$ are respectively invariant and reduced invariant of the Cauchy-Green deformation tensor $\underline{\underline{\bar{C}}}$, and $\bar{J}$ represents the relative change of volume.)

study	Energy Potential	Model parameters
[Bel-Brunon et al., 2014]	$\bar{\Psi} = \frac{\bar{k}_1}{2\bar{k}_2}\left(\exp\left(\bar{k}_2\left(\frac{\bar{J}_1}{3}\right)-1\right)\right) + \frac{\bar{\kappa}}{4}\left(-2\ln\bar{J}+\bar{J}^2-1\right)$	$\bar{k}_1 = 4.34\ kPa, \bar{k}_2 = 5.02, \bar{\kappa} = 72.5\ Pa$
[Birzle and Wall, 2019]	$\bar{\Psi} = c\left(\bar{I}_1-3\right) + \frac{c}{\beta}\left(\bar{I}_3^{-\beta}-1\right) + c_1\left(\bar{I}_3^{-\frac{1}{3}}\bar{I}_1-3\right)^{d_1} + c_3\left(\bar{I}_3^{\frac{1}{3}}-1\right)^{d_3}$	$c = 356.7\ Pa, \bar{\beta} = 1.075, \bar{c}_1 = 278.2\ Pa,$ $\bar{c}_3 = 5.766\ Pa, \bar{c}_1 = 3, \bar{d}_3 = 6$
[Tawhai et al., 2009]	$\bar{\Psi} = \bar{c}\exp\left(\bar{a}\bar{I}_1+\bar{b}\bar{I}_2\right)$	$\bar{a} = 0.433, \bar{b} = -0.611, \bar{c} = 2.5\ kPa$
[Rausch et al., 2011]	$\bar{\Psi} = \bar{c}_{quad}\left(\bar{J}_1-3\right)^2 + \bar{c}_{cub}\left(\bar{J}_1-3\right)^3 + \frac{\bar{\kappa}}{4}\left(-2\ln\bar{J}+\bar{J}^2-1\right)$	$\bar{c}_{quad} = 4.1\ kPa, \bar{c}_{cub} = 20.7\ kPa,$ $\bar{\kappa} = 16.6\ kPa$
[Ma et al., 2013]	$\bar{\Psi} = \bar{c}\exp\left(\bar{a}\bar{I}_1^2+\bar{b}\bar{I}_2\right)$	$\bar{a} = 0.43, \bar{b} = -0.6, \bar{c} = 2\ kPa$

The tissue-scale models proposed in the literature are broadly categorized into two groups: (i) the ones treating the entire tissue as a compressible hyperelastic material and (ii) the ones proposing a poroelastic model for the tissue that distinguishes fluid behavior from incompressible solid behavior.

Modeling the tissue based on compressible hyperelastic behavior

Many authors have modeled the lung parenchyma tissue as a continuum material undergoing finite strains. [Bel-Brunon et al., 2014] proposes a nonlinear viscoelastic model of the lung parenchyma, considering compressible properties to track the volume change. The constitutive model comprises a hyperelastic potential split into volumetric, isochoric, and viscous contributions. The volumetric contribution includes an exponential potential to capture the real behavior of the lung parenchyma. Such material models can be used for nonlinear finite element simulations of the lung parenchyma to quantify the stress-strain relation of the lung tissue during breathing [Birzle and Wall, 2019]. Similarly, [Rausch et al., 2011] use a hyperelastic potential containing three terms to consider the contribution of the elastin and collagen fibers and control volumetric change. [Ma et al., 2013] follows [Tawhai et al., 2009] to model the compressible lung-air matrix in finite strains, considering nonlinear and isotropic material properties.

The mentioned hyperelastic models are presented in Table 1.1 as well as the prescribed coefficients. Figure 1.5 shows a comparison of stress-deformation behavior for these models undergoing volumetric and isochoric deformation with the corresponding deformation gradient

$$\underline{\underline{\bar{F}}}^{vol} = \begin{bmatrix} 1+\alpha & 0 & 0 \\ 0 & 1+\alpha & 0 \\ 0 & 0 & 1+\alpha \end{bmatrix}, \underline{\underline{\bar{F}}}^{iso} = \begin{bmatrix} \beta & 0 & 0 \\ 0 & \frac{1}{\sqrt{\beta}} & 0 \\ 0 & 0 & \frac{1}{\sqrt{\beta}} \end{bmatrix}. \tag{1.17}$$

Different stress-deformation behaviors of the compared models were influenced not only by the choice of constitutive behavior but also by the selection of model parameters. Many of these models utilize experimental data to propose a model to be as realistic as possible to the behavior of the lung parenchyma at the tissue scale. Consequently, the significant difference in the behavior of the models arises from different experimental protocols, as discussed in Seciton 1.3.

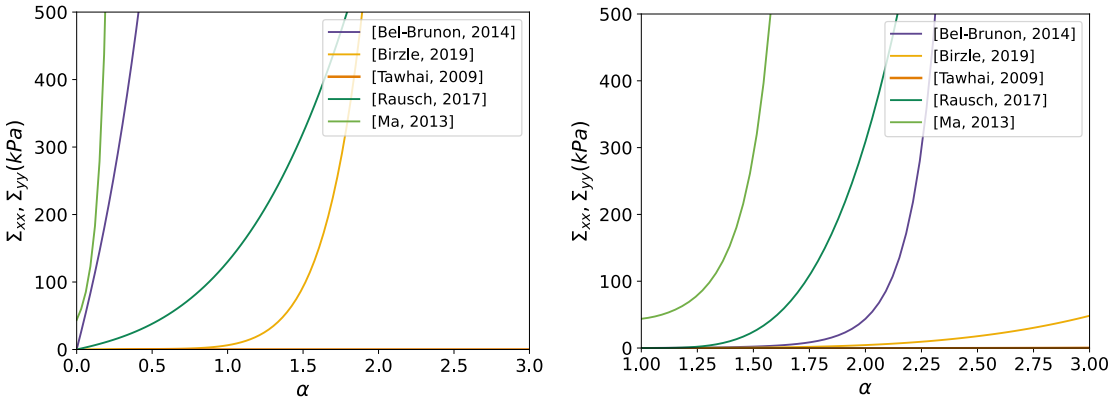

(a) Volumetric deformation

(b) Isochoric deformation

Figure 1.5: Comparing the stress-deformation behavior for the material models proposed in the literature by [Bel-Brunon et al., 2014, Birzle and Wall, 2019, Tawhai et al., 2009, Rausch et al., 2011, Rausch et al., 2017].

Modeling the tissue based on poroelastic laws

Some authors approximate the lung parenchyma as a continuous poroelastic material, considering an incompressible or quasi-incompressible behavior for the tissue as the solid phase. Such poroelastic models introduce elastic and bulk moduli to prescribe the relation between the macroscopic stress and strain in solid as well as the fluid pressure and volume fraction of fluid or solid [Berger et al., 2016, Patte et al., 2022b]. Poroelastic modeling of the lung parenchyma first has been proposed by [Kowalczyk, 1993], considering two phases, one of a highly deformable solid for thin-wall tissue structure and the air as an incompressible fluid, based on which the quasi-static coupled problem has been developed. In this coupled formulation, large deformations and material nonlinearities are considered. Similarly, [Berger et al., 2016] proposes a novel model to approximate the lung parenchyma behavior, using a poroelastic coupled with an airway network model. Such a poroelastic model couples the tissue deformation with ventilation, where the tissue behavior in deformation is linked to the internal air pressure.

[Patte et al., 2022b] has used a modified neo-Hookean-Ciarlet-Geymonat model incorporating an exponential term. This modification is particularly relevant for modeling the lung parenchyma, as it captures the observed hardening behavior under finite strains and offers a closer representation of the lung parenchyma mechanical behavior, which exhibits significant nonlinearity and strain-dependent stiffening. The skeleton and bulk free energy are introduced in this model as:

$$\begin{cases} \overline{W}_{skel}\left(\bar{\underline{\underline{E}}}\right) = \bar{\beta}_1\left(\bar{I}_1 - 3 - 2\ln\bar{J}\right) + \bar{\beta}_2\left(\bar{I}_1 - 3 - 4\ln\bar{J}\right) \\ \qquad\qquad +\bar{\alpha}\left(e^{\bar{\delta}\left(\bar{J}^2 - 1 - \ln\bar{J}\right)} - 1\right) \\ \overline{W}_{bulk}\left(\bar{\Phi}_s\right) = \bar{\kappa}\left(\dfrac{\bar{\Phi}_s}{1-\bar{\Phi}_{f0}} - 1 - \ln\left(\dfrac{\bar{\Phi}_s}{1-\bar{\Phi}_{f0}}\right)\right) \end{cases}, \tag{1.18}$$

where $\bar{\beta}_1$, $\bar{\beta}_2$, $\bar{\alpha}$ and $\bar{\delta}$ are the parameters of the model as well as the bulk modulus $\bar{\kappa}$. Incorporating the proposed hyperelastic potentials in Equations 1.13 and 1.14, the relation between the mixture variables $\bar{\Phi}_f$ and $\bar{\Phi}_s$, and the state variable $\bar{p}_f$ is shown in Figure 1.6 for different values of bulk modulus $\bar{\kappa}$, and considering zero macroscopic stress. This example also shows the effect of bulk modulus on the behavior of the solid, pointing out that high values of the bulk modulus correspond to the incompressibility of the solid tissue.

Consequently, for high values of the bulk modulus, the volume of the solid barely changes with respect to fluid pressure.

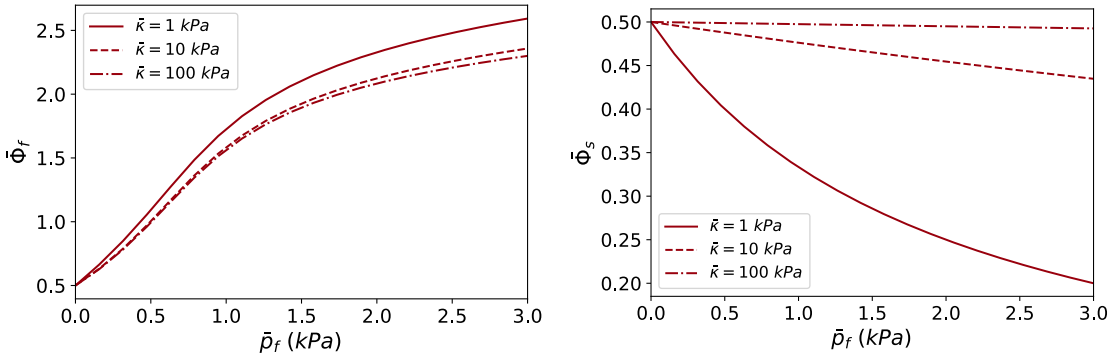

(a) Volume fraction of fluid with respect to fluid pressure.

(b) Volume fraction of solid with respect to fluid pressure.

Figure 1.6: Mixture variables with respect to fluid pressure based on the constitutive behavior proposed by [Patte et al., 2022b].

1.2.2 Alveolar-scale modeling

Tissue-scale models, as discussed in the previous Section, are relatively low computational cost models to specify the behavior of the lung at the macroscopic scale. Nonetheless, they have limitations for representing complex physiological phenomena, such as surface tension [Coussy, 2010] or tissue growth [Genet, 2019]. Moreover, tissue-scale models only characterize the average strain and stress values at the macroscopic scale.

In contrast, alveolar-scale models can overcome such limitations and are better suited for microscopic investigations, including the microscopic parameters and features. Alveolar-scale modeling is linked to micromechanical modeling of the lung parenchyma, including **microstructure modeling**, **behavior laws**, **equilibrium equations**, and **boundary conditions**.

In this Section, we discuss the microstructural and micromechanical modeling of the lung parenchyma, noting that such micromechanical approaches find applications beyond the lungs [Dormieux, 2005], extending to areas like skeletal muscles [Spyrou et al., 2019] or geomechanics.

1.2.2.1 Microstructural modeling

Microstructural modeling of the lung aims to construct a geometrical microstructure that closely resembles the microarchitecture of the lung parenchyma. Microscopic-scale images of the lung parenchyma help better understand the lung parenchyma microstructure. Figure 1.7 shows an example of such images, where the alveoli exhibit polygonal shapes with varying dimensions and face counts.

In the literature, the microstructure of the lung parenchyma is modeled either by directly reconstructing the exact geometry from microscopic images or by employing simplified geometrical shapes representing the average alveoli shape.

Extracting the microstructure from the images

A natural but costly method to obtain the geometrical microstructure of the lung is using high-resolution micro-CT images of an intact acinus, where the tissue structure

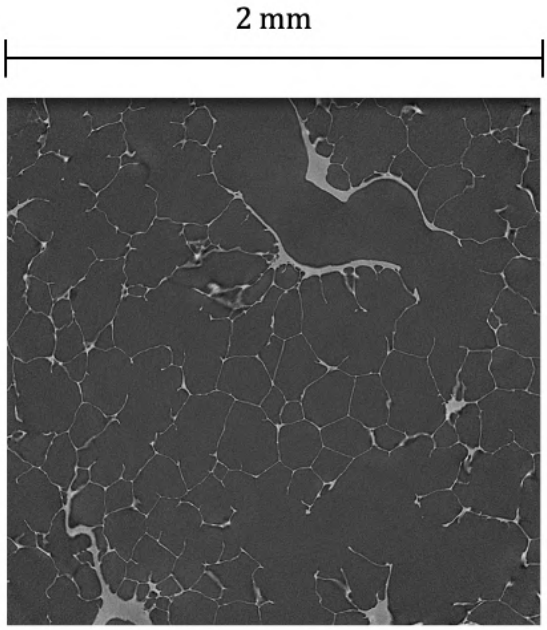

Figure 1.7: Porcine lung microstructure (spatial resolution = $2\mu m$) [LaMCoS/LBMC/MATEIS].

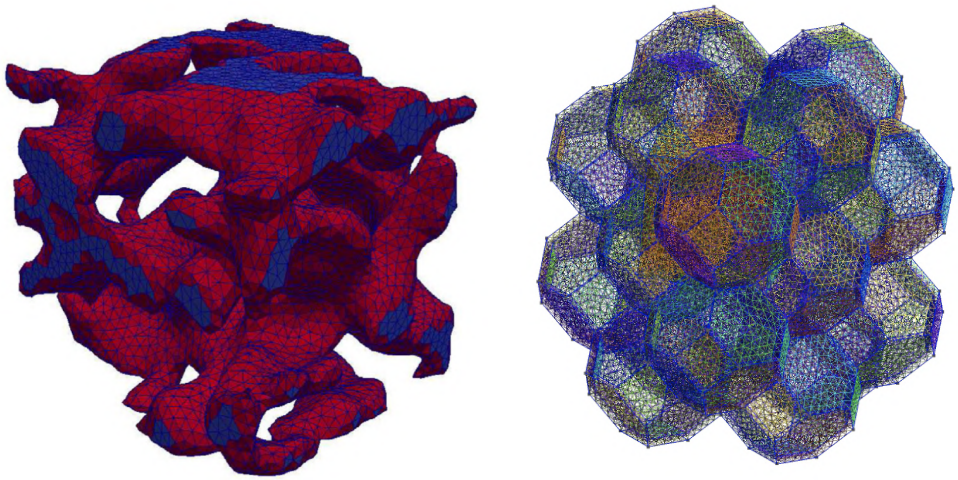

(a) Image-based microstructure [Álvarez-Barrientos et al., 2021].

(b) TetraKaiDecahedron elements-based microstructure.

Figure 1.8: An image-based microstructure vs. a microstructure based on TKD element.

model is constructed based on the airspace geometry [Koshiyama et al., 2018]. One of the most common methods to extract the data relies on image segmentation, where a combination of binary image processing can be used based on gray-scale images to extract the microstructure of the acinus [Xiao et al., 2013, Xiao et al., 2016]. Figure 1.8a by [Álvarez-Barrientos et al., 2021] shows an image-based microstructure where the meshed area distinguishes the parenchyma tissue from the airways.

Creating the microstructure based on simplified geometrical elements

The microstructure can be generated more straightforwardly using regular geometrical elements instead of segmenting CT images of the lung parenchyma. As observed in the images (cf. Figure 1.7), the alveoli have polygonal shapes with varying characteristics such as shapes, sizes, and face counts. A Representative Volume Element (RVE) can be introduced based on the average shape of the alveoli. Octahedrons [Denny and Schroter, 2000] and TetraKaiDecahedrons (TKD) [Dale et al., 1980, Wiechert et al., 2009, Roth et al., 2017, Concha et al., 2018] are among the elements used to model the geometry of the alveoli as they have sphere-like shapes and fill space. Figure 1.8b shows an example of a microstructure based on TKD elements.

Similarly, 2D geometries are employed to simulate the parenchyma in the plane, using a hexagonal element to construct the microstructure [Cavalcante et al., 2005] as it is close to the average polygonal shape of the alveoli observed in the planar layers of the images, and its space-filling characteristic. Another privilege of using hexagonal microstructure is its isotropic behavior in plane due to 60° of rotational symmetry [Ptashnyk and Seguin, 2016].

Constructing the airways in the microstructure

One geometrical characteristic of the lung parenchyma, which can be considered in the microstructural modeling, is the interconnection of the airways between the alveoli. This characteristic is automatically incorporated into image-based microstructures and can be added to simplified geometrical models as well. In what follows, we explain an algorithm by [Koshiyama and Wada, 2015] to generate a random microstructure based on seed distribution and open the airways by eliminating specific alveolar walls.

In the first step, some seeds are scattered randomly in a unit cell by a pseudo-random algorithm and picking a real number between zero and the length of the cell. In contrast, the two parameters of the density of the seeds and minimum distance between seeds are controlled as in Figure 1.9.A. Each seed has information about the edges of its polygon generated based on Voronoi tessellation as shown in Figure 1.9.B. This tessellation characterized and array of alveoli. The same logic is implemented in 3D modeling.

The logic of creating the pathway is based on the seeds connection. So, a Delauney tessellation is generated based on the background of the previous Voronoi tessellation, supposing the boundary seeds become isolated and supposing an entrance seed as the terminal bronchiole of the ductal tree, as shown in Figure 1.9.C. A seed is supposed as the terminal bronchiole entry, and an arbitrary ductal tree is created by random connections between the seeds and entrance, as in Figure 1.9.D. Each seed has a unique path to the entrance seed, meaning there is no cycle inside, and the number of daughter (downstream) branches from each seed is less than three.

Each ductal tree is supposed to be a solution, and for each solution, there is information for each seed containing the parent branch seed number and daughter seed number. Each solution would be compared with a neighbor solution on which the parent seed of a random seed would randomly change, and the aim is to minimize the gas exchange path or maximize

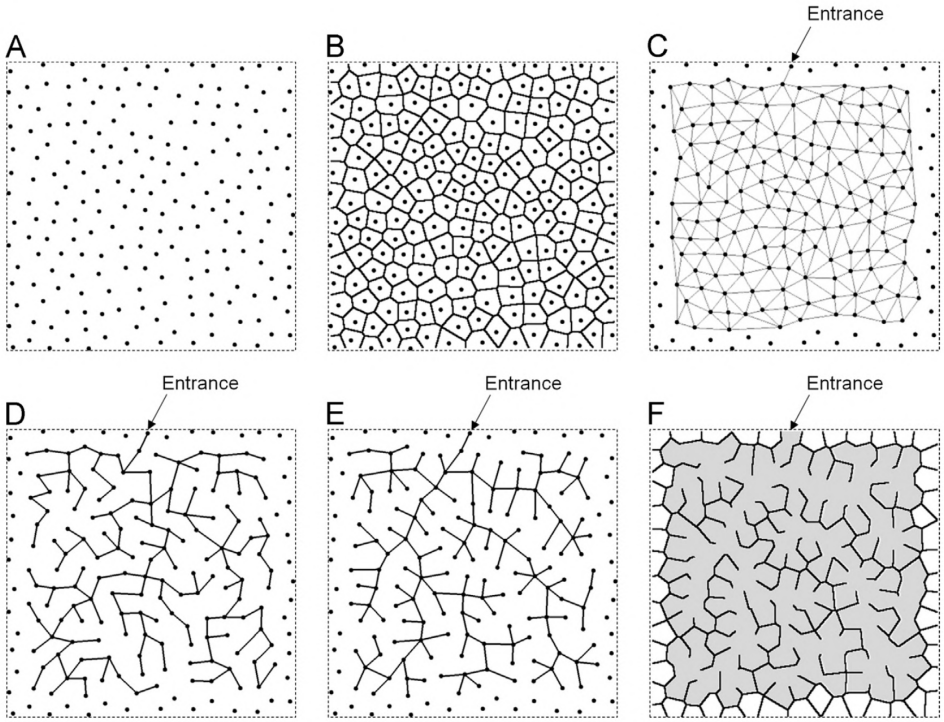

Figure 1.9: Different step for the creation of the optimum acinus microstructure (A) Scattering random seeds (B) Voronoi tessellation based on the random seeds (C) Delaunay Tessellation (D) A random ductal tree (E) Optimal ductal tree (F) The optimal acinus microstructure based on optimal ductal tree [Koshiyama and Wada, 2015].

the number of alveoli. So, two parameters will be defined for the cost function:

$$C_1 = N_t - N_a, \tag{1.19}$$

where N_t is the number of total seeds, and N_a is the number of terminal seeds. The other parameter

$$C_2 = \frac{1}{N_a}\sum_{i=1}^{N_a} l_i, \tag{1.20}$$

in which l_i is the path of seed number i to the entrance seed. Finally, the cost function is defined as below:

$$C = \omega C_1 + (1-\omega)C_2. \tag{1.21}$$

The weight factor ω is between zero and one in the above equation. Figure 1.9.E shows the optimal solution for the ductal tree, and Figure 1.9.F shows the alveolar microstructure with opening walls corresponding to the ductal tree.

This process is similarly done in 3D, knowing that the number of voxels characterizes the dimensions, such as wall thickness, and these parameters are selected to align with experimental data. For instance, in the case of rat lung, the wall thickness is assumed to be 4 μm while the voxel size is 2 μm, resulting in the configuration of 5000 voxels within a single cube as in Figure 1.10.

1.2.2.2 Micromechanical modeling

Micromechanical modeling is a computational approach to studying non-homogeneous materials at the microscopic scale, such as composite or porous materials. Two re-

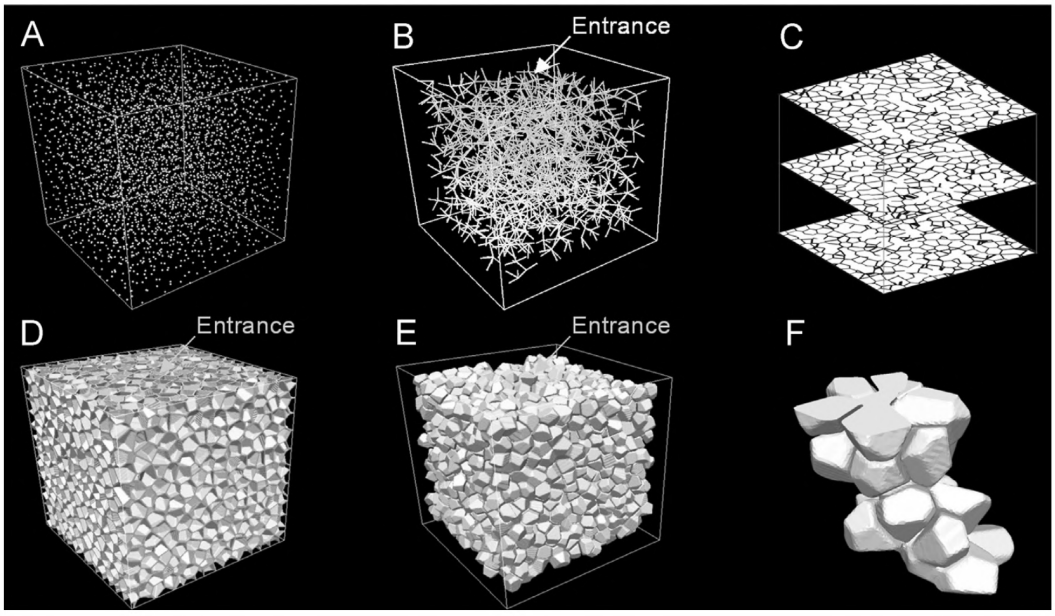

Figure 1.10: Different step for the creation of the optimum acinus microstructure (A) Scattering random seeds (B)Optimal ductal tree (C) stack of the 2D images (D) wall region rendering (E) airspace rendering (F) part of the acinus model [Koshiyama and Wada, 2015]

sulting aspects of such a computational study are (i) investigating the distribution of microscopic properties, such as strain and stress resulting from different boundary conditions [Álvarez-Barrientos et al., 2021] or other microscopic features such as microcracks [Dormieux et al., 2002]; (ii) analyzing effective properties based on the microscopic features, such as morphological parameters [Zhu et al., 2017] or the size of inhomogeneities [Duan et al., 2005].

The micromechanical approach can be employed to model the behavior of lung parenchyma at the alveolar scale, where the interaction between the interstitium tissue and the air, and stress and strain distribution within the tissue, can be studied under different loadings [Concha et al., 2018].

A variational framework can be employed for micromechanical modeling of the lung parenchyma at the alveolar scale, where the behavior laws, equilibrium equations, and boundary conditions are incorporated. The variational formulation provides an approach to capture the mechanical behavior and interactions within the lung microstructure, allowing to compute quantities of interest. This involves formulating the energy function that accounts for the deformation energy, fluid pressure, surface tension, and other relevant energy contributions. The objective is to find the unknown of the problem (which can be deformation, stress field, or any other field of interest) that minimizes the energy functional, representing the equilibrium state [Álvarez-Barrientos et al., 2021]. based on this approach, the total potential energy can be defined as

$$\Pi_{tot} = \Pi_{int} + \Pi_{ext}, \tag{1.22}$$

where Π_{int} characterizes the elastic energy, and Π_{ext} characterizes the external work. Alternatively, the variational formulation can mainly be constructed from strong equations. Nonetheless, with some assumptions, the principle of the minimum potential energy [Budiansky and Kimmel, 1987, Concha et al., 2018] can be used to derive the variational formulation directly from the potential energy. The choice of potential energy is

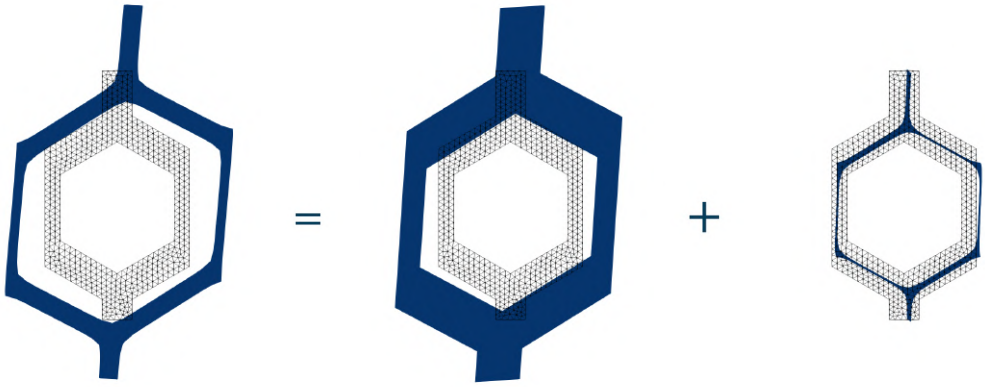

Figure 1.11: Decomposition of the total deformation of the RVE into an affine part and a periodic perturbation.

dictated by the chosen constitutive model. Different constitutive behaviors are suggested to model the lung parenchyma, which is discussed in the following after introducing the kinematics for a micromechanical problem.

Kinematics

We define the micromechanical framework by defining the total displacement $\underline{U}$ of the RVE, being additively decomposed into an affine part, characterized by the symmetric tensor $\underline{\underline{\tilde{\epsilon}}}$, and a periodic part, characterized by the displacement field $\underline{\widehat{U}}$ (cf. Figure 1.11):

$$\underline{U}\left(\underline{X}\right) = \underline{\underline{\tilde{\epsilon}}} \cdot \left(\underline{X} - \underline{X}_0\right) + \underline{\widehat{U}}\left(\underline{X}\right), \tag{1.23}$$

where $\underline{X}_0$ is an arbitrary point in the microstructure. We can then express all standard kinematic variables as a function of $\underline{\underline{\tilde{\epsilon}}}$ and $\underline{\widehat{U}}$, namely the deformation gradient

$$\underline{\underline{F}} := \underline{\underline{1}} + \underline{\underline{\mathrm{Grad}}}\left(\underline{U}\right) = \underline{\underline{1}} + \underline{\underline{\tilde{\epsilon}}} + \underline{\underline{\mathrm{Grad}}}\left(\underline{\widehat{U}}\right), \tag{1.24}$$

the Jacobian of the transformation

$$J := \mathrm{Det}\left(\underline{\underline{F}}\right), \tag{1.25}$$

the right Cauchy-Green dilatation tensor with its first invariant and first reduced invariants

$$\underline{\underline{C}} := \underline{\underline{F}}^T \cdot \underline{\underline{F}}, \quad I_1 := \mathrm{Tr}\left(\underline{\underline{C}}\right), \quad J_1 := J^{-2/3} I_1, \tag{1.26}$$

and the fourth invariant of the Cauchy-Green deformation tensor

$$I_4 = \mathrm{Tr}\left(\underline{\underline{H}}\ \underline{\underline{C}}\right), \tag{1.27}$$

where $\underline{\underline{H}}$ is a general structural tensor [Gasser et al., 2006].

Constitutive behavior of the tissue

The constitutive choice characterizes the relation between the stress and deformation within the solid, or similarly in interstitium tissue. Different hyperelastic potentials

are suggested to define the constitutive behavior of the interstitium tissue. For example, [Wiechert et al., 2009] uses a potential following [Holzapfel et al., 2004] to describe the constitutive behavior of the interstitium tissue with multiple terms. Based on that, the elastic potential is defined by the sum of different potentials as the function of the Cauchy-Green deformation tensor $\underline{\underline{C}}$:

$$W(\underline{\underline{C}}) = W_{gs}(\underline{\underline{C}}) + W_{fib}(\underline{\underline{C}}) + W_{pen}(\underline{\underline{C}}), \tag{1.28}$$

where W_{gs} represent the elastin fiber system

$$W_{gs} = c\left(\frac{I_1}{J^{\frac{2}{3}}} - 3\right), \tag{1.29}$$

W_{fib} describe the strain energy function of the lung collagen fiber network

$$W_{fib} = \begin{cases} \frac{k_1}{2k_2}\left(\exp\left(k_2\left(I_4 - 1\right)^2\right) - 1\right) & \text{for } I_4 \geq 1 \\ 0 & \text{for } I_4 < 1 \end{cases}, \tag{1.30}$$

and also, W_{pen} enforces the quasi-incompressibility of the interstitium tissue. Note that c represents a shear modulus-like parameter, respectively, $k_1 \geq 0$ a stress-like parameter and $k_2 > 0$ a dimensionless parameter.

In [Roth et al., 2017], a neo-Hookean potential is proposed to define the tissue material behavior

$$W = \frac{E_s}{4 - 4\nu_s}\left(I_1 - 3\right) + \frac{E_s\left(1 - 2\nu_s\right)}{4\nu_s + 4\nu_s^2}\left(J^{\frac{2\nu_s}{1-2\nu_s}} - 1\right), \tag{1.31}$$

in which E_s is the elastic modulus corresponding to the interstitium tissue. In this model, the Poisson ratio is set to be $\nu_s = 0.49$ to impose low compressibility or quasi-incompressibility of the alveolar tissue.

Additionally there are models which use reduced invariants of the Cauchy-Green deformation tensor instead, as proposed by [Koshiyama et al., 2018]:

$$W = C_1\left(J_1 - 3\right)^2 + C_2\left(J_1 - 3\right)^2 + C_3\left(-\ln J^2 + J^2 - 1\right), \tag{1.32}$$

where J_1 is the reduced first invariant of the Cauchy-Green deformation tensor, and C_1, C_2, and C_3 are model parameters.

1.2.2.3 Surface tension modeling

A generic micromechanical model of the lung facilitates the consideration of different physiological phenomena; for instance, surface tension is a microscopic characteristic of the lung parenchyma, which can be incorporated into the micromechanical model. To this end, the surface tension potential is defined as the work done by the surface tension in changing the interfacial area from its initial value A_0 to a current value A as described by [Karakaplan et al., 1980, Kowe et al., 1986]:

$$\Pi\left(\gamma\right) = \int_{A_0}^{A} \gamma dS, \tag{1.33}$$

where γ is the surface tension. There are different approaches to treating surface tension in lung micromechanical modeling, which can be categorized into three main ones: (i) constant surface tension; (ii) surface tension depending on the interfacial surface area; and (iii) surface tension depending on the interfacial surface area and its rate.

Surface-dependent surface tension

Some authors consider the surface tension γ to be a function of the surface area [Shuttleworth, 1950] and imply an exponential relation between the surface tension and surface area in inflation [Kowe et al., 1986, Koshiyama et al., 2018]:

$$\gamma\left(A^*\right) = \gamma_{max}\left(1 - d_1 \exp\left(-d_2 A^*\right)\right), \tag{1.34}$$

where γ_{max} is the maximum value of the surface tension, d_1 and d_2 are constants, and relative surface area

$$A^* = \frac{A}{A_0}, \tag{1.35}$$

where A is the total surface area inside pulmonary acinus, and A_0 is its initial value. In [Koshiyama et al., 2018], d_1 and d_2 are chosen to be equal to 10.0 and 2.35 respectively. The relation between surface tension and relative surface area is shown in Figure 1.12 for different sets of d_1 and d_2 based on Equation 1.34. This models describe the increase of the surface tension by increasing the surface area due to the decrease in surfactant concentration. As far as the increase in the surface tension in inflation is limited and almost constant more than a specific volume, the parameters d_1 and d_2 can be tuned to show the saturation limit of surface tension.

Surface rate-dependent surface tension

Some authors have used a more physiological behavior to model the surface tension by assuming it is a function of surface area and its rate of change. Such modeling is more compatible with the physiological behavior of the surface tension as it creates a history-dependent behavior that results in hysteresis in the pressure-volume inflation-deflation cycle, similar to the behavior of the biological lung based on the experiments which are shown in Figure 1.13.

Surfactant molecules naturally commute between the bulk suspension (where the surfactant molecules are dispersed) and interface inside the alveoli to minimize the free energy of the system. Surface tension increase is due to decreased surfactant molecules on the interface and vice versa. Based on this theory which is proposed by [Otis et al., 1994] and also used in [Denny and Schroter, 2000, Wiechert et al., 2009], the transport of the surfactant to the surface is supposed to be adsorption limited. The adsorption and desorption kinetics is defined by three phases for interfacial surfactant concentration (Γ), as shown in Figure 1.14. In this model, the surface tension γ is a function of the interfacial concentration of the surfactant molecules Γ.

- In the first phase, Γ is less than the maximum equilibrium concentration Γ^*, and surfactant adsorption to the surface is assumed to follow Langmuir kinetic:

$$\frac{d}{dt}\left(\frac{\Gamma}{\Gamma^*}S\right) = S\left(k_1 C\left(1 - \frac{\Gamma}{\Gamma^*}\right) - k_2\frac{\Gamma}{\Gamma^*}\right), \tag{1.36}$$

  with k_1 and k_2 being the adsorption and desorption coefficient respectively, and C denotes the bulk conectration of surfactant molecules [Wiechert et al., 2009]. Note that ΓS represents the amount of surfactant in the interface. The following relation computes the surface tension from the surfactant concentration:

$$\gamma = \gamma_0 - m_1\frac{\Gamma}{\Gamma^*}, \tag{1.37}$$

  where γ_0 is the reference surface tension of water, and m_1 refers to the experimentally-derived slope for the first phase [Wiechert et al., 2009].

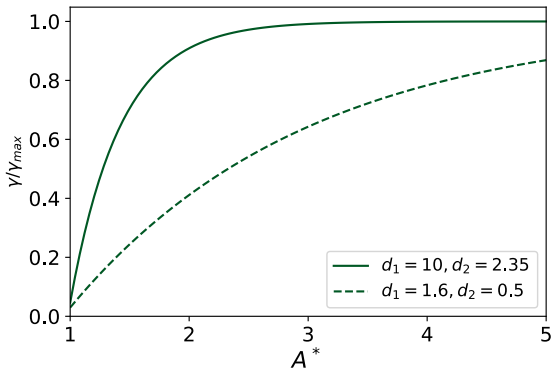

Figure 1.12: surface tension with respect to relative surface area for two sets of variables.

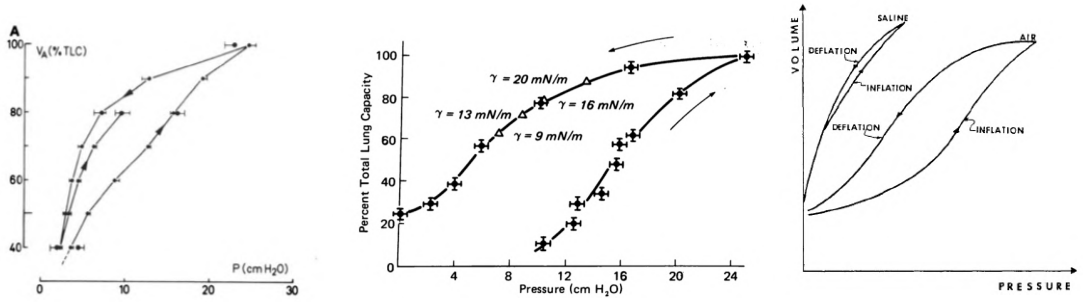

(a) Average pressure-volume of 11 rabbit lungs. [Bachofen et al., 1987]

(b) Typical pressure-volume characteristic of rat lungs at 37° [Schürch et al., 1976]

(c) Pressure-volume behavior using air or saline as the inflation substance. [Liu and Lee, 1978]

Figure 1.13: History dependency of pressure-volume behavior in the lung caused by surface tension.

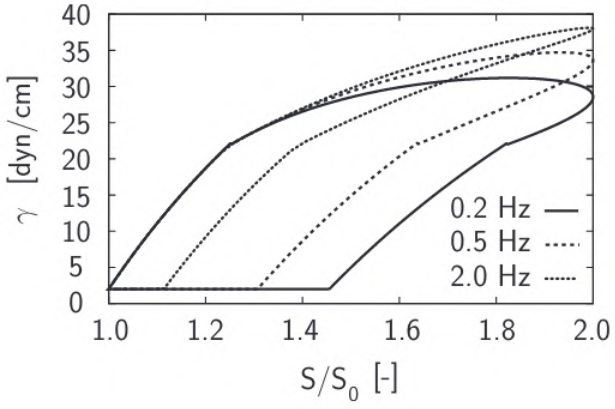

Figure 1.14: surface tension with respect to normalized surface area [Wiechert et al., 2009].

- In the second phase, $\Gamma^* \leq \Gamma < \Gamma_{max}$ (where Γ_{max} is the maximum surfactant concentration), there is no exchange of surfactant material, and Γ changes only due to change in surface area S; as S decreases, the surfactant concentration increases [Otis et al., 1994]:

$$\frac{\Gamma}{\Gamma^*} S = \text{const.} \tag{1.38}$$

  Similarly to the first phase, surface tension can be calculated according to

$$\gamma = \gamma^* - m_2 \left(\frac{\Gamma}{\Gamma^*} - 1 \right), \tag{1.39}$$

  with γ^* being the minimum equilibrium surface stress, and m_2 denoting the slope for the second phase.

- In the third phase, when Γ reaches the maximum surfactant concentration Γ_{max}, the surfactant molecules are packed as tightly as possible in the interface, and Γ can not rise any higher. Consequently, γ reaches its minimum γ_{min}, and any further compression results in a loss of surfactant materials to the bulk suspension [Otis et al., 1994].

1.2.2.4 Boundary conditions

Boundary conditions are essential constraints in micromechanical modeling, which simulate the interaction of the microstructure with the surroundings. The choice of boundary condition, which depends on the specificity of the problem, results in different mechanical behavior. Here are reviewed some kinematical constraints (and their illustrations in Figure 1.15), used in [De Souza Neto and Feijóo, 2010, Álvarez-Barrientos et al., 2021], applicable in micromechanical modeling of the lung parenchyma. Note that in the supposed micromechanical problem, the total deformation comprises an affine part and a fluctuation.

- Periodic displacement boundary condition (PBC): Used to describe materials with periodic microstructure. In this case, the perturbation of two periodic pairs on the boundary is imposed to be equal, for instance, for points M and N in Figure 1.15a

$$\widehat{\underline{U}}(M) = \widehat{\underline{U}}(N). \tag{1.40}$$

- Kinematic uniform boundary condition (KUBC): The strain is uniform inside the RVE and perturbation $\widehat{\underline{U}} = 0$ for any point on the boundary as in Figure 1.15b.

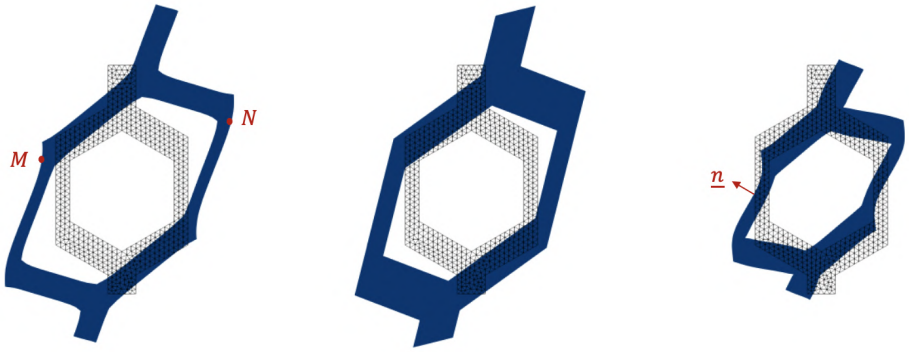

(a) PBC (b) KUBC (c) SUBC

Figure 1.15: Schematical illustrations of different boundary conditions used in micromechanical modeling.

- Uniform traction boundary condition (also known as stress uniform boundary conditions, SUBC): The traction is uniform on the boundary, with the first Piola–Kirchhoff stress tensor constant, resulting in traction force on the boundary

$$\underline{t} = \underline{\underline{\tilde{\sigma}}} \cdot \underline{n}, \tag{1.41}$$

  where $\underline{\underline{\tilde{\sigma}}}$ is the macroscopic stress tensor and $\underline{n}$ is the surface normal vector as shown in Figure 1.15c. This boundary condition is applied to impose external forces on the boundary.

1.2.3 Upscaling and homogenization

The mechanical behaviors at the tissue/macroscopic and alveolar/microscopic scale can be linked through an averaging approach. At the microscopic scale, the heterogeneous lung parenchyma comprises two phases of interstitium tissue and air. Each phase has different properties, while an average equivalent property is attributed to the macroscopic scale models at each point. The average value of the microscopic quantities can be linked to the macroscopic ones through **homogenization**. In general, homogenization attributes the average properties to materials composed of several constituents (also known as composites) [Alouges, 2016]. Consequently, homogenization techniques are used to model the heterogenous medium as a simpler equivalent continuous medium, whose description is valid at a very large scale compared to that of the heterogenities [Auriault et al., 2009]. Homogenization problems can be formulated for periodic and random materials that apply to real materials, which are neither perfectly periodic nor perfectly random [Auriault et al., 2009].

Performing homogenization on a medium with a high density of heterogeneities is only possible by considering regions containing many of these heterogenities [Sanchez-Palencia, 1974]. Note that homogenization can go beyond two phases. For instance, double poroelastic materials, comprising a matrix with embedded subphases, can be studied using the two-scale homogenization method [Miller and Penta, 2021].

Homogenization of porous media

Porous materials are a specific type of composite materials as they have microscopic heterogeneity due to the existence of voids inside a solid matrix. Homogenization also applies to fluid flow within porous materials, usually modeled using Darcy's law [Alouges, 2016].

In addition to the pores, cracks at the microscopic scale may exist. The interconnection of these micro-cracks to the pores, while the medium undergoes internal pressure, results in different behavior at the macroscopic scale, which can be studied by homogenization methods [Dormieux et al., 2002].

Homogenization is employed to study porous biological tissues [Royer et al., 2018, Moreno et al., 2020]. Lung parenchyma is an example of porous material. The homogenized behavior of the lung parenchyma is a matter of interest as, in many scientific works, it is modeled as a homogenized domain [Yoshihara et al., 2017], and macroscopic equations have been derived for average air flows and solid tissue displacements in the respiratory lung tissue [Owen and Lewis, 2001]. Homogenization is employed to compute the effective behavior of the micromechanical model and its parameters which is the key to upscaling and comparing to macroscopic-scale models.

1.2.3.1 Analytical homogenization

An analytical approach can be employed to perform homogenization on simple RVEs, based on the averaging Hill-Mandel [Hill, 1963, Mandel, 1972] principle, which specifies the energy equivalence at two different scales of macroscopic and microscopic. Based on this approach, analytical relations are suggested to obtain the effective elastic moduli for porous materials, knowing the porosity and solid properties and considering an isotropic behavior. For instance, a dilute scheme proposed by [Dormieux et al., 2006] implies a relation between homogenized and microscopic properties, considering the mechanical interaction between the pores to be negligible. It implies a linear relation between the homogenized shear modulus $\tilde{\mu}$, bulk modulus $\tilde{k}$, and the solid shear and bulk moduli μ_s and k_s as well as the porosity:

$$\begin{cases} \tilde{k} = k_s \left(1 - \bar{\Phi}_{f0} \left(1 + \dfrac{3k_s}{4\mu_s}\right)\right) \\ \tilde{\mu} = \mu_s \left(1 - 5\bar{\Phi}_{f0} \dfrac{3k_s + 4\mu_s}{9k_s + 8\mu_s}\right) \end{cases} . \tag{1.42}$$

This scheme gives a reasonable estimation of effective elastic properties for porosities $\bar{\Phi}_{f0} << 1$. On the other hand, a differential scheme is also proposed by [Dormieux et al., 2006], which overcomes the limitation of the dilute scheme and introduces a homogeneous medium identical to the solid matrix. This brings the following coupled equations, valid for the solid Poisson ratio $\nu_s > 0.2$:

$$\begin{cases} \dfrac{\left(1 + 4\mu_s/3k_s\right)\left(\tilde{\mu}/\mu_s\right)^3}{2 - \left(1 - 4\mu_s/3k_s\right)\left(\tilde{\mu}/\mu_s\right)^{\frac{3}{5}}} = \left(1 - \bar{\Phi}_{f0}\right)^6 \\ \dfrac{\tilde{\mu}}{\mu_s} = \dfrac{\left(1 - \frac{4}{3}\tilde{\mu}/\tilde{k}\right)^{\frac{5}{3}}}{\left(1 - \frac{4}{3}\mu_s/k_s\right)^{\frac{5}{3}}} \end{cases} , \tag{1.43}$$

and for the solid Poisson ratio $\nu_s < 0.2$:

$$\begin{cases} \dfrac{\left(1 + 4\mu_s/3k_s\right)\left(\tilde{\mu}/\mu_s\right)^3}{2 + \left(4\mu_s/3k_s - 1\right)\left(\tilde{\mu}/\mu_s\right)^{\frac{3}{5}}} = \left(1 - \bar{\Phi}_{f0}\right)^6 \\ \dfrac{\tilde{\mu}}{\mu_s} = \dfrac{\left(\frac{4}{3}\tilde{\mu}/\tilde{k} - 1\right)^{\frac{5}{3}}}{\left(\frac{4}{3}\mu_s/k_s - 1\right)^{\frac{5}{3}}} \end{cases} . \tag{1.44}$$

Figure 1.16 shows effective elastic parameters with respect to porosity Φ_{f0} based on the dilute and differential schemes [Dormieux et al., 2006]. The normalized bulk and shear

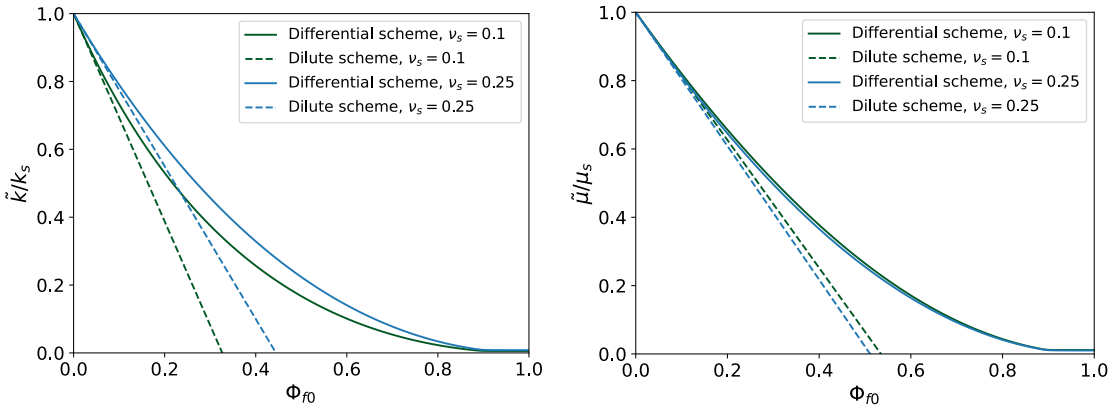

(a) Normalized bulk modulus with respect to porosity.

(b) Normalized shear modulus with respect to porosity.

Figure 1.16: Effective parameters of a porous solid matrix with respect to porosity Φ_{f0} based on Dilute and Differential scheme proposed by [Dormieux et al., 2006].

moduli are computed for solid properties with Young modulus $E_s = 1kPa$ and two different Poisson ratios of $\nu_s = 0.1$ and $\nu_s = 0.25$. We note that the relation between the bulk and shear modulus, and Young modulus and Poisson ratio

$$\mu_s = \frac{E_s}{2(1+\nu_s)}, \tag{1.45}$$

$$k_s = \frac{E_s}{3(1-2\nu_s)}. \tag{1.46}$$

1.2.3.2 Computational homogenization

Computational approaches can be employed to estimate the homogenized behavior of more complex microstructures, where *multi-scale expansion* can be used as an accurate method in capturing fine-scale variations and anisotropy, in addition to the Hill-Mandel principle. Homogenization using multiple scale expansion for small-scale periodic structure technique, founded by [Sanchez-Palencia, 1974] and also introduced by others [Keller, 1977, Bensoussan et al., 1978, Sanchez-Palencia, 1980, Auriault et al., 2009]. This method is based on the assumption of periodic microstructures with repeating unit cells or Representative Volume Elements (RVE). Multi-scale homogenization is applicable when the characteristic length of the microscopic scale L_2 is much smaller than the macroscopic one L_1 (schematically shown in Figure 1.17)

$$\frac{L_2}{L_1} << 1. \tag{1.47}$$

Note that the multi-scale expansion methods are impractical for materials with random microstructure, where *Statistical modeling* can be employed [Gittus and Zarka, 1986], which handles uncertainties in material properties.

The computational problem can be solved on the RVE using the finite element method (FEM) for periodic microstructures [Iltchev et al., 2015, Lukeš and Rohan, 2022] or Fast Fourier Transforms [Michel et al., 1999]. In the following, we recall a linear homogenization problem that can be performed on an RVE using the finite element method.

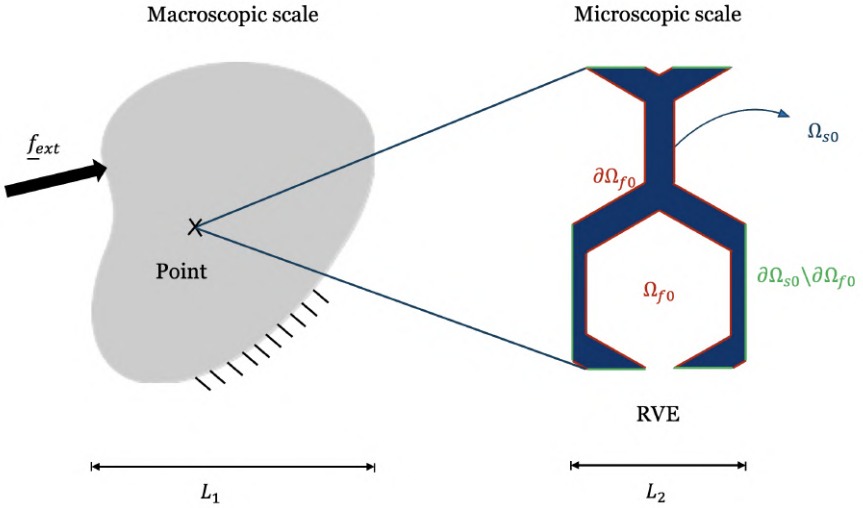

Figure 1.17: Schematic of two different scales of macroscopic with characteristic length L_1, and microscopic with characteristic length L_2.

Linear homogenization

A linear homogenization problem to compute the apparent elastic moduli of the homogenized medium associated with a given microstructure with given microscopic quantities, comes down to solving the auxiliary problem to find the periodic perturbation $\underline{\widehat{U}}$ such that

$$\begin{cases} \underline{\mathrm{div}}\left(\underline{\underline{\sigma}}\right) = 0 & \text{in } \Omega_{s0} \\ {}^{t}\underline{\underline{\sigma}} = \underline{\underline{\sigma}} & \text{in } \Omega_{s0} \\ \underline{\underline{\sigma}} = \underline{\underline{\underline{\underline{C}}}}\left(\underline{X}\right) : \underline{\underline{\epsilon}} & \text{in } \Omega_{s0} \\ \underline{\underline{\epsilon}} = \underline{\underline{\tilde{\epsilon}}} + \nabla\underline{\widehat{U}} & \text{in } \Omega_0 \end{cases}, \tag{1.48}$$

where $\underline{\underline{\tilde{\epsilon}}}$ is the given macroscopic strain and $\underline{\underline{\underline{\underline{C}}}}\left(\underline{X}\right)$ is the heterogeneous elasticity tensor which depends on the microscopic space variable $\underline{X} \in \Omega_0$. The average of the local microscopic strain of the whole domain ($\Omega_0 = \Omega_{s0} \cup \Omega_{f0}$) is equal to the macroscopic strain: $< \underline{\underline{\epsilon}} > = \frac{1}{|\Omega_0|}\int_{\Omega_0} \underline{\underline{\epsilon}}\left(\underline{x}\right) d\Omega_0 = \underline{\underline{\tilde{\epsilon}}}$, and similarly the macroscopic stress is equal to the average of microscopic stress: $\underline{\underline{\tilde{\sigma}}} =< \underline{\underline{\sigma}} >= \frac{1}{|\Omega_0|}\int_{\Omega_0} \underline{\underline{\sigma}}\left(\underline{x}\right) d\Omega_0$. There is a linear relation between the auxiliary problem loading parameters $\underline{\underline{\tilde{\epsilon}}}$, and the resulting macroscopic stress

$$\underline{\underline{\tilde{\sigma}}} = \underline{\underline{\underline{\underline{\widetilde{C}}}}} : \underline{\underline{\tilde{\epsilon}}}, \tag{1.49}$$

where $\underline{\underline{\underline{\underline{\widetilde{C}}}}}$ is the homogenized elasticity tensor of the medium, depending on the microscopic quantities. Solving the mentioned auxiliary problem results in finding the homogenized elasticity tensor

$$\underline{\underline{\underline{\underline{\widetilde{C}}}}} = \begin{bmatrix} \frac{1}{\tilde{E}_1} & -\frac{\tilde{\nu}_{21}}{\tilde{E}_2} & -\frac{\tilde{\nu}_{31}}{\tilde{E}_3} & 0 & 0 & 0 \\ -\frac{\tilde{\nu}_{12}}{\tilde{E}_1} & \frac{1}{\tilde{E}_2} & -\frac{\tilde{\nu}_{32}}{\tilde{E}_3} & 0 & 0 & 0 \\ -\frac{\tilde{\nu}_{13}}{\tilde{E}_1} & -\frac{\tilde{\nu}_{23}}{\tilde{E}_2} & \frac{1}{\tilde{E}_3} & 0 & 0 & 0 \\ 0 & 0 & 0 & \frac{1}{\tilde{G}_{23}} & 0 & 0 \\ 0 & 0 & 0 & 0 & \frac{1}{\tilde{G}_{13}} & 0 \\ 0 & 0 & 0 & 0 & 0 & \frac{1}{\tilde{G}_{12}} \end{bmatrix}, \tag{1.50}$$

where $\tilde{E}_i$ is Young modulus, $\tilde{G}_{ij}$ Kirchhoff modulus and $\tilde{\nu}_{ij}$ Poisson ratio of the homogenized material. The behavior of the solid matrix can be interpreted based on the components of the homogenized elasticity tensor $\underset{\equiv\equiv}{\widetilde{C}}$ to determine whether it exhibits isotropic or anisotropic behavior. Moreover, the homogenized parameters remain within a specific range.

Remark 1: Bounds for material parameters

There are twelve material constants in 1.50, but only nine of them are independent due to the existing symmetry [Obara, 2018]:

$$\tilde{\nu}_{ij} = \tilde{\nu}_{ji}\frac{\widetilde{E}_j}{\widetilde{E}_i}. \tag{1.51}$$

Regarding the strain energy being positive-definite, the compliance matrix should be positive-definite as well [Ostrosablin, 1994, Ting, 1996]. This leads to the following inequalities presented by [Lempriere, 1968, Zheng and Chen, 2001, Obara, 2018]:

$$\begin{cases} \tilde{E}_1 > 0, \tilde{E}_2 > 0, \tilde{E}_3 > 0, \tilde{G}_{23} > 0, \tilde{G}_{13} > 0, \tilde{G}_{12} > 0 \\ 1 - \tilde{\nu}_{12}\tilde{\nu}_{21} - \tilde{\nu}_{23}\tilde{\nu}_{32} - \tilde{\nu}_{13}\tilde{\nu}_{31} - 2\tilde{\nu}_{12}\tilde{\nu}_{32}\tilde{\nu}_{13} > 0 \\ \tilde{\nu}_{12}\tilde{\nu}_{21} < 1, \tilde{\nu}_{23}\tilde{\nu}_{32} < 1, \tilde{\nu}_{13}\tilde{\nu}_{31} < 1 \end{cases}. \tag{1.52}$$

Comparing the above relations to Equation 1.51, results in the range of Poisson ratios as pointed out in [Lempriere, 1968, Mentrasti et al., 2021]:

$$\begin{cases} |\tilde{\nu}_{12}| < \sqrt{\frac{\tilde{E}_2}{\tilde{E}_1}}, & |\tilde{\nu}_{21}| < \sqrt{\frac{\tilde{E}_1}{\tilde{E}_2}} \\ |\tilde{\nu}_{23}| < \sqrt{\frac{\tilde{E}_3}{\tilde{E}_2}}, & |\tilde{\nu}_{32}| < \sqrt{\frac{\tilde{E}_2}{\tilde{E}_3}} \\ |\tilde{\nu}_{31}| < \sqrt{\frac{\tilde{E}_1}{\tilde{E}_3}}, & |\tilde{\nu}_{13}| < \sqrt{\frac{\tilde{E}_3}{\tilde{E}_1}} \end{cases} \tag{1.53}$$

.

Remark 2: Distance from isotropy

The homogenized elasticity tensor specifies whether the homogenized behavior is isotropic. An overall isotropy criterion is defined to compare the homogenized elasticity tensor to the isotropic case [Zhu et al., 2017]. Based on this criterion, the projection of the effective elasticity tensor over the isotropic basis is defined as

$$\zeta\left(\underset{\equiv\equiv}{\widetilde{C}}\right) = 1 - \frac{||\underset{\equiv\equiv}{\widetilde{C}} - Proj\left(\underset{\equiv\equiv}{\widetilde{C}}\right)||}{||\underset{\equiv\equiv}{\widetilde{C}}||}. \tag{1.54}$$

Note that $\zeta\left(\underset{\equiv\equiv}{\widetilde{C}}\right)$ is equal 1 for an isotropic tensor $\underset{\equiv\equiv}{\widetilde{C}}$. This means the closer the behavior is to isotropy, the closer $\zeta\left(\underset{\equiv\equiv}{\widetilde{C}}\right)$ is to one. In the above relation, $Proj\left(\underset{\equiv\equiv}{\widetilde{C}}\right)$ is computed as:

$$Proj\left(\underset{\equiv\equiv}{\widetilde{C}}\right) = \left(\frac{\underset{\equiv\equiv}{\widetilde{C}} :: \underset{\equiv\equiv}{J}}{\underset{\equiv\equiv}{J} :: \underset{\equiv\equiv}{J}}\ \underset{\equiv\equiv}{J} + \frac{\underset{\equiv\equiv}{\widetilde{C}} :: \underset{\equiv\equiv}{K}}{\underset{\equiv\equiv}{K} :: \underset{\equiv\equiv}{K}}\ \underset{\equiv\equiv}{K}\right). \tag{1.55}$$

where $\underline{\underline{\underline{\underline{J}}}}$ and $\underline{\underline{\underline{\underline{K}}}}$ are the classical isotropy basis [Zhu et al., 2017]

$$\underline{\underline{\underline{\underline{J}}}} = \begin{bmatrix} \frac{1}{3} & \frac{1}{3} & \frac{1}{3} & 0 & 0 & 0 \\ \frac{1}{3} & \frac{1}{3} & \frac{1}{3} & 0 & 0 & 0 \\ \frac{1}{3} & \frac{1}{3} & \frac{1}{3} & 0 & 0 & 0 \\ 0 & 0 & 0 & 0 & 0 & 0 \\ 0 & 0 & 0 & 0 & 0 & 0 \\ 0 & 0 & 0 & 0 & 0 & 0 \end{bmatrix}, \underline{\underline{\underline{\underline{K}}}} = \begin{bmatrix} \frac{2}{3} & -\frac{1}{3} & -\frac{1}{3} & 0 & 0 & 0 \\ -\frac{1}{3} & \frac{2}{3} & -\frac{1}{3} & 0 & 0 & 0 \\ -\frac{1}{3} & -\frac{1}{3} & \frac{2}{3} & 0 & 0 & 0 \\ 0 & 0 & 0 & 1 & 0 & 0 \\ 0 & 0 & 0 & 0 & 1 & 0 \\ 0 & 0 & 0 & 0 & 0 & 1 \end{bmatrix}. \tag{1.56}$$

Computing the homogenized material parameters based on the analytical relations, which are aligned with isotropic behavior, are low-cost estimations that only take into account the solid material parameters and porosity. On the contrary, computational homogenization returns a more precise estimation of the homogenized parameters based on the microstructure quantities, which also depend on the geometry.

1.3 Experiments

The experiments conducted on the lung parenchyma provide practical information about the behavior of the tissue under various loading conditions. The experimental data serve as a input data for comparing and adapting tissue-scale and alveolar-scale models, including their behavior and parameters. Many researchers proposing mechanical models for lung behavior have compared their model predictions with actual lung data, aiming to identify model parameters that closely match the lung behavior.

Experiments have been conducted using diverse protocols, encompassing in vivo and ex vivo settings and involving various species, including humans and different animals. These variations contribute to the observed range of behaviors. This section reviews a range of experiments conducted under different protocols.

1.3.1 Experimental protocols

Experiments are categorized into two main groups; in vivo and ex vivo.

1.3.1.1 In vivo experiments

In vivo experiments refer to experiments conducted within a living organism. Due to the limitations in collecting data on humans, in vivo experiments can be performed on the human lung in which there is no need to extract the lung from the body, considering ethical and practical constraints.

Geometry In in vivo experiments, the geometry is supposed to be the whole lung as it is studied in the living body.

Loading In this type of experiment, the lung deformation is due to spontaneous breathing or mechanical ventilation, performed with a ventilator machine [Nelson et al., 2023].

Measurements Measurements concern not only the deformation of the lung but also the internal pressure as the loading in such experiments. The alveolar pressure can be supposed to be the sum of the pleural surface pressure and the elastic recoil pressure of the lung. In the case of breath holding with an open airway, it can be supposed that

the alveolar and mouth pressure is equal to the atmospheric pressure, so the lung recoil pressure can be measured from an estimate of pleural pressure alone, using oesophageal balloon technique [Gibson and Pride, 1976]. Similarly, changes in oesophageal pressure can be taken to represent pleural pressure changes [Salazar and Knowles, 1964].

In addition to measuring the pressure, there are multiple ways to measure the deformation or volume change. The volume change can be computed by measuring the inhaled air volume change by integrating the airflow over time. Moreover, the deformation field can be extracted from the computed tomography (CT) [Leclerc et al., 2009, Lovric et al., 2017], or Magnetic Resonance Imaging (MRI) [Boucneau et al., 2020] of the lung. Images can be taken at different time steps based on which surface deformation can be tracked through image registration [Patte et al., 2022a, Laville et al., 2023].

1.3.1.2 Ex vivo experiments

Ex vivo experiments are conducted on organs removed from a living organism and studied outside their natural environment. Unlike in vivo experiments, ex vivo experiments involve isolating the biological specimen.

Geometry

There are ex vivo experiments on human lungs, conducted on isolated lungs [Lai-Fook and Hyatt, 2000] or extracted pieces of the lung at the surgery or autopsy [Sugihara et al., 1971]. Additionally, various ex vivo experiments have been conducted on animal models, involving lung samples extracted from rats [Schürch et al., 1976, Rausch et al., 2011, Bel-Brunon et al., 2014, Perlman and Wu, 2014, Birzle and Wall, 2019, Jorba et al., 2019], pigs [Mariano et al., 2020], mouse [Mariano et al., 2020], dogs [Navajas et al., 1995], and isolated rabbit lung [D'Angelo, 1972, Bachofen et al., 1987].

Loading

There are two standard ex vivo experiments commonly used to investigate lung behavior: **Tensile** tests, which help compare stress-strain behavior with poroelastic and viscoelastic models, and **pressure-volume** experiments, which generate volumetric deformations and closely resemble actual physiological (or pathological) loading conditions.

- **Tensile** tests can be done either to study the elasticity behavior of the tissue or the hysteresis caused by viscoelasticity as conducted in [Birzle and Wall, 2019]. The tensile test is practical to study the elastic behavior of the tissue, in which other factors, such as surface tension, do not significantly affect the behavior [Birzle et al., 2019].
- **Pressure-volume** experiments are mostly conducted on the isolated specimen where it is possible to inflate the whole lung with a tube inserted into the trachea and ventilated with a calibrated glass syringe [Bachofen et al., 1987]. Also, the trachea can be connected to a volume manometer with a syringe [Schürch et al., 1976] to compute inlet pressure. In pressure-volume experiments, the effect of the surface tension can be studied as well.

The lung parenchyma may show different behavior in inflation and deflation, as shown in Figure 1.18 due to history-dependent characteristics of the parenchyma. This characteristic arises from the viscosity of the tissue or surface tension which can be studied by

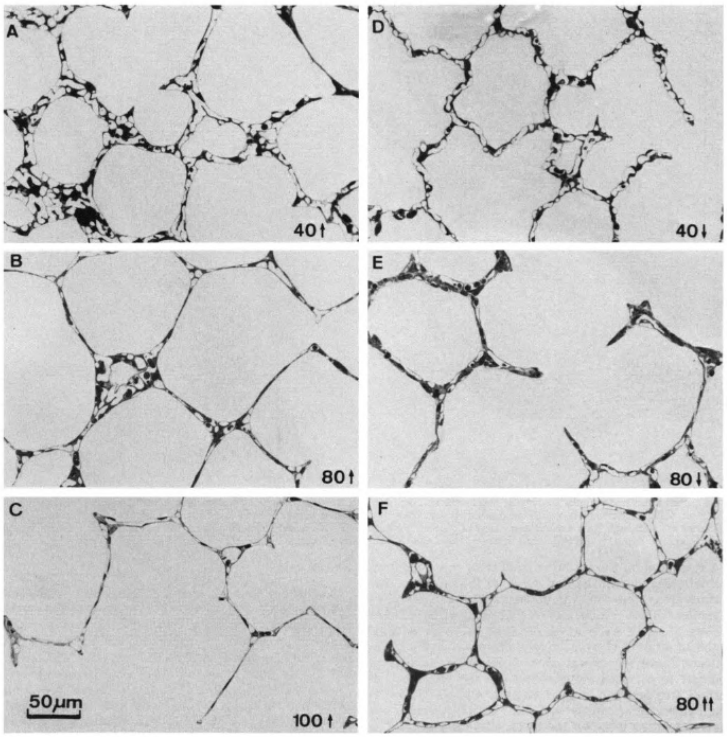

Figure 1.18: Light micrographs of rabbit lung fixed and dehydrated by vascular perfusion. A-C: at 40,80, and 100% total lung capacity (TLC) on inflation limb of P-V curve: D and E: at 40 and 80% TLC on deflation limb; and F: at 80% TLC on re-inflation from 40% TLC. [Bachofen et al., 1987]

applying inflation deflation cycles [Navajas et al., 1995] created by a mechanical ventilation mechanism [Mariano et al., 2020, Arora et al., 2021]. Such viscous behavior results in different loops of the inflation-deflation cycle in the experiments. Nevertheless, an inflation-deflation loop reaches stability after several cycles, as shown in Figure 1.19. Different loading frequencies lead to different behaviors as the material appears stiffer with higher frequencies [Birzle and Wall, 2019]. On the other hand, in some experiments, the frequency effect has been reported to be negligible [Rausch et al., 2011].

Measurements

In ex vivo experiments, the specimen dimensions, applied force, and the corresponding deformation are matters of interest to measure. Different methods have been proposed to measure each of the mentioned quantities:

- Sample dimensions: The sample dimensions are the primary measurements needed to be performed so that the deformation field can be compared to it. The samples are either slices of the tissue or the whole lung. The tissue slices can be measured through microscope and micrometer [Bel-Brunon et al., 2014]. On the other hand, measuring the volume of the whole lung can not be performed by measuring the dimensions due to the irregular shape of the lung. Immersing it in water is a simple way to measure the whole lung volume. This means the change in the volume of the water equals the volume of the immersed lung [D'Angelo, 1972, Lai-Fook and Hyatt, 2000].

- Deformation field: The deformation field can be measured or tracked using a camera that captures the sample [Birzle and Wall, 2019]. On the other hand, noting that the lung does not deform homogeneously, regional deformation can be tracked

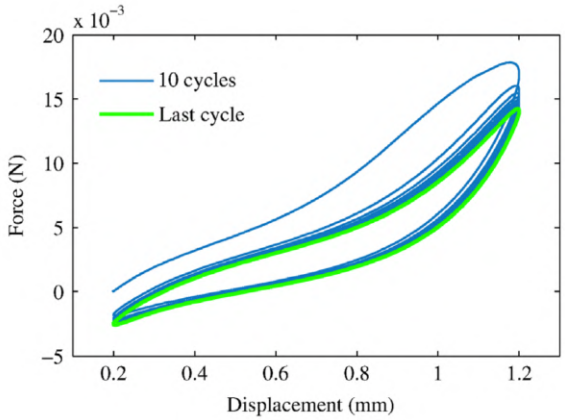

Figure 1.19: Example of a measured curve over ten cycles of tension loading. Hysteresis comes from viscoelasticity and stabilizes after some cycles [Bel-Brunon et al., 2014]

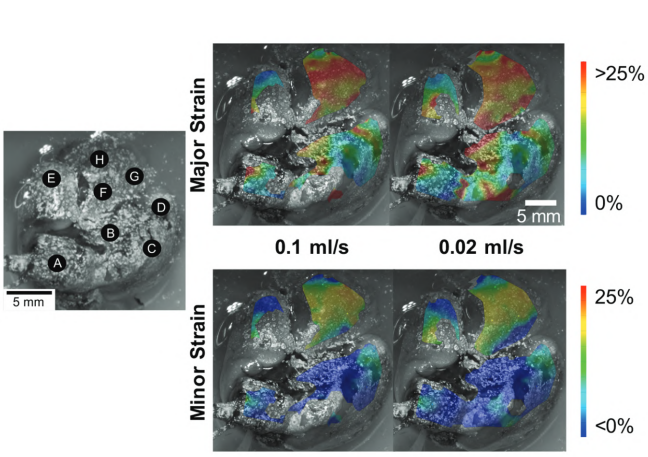

(a) Remarking the regional deformation [Mariano et al., 2020]

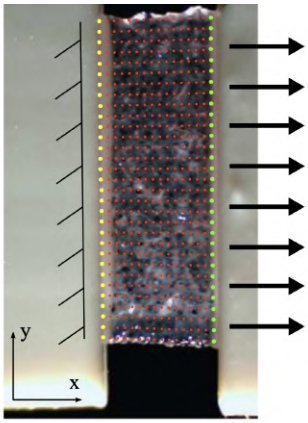

(b) Computing the deformation from image registration [Bel-Brunon et al., 2014]

Figure 1.20: Tracking the specimen deformation field from imaging.

on the whole isolated lung through imaging [Tawhai et al., 2009, Pallière et al., 2019, Mariano et al., 2020, Mariano et al., 2022] (cf. Figure 1.20). Similarly, stereo-Digital Image Correlation (DIC) [Arora et al., 2021] can be employed to compute the regional strain. More complex experiments need measurement of the deformation field with respect to time. In such cases, the surface deformation can be tracked during ventilation [Richardson et al., 2019] by image registration or Magnetic Resonance Imaging (MRI) [Škardová et al., 2019, Stimm et al., 2021, Berberoglu et al., 2022] using the finite element method [Genet et al., 2018, Lee and Genet, 2019].

- Force: In tensile tests, force and displacement are measured using a force transducer and a displacement transducer, respectively. If not measured by DIC, deformation can be extracted from the measured displacement [Rausch et al., 2011].

Environments

Surface tension is a physiological phenomenon inside the alveoli controlled by surfactants. Conducting the experiments in different environments results in different surface tensions

and different behavior of the lung at the tissue scale or organ scale. There are three main treatments of surfactants in pressure-volume experiments.

- **Rinsing-off** the surfactant [Bel-Brunon et al., 2014, Birzle and Wall, 2019] from the alveoli, results in the highest values of the surface tension created due to the direct contact of the tissue and air. According to [Bachofen and Schürch, 2001], a lung rinsed with a detergent has a surface tension of approximately 20 dyn/cm.
- **Saline-filled** lung shows zero surface tension, as no surface tension is created in the interface of the tissue and saline [Bachofen and Schürch, 2001]. Saline is used in some experiments, as in the internal fluid in the lung, to remove the effect of the surface tension [Lai-Fook and Hyatt, 2000, Bou Jawde et al., 2020]. In [Birzle and Wall, 2019], the specimen has been filled with gelatin and cooled to solidify the gelatin before the measurements. This method removes the effect of the surface tension, similar to the saline-filled experiments.
- **Air-filled** lung shows a surface tension value between the saline-filled, which is zero, and surfactant-washed lung, which has a value around 10 dyn/cm [Bachofen and Schürch, 2001]. This shows the effect of the surfactant to contradict the surface tension. Besides, inflation with air and inflation with air almost saturated with the vapor of the test fluid has no measurable difference [Schürch et al., 1976].

Even though the surface tension appears in the pressure-volume experiments due to the interaction of the lung tissue and the filling fluid, this effect does not create any difference in the tensile test. Tensile tests have shown no differences between the air-filled and saline-filled specimens [Rausch et al., 2011, Birzle et al., 2019].

The value of the surface tension itself is not precisely obtainable from the pressure-volume experiments conducted on the lung specimen. On the other hand, there are experiments, such as improved microdroplet method [Bachofen et al., 1987] to measure the surface tension directly. [Otis et al., 1994] use a spherical bubble whose radius and the pressure difference across the bubble allows to calculate the dynamic surface tension through the Laplace law.

1.3.2 Post processing the data

The experimental data can be used to identify the parameters of the lung mechanical model, which characterized the lung tissue parameters [Birzle et al., 2019, Bou Jawde et al., 2020]. The behavior of such mechanical models depends not only on the constitutive behavior chosen to describe the tissue but also on the experimental protocols based on which the model parameters are identified. Figure 1.21 shows the behavior of different tissue-scale models whose parameters are identified based on the experimental data. The significant behavior difference arises from various experimental protocols identifying the parameters. Besides, in similar experimental protocols, different specimens result in different behaviors as the pulmonary disease [Patte et al., 2022a] or the age of the specimen plays an important role in the behavior [Sugihara et al., 1971, Tanaka and Ludwig, 1999, Lai-Fook and Hyatt, 2000]. Even in a simple lung, the tissue stiffness is not equal in every region, and more concretely, certain diseases may affect the stiffness in different regions.

Notably, the tangent modulus of the tissue depends on the strain. The marked nonlinear behavior of the lung extracellular matrix measured at the microscale indicates that lung cells are surrounded by a microenvironment stiffer than in the relaxed tissue under physiological conditions [Jorba et al., 2019].

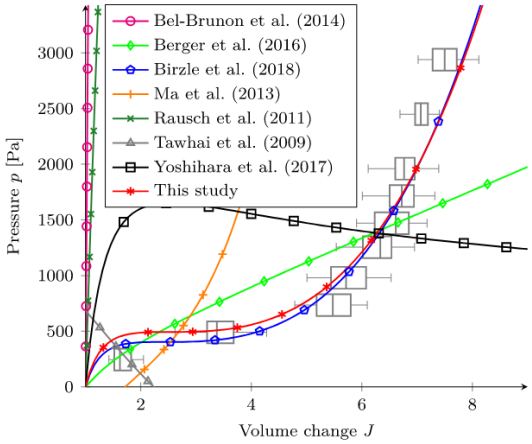

Figure 1.21: Comparing the experimental data to the poroelastic law, which parameters have been obtained from the identification from the experimental data [Birzle and Wall, 2019]. This model has been compared to the other poro-elastic models from [Bel-Brunon et al., 2014], [Berger et al., 2016], [Birzle et al., 2018], [Ma et al., 2013], [Rausch et al., 2011], [Tawhai et al., 2009], and [Yoshihara et al., 2017].

There are different approaches to identifying the material parameters, which also depend on the measurement of the data. *Zero-dimensional* measurements are obtained at a single point, while *full-field* measurements capture the information across a larger spatial domain, allowing the analysis of spatial variations. Material parameters identification can be performed, based on the measured data, either by **sequential** approach [Moireau et al., 2008], which involves a step-by-step procedure where material parameters are identified over time, or **variational** approach in which all material parameters are identified simultaneously as an optimization problem. In addition, there are different methods to identify the material parameters, namely the finite element model updating method (FEMU), the constitutive equation gap method (CEGM), the virtual fields method (VFM), the equilibrium gap method (EGM), and the reciprocity gap method (RGM) [Avril et al., 2008].

Bibliography

[Almeida and Spilker, 1998] Almeida, E. S. and Spilker, R. L. (1998). Finite element formulations for hyperelastic transversely isotropic biphasic soft tissues. *Computer Methods in Applied Mechanics and Engineering*, 151(3-4):513–538.

[Alouges, 2016] Alouges, F. (2016). Introduction to Periodic Homogenization. *Interdisciplinary Information Sciences*, 22(2):147–186.

[Álvarez-Barrientos et al., 2021] Álvarez-Barrientos, F., Hurtado, D. E., and Genet, M. (2021). Pressure-driven micro-poro-mechanics: A variational framework for modeling the response of porous materials. *International Journal of Engineering Science*, 169:103586.

[Ananda Rao and Johncy, 2022] Ananda Rao, A. and Johncy, S. (2022). Tennis Courts in the Human Body: A Review of the Misleading Metaphor in Medical Literature. *Cureus*.

[Arora et al., 2021] Arora, H., Mitchell, R., Johnston, R., Manolesos, M., Howells, D., Sherwood, J., Bodey, A., and Wanelik, K. (2021). Correlating Local Volumetric Tissue Strains with Global Lung Mechanics Measurements. *Materials*, 14(2):439.

[Auriault et al., 2009] Auriault, J.-L., Boutin, C., and Geindreau, C. (2009). *Homogenization of Coupled Phenomena in Heterogenous Media*.

[Avril et al., 2008] Avril, S., Bonnet, M., Bretelle, A.-S., Grédiac, M., Hild, F., Ienny, P., Latourte, F., Lemosse, D., Pagano, S., Pagnacco, E., and Pierron, F. (2008). Overview of Identification Methods of Mechanical Parameters Based on Full-field Measurements. *Experimental Mechanics*, 48(4):381–402.

[Bachofen et al., 1987] Bachofen, H., Schurch, S., Urbinelli, M., and Weibel, E. R. (1987). Relations among alveolar surface tension, surface area, volume, and recoil pressure. *Journal of Applied Physiology*, 62(5):1878–1887.

[Bachofen and Schürch, 2001] Bachofen, H. and Schürch, S. (2001). Alveolar surface forces and lung architecture. *Comparative Biochemistry and Physiology Part A: Molecular & Integrative Physiology*, 129(1):183–193.

[Baudet et al., 2003] Baudet, V., Villard, P.-F., Jaillet, F., Beuve, M., and Shariat, B. (2003). Towards accurate tumour tracking in lungs. In *Proceedings on Seventh International Conference on Information Visualization, 2003. IV 2003.*, pages 338–343, London, UK. IEEE Comput. Soc.

[Bedford and Drumheller, 1979] Bedford, A. and Drumheller, D. (1979). A variational theory of porous media. *International Journal of Solids and Structures*, 15(12):967–980.

[Bel-Brunon et al., 2014] Bel-Brunon, A., Kehl, S., Martin, C., Uhlig, S., and Wall, W. (2014). Numerical identification method for the non-linear viscoelastic compressible behavior of soft tissue using uniaxial tensile tests and image registration – Application to rat lung parenchyma. *Journal of the Mechanical Behavior of Biomedical Materials*, 29:360–374.

[Bensoussan et al., 1978] Bensoussan, A., Lions, J.-L., and Papanicolaou, G. (1978). *Asymptotic analysis for periodic structures*. Number v. 5 in Studies in mathematics and its applications. North-Holland Pub. Co. Sole distributors for the U.S.A. and Canada, Elsevier North-Holland, Amsterdam New York.

[Berberoglu et al., 2022] Berberoglu, E., Stoeck, C. T., Kozerke, S., and Genet, M. (2022). Quantification of left ventricular strain and torsion by joint analysis of 3D tagging and cine MR images. *Medical Image Analysis*, 82:102598.

[Berger et al., 2016] Berger, L., Bordas, R., Burrowes, K., Grau, V., Tavener, S., and Kay, D. (2016). A poroelastic model coupled to a fluid network with applications in lung modelling. *International Journal for Numerical Methods in Biomedical Engineering*, 32(1).

[Biot, 1941] Biot, M. A. (1941). General Theory of Three-Dimensional Consolidation. *Journal of Applied Physics*, 12(2):155–164.

[Biot and Temple, 1972] Biot, M. A. and Temple, G. (1972). Theory of Finite Deformations of Porous Solids. *Indiana University Mathematics Journal*, 21(7):597–620. Publisher: Indiana University Mathematics Department.

[Birzle et al., 2019] Birzle, A. M., Martin, C., Uhlig, S., and Wall, W. A. (2019). A coupled approach for identification of nonlinear and compressible material models for soft tissue based on different experimental setups – Exemplified and detailed for lung parenchyma. *Journal of the Mechanical Behavior of Biomedical Materials*, 94:126–143.

[Birzle et al., 2018] Birzle, A. M., Martin, C., Yoshihara, L., Uhlig, S., and Wall, W. A. (2018). Experimental characterization and model identification of the nonlinear compressible material behavior of lung parenchyma. *Journal of the Mechanical Behavior of Biomedical Materials*, 77:754–763.

[Birzle and Wall, 2019] Birzle, A. M. and Wall, W. A. (2019). A viscoelastic nonlinear compressible material model of lung parenchyma – Experiments and numerical identification. *Journal of the Mechanical Behavior of Biomedical Materials*, 94:164–175.

[Bou Jawde et al., 2020] Bou Jawde, S., Takahashi, A., Bates, J. H. T., and Suki, B. (2020). An Analytical Model for Estimating Alveolar Wall Elastic Moduli From Lung Tissue Uniaxial Stress-Strain Curves. *Frontiers in Physiology*, 11:121.

[Boucneau et al., 2020] Boucneau, T., Fernandez, B., Larson, P., Darrasse, L., and Maître, X. (2020). 3D Magnetic Resonance Spirometry. *Scientific Reports*, 10(1):9649.

[Bowen, 1982] Bowen, R. M. (1982). Compressible porous media models by use of the theory of mixtures. *International Journal of Engineering Science*, 20(6):697–735.

[Brock et al., 2005] Brock, K. K., Sharpe, M. B., Dawson, L. A., Kim, S. M., and Jaffray, D. A. (2005). Accuracy of finite element model-based multi-organ deformable image registration: Accuracy of FEM-based multi-organ deformable image registration. *Medical Physics*, 32(6Part1):1647–1659.

[Budiansky and Kimmel, 1987] Budiansky, B. and Kimmel, E. (1987). Elastic Moduli of Lungs. *Journal of Applied Mechanics*, 54(2):351.

[Cavalcante et al., 2005] Cavalcante, F. S. A., Ito, S., Brewer, K., Sakai, H., Alencar, A. M., Almeida, M. P., Andrade, J. S., Majumdar, A., Ingenito, E. P., and Suki, B. (2005). Mechanical interactions between collagen and proteoglycans: implications for the stability of lung tissue. *Journal of Applied Physiology*, 98(2):672–679.

[Chapelle et al., 2010] Chapelle, D., Gerbeau, J.-F., Sainte-Marie, J., and Vignon-Clementel, I. E. (2010). A poroelastic model valid in large strains with applications to perfusion in cardiac modeling. *Computational Mechanics*, 46(1):91–101.

[Chapelle and Moireau, 2014] Chapelle, D. and Moireau, P. (2014). General coupling of porous flows and hyperelastic formulations—From thermodynamics principles to energy balance and compatible time schemes. *European Journal of Mechanics - B/Fluids*, 46:82–96.

[Concha et al., 2018] Concha, F., Sarabia-Vallejos, M., and Hurtado, D. E. (2018). Micromechanical model of lung parenchyma hyperelasticity. *Journal of the Mechanics and Physics of Solids*, 112:126–144.

[Coussy, 2004] Coussy, O. (2004). *Poromechanics*. John Wiley & Sons.

[Coussy, 2010] Coussy, O. (2010). Mechanics and Physics of Porous Solids.

[Dale et al., 1980] Dale, P., Matthews, F. L., and Schroter, R. C. (1980). Finite element analysis of lung alveolus. *Journal of Biomechanics*, 13(10):865–873.

[D'Angelo, 1972] D'Angelo, E. (1972). Local alveolar size and transpulmonary pressure in situ and in isolated lungs. *Respiration Physiology*, 14(3):251–266.

[De Boer and Ehlers, 1988] De Boer, R. and Ehlers, W. (1988). A historical review of the formulation of porous media theories. *Acta Mechanica*, 74(1-4):1–8.

[De Souza Neto and Feijóo, 2010] De Souza Neto, E. A. and Feijóo, R. A. (2010). Variational Foundations of Large Strain Multiscale Solid Constitutive Models: Kinematical Formulation. In Vaz, M., De Souza Neto, E. A., and Muñoz-Rojas, P. A., editors, *Advanced Computational Materials Modeling*, pages 341–378. Wiley, 1 edition.

[Denny and Schroter, 2000] Denny, E. and Schroter, R. C. (2000). Viscoelastic Behavior of a Lung Alveolar Duct Model. *Journal of Biomechanical Engineering*, 122(2):143–151.

[Dormieux, 2005] Dormieux, L., editor (2005). *Applied micromechanics of porous materials*. Number 480 in CISM courses and lectures. Springer, Wien.

[Dormieux et al., 2006] Dormieux, L., Kondo, D., and Ulm, F.-J. (2006). *Microporomechanics*. John Wiley & Sons, Chichester, West Sussex, England ; Hoboken, NJ.

[Dormieux et al., 2002] Dormieux, L., Molinari, A., and Kondo, D. (2002). Micromechanical approach to the behavior of poroelastic materials. *Journal of the Mechanics and Physics of Solids*, 50(10):2203–2231.

[Duan et al., 2005] Duan, H., Wang, J., Huang, Z., and Karihaloo, B. (2005). Size-dependent effective elastic constants of solids containing nano-inhomogeneities with interface stress. *Journal of the Mechanics and Physics of Solids*, 53(7):1574–1596.

[Fuerst et al., 2015] Fuerst, B., Mansi, T., Carnis, F., Salzle, M., Zhang, J., Declerck, J., Boettger, T., Bayouth, J., Navab, N., and Kamen, A. (2015). Patient-Specific Biomechanical Model for the Prediction of Lung Motion From 4-D CT Images. *IEEE Transactions on Medical Imaging*, 34(2):599–607.

[Gasser et al., 2006] Gasser, T. C., Ogden, R. W., and Holzapfel, G. A. (2006). Hyperelastic modelling of arterial layers with distributed collagen fibre orientations. *Journal of The Royal Society Interface*, 3(6):15–35.

[Genet, 2019] Genet, M. (2019). A relaxed growth modeling framework for controlling growth-induced residual stresses. *Clinical Biomechanics*, 70:270–277.

[Genet et al., 2018] Genet, M., Stoeck, C., Von Deuster, C., Lee, L., and Kozerke, S. (2018). Equilibrated warping: Finite element image registration with finite strain equilibrium gap regularization. *Medical Image Analysis*, 50:1–22.

[Gibson and Pride, 1976] Gibson, G. and Pride, N. (1976). Lung distensibility. The static pressure-volume curve of the lungs and its use in clinical assessment. *British Journal of Diseases of the Chest*, 70:143–184.

[Gittus and Zarka, 1986] Gittus, J. and Zarka, J., editors (1986). *Modelling Small Deformations of Polycrystals*. Springer Netherlands, Dordrecht.

[Hill, 1963] Hill, R. (1963). Elastic properties of reinforced solids: Some theoretical principles. *Journal of the Mechanics and Physics of Solids*, 11(5):357–372.

[Holzapfel et al., 2004] Holzapfel, G. A., Gasser, T. C., and Ogden, R. W. (2004). A new Constitutive Framework for Arterial Wall Mechanics and a Comparative Study of Material Models. In Cowin, S. C. and Humphrey, J. D., editors, *Cardiovascular Soft Tissue Mechanics*, pages 1–48. Kluwer Academic Publishers, Dordrecht.

[Hoppin et al., 1975] Hoppin, F. G., Lee, G. C., and Dawson, S. V. (1975). Properties of lung parenchyma in distortion. *Journal of Applied Physiology*, 39(5):742–751.

[Iltchev et al., 2015] Iltchev, A., Marcadon, V., Kruch, S., and Forest, S. (2015). Computational homogenisation of periodic cellular materials: Application to structural modelling. *International Journal of Mechanical Sciences*, 93:240–255.

[Jorba et al., 2019] Jorba, I., Beltrán, G., Falcones, B., Suki, B., Farré, R., García-Aznar, J. M., and Navajas, D. (2019). Nonlinear elasticity of the lung extracellular microenvironment is regulated by macroscale tissue strain. *Acta Biomaterialia*, 92:265–276.

[Karakaplan et al., 1980] Karakaplan, A. D., Bieniek, M. P., and Skalak, R. (1980). A Mathematical Model of Lung Parenchyma. *Journal of Biomechanical Engineering*, 102(2):124–136.

[Keller, 1977] Keller, J. B. (1977). Darcy's Law for Flow in Porous Media and the Two-Space Method,.

[Koshiyama et al., 2018] Koshiyama, K., Nishimoto, K., Ii, S., Sera, T., and Wada, S. (2018). Heterogeneous structure and surface tension effects on mechanical response in pulmonary acinus: A finite element analysis. *Clinical Biomechanics*.

[Koshiyama and Wada, 2015] Koshiyama, K. and Wada, S. (2015). Mathematical model of a heterogeneous pulmonary acinus structure. *Computers in Biology and Medicine*, 62:25–32.

[Kowalczyk, 1993] Kowalczyk, P. (1993). Mechanical model of lung parenchyma as a two-phase porous medium. *Transport in Porous Media*, 11(3):281–295.

[Kowe et al., 1986] Kowe, R., Schroter, R., Matthews, F., and Hitchings, D. (1986). Analysis of elastic and surface tension effects in the lung alveolus using finite element methods. *Journal of Biomechanics*, 19(7):541–549.

[Kubik, 1986] Kubik, J. (1986). A macroscopic description of geometrical pore structure of porous solids. *International Journal of Engineering Science*, 24(6):971–980.

[Lai-Fook and Hyatt, 2000] Lai-Fook, S. J. and Hyatt, R. E. (2000). Effects of age on elastic moduli of human lungs. *Journal of Applied Physiology*, 89(1):163–168.

[Laville et al., 2023] Laville, C., Fetita, C., Gille, T., Brillet, P.-Y., Nunes, H., Bernaudin, J.-F., and Genet, M. (2023). Comparison of optimization parametrizations for regional lung compliance estimation using personalized pulmonary poromechanical modeling. *Biomechanics and Modeling in Mechanobiology*.

[Leclerc et al., 2009] Leclerc, H., Périé, J.-N., Roux, S., and Hild, F. (2009). Integrated Digital Image Correlation for the Identification of Mechanical Properties. In Gagalowicz, A. and Philips, W., editors, *Computer Vision/Computer Graphics CollaborationTechniques*, volume 5496, pages 161–171. Springer Berlin Heidelberg, Berlin, Heidelberg.

[Lee and Genet, 2019] Lee, L. C. and Genet, M. (2019). Validation of Equilibrated Warping—Image Registration with Mechanical Regularization—On 3D Ultrasound Images. In Coudière, Y., Ozenne, V., Vigmond, E., and Zemzemi, N., editors, *Functional Imaging and Modeling of the Heart*, volume 11504, pages 334–341. Springer International Publishing, Cham.

[Lempriere, 1968] Lempriere, B. M. (1968). Poisson's ratio in orthotropic materials. *AIAA Journal*, 6(11):2226–2227.

[Li et al., 2004] Li, C., Borja, R. I., and Regueiro, R. A. (2004). Dynamics of porous media at finite strain. *Computer Methods in Applied Mechanics and Engineering*, 193(36-38):3837–3870.

[Liu and Lee, 1978] Liu, J.-T. and Lee, G. C. (1978). Static Finite Deformation Analysis of the Lung. *Journal of the Engineering Mechanics Division*, 104(1):225–238.

[Lovric et al., 2017] Lovric, G., Mokso, R., Arcadu, F., Vogiatzis Oikonomidis, I., Schittny, J. C., Roth-Kleiner, M., and Stampanoni, M. (2017). Tomographic in vivo microscopy for the study of lung physiology at the alveolar level. *Scientific Reports*, 7(1):12545.

[Lukeš and Rohan, 2022] Lukeš, V. and Rohan, E. (2022). Homogenization of large deforming fluid-saturated porous structures. *Computers & Mathematics with Applications*, 110:40–63.

[Ma et al., 2013] Ma, B., Breen, B., and Bates, J. H. (2013). Influence of parenchymal heterogeneity on airway-parenchymal interdependence. *Respiratory Physiology & Neurobiology*, 188(2):94–101.

[Mandel, 1972] Mandel, J. (1972). *Plasticité Classique Et Viscoplasticité: Course Held at the Department of Mechanics of Solids, September-October, 1971*. Springer.

[Mariano et al., 2020] Mariano, C. A., Sattari, S., Maghsoudi-Ganjeh, M., Tartibi, M., Lo, D. D., and Eskandari, M. (2020). Novel Mechanical Strain Characterization of Ventilated ex vivo Porcine and Murine Lung using Digital Image Correlation. *Frontiers in Physiology*, 11:600492.

[Mariano et al., 2022] Mariano, C. A., Sattari, S., Quiros, K. A. M., Nelson, T. M., and Eskandari, M. (2022). Examining lung mechanical strains as influenced by breathing volumes and rates using experimental digital image correlation. *Respiratory Research*, 23(1):92.

[Mentrasti et al., 2021] Mentrasti, L., Molari, L., and Fabiani, M. (2021). Poisson's ratio bounds in orthotropic materials. Application to natural composites: wood, bamboo and Arundo donax. *Composites Part B: Engineering*, 209:108612.

[Michel et al., 1999] Michel, J., Moulinec, H., and Suquet, P. (1999). Effective properties of composite materials with periodic microstructure: a computational approach. *Computer Methods in Applied Mechanics and Engineering*, 172(1-4):109–143.

[Miller and Penta, 2021] Miller, L. and Penta, R. (2021). Double poroelasticity derived from the microstructure. *Acta Mechanica*, 232(10):3801–3823.

[Moireau et al., 2008] Moireau, P., Chapelle, D., and Tallec, P. L. (2008). Joint state and parameter estimation for distributed mechanical systems. *Computer Methods in Applied Mechanics and Engineering*, 197(6-8):659–677.

[Moreno et al., 2020] Moreno, A., Quintard, M., Mancini, A., Gomez-Brouchet, A., Swider, P., and Assemat, P. (2020). Upscaling of fluid flow in spatially heterogeneous bone tumors.

[Navajas et al., 1995] Navajas, D., Maksym, G. N., and Bates, J. H. (1995). Dynamic viscoelastic nonlinearity of lung parenchymal tissue. *Journal of Applied Physiology*, 79(1):348–356.

[Nelson et al., 2023] Nelson, T. M., Quiros, K. A. M., Dominguez, E. C., Ulu, A., Nordgren, T. M., and Eskandari, M. (2023). Diseased and healthy murine local lung strains evaluated using digital image correlation. *Scientific Reports*, 13(1):4564.

[Obara, 2018] Obara, P. (2018). Verification of Orthotropic Model of Wood. *Archives of Civil Engineering*, 64(3):31–44.

[Ostrosablin, 1994] Ostrosablin, N. I. (1994). Equations of the linear theory of elasticity of anisotropic materials, reduced to three independent wave equations. *Journal of Applied Mechanics and Technical Physics*, 35(6):949–956.

[Otis et al., 1994] Otis, D. R., Ingenito, E. P., Kamm, R. D., and Johnson, M. (1994). Dynamic surface tension of surfactant TA: experiments and theory. *Journal of Applied Physiology*, 77(6):2681–2688.

[Owen and Lewis, 2001] Owen, M. R. and Lewis, M. A. (2001). The Mechanics of Lung Tissue under High-Frequency Ventilation. *SIAM Journal on Applied Mathematics*, 61(5):1731– 1761.

[Pallière et al., 2019] Pallière, T., Lanel, A., Bel-Brunon, A., Bruyère-Garnier, K., Biboulet, N., and Lubrecht, T. (2019). Experimental protocol to evaluate lung parenchyma properties under inflation. In *Computer Methods in Biomechanics and Biomedical Engineering*, volume 22, pages S14–S16. Taylor & Francis.

[Patte et al., 2022a] Patte, C., Brillet, P.-Y., Fetita, C., Bernaudin, J.-F., Gille, T., Nunes, H., Chapelle, D., and Genet, M. (2022a). Estimation of Regional Pulmonary Compliance in Idiopathic Pulmonary Fibrosis Based on Personalized Lung Poromechanical Modeling. *Journal of Biomechanical Engineering*, 144(9):091008.

[Patte et al., 2022b] Patte, C., Genet, M., and Chapelle, D. (2022b). A quasi-static poromechanical model of the lungs. *Biomechanics and Modeling in Mechanobiology*.

[Perlman and Wu, 2014] Perlman, C. E. and Wu, Y. (2014). In situ determination of alveolar septal strain, stress and effective Young's modulus: an experimental/computational approach. *American Journal of Physiology-Lung Cellular and Molecular Physiology*, 307(4):L302–L310.

[Ptashnyk and Seguin, 2016] Ptashnyk, M. and Seguin, B. (2016). Periodic Homogenization and Material Symmetry in Linear Elasticity. *Journal of Elasticity*, 124(2):225–241.

[Rausch et al., 2017] Rausch, M. K., Genet, M., and Humphrey, J. D. (2017). An augmented iterative method for identifying a stress-free reference configuration in image-based biomechanical modeling. *Journal of Biomechanics*, 58:227–231.

[Rausch et al., 2011] Rausch, S., Martin, C., Bornemann, P., Uhlig, S., and Wall, W. (2011). Material model of lung parenchyma based on living precision-cut lung slice testing. *Journal of the Mechanical Behavior of Biomedical Materials*, 4(4):583–592.

[Richardson et al., 2019] Richardson, S., Gamage, T. P. B., HajiRassouliha, A., Jackson, T., Hedges, K., Clark, A., Taberner, A., Tawhai, M. H., and Nielsen, P. M. F. (2019). Towards a Real-Time Full-Field Stereoscopic Imaging System for Tracking Lung Surface Deformation Under Pressure Controlled Ventilation. In Nielsen, P. M. F., Wittek, A., Miller, K., Doyle, B., Joldes, G. R., and Nash, M. P., editors, *Computational Biomechanics for Medicine*, pages 119–130. Springer International Publishing, Cham.

[Romero, 1998] Romero, F. (1998). A recruitment-based rheological model for mechanical behavior of soft tissues. *Biorheology*, 35(1):17–35.

[Roth et al., 2017] Roth, C. J., Yoshihara, L., and Wall, W. A. (2017). A simplified parametrised model for lung microstructures capable of mimicking realistic geometrical and mechanical properties. *Computers in Biology and Medicine*, 89:104–114.

[Royer et al., 2018] Royer, P., Swider, P., and Assemat, P. (2018). Homogenization of advection-diffusion and solid diffusion in poroelastic media for modelling transport of soluble factors in biological tissues.

[Salazar and Knowles, 1964] Salazar, E. and Knowles, J. H. (1964). An analysis of pressure-volume characteristics of the lungs. *Journal of Applied Physiology*, 19(1):97–104.

[Sanchez-Palencia, 1974] Sanchez-Palencia, E. (1974). Comportements local et macroscopique d'un type de milieux physiques heterogenes. *International Journal of Engineering Science*, 12(4):331–351.

[Sanchez-Palencia, 1980] Sanchez-Palencia, (1980). *Non-homogeneous media and vibration theory*. Number 127 in Lecture notes in physics. Springer, Berlin.

[Schürch et al., 1976] Schürch, S., Goerke, J., and Clements, J. A. (1976). Direct determination of surface tension in the lung. *Proceedings of the National Academy of Sciences*, 73(12):4698–4702.

[Shuttleworth, 1950] Shuttleworth, R. (1950). The Surface Tension of Solids. *Proceedings of the Physical Society, Section A*, 63(5).

[Siddique et al., 2017] Siddique, J., Ahmed, A., Aziz, A., and Khalique, C. (2017). A Review of Mixture Theory for Deformable Porous Media and Applications. *Applied Sciences*, 7(9):917.

[Sobin et al., 1988] Sobin, S. S., Fung, Y. C., and Tremer, H. M. (1988). Collagen and elastin fibers in human pulmonary alveolar walls. *Journal of Applied Physiology*, 64(4):1659–1675.

[Spyrou et al., 2019] Spyrou, L., Brisard, S., and Danas, K. (2019). Multiscale modeling of skeletal muscle tissues based on analytical and numerical homogenization. *Journal of the Mechanical Behavior of Biomedical Materials*, 92:97–117.

[Stimm et al., 2021] Stimm, J., Buoso, S., Berberoglu, E., Kozerke, S., Genet, M., and Stoeck, C. T. (2021). A 3D personalized cardiac myocyte aggregate orientation model using MRI data-driven low-rank basis functions. *Medical Image Analysis*, 71:102064.

[Sugihara et al., 1971] Sugihara, T., Martin, C. J., and Hildebrandt, J. (1971). Length-tension properties of alveolar wall in man. *Journal of Applied Physiology*, 30(6):874–878.

[Suki et al., 2011] Suki, B., Stamenović, D., and Hubmayr, R. (2011). Lung Parenchymal Mechanics. In *Comprehensive Physiology*, pages 1317–1351. John Wiley & Sons, Ltd.

[Tai and Lee, 1981] Tai, R. C. and Lee, G. C. (1981). Isotropy and homogeneity of lung tissue deformation. *Journal of Biomechanics*, 14(4):243–252.

[Tanaka and Ludwig, 1999] Tanaka, R. and Ludwig, M. S. (1999). Changes in viscoelastic properties of rat lung parenchymal strips with maturation. *Journal of Applied Physiology*, 87(6):2081–2089.

[Tawhai et al., 2009] Tawhai, M. H., Nash, M. P., Lin, C.-L., and Hoffman, E. A. (2009). Supine and prone differences in regional lung density and pleural pressure gradients in the human lung with constant shape. *Journal of Applied Physiology*, 107(3):912–920.

[Terzaghi, 1943] Terzaghi, K. (1943). *Theoretical Soil Mechanics*. John Wiley & Sons, Inc., Hoboken, NJ, USA.

[Ting, 1996] Ting, T. C. T. (1996). Positive Definiteness of Anisotropic Elastic Constants. *Mathematics and Mechanics of Solids*, 1(3):301–314.

[Škardová et al., 2019] Škardová, K., Rambausek, M., Chabiniok, R., and Genet, M. (2019). Mechanical and Imaging Models-Based Image Registration. In Tavares, J. M. R. S. and Natal Jorge, R. M., editors, *VipIMAGE 2019*, volume 34, pages 77–85. Springer International Publishing, Cham.

[Werner et al., 2009] Werner, R., Ehrhardt, J., Schmidt, R., and Handels, H. (2009). Patient-specific finite element modeling of respiratory lung motion using 4D CT image data: Finite element modeling of respiratory lung motion. *Medical Physics*, 36(5):1500–1511.

[Wiechert et al., 2009] Wiechert, L., Metzke, R., and Wall, W. A. (2009). Modeling the Mechanical Behavior of Lung Tissue at the Microlevel. *Journal of Engineering Mechanics*, 135(5):434–438.

[Xiao et al., 2013] Xiao, L., Sera, T., Koshiyama, K., and Wada, S. (2013). A Semiautomatic Segmentation Algorithm for Extracting the Complete Structure of Acini from Synchrotron Micro-CT Images. *Computational and Mathematical Methods in Medicine*, 2013:1–10.

[Xiao et al., 2016] Xiao, L., Sera, T., Koshiyama, K., and Wada, S. (2016). Morphological Characterization of Acinar Cluster in Mouse Lung Using a Multiscale-based Segmentation Algorithm on Synchrotron Micro-CT Images. *The Anatomical Record*, 299(10):1424–1434.

[Yoshihara et al., 2017] Yoshihara, L., Roth, C. J., and Wall, W. A. (2017). Fluid-structure interaction including volumetric coupling with homogenised subdomains for modeling respiratory mechanics. *International Journal for Numerical Methods in Biomedical Engineering*, 33(4):e2812.

[Zhang et al., 2004] Zhang, T., Orton, N. P., Mackie, T. R., and Paliwal, B. R. (2004). Technical note: A novel boundary condition using contact elements for finite element based deformable image registration. *Medical Physics*, 31(9):2412–2415.

[Zheng and Chen, 2001] Zheng, Q. S. and Chen, T. (2001). New perspective on Poisson's ratios of elastic solids. *Acta Mechanica*, 150(3-4):191–195.

[Zhu et al., 2017] Zhu, W., Blal, N., Cunsolo, S., and Baillis, D. (2017). Micromechanical modeling of effective elastic properties of open-cell foam. *International Journal of Solids and Structures*, 115-116:61–72.

CHAPTER 2

Finite strain micro-poro-mechanics: formulation and compared analysis with macro-poro-mechanics

In this chapter, we review the theory of poromechanics and discuss the macroscopic modeling of porous media based on this theory. Additionally, we introduce a micro-poro-mechanical m odel capable of computing the response of any periodic porous microstructure subjected to fluid pressure, macroscopic stress, or macroscopic strain. The global response of the micro-poro-mechanical model is then compared to macro-poromechanics for small and large strains to investigate compressibility, strain-pressure coupling, and deviatoric-volumetric strain coupling. This comparison is made while the macroscopic parameters are derived based on the microscopic model, emphasizing the dependency of such parameters on microscopic features. Such a general micro-poro-mechanical model provides a robust foundation for modeling porous materials under finite strains, particularly the lung parenchyma, which is discussed in more detail in Chapter 4.

Contents

Finite strain micro-poro-mechanics: formulation and compared analysis with macro-poro-mechanics

Mahdi Manoochehrtayebi[1,2], Aline Bel-Brunon[3], Martin Genet[1,2]

[1] Laboratoire de Mécanique des Solides (LMS),
École Polytechnique/IPP/CNRS, Palaiseau, France
[2] Équipe MΞDISIM, INRIA, Palaiseau, France
[3] Laboratoire de Mécanique des Contacts et des Structures (LaMCoS),
INSA-Lyon/CNRS, Villeurbanne, France

Abstract

Porous materials are ubiquitous in nature –notably living tissues, which often undergo large deformations– and engineering applications. Poromechanics is an established theory to model the response of such materials; however, it is limited in its description of microscale phenomena, and structure-properties relationships. In this paper, we propose a microscopic poromechanical model based on a novel formulation of the micro-poro-mechanics problem, which allows to compute the response of a periodic porous microstructure to any loading involving fluid pressure, macroscopic strain, and/or macroscopic stress. We systematically compare the global response of our micro-model to macro-poromechanics, in both the infinitesimal and finite strain settings, and investigate in particular three mechanisms, namely solid compressibility, strain-pressure coupling and deviatoric-volumetric strain coupling. We notably illustrate how the micro-model can be used to derive macroscopic parameters, and how these parameters depend on microscopic features like pore shape, porosity, material properties, etc. This modeling framework will be the basis for powerful micro-poro-mechanical models of various materials and tissues, where pore-scale phenomena can be incorporated explicitly.

Keywords

Poromechanics; Micro-poro-mechanics; Finite deformations; Variational formulations; Finite element method.

2.1 Introduction

Porous materials are ubiquitous in nature and engineering applications. For instance, most biological tissues –namely bones, muscles, the brain, the liver, the lung, etc.– can be considered as porous media when observed at the tissue scale. Indeed, at this scale, the tissue can be seen as a fluid phase –mostly blood or air– interacting with a deformable skeleton which stress state is related to tissue deformation as well as fluid pressure. In the case of the lung for instance, during natural breathing, the skeleton experiences very large deformations induced by the negative pleural pressure (which is controlled by the contraction of the diaphragm and intercostal muscles), leading to the inspiration of air at atmospheric pressure; during mechanical ventilation, air is forced into the lung and its pressure deforms the skeleton, opening the alveoli and promoting gaz exchange, through, again, large deformations. Thus, a poro-mechanical formulation adapted to the finite strain setting is required in various application domains such as biomedical engineering.

Modern poromechanics was initially formulated in [Biot, 1941, Terzaghi, 1943, Biot and Temple, 1972], which represents porous media as a mixture of fluid and solid using the volume fraction concept [De Boer and Ehlers, 1988]. A general non-linear poromechanical formulation was proposed by [Chapelle and Moireau, 2014], coupling general solid and fluid models and satisfying fundamental energy and entropy principles. Such poromechanical models can be applied to study the behavior of biological tissues such as cardiac perfusion [Chapelle et al., 2010] or lung parenchyma [Berger et al., 2016, Patte et al., 2022b, Peyraut and Genet, 2023], as well as natural or engineering materials. Some of the parameters of [Patte et al., 2022b]'s model have been identified based on clinical images for patients suffering from fibrosis in order to address clinical challenges [Patte et al., 2022a, Laville et al., 2023]. However, at this scale, these parameters only phenomenologically reflect the micromechanisms at stake at the microscale; there is no general way to relate the parameters to microscopic features such as pore shape, skeleton stiffness, etc.

To better understand and quantify the interactions between microscale phenomena and macroscale properties, multiscale modeling approaches can be employed [Sanchez-Palencia, 1980, Genet et al., 2014, Tueni et al., 2023]. In the context of porous media, this means explicitly representing the solid and fluid domains [Budiansky and Kimmel, 1987, Dormieux et al., 2002, Lopez-Pamies and Ponte Castañeda, 2007]. In addition to allowing to derive structure-properties relationships, this micromechanical approach notably enables to investigate strain and stress distributions within the solid skeleton due to fluid pressure, macroscopic strain and/or macroscopic stress [Dormieux et al., 2006, Lopez-Pamies et al., 2012].

Micromechanical modeling requires first a geometrical microstructure. It can be generated directly from micro-imaging (e.g., micro-tomography) of the porous medium [Bargmann et al., 2018], which has already been performed for instance on polyurethane foams [Youssef et al., 2005], metallic foams [Kantzos et al., 2018] or the lung parenchyma [Toshima et al., 2004, Vasilescu et al., 2012, Rausch et al., 2011, Concha and Hurtado, 2020]. Geometry generation from CT-imaging is very complex and led to the development of semi-automatic segmentation algorithms [Xiao et al., 2016, Bargmann et al., 2018]; however, obtaining a geometry and a mesh suitable for computational mechanics is still a complex task, and the associated computations remain expensive. As an alternative, simplified geometries can be employed to simulate the microstructure based on morphological features, such as the distribution of grain size, shape and orientation [Groeber, 2008]. Randomness can be introduced by considering ellipsoidal [Mebatsion et al., 2006], Voronoi [Alsayednoor and Harrison, 2016] or Poisson-Voronoi [Kumar et al., 1996] tessellations with random seed distributions. Specifically for the lung, various microstructures have been proposed, based on tetrakaidecahedra [Budiansky and Kimmel, 1987, Wiechert et al., 2009, Concha et al., 2018] or Voronoi [Koshiyama and Wada, 2015] tesselations.

As it is excluded to simulate a full structure based on a microscale model, several methods have been proposed to bridge the scales between the micro- and macro-mechanical models. Based on the existence of a Representative Volume Element (RVE), homogenization can be employed to model heterogeneous media composed of several constituents as equivalent homogeneous media [Dormieux et al., 2002, Rohan, 2006, Auriault et al., 2009, Ponte Castañeda, 2016]. The averaging Hill-Mandel principle [Hill, 1963, Mandel, 1972] specifies the equivalence of energy in the two different scales. For some specific configurations, analytical expressions for the macro-mechanical model can be proposed based on an idealized microstruc-

ture [Dormieux et al., 2006, Miller and Penta, 2021, Lukeš and Rohan, 2022]. But in the general case, an explicit meshed microstructure is required to perform mechanical computations at the microscale for the homogenization process.

In this work, we focus on micro- and macro-poro-mechanical modeling in the large strain regime. Even though we illustrate our developments in the context of lung modeling, they are in fact more general and could be applied to any porous material. The Methods and Results Sections 2.2 and 2.3 of the paper are organized as follows. In Section 2.2.1, we start by recalling the Biot macroscopic poromechanical framework, and define a generic poromechanical behavior law. Then, in Section 2.2.2, we introduce a novel formulation of the micro-poro-mechanics problem, such that the microscopic RVE can be loaded by internal pressure, macroscopic strain and/or macroscopic stress. And in Section 2.2.3, we theoretically compare both macro- and micro-models after linearization. In Sections 2.3.1 and 2.3.2, we illustrate the linear and nonlinear responses of the micro-model and the impact of many model parameters, and compare them to the one of the macro-model.

2.2 Methods

2.2.1 Macro-poro-mechanical modeling

2.2.1.1 The Biot poromechanics framework

General considerations. Let us first recall the main elements of the Biot formulation of poromechanics [Biot, 1941, Biot and Temple, 1972]. More details on the Biot formulation can be found in [Coussy, 2004], a very general formulation in [Chapelle and Moireau, 2014], and details on the present formulation in [Patte et al., 2022b]. Thus, we consider a two-phase mixture of a porous solid with interconnected pores and a fluid. In terms of notations, the quantities related to the solid are denoted with the subscript "s", the quantities related to the fluid with the subscript "f", and the quantities related to the mixture with a bar.

In this paper, we restrict our analysis to quasi-static and isothermal transformations. One consequence of the quasi-static hypothesis, together with the pore interconnection hypothesis, is notably that the fluid pressure is homogeneous within the structure. For the sake of simplicity we will consider an incompressible fluid, though all developments could be extended to compressible fluids.

The domains occupied by the mixture in reference and deformed configurations are denoted by $\bar{\Omega}_0$, with boundary $\partial\bar{\Omega}_0$, and $\bar{\omega}$, with boundary $\partial\bar{\omega}$, respectively (cf. Figure 2.1). In terms of notations, we denote the quantities defined in the reference configuration in uppercase and the ones defined in the deformed configuration in lowercase. Also, a subscript "0" is used for all quantities characterizing the reference configuration.

Kinematic variables. The displacement (denoted by $\underline{\bar{U}} : \bar{\Omega}_0 \to \mathbb{R}^n$) is defined as the difference between the positions of material points in the reference (denoted by $\underline{\bar{X}} \in \bar{\Omega}_0$) and deformed (denoted by $\underline{\bar{x}} \in \bar{\omega}$) configurations through the mapping (denoted by $\underline{\bar{\chi}} : \bar{\Omega}_0 \to \bar{\omega}$, cf. Figure 2.1):

$$\underline{\bar{U}}\left(\underline{\bar{X}}\right) := \underline{\bar{\chi}}\left(\underline{\bar{X}}\right) - \underline{\bar{X}} = \underline{\bar{x}}\left(\underline{\bar{X}}\right) - \underline{\bar{X}}. \tag{2.1}$$

From it we define kinematic variables describing the deformation of the mixture, namely the deformation gradient

$$\underline{\underline{\bar{F}}} := \underline{\underline{\mathrm{Grad}}}\left(\underline{\bar{\chi}}\right) = \underline{\underline{1}} + \underline{\underline{\mathrm{Grad}}}\left(\underline{\bar{U}}\right), \tag{2.2}$$

the relative change of volume

$$\bar{J} := \mathrm{Det}\left(\underline{\underline{\bar{F}}}\right), \tag{2.3}$$

the right Cauchy-Green dilatation tensor with its first invariant and first reduced invariants

$$\underline{\underline{\bar{C}}} := {}^t\underline{\underline{\bar{F}}} \cdot \underline{\underline{\bar{F}}}, \quad \bar{I}_1 := \mathrm{Tr}\left(\underline{\underline{\bar{C}}}\right), \quad \bar{J}_1 := \bar{J}^{-2/3}\bar{I}_1, \tag{2.4}$$

and the Green-Lagrange strain tensor

$$\underline{\underline{\bar{E}}} := \frac{1}{2}\left(\underline{\underline{\bar{C}}} - \underline{\underline{1}}\right). \tag{2.5}$$

All illustrations of this paper will in 2D, under the plane strain hypothesis. Thus, from now on, all tensors actually represent the planar components of the considered quantities. Regarding the invariants, let us simply recall the following relations between the invariants of the full tensors and the invariants of the tensors restricted to the planar components, which are derived in Appendix A:

$$\bar{J}^{3D} = \bar{J}^{2D}, \quad \bar{I}_1^{3D} = \bar{I}_1^{2D} + 1, \quad \bar{J}_1^{3D} = \left(\bar{J}^{2D}\right)^{-2/3}\left(\bar{I}_1^{2D} + 1\right). \tag{2.6}$$

As for the tensors, from now on, all invariants represent the invariants of the tensors restricted to the planar components.

Mixture variables. The infinitesimal domain in the reference and deformed configurations are denoted by $d\bar{\Omega}_0$ and $d\bar{\omega}_0$, respectively (cf. Figure 2.1). Each domain is decomposed into a solid phase and a fluid phase so that $d\bar{\Omega}_0 = d\Omega_{f0} \cup d\Omega_{s0}$, and $d\bar{\omega} = d\omega_f \cup d\omega_s$. We introduce the volume fractions of fluid (i.e., porosity) and solid in the mixture, both in the reference or the deformed configurations:

$$\begin{cases} \bar{\Phi}_{f0} := \dfrac{|d\Omega_{f0}|}{|d\bar{\Omega}_0|}, & \bar{\phi}_f := \dfrac{|d\omega_f|}{|d\bar{\omega}|} \\ \bar{\Phi}_{s0} := \dfrac{|d\Omega_{s0}|}{|d\bar{\Omega}_0|}, & \bar{\phi}_s := \dfrac{|d\omega_s|}{|d\bar{\omega}|} \end{cases}, \tag{2.7}$$

which are such that $\bar{\Phi}_{f0} + \bar{\Phi}_{s0} = \bar{\phi}_f + \bar{\phi}_s = 1$; similarly, the deformed volume fractions of fluid (i.e., porosity) and solid pulled back into the reference configuration:

$$\begin{cases} \bar{\Phi}_f := \dfrac{|d\omega_f|}{|d\bar{\Omega}_0|} = \bar{J} \cdot \left(\bar{\phi}_f \circ \underline{\chi}\right) \\ \bar{\Phi}_s := \dfrac{|d\omega_s|}{|d\bar{\Omega}_0|} = \bar{J} \cdot \left(\bar{\phi}_s \circ \underline{\chi}\right) \end{cases}, \tag{2.8}$$

are such that $\bar{\Phi}_f + \bar{\Phi}_s = \bar{J}$.

We have the same decomposition for the mass as for the volume, i.e., $d\bar{M}_0 = dM_{f0} + dM_{s0}$ and $d\bar{m} = dm_f + dm_s$. Regarding mass densities, it is important to distinguish constituents *actual* densities, defined as mass per unit constituent volume:

$$\begin{cases} \rho_{f0} := \dfrac{dM_{f0}}{|d\Omega_{f0}|}, & \varrho_f := \dfrac{dm_f}{|d\omega_f|} \\ \rho_{s0} := \dfrac{dM_{s0}}{|d\Omega_{s0}|}, & \varrho_s := \dfrac{dm_s}{|d\omega_s|} \end{cases}, \tag{2.9}$$

from constituents *apparent* densities, defined as mass per unit mixture volume:

$$\begin{cases} \bar{\rho}_{f0} := \dfrac{dM_{f0}}{|d\bar{\Omega}_0|} = \rho_{f0}\bar{\Phi}_{f0}, & \bar{\varrho}_f := \dfrac{dm_f}{|d\bar{\omega}|} = \varrho_f\bar{\phi}_f \\ \bar{\rho}_{s0} := \dfrac{dM_{s0}}{|d\bar{\Omega}_0|} = \rho_{s0}\bar{\Phi}_{s0}, & \bar{\varrho}_s := \dfrac{dm_s}{|d\bar{\omega}|} = \varrho_s\bar{\phi}_s \end{cases}, \tag{2.10}$$

as well as *deformed apparent* densities pulled back into the reference configuration:

$$\begin{cases} \bar{\rho}_f := \dfrac{dm_f}{\left|d\bar{\Omega}_0\right|} = \bar{J} \cdot \left(\bar{\varrho}_f \circ \underline{\chi}\right) \\ \bar{\rho}_s := \dfrac{dm_s}{\left|d\bar{\Omega}_0\right|} = \bar{J} \cdot \left(\bar{\varrho}_s \circ \underline{\chi}\right) \end{cases} . \tag{2.11}$$

Thus, the mixture mass density, in both reference and deformed configurations, can be decomposed into fluid and solid mass densities:

$$\bar{\rho}_0 := \frac{d\bar{M}_0}{\left|d\bar{\Omega}_0\right|} = \bar{\rho}_{f0} + \bar{\rho}_{s0}, \quad \bar{\varrho} := \frac{d\bar{m}}{\left|d\bar{\omega}\right|} = \bar{\varrho}_f + \bar{\varrho}_s, \quad \bar{\rho} := \frac{d\bar{m}}{\left|d\bar{\Omega}_0\right|} = \bar{\rho}_f + \bar{\rho}_s. \tag{2.12}$$

Conservation of mass induces that $dm_s = dM_{s0}$, but not for the fluid, as it can be added or subtracted from material points. Thus, we define the added fluid mass density:

$$\bar{\rho}_{f\pm} := \frac{dm_f - dM_{f0}}{\left|d\bar{\Omega}_0\right|} = \bar{\rho}_f - \bar{\rho}_{f0}. \tag{2.13}$$

This quantity is positive in the case of inflation, i.e., when fluid is added to the medium, and negative in the case of deflation, i.e., when fluid is subtracted from the medium. Note that in the case of incompressibility of the fluid, we have $\varrho_f = \rho_{f0}$, and thus $\bar{\rho}_{f\pm} = \rho_{f0}\left(\bar{\Phi}_f - \bar{\Phi}_{f0}\right)$.

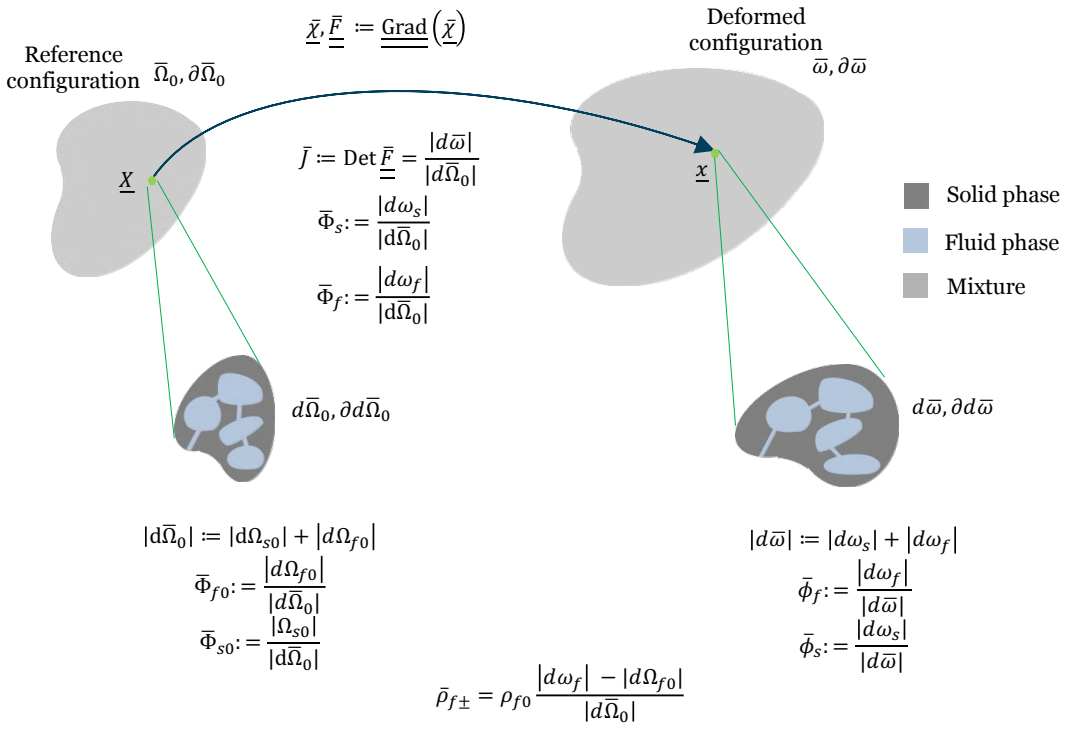

Figure 2.1: Porous medium at macroscopic and microscopic scales, in reference and deformed configurations. Definition of kinematic and mixture variables.

2.2.1.2 Constitutive framework

We characterize the constitutive behavior of the mixture through its Helmholtz free energy density per unit reference mixture volume, denoted by $\bar{\Psi}$. Classically, we consider

as state variables the Green-Lagrange strain tensor $\bar{\underline{\underline{E}}}$ and the added fluid mass density $\bar{\rho}_{f\pm}$ [Coussy, 2004, Chapelle and Moireau, 2014]. In accordance with one of the fundamental principles of poromechanics, we additively decompose the free energy density into solid and fluid parts [Coussy, 2004, Chapelle and Moireau, 2014], which implies some kind of decoupling between the solid and fluid contributions to the mixture behavior. Furthermore, it is convenient to express the solid and fluid free energy densities using solid and fluid volume fractions:

$$\bar{\Psi}\left(\bar{\underline{\underline{E}}}, \bar{\rho}_{f\pm}\right) = \bar{\Psi}_s\left(\bar{\underline{\underline{E}}}, \bar{\Phi}_s\right) + \bar{\Psi}_f\left(\bar{\Phi}_f\right), \tag{2.14}$$

recalling the following simplified identities in the case of fluid incompressibility:

$$\begin{cases} \bar{\Phi}_s\left(\bar{\underline{\underline{E}}}, \bar{\rho}_{f\pm}\right) = \bar{J}\left(\bar{\underline{\underline{E}}}\right) - \bar{\Phi}_f\left(\bar{\rho}_{f\pm}\right) \\ \bar{\Phi}_f\left(\bar{\rho}_{f\pm}\right) = \bar{\Phi}_{f0} + \dfrac{\bar{\rho}_{f\pm}}{\rho_{f0}} \end{cases}. \tag{2.15}$$

Under the assumptions of fluid incompressibility and isothermal conditions, the fluid free energy density can simply be expressed as:

$$\bar{\Psi}_f(\bar{\Phi}_f) = -\bar{p}_{f0}\bar{\Phi}_f, \tag{2.16}$$

where $\bar{p}_{f0}$ is a reference pressure [Chapelle and Moireau, 2014]. As for the solid free energy density, it will be specified in the next Section.

Based on the second principle of thermodynamics, the second Piola-Kirchhoff stress tensor derives from the free energy density potential:

$$\begin{aligned} \bar{\underline{\underline{\Sigma}}}\left(\bar{\underline{\underline{E}}}, \bar{\rho}_{f\pm}\right) &= \frac{\partial \bar{\Psi}\left(\bar{\underline{\underline{E}}}, \bar{\rho}_{f\pm}\right)}{\partial \bar{\underline{\underline{E}}}} \\ &= \left.\frac{d\bar{\Psi}_s\left(\bar{\underline{\underline{E}}}, \bar{\Phi}_s\right)}{d\bar{\underline{\underline{E}}}}\right|_{\bar{\rho}_{f\pm}} + \left.\frac{d\bar{\Psi}_f\left(\bar{\Phi}_f\right)}{d\bar{\underline{\underline{E}}}}\right|_{\bar{\rho}_{f\pm}} \\ &= \frac{\partial \bar{\Psi}_s\left(\bar{\underline{\underline{E}}}, \bar{\Phi}_s\right)}{\partial \bar{\underline{\underline{E}}}} + \frac{\partial \bar{\Psi}_s\left(\bar{\underline{\underline{E}}}, \bar{\Phi}_s\right)}{\partial \bar{\Phi}_s} \cdot \frac{\partial \bar{\Phi}_s}{\partial \bar{\underline{\underline{E}}}} + \frac{\partial \bar{\Psi}_f\left(\bar{\Phi}_f\right)}{\partial \bar{\Phi}_f} \cdot \frac{\partial \bar{\Phi}_f}{\partial \bar{\underline{\underline{E}}}} \\ &= \frac{\partial \bar{\Psi}_s\left(\bar{\underline{\underline{E}}}, \bar{\Phi}_s\right)}{\partial \bar{\underline{\underline{E}}}} - \bar{p}_s \bar{J} \bar{\underline{\underline{C}}}^{-1}, \end{aligned} \tag{2.17}$$

where $\bar{p}_s := -\frac{\partial \bar{\Psi}_s\left(\bar{\underline{\underline{E}}}, \bar{\Phi}_s\right)}{\partial \bar{\Phi}_s}$ represents the solid hydrostatic pressure associated to solid volume fraction change. Another fundamental principle of poromechanics states that the equality of such solid hydrostatic pressure with the fluid pressure:

$$\bar{p}_s = \bar{p}_f, \tag{2.18}$$

which basically imposes the internal equilibrium of the mixture [Coussy, 2004, Chapelle and Moireau, 2014]. The fluid pressure $\bar{p}_f$ is the dual variable of the added fluid mass density $\bar{\rho}_{f\pm}$. In practice it can be known or unknown depending on if the added fluid mass density is prescribed or free. Nevertheless, this internal equilibrium induces a strong coupling between the fluid and solid states in the mixture response, as seen in the following expression of the states laws:

$$\begin{cases} \bar{\underline{\underline{\Sigma}}} = \dfrac{\partial \bar{\Psi}_s\left(\bar{\underline{\underline{E}}}, \bar{\Phi}_s\right)}{\partial \bar{\underline{\underline{E}}}} - \bar{p}_f \bar{J} \bar{\underline{\underline{C}}}^{-1} \\ \bar{p}_f = -\dfrac{\partial \bar{\Psi}_s\left(\bar{\underline{\underline{E}}}, \bar{\Phi}_s\right)}{\partial \bar{\Phi}_s} \end{cases}. \tag{2.19}$$

Classically, we additively decompose the contributions of the strain and solid volume fraction to the solid free energy density:

$$\bar{\Psi}_s\left(\underline{\underline{\bar{E}}}, \bar{\Phi}_s\right) = \bar{\Psi}_{skel}\left(\underline{\underline{\bar{E}}}\right) + \bar{\Psi}_{bulk}\left(\bar{\Phi}_s\right), \tag{2.20}$$

where $\bar{\Psi}_{skel}$ basically characterizes the mechanical response of the skeleton as a structure, while $\bar{\Psi}_{bulk}$ basically characterizes its response to solid volume change [Coussy, 2004, Chapelle and Moireau, 2014]. Based on this decomposition, we can express the stress tensor and the internal pressure as

$$\begin{cases} \underline{\underline{\bar{\Sigma}}} = \dfrac{\partial \bar{\Psi}_{skel}}{\partial \underline{\underline{\bar{E}}}} - \bar{p}_f \bar{J} \underline{\underline{\bar{C}}}^{-1} \\ \bar{p}_f = -\dfrac{\partial \bar{\Psi}_{bulk}}{\partial \bar{\Phi}_s} \end{cases}. \tag{2.21}$$

One can note that, as discussed in [Chapelle and Moireau, 2014], this additive decomposition induces that the model verifies the Terzaghi principle, and that the Biot tensor is the identity tensor, which is only valid for a mixture with an incompressible solid. This hypothesis will be further discussed in light of our micro-poro-mechanical modeling.

2.2.1.3 Constitutive law

Many constitutive laws have been proposed for poroelastic media [Coussy, 2004, Dormieux et al., 2006]. For the sake of illustration, in this paper we will consider only simple potentials, namely Neo-Hookean Ogden-Ciarlet-Geymonat potentials [Ogden, 1972, Ciarlet and Geymonat, 1982]. However, in order to study the coupling between deviatoric and volumetric responses in light of our micro-poro-mechanical model, we will consider two variants for the skeleton energy, based on invariants and reduced invariants, respectively.

Thus, in the 2D plane strain setting, the "coupled" version of the Neo-Hookean Ogden-Ciarlet-Geymonat is expressed as

$$\bar{\Psi}_{skel}^{coup}\left(\underline{\underline{\bar{E}}}\right) = \frac{\bar{\lambda}}{4}\left(\bar{J}^2 - 1 - 2\ln\left(\bar{J}\right)\right) + \frac{\bar{\mu}}{2}\left(\bar{I}_1 - 2 - 2\ln\left(\bar{J}\right)\right), \tag{2.22}$$

and the "decoupled" version as

$$\bar{\Psi}_{skel}^{decoup}\left(\underline{\underline{\bar{E}}}\right) = \frac{\bar{k}}{4}\left(\bar{J}^2 - 1 - 2\ln\left(\bar{J}\right)\right) + \frac{\bar{\mu}}{2}\left(\bar{J}^{-2/3}\left(\bar{I}_1 + 1\right) - 3\right), \tag{2.23}$$

where $\bar{\lambda}$, $\bar{\mu}$ and $\bar{k} := \frac{3\bar{\lambda}+2\bar{\mu}}{3}$ are material parameters: first Lamé constant, second Lamé constant/shear modulus and bulk modulus of the mixture. Note that these two models generate two fundamentally different responses, and cannot be made equivalent by adapting their parameters. For the bulk energy we simply use a modified Ogden-Ciarlet-Geymonat potential:

$$\bar{\Psi}_{bulk}\left(\bar{\Phi}_s\right) = \frac{\bar{\kappa}}{4}\left(\bar{\Phi}_s^2 - \bar{\Phi}_{s0}^2 - 2\ln\left(\frac{\bar{\Phi}_s}{\bar{\Phi}_{s0}}\right)\right), \tag{2.24}$$

with $\bar{\kappa}$ the bulk modulus of the solid phase.

In fine, by substituting Equations (2.22) or (2.23) and (2.24) into Equation (2.21), we can derive the relation between the second Piola-Kirchhoff stress tensor, the Green-Lagrange strain tensor, and the fluid pressure:

$$\begin{cases} \underline{\underline{\bar{\Sigma}}}^{coup} = \frac{\bar{\lambda}}{2}\left(\bar{J} - \dfrac{1}{\bar{J}}\right)\bar{J}\underline{\underline{\bar{C}}}^{-1} + \bar{\mu}\left(\underline{\underline{1}} - \underline{\underline{\bar{C}}}^{-1}\right) - \bar{p}_f \bar{J}\underline{\underline{\bar{C}}}^{-1} \\ \underline{\underline{\bar{\Sigma}}}^{decoup} = \frac{\bar{k}}{2}\left(\bar{J} - \dfrac{1}{\bar{J}}\right)\bar{J}\underline{\underline{\bar{C}}}^{-1} + \dfrac{\bar{\mu}}{\bar{J}^{2/3}}\left(\underline{\underline{1}} - \dfrac{\bar{I}_1 + 1}{3}\underline{\underline{\bar{C}}}^{-1}\right) - \bar{p}_f \bar{J}\underline{\underline{\bar{C}}}^{-1} \\ \bar{p}_f = -\dfrac{\bar{\kappa}}{2}\left(\bar{\Phi}_s - \dfrac{1}{\bar{\Phi}_s}\right) \end{cases}. \tag{2.25}$$

We can also push forward these relations to the deformed configuration, and express the constitutive laws in terms of the Cauchy stress tensor (i.e., $\underline{\underline{\bar{\sigma}}} = \frac{1}{\bar{J}}\underline{\underline{\bar{F}}} \cdot \underline{\underline{\bar{\Sigma}}} \cdot {}^t\underline{\underline{\bar{F}}}$, omitting the compositions with the mapping $\underline{\chi}$ for the sake of conciseness):

$$\begin{cases} \underline{\underline{\bar{\sigma}}}^{coup} = \frac{\bar{\lambda}}{2}\left(\bar{J} - \frac{1}{\bar{J}}\right)\underline{\underline{1}} + \frac{\bar{\mu}}{\bar{J}}\left(\underline{\underline{\bar{b}}} - \underline{\underline{1}}\right) - \bar{p}_f\underline{\underline{1}} \\ \underline{\underline{\bar{\sigma}}}^{decoup} = \frac{\bar{k}}{2}\left(\bar{J} - \frac{1}{\bar{J}}\right)\underline{\underline{1}} + \frac{\bar{\mu}}{\bar{J}^{5/3}}\left(\underline{\underline{\bar{b}}} - \frac{\bar{I}_1 + 1}{3}\underline{\underline{1}}\right) - \bar{p}_f\underline{\underline{1}} \\ \bar{p}_f = -\frac{\bar{\kappa}}{2}\left(\bar{\Phi}_s - \frac{1}{\bar{\Phi}_s}\right) \end{cases}, \tag{2.26}$$

where $\underline{\underline{\bar{b}}} := \underline{\underline{\bar{F}}} \cdot {}^t\underline{\underline{\bar{F}}}$ is the left Cauchy-Green deformation tensor.

2.2.1.4 Linearization

Before moving to the micro-mechanical model, we propose to linearize the macro-poro-mechanical model that has just been described. This will be useful to match those two models around their rest state, to further explore their differences at larger strains. Let us recall the following linearized expressions under the plane strain hypothesis:

$$\bar{J} \approx 1 + \mathrm{tr}\left(\underline{\underline{\bar{\epsilon}}}\right), \quad \underline{\underline{\bar{b}}} \approx \underline{\underline{1}} + 2\underline{\underline{\bar{\epsilon}}}, \quad \bar{I}_1 \approx 2 + 2\mathrm{tr}\left(\underline{\underline{\bar{\epsilon}}}\right), \quad \bar{\Phi}_s \approx \bar{\Phi}_{s0} + \mathrm{tr}\left(\underline{\underline{\bar{\epsilon}}}\right) - \frac{\bar{\rho}_{f\pm}}{\rho_{f0}}, \tag{2.27}$$

where $\underline{\underline{\bar{\epsilon}}} := \left(\underline{\underline{\mathrm{Grad}}}\left(\underline{\bar{U}}\right)\right)_{sym} = \frac{1}{2}\left(\underline{\underline{\mathrm{Grad}}}\left(\underline{\bar{U}}\right) + {}^t\underline{\underline{\mathrm{Grad}}}\left(\underline{\bar{U}}\right)\right)$ is the infinitesimal deformation tensor. Introducing Equations (2.27) in Equations (2.25), we end up with the following linear relation between stress and strain:

$$\begin{cases} \underline{\underline{\bar{\sigma}}}^{coup} \approx \bar{\lambda}\ \mathrm{tr}\left(\underline{\underline{\bar{\epsilon}}}\right)\underline{\underline{1}} + 2\bar{\mu}\ \underline{\underline{\bar{\epsilon}}} - \bar{p}_f\underline{\underline{1}} \\ \underline{\underline{\bar{\sigma}}}^{decoup} \approx 3\bar{k}\ \underline{\underline{\bar{\epsilon}}}^S + 2\bar{\mu}\ \underline{\underline{\bar{\epsilon}}}^D - \bar{p}_f\underline{\underline{1}} \\ \bar{p}_f \approx -\bar{\kappa}\left(\mathrm{tr}\left(\underline{\underline{\bar{\epsilon}}}\right) - \frac{\bar{\rho}_{f\pm}}{\rho_{f0}}\right) \end{cases}, \tag{2.28}$$

where $\underline{\underline{\bar{\epsilon}}}^S := \frac{1}{3}\mathrm{tr}\left(\underline{\underline{\bar{\epsilon}}}\right)\underline{\underline{1}}$ and $\underline{\underline{\bar{\epsilon}}}^D := \underline{\underline{\bar{\epsilon}}} - \underline{\underline{\bar{\epsilon}}}^S$ are the spherical and deviatoric parts of the infinitesimal deformation tensor, characterizing all volumetric (i.e., all inflations and deflations) and non-volumetric (i.e., all shears) deformations, respectively. Note that, contrary to the nonlinear regime, in the linear regime the "coupled" and "decoupled" models could be made fully equivalent by adapting their parameters–they are two different expressions of the same stress-strain response. Indeed, the different couplings between volumetric and deviatoric strains present in the original nonlinear potentials are only activated in the finite strain regime, not in the infinitesimal strain regime.

2.2.2 Micro-poro-mechanical modeling

The poromechanical model presented in the previous Section is useful to study material-scale behavior and perform structural-scale simulations for a relatively small computational cost. However, it does not rely on an explicit representation of the microstructure: basically there is no direct structure-properties-state bridge. More precisely, (i) the macroscopic parameters are not directly linked to the microscopic structure and properties (a linear dependency of the stiffness to the porosity has been considered in [Patte et al., 2022a, Laville et al., 2023]; more physically sound dependencies have been obtained through homogenization in [Dormieux et al., 2006], albeit for spherical pores and in the small strain setting); (ii) the description of complex deformation mechanisms such

as the coupling between deviatoric and volumetric deformations, or between strain-induced and pressure-induced deformations, as well as the description of complex physical mechanisms such as surface tensions [Coussy, 2010] or tissue growth [Genet, 2019], is not straightforward and remains purely phenomenological; (iii) the macroscopic model only characterizes the strain and stress of a given material point using a single tensor, and although it can be decomposed into solid and fluid parts [Patte et al., 2022b, Patte et al., 2022a], it still represents an averaging of the strain and stress fields actually seen by the microstructure, while they can be significantly dispersed [Rausch et al., 2011].

To address such limitations, let us now introduce the microscopic counterpart to our macroscopic poromechanics model. We assume the same quasi-static & isothermal restrictions. A first formulation of micro-poro-mechanics was proposed in [Álvarez-Barrientos et al., 2021], but we now introduce a better formulation, valid for any microstructure, as detailed in Appendix B. As for the macroscopic model, we consider two-dimensional plane strain conditions.

2.2.2.1 Geometry

We consider various periodic porous RVEs, starting with regular microstructures with circular or hexagonal inclusions (cf. Figure 2.2). The inclusions are arranged in a hexagonal pattern in order to maintain 60° rotational invariance, which induces an isotropic homogenized response in the linear elastic regime [Ptashnyk and Seguin, 2016]. An important difference between both is that circular inclusions are fundamentally limited to ca. 91% porosity while hexagonal inclusions can reach arbitrary porosities.

We also consider RVEs with random polygonal inclusions, generated by creating a Voronoi tesselation of randomly distributed seed points (cf. Figure 2.2). In order to obtain periodic microstructures, the seeds are duplicated in the eight boxes surrounding the RVE, the full tesselation is created and then cut at the RVE borders, as proposed in [Spyrou et al., 2019]. Any porosity can be reached by adapting the thickness of the walls. These microstructures are in general not isotropic, though they tend toward isotropy when increasing the number of seeds.

Definition of the geometry and meshing is performed using GMSH [Geuzaine and Remacle, 2009]. Due to the quasi-static assumption of this work, fluid velocity is null and fluid pressure is homogeneous; hence, there is no need to solve a fluid problem, and only the solid part is meshed.

(a) Circular inclusions (b) Hexagonal inclusions (c) Polygonal inclusions

Figure 2.2: Various periodic porous microstructures considered for the micro-poro-mechanical model.

2.2.2.2 Micro-poro-mechanics framework

General considerations. We expand upon the framework of [Álvarez-Barrientos et al., 2021] to compute the poromechanical response of our microstructures. The reference configuration is denoted by Ω_0, which is composed of a solid phase, denoted by Ω_{s0}, and a fluid phase, denoted by Ω_{f0}, such that $\Omega_0 = \Omega_{s0} \cup \Omega_{f0}$ (cf. Figure 2.3). We denote by $\partial\Omega_{f0}$ the fluid-solid interface, and by $\partial\Omega_{s0}\backslash\partial\Omega_{f0}$ the periodic cuts of the solid phase. In the deformed configuration, the RVE, solid and fluid domains are denoted by $\omega = \omega_s \cup \omega_f$, and the associated surfaces $\partial\omega_f$ and $\partial\omega_s\backslash\partial\omega_f$. Furthermore, in the microscopic model we denote all global –or homogenized– quantities with a tilde, which can then be directly compared with quantities of the macroscopic model denoted with a bar. For instance, we define similar volume fractions as for the macroscopic model:

$$\begin{cases} \tilde{\Phi}_{s0} := \dfrac{|\Omega_{s0}|}{|\Omega_0|}, & \tilde{\phi}_s := \dfrac{|\omega_s|}{|\omega|}, & \tilde{\Phi}_s := \dfrac{|\omega_s|}{|\Omega_0|} \\ \tilde{\Phi}_{f0} := \dfrac{|\Omega_{f0}|}{|\Omega_0|}, & \tilde{\phi}_f := \dfrac{|\omega_f|}{|\omega|}, & \tilde{\Phi}_f := \dfrac{|\omega_f|}{|\Omega_0|} \end{cases} . \tag{2.29}$$

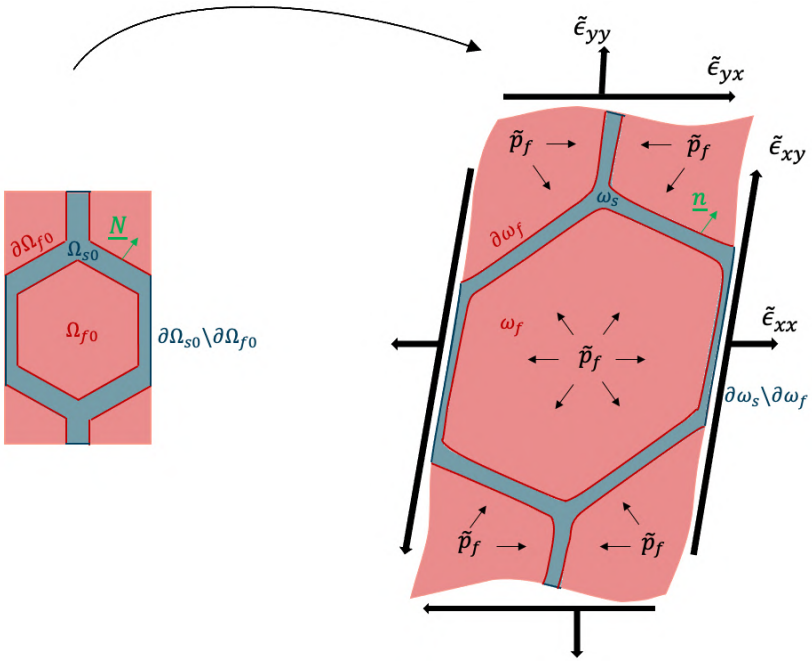

Figure 2.3: Porous medium at the microscopic scale in the reference and deformed configuration.

Kinematics. Without loss of generality, the total displacement $\underline{U}$ is additively decomposed into an affine part, characterized by the symmetric tensor $\underline{\underline{\tilde{\epsilon}}}$, and a periodic part, characterized by the displacement field $\underline{\widehat{U}}$ (cf. Figure 2.4):

$$\underline{U}\,(\underline{X}) = \underline{\underline{\tilde{\epsilon}}} \cdot (\underline{X} - \underline{X}_0) + \underline{\widehat{U}}\,(\underline{X})\,, \tag{2.30}$$

where $\underline{X}_0$ is an arbitrary point in the microstructure, the "center" of the affine transformation. The symmetry of the macroscopic strain $\underline{\underline{\tilde{\epsilon}}}$ ensures that the affine part does not contain any rotation. Note also that other boundary conditions could be used for the perturbation $\underline{\widehat{U}}$ instead of periodicity, such as kinematically uniform boundary conditions (i.e., vanishing perturbation at the boundary), stress uniform boundary conditions (i.e., vanishing

stress at the boundary), etc., cf. [Álvarez-Barrientos et al., 2021]; here we focus on periodic boundary conditions because they are the most rigorous and lead, after homogenization, directly to the classical asymptotic homogenization framework [Sanchez-Palencia, 1980], cf. Section 2.2.2.6.

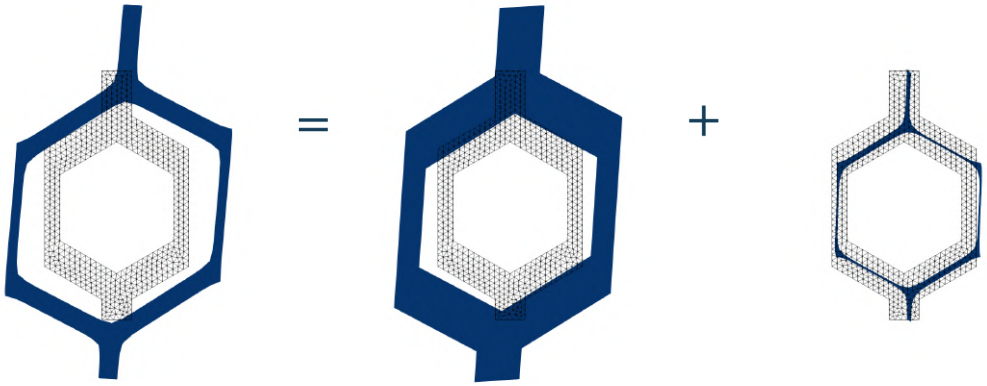

Figure 2.4: Decomposition of the total deformation of the RVE into an affine part and a periodic perturbation.

We can then express all standard kinematic variables as a function of $\underline{\underline{\tilde{\epsilon}}}$ and $\underline{\widehat{U}}$, namely the deformation gradient

$$\underline{\underline{F}} := \underline{\underline{1}} + \underline{\underline{\mathrm{Grad}}}\,(\underline{U}) = \underline{\underline{1}} + \underline{\underline{\tilde{\epsilon}}} + \underline{\underline{\mathrm{Grad}}}\left(\underline{\widehat{U}}\right), \tag{2.31}$$

the Jacobian of the transformation

$$J := \mathrm{Det}\left(\underline{\underline{F}}\right), \tag{2.32}$$

the right Cauchy-Green dilatation tensor with its first invariant

$$\underline{\underline{C}} := {}^{t}\underline{\underline{F}} \cdot \underline{\underline{F}}, \quad I_1 := \mathrm{Tr}\left(\underline{\underline{C}}\right), \tag{2.33}$$

and the Green-Lagrange strain tensor

$$\underline{\underline{E}} := \frac{1}{2}\left(\underline{\underline{C}} - \underline{\underline{1}}\right). \tag{2.34}$$

Because of the periodicity of $\underline{\widehat{U}}$, it does not contribute to the RVE global deformation, which is thus only characterized by $\underline{\underline{\tilde{\epsilon}}}$:

$$\underline{\underline{\tilde{F}}} := \frac{1}{|\omega|}\left(\int_{\Omega} \underline{\underline{F}}\, d\Omega\right) = \underline{\underline{1}} + \underline{\underline{\tilde{\epsilon}}}, \quad \tilde{J} := \mathrm{Det}\left(\underline{\underline{\tilde{F}}}\right). \tag{2.35}$$

Thus, and as detailed in Appendix B, the deformed volumes can be expressed as:

$$|\omega| = \tilde{J}\ |\Omega_0|, \quad |\omega_f| = |\omega| - |\omega_s|, \quad |\omega_s| = \int_{\Omega_{s0}} J\ d\Omega_{s0}, \tag{2.36}$$

such that the deformed volume fractions can be expressed as:

$$\tilde{\Phi}_f = \tilde{J} - \tilde{\Phi}_s, \quad \tilde{\Phi}_s = \frac{1}{|\Omega_0|}\int_{\Omega_{s0}} J\ d\Omega_{s0}. \tag{2.37}$$

Macroscopic stress. Let us introduce the dual energetic counterpart to the macroscopic strain, i.e., the macroscopic stress, expressed here in both deformed and reference configurations:

$$\underline{\underline{\tilde{\sigma}}} := \frac{1}{|\omega|}\left(\int_{\omega_s} \underline{\underline{\sigma_s}}\, d\omega_s - |\omega_f|\,\tilde{p}_f \underline{\underline{1}}\right) = \frac{1}{|\omega|}\left(\int_{\Omega_{s0}} \underline{\underline{F}} \cdot \underline{\underline{\Sigma_s}} \cdot {}^t\underline{\underline{F}}\, d\Omega_{s0} - |\omega_f|\,\tilde{p}_f \underline{\underline{1}}\right), \tag{2.38}$$

where $\underline{\underline{\sigma_s}}$ and $\underline{\underline{\Sigma_s}}$ denote the Cauchy and second Piola-Kirchhoff stress respectively, verifying $\underline{\underline{\sigma_s}} = \frac{1}{J}\underline{\underline{F}} \cdot \underline{\underline{\Sigma_s}} \cdot {}^t\underline{\underline{F}}$ (mappings between the reference and deformed configurations is omitted for the sake of conciseness), and where $\tilde{p}_f$ denotes the fluid pressure, which is homogeneous within the pores because of the quasi-static and pore interconnection hypotheses.

Macroscopic added fluid mass density. We can also introduce the dual variable of the fluid pressure, i.e., the macroscopic added fluid mass density:

$$\tilde{\rho}_{f\pm} := \frac{\varrho_f\,|\omega_f| - \rho_{f0}\,|\Omega_{f0}|}{|\Omega_0|} = \varrho_f \tilde{\Phi}_f - \rho_{f0}\tilde{\Phi}_{f0}. \tag{2.39}$$

2.2.2.3 Solid constitutive law

We assume that the solid obeys a standard elastic law, such that its stress-strain relation derives from its free energy potential:

$$\underline{\underline{\Sigma_s}} = \frac{\partial \Psi_s}{\partial \underline{\underline{E}}}. \tag{2.40}$$

Because here the solid is considered a standard continuum, its free energy has only one contribution, namely the elastic energy: $\Psi_s = W_s$. Following the choices made for the macroscopic model, we consider the simple Ogden-Ciarlet-Geymonat-Neohookean law, in its coupled and uncoupled forms, in plane strain (cf. Appendix A):

$$\begin{cases} W_s^{coup} = \dfrac{\lambda_s}{4}\left(J^2 - 1 - 2\ln(J)\right) + \dfrac{\mu_s}{2}\left(I_1 - 2 - 2\ln(J)\right) \\ W_s^{decoup} = \dfrac{k_s}{4}\left(J^2 - 1 - 2\ln(J)\right) + \dfrac{\mu_s}{2}\left(J^{-2/3}\left(I_1 + 1\right) - 3\right) \end{cases}, \tag{2.41}$$

where λ_s and μ_s are the first and second (i.e., shear modulus) Lamé constants, and k_s is the bulk modulus. We recall the following relations:

$$\lambda_s = \frac{E_s \nu_s}{(1+\nu_s)(1-2\nu_s)},\ \mu_s = \frac{E_s}{2(1+\nu_s)},\ k_s = \frac{3\lambda_s + 2\mu_s}{3}, \tag{2.42}$$

with E_s and ν_s the Young modulus and Poisson ratio respectively.

2.2.2.4 Solid equilibrium equations

The internal equilibrium of the solid can be expressed, in the deformed configuration, as:

$$\begin{cases} \underline{\mathrm{div}}\left(\underline{\underline{\sigma_s}}\right) = 0 & \text{in } \omega_s \\ {}^t\underline{\underline{\sigma_s}} = \underline{\underline{\sigma_s}} & \text{in } \omega_s \\ [\![\, \underline{\underline{\sigma_s}} \cdot \underline{n} \,]\!] = 0 & \text{on } \partial\omega_s \backslash \partial\omega_f \end{cases} \tag{2.43}$$

The first equation represents the balance of linear momentum, the second the balance of angular momentum, and the third the continuity of the traction vector at the periodic interfaces, $\underline{n}$ being the outward normal to the solid. We also have the external equilibrium of the solid, i.e., the equilibrium between the solid and fluid:

$$\underline{\underline{\sigma_s}} \cdot \underline{n} = -\tilde{p}_f\, \underline{n} \text{ on } \partial\omega_f. \tag{2.44}$$

2.2.2.5 Micro-poro-mechanics problem

Macroscopic strain/stress constraints. Solving the microscopic problem requires to prescribe, for each component, either the macroscopic strain or the macroscopic stress, and solve for the other one. This is analogous to the macroscopic model which can be solved in terms of the stress response to an applied strain or vice-versa (component-wise). Let us call IJ the set of prescribed strain components, and by $\tilde{\epsilon}'_{ij}\ \forall ij \in IJ$ the prescribed values; for the prescribed stress components we use KL and $\tilde{\sigma}'_{kl}\ \forall kl \in KL$.

Weak formulation. The process of deriving the weak formulation is detailed in Appendix B, and we only recall here the final formulation:

$$\text{Given } (\tilde{\epsilon}_{ij}, \tilde{p}_f)\,, \text{ find } \left(\tilde{\epsilon}_{kl}, \underline{\widehat{U}} \text{ periodic}\right) \text{ such that, for all } \left(\tilde{\epsilon}^*_{kl}, \underline{\widehat{U}}^* \text{ periodic}\right),$$
$$\int_{\Omega_{s0}} \underline{\underline{\Sigma_s}} : \delta_{\underline{U};\underline{\widehat{U}}^*} \underline{\underline{E}}\ d\Omega_{s0} = \int_{\partial\Omega_{f0}} -\tilde{p}_f\ \underline{N} \cdot \underline{\underline{F}}^{-1} \cdot \underline{\widehat{U}}^*\, J\ d\partial\Omega_{f0} + |\omega| \sum_{kl} \tilde{\epsilon}^*_{kl} \cdot \left(\tilde{\sigma}_{kl} - \tilde{\sigma}'_{kl}\right), \quad (2.45)$$

where $\delta_{\underline{U};\underline{\widehat{U}}^*} \underline{\underline{E}} = \left({}^t\underline{\underline{F}} \cdot \underline{\underline{\text{Grad}}}\left(\underline{\widehat{U}}^*\right)\right)_{sym} = \frac{1}{2}\left({}^t\underline{\underline{F}} \cdot \underline{\underline{\text{Grad}}}\left(\underline{\widehat{U}}^*\right) + {}^t\underline{\underline{\text{Grad}}}\left(\underline{\widehat{U}}^*\right) \cdot \underline{\underline{F}}\right)$ is the differential of the Green-Lagrange strain tensor with respect to the displacement perturbation vector. Note that in principle, as for the macroscopic stress/macroscopic strain duality, we could consider cases where we prescribe the added fluid mass density and solve for the fluid pressure; however, here we only consider the case of prescribed fluid pressure, where the added fluid mass density (or equivalently the volume fraction of solid or fluid) can be computed in post-processing of the solution. Furthermore, because of the periodicity conditions on the perturbation field $\underline{\widehat{U}}$, the rigid body rotations are effectively blocked; rigid body translation, however, which are indeed periodic, are not naturally blocked, so we block them by imposing zero perturbation at one arbitrary mesh node.

2.2.2.6 Linearization

A linear micro-poro-mechanics problem is obtained by linearizing Problem (2.46):

$$\text{Given } (\tilde{\epsilon}_{ij}, \tilde{p}_f)\,, \text{ find } \left(\tilde{\epsilon}_{kl}, \underline{\widehat{U}} \text{ periodic}\right) \text{ such that, for all } \left(\tilde{\epsilon}^*_{kl}, \underline{\widehat{U}}^* \text{ periodic}\right),$$
$$\int_{\Omega_{s0}} \underline{\underline{\sigma_s}} : \underline{\underline{\hat{\epsilon}}}^*\, d\Omega_{s0} = \int_{\partial\Omega_{f0}} -\tilde{p}_f\ \underline{N} \cdot \underline{\widehat{U}}^*\, d\partial\Omega_{f0} + |\Omega_0| \sum_{kl} \tilde{\epsilon}^*_{kl} \cdot \left(\tilde{\sigma}_{kl} - \tilde{\sigma}'_{kl}\right), \quad (2.46)$$

where $\underline{\underline{\sigma_s}} \approx \underline{\underline{\underline{\underline{K_s}}}} : \left(\underline{\underline{\tilde{\epsilon}}} + \underline{\underline{\hat{\epsilon}}}\right)$ is the linearized Cauchy stress tensor, with $\underline{\underline{\underline{\underline{K_s}}}}$ the elastic stiffness tensor and $\underline{\underline{\hat{\epsilon}}} := \left(\underline{\underline{\text{Grad}}}\left(\underline{\widehat{U}}\right)\right)_{sym} = \frac{1}{2}\left(\underline{\underline{\text{Grad}}}\left(\underline{\widehat{U}}\right) + {}^t\underline{\underline{\text{Grad}}}\left(\underline{\widehat{U}}\right)\right)$, where $\underline{\underline{\hat{\epsilon}}}^* := \left(\underline{\underline{\text{Grad}}}\left(\underline{\widehat{U}}^*\right)\right)_{sym} = \frac{1}{2}\left(\underline{\underline{\text{Grad}}}\left(\underline{\widehat{U}}^*\right) + {}^t\underline{\underline{\text{Grad}}}\left(\underline{\widehat{U}}^*\right)\right)$, and where the macroscopic stress linearizes into:

$$\underline{\underline{\tilde{\sigma}}} \approx \frac{1}{|\Omega_0|}\left(\int_{\Omega_{s0}} \underline{\underline{\sigma_s}}\ d\Omega_{s0} - |\Omega_{f0}|\,\tilde{p}_f \underline{\underline{1}}\right). \quad (2.47)$$

Similarly, the macroscopic added fluid mass density linearizes into:

$$\tilde{\rho}_{f\pm} \approx \rho_{f0}\left(\tilde{\Phi}_{f0}\ \text{tr}\left(\underline{\underline{\tilde{\epsilon}}}\right) - \tilde{\Phi}_{s0}\frac{1}{|\Omega_{s0}|}\int_{\Omega_{s0}} \text{tr}\left(\underline{\underline{\hat{\epsilon}}}\right)\ d\Omega_{s0}\right). \quad (2.48)$$

In order to express the linearized macroscopic stress-strain and pressure-added fluid mass density relationships, let us consider the case where all components of the macroscopic strain are imposed and all components of the macroscopic stress are computed at post-processing, i.e., $KL = \emptyset$. Thanks to the linearity of the problem, we can write the solution, for instance in terms of strain (which is a linear function of the displacement), as a linear combination of the macroscopic strain and fluid pressure (which are the "loading" quantities of the problem):

$$\hat{\underline{\underline{\epsilon}}}\,(\underline{x}) = \underline{\underline{\underline{\underline{\widehat{A}}}}}\,(\underline{x}) : \tilde{\underline{\underline{\epsilon}}} - \underline{\underline{\widehat{B}}}\,(\underline{x}) \cdot \tilde{p}_f, \tag{2.49}$$

where $\underline{\underline{\underline{\underline{\widehat{A}}}}}$ & $\underline{\underline{\widehat{B}}}$ are localization tensors associated to canonical macroscopic strains and fluid pressure. Hence, the macroscopic stress can be written as:

$$\begin{aligned}\tilde{\underline{\underline{\sigma}}} &\approx \frac{1}{|\Omega_0|}\left(\int_{\Omega_{s0}} \underline{\underline{\underline{\underline{K_s}}}} : \left(\underline{\underline{1}} + \underline{\underline{\underline{\underline{\widehat{A}}}}}\right) : \tilde{\underline{\underline{\epsilon}}}\; d\Omega_{s0} - \int_{\Omega_{s0}} \underline{\underline{\underline{\underline{K_s}}}} : \underline{\underline{\widehat{B}}} \cdot \tilde{p}_f\; d\Omega_{s0} - |\Omega_{f0}|\,\tilde{p}_f \underline{\underline{1}}\right) \\ &= \underline{\underline{\underline{\underline{\tilde{K}}}}} : \tilde{\underline{\underline{\epsilon}}} - \tilde{p}_f\left(\tilde{\Phi}_{f0}\underline{\underline{1}} + \tilde{\Phi}_{s0}\underline{\underline{\tilde{D}}}\right),\end{aligned} \tag{2.50}$$

where $\underline{\underline{\underline{\underline{\tilde{K}}}}} := \frac{\tilde{\Phi}_{s0}}{|\Omega_{s0}|}\int_{\Omega_{s0}} \underline{\underline{\underline{\underline{K_s}}}} : \left(\underline{\underline{1}} + \underline{\underline{\underline{\underline{\widehat{A}}}}}\right)\; d\Omega_{s0}$ is the macroscopic, or homogenized, stiffness tensor, and where $\underline{\underline{\tilde{D}}} := \frac{1}{|\Omega_{s0}|}\int_{\Omega_{s0}} \underline{\underline{\underline{\underline{K_s}}}} : \underline{\underline{\widehat{B}}}\; d\Omega_{s0}$ is such that $\tilde{\Phi}_{f0}\underline{\underline{1}} + \tilde{\Phi}_{s0}\underline{\underline{\tilde{D}}}$ is the so-called Biot tensor [Dormieux et al., 2006]. Note that in the case of an incompressible solid, we have $\underline{\underline{\widehat{B}}} \longrightarrow 0$, but $\underline{\underline{\underline{\underline{K_s}}}} \longrightarrow +\infty$ such that $\underline{\underline{\tilde{D}}} \longrightarrow 1$ and $\tilde{\underline{\underline{\sigma}}} \longrightarrow \underline{\underline{\underline{\underline{\tilde{K}}}}} : \tilde{\underline{\underline{\epsilon}}} - \tilde{p}_f\underline{\underline{1}}$ [Dormieux et al., 2006]. Moreover, in the case of isotropy (which we consider here since we defined an isotropic solid, and 60° rotationally invariant or globally isotropic microstructures), the macroscopic stiffness tensor can be reduced to a set of two scalars (the Lamé constants or bulk and shear moduli), such that we can write:

$$\tilde{\underline{\underline{\sigma}}} \approx \tilde{\lambda}\;\mathrm{tr}\left(\tilde{\underline{\underline{\epsilon}}}\right)\underline{\underline{1}} + 2\tilde{\mu}\;\tilde{\underline{\underline{\epsilon}}} - \tilde{p}_f\underline{\underline{1}} = 3\tilde{k}\;\tilde{\underline{\underline{\epsilon}}}^S + 2\tilde{\mu}\;\tilde{\underline{\underline{\epsilon}}}^D - \tilde{p}_f\underline{\underline{1}}, \tag{2.51}$$

where $\tilde{\underline{\underline{\epsilon}}}^S := \frac{1}{3}\mathrm{tr}\left(\tilde{\underline{\underline{\epsilon}}}\right)\underline{\underline{1}}$ and $\tilde{\underline{\underline{\epsilon}}}^D := \tilde{\underline{\underline{\epsilon}}} - \tilde{\underline{\underline{\epsilon}}}^S$ are the spherical and deviatoric parts of the macroscopic strain tensor, and where $3\tilde{k} := \underline{\underline{\underline{\underline{\tilde{K}}}}} :: \underline{\underline{\underline{\underline{P^S}}}}/\underline{\underline{\underline{\underline{P^S}}}} :: \underline{\underline{\underline{\underline{P^S}}}}$, $2\tilde{\mu} := \underline{\underline{\underline{\underline{\tilde{K}}}}} :: \underline{\underline{\underline{\underline{P^D}}}}/\underline{\underline{\underline{\underline{P^D}}}} :: \underline{\underline{\underline{\underline{P^D}}}}$ and $3\tilde{\lambda} := 3\tilde{k} - 2\tilde{\mu}$ with $\underline{\underline{\underline{\underline{P^S}}}} := \underline{\underline{1}} \otimes \underline{\underline{1}}/3$ and $\underline{\underline{\underline{\underline{P^D}}}} := \underline{\underline{\underline{\underline{1}}}} - \underline{\underline{\underline{\underline{P^S}}}}$ [Zhu et al., 2017]. This final expression is directly comparable to the linearized expression of the macroscopic model (2.28), which assumed solid incompressibility and mixture isotropy.

Similarly, the added fluid mass density can be written as:

$$\frac{\tilde{\rho}_{f\pm}}{\rho_{f0}} \approx \left(\tilde{\Phi}_{f0}\;\underline{\underline{1}} - \frac{\tilde{\Phi}_{s0}}{|\Omega_{s0}|}\int_{\Omega_{s0}} \underline{\underline{1}} : \underline{\underline{\underline{\underline{\widehat{A}}}}}\; d\Omega_{s0}\right) : \tilde{\underline{\underline{\epsilon}}} + \left(\frac{\tilde{\Phi}_{s0}}{|\Omega_{s0}|}\int_{\Omega_{s0}} \underline{\underline{1}} : \underline{\underline{\widehat{B}}}\; d\Omega_{s0}\right)\tilde{p}_f, \tag{2.52}$$

which leads to the following expression of the fluid pressure:

$$\tilde{p}_f = -\tilde{\kappa}\left(\left(\tilde{\Phi}_{f0}\underline{\underline{1}} - \tilde{\Phi}_{s0}\underline{\underline{\tilde{G}}}\right) : \tilde{\underline{\underline{\epsilon}}} - \frac{\tilde{\rho}_{f\pm}}{\rho_{f0}}\right), \tag{2.53}$$

where $1/\tilde{\kappa} := \frac{\tilde{\Phi}_{s0}}{|\Omega_{s0}|}\int_{\Omega_{s0}} \underline{\underline{1}} : \underline{\underline{\widehat{B}}}\; d\Omega_{s0}$ is the inverse of the poromechanical bulk coefficient, and $\underline{\underline{\tilde{G}}} := \frac{1}{|\Omega_{s0}|}\int_{\Omega_{s0}} \underline{\underline{1}} : \underline{\underline{\underline{\underline{\widehat{A}}}}}\; d\Omega_{s0}$. Note that it can be shown, using the Maxwell-Betti theorem, that $\underline{\underline{\tilde{G}}} = -\underline{\underline{\tilde{D}}}$, which basically ensures that the model can be derived from a thermodynamics potential [Dormieux et al., 2006]. Hence, in the quasi-incompressible solid limit, as for the macroscopic stress we have for the fluid pressure $\tilde{p}_f \longrightarrow -\tilde{\kappa}\left(\mathrm{tr}\left(\tilde{\underline{\underline{\epsilon}}}\right) - \frac{\tilde{\rho}_{f\pm}}{\rho_{f0}}\right)$, which is directly comparable to the linearized expression of the macroscopic model (2.28).

2.2.3 Micro-macro bridge and compared analysis

2.2.3.1 Micro-macro bridge

One important question is how to bridge the microscopic and macroscopic models. In general, it is not possible to match the responses of both models. In principle we could compute the global response of the microscopic model to various loading, and then identify the parameters of the macroscopic model to best match the response of the microscopic model over a given range of loadings. This could also be done from the macroscopic model to the microscopic one.

In general the macroscopic model formulated in Section 2.2.1 has two functional parameters, namely $\bar{\Psi}_{skel}$ and $\bar{\Psi}_{bulk}$. With the specific constitutive choices made in Section 2.2.1.2, the set of parameters reduces to three scalars, namely $\bar{\lambda}$, $\bar{\mu}$ and $\bar{\kappa}$. Interestingly, thanks to the choice of simple –only weakly nonlinear– laws, all three parameters are also present in the linearized model described by the system of Equations (2.28). This would not be the case for more complex constitutive laws, where nonlinear terms might only be activated in the finite strain regime and vanish in the infinitesimal regime, see, e.g., discussion on power laws in [Genet et al., 2023a]. The presence of the three macroscopic model parameters in the linearized formulation will simplify the compared analysis with the microscopic model. Indeed, identifying Equation (2.28) to Equation (2.50) and to Equation (2.53) yields $\bar{\mu} = \tilde{\mu}$, $\bar{\lambda} = \tilde{\lambda}$ and $\bar{\kappa} = \tilde{\kappa}$.

2.2.3.2 Strain-pressure coupling behavior

Based on the current constitutive choices made in Section 2.2.1.2 for the macro-poromechanical model, the effect of pressure and strain on the macroscopic stress are somehow decoupled. Benefiting from a generic microscopic model, we can investigate how relevant that choice is. In other terms, the question is: how does the fluid pressure impact the stress-strain response, and how does the strain impact the pressure-volume response?

Thus, to explore the impact of strain-pressure coupling on both the macroscopic and microscopic models, we use the Terzaghi stress tensor [Coussy, 2004, Chapelle and Moireau, 2014]. In the context of the considered macroscopic model, it is defined as:

$$\bar{\underline{\underline{\Sigma}}}_T := \bar{\underline{\underline{\Sigma}}}\left(\bar{\underline{\underline{E}}}, \bar{p}_{f\pm}\right) + \bar{p}_f \bar{J} \bar{\underline{\underline{C}}}^{-1} = \frac{\partial \bar{\Psi}_{skel}}{\partial \bar{\underline{\underline{E}}}}\left(\bar{\underline{\underline{E}}}\right). \tag{2.54}$$

One can see that the right-hand side only depends on the Green-Lagrange strain tensor $\bar{\underline{\underline{E}}}$, which means that, by construction, the Terzaghi stress is independent from fluid pressure. On the other hand, in the microscopic model, the Terzaghi stress is defined based on the macroscopic stress tensor in which the strain and pressure are implicitly coupled:

$$\tilde{\underline{\underline{\Sigma}}}_T := \tilde{\underline{\underline{\Sigma}}} + \tilde{p}_f \tilde{J} \tilde{\underline{\underline{C}}}^{-1} = \tilde{J} \tilde{\underline{\underline{F}}}^{-1} \cdot \tilde{\underline{\underline{\sigma}}} \cdot {}^t\tilde{\underline{\underline{F}}}^{-1} + \tilde{p}_f \tilde{J} \tilde{\underline{\underline{C}}}^{-1}. \tag{2.55}$$

In Section 2.3.2.3, we compare Terzaghi stress in the microscopic and macroscopic models with respect to the combined loading of strain and pressure to show the intrinsic coupling between the strain and fluid pressure in the microscopic model, in comparison to the macroscopic model where Terzaghi stress is independent of the fluid pressure.

2.2.3.3 Volumetric-deviatoric coupling behavior

In Section 2.2.1.3, we explained that the skeleton free energy could be chosen such that the deviatoric and volumetric deformations are simply additively superposed, or combined in a more complex manner. To study this choice and be able to compare it to the behavior of the

micro-poro-mechanical model, we define the hydrostatic pressure and von Mises deviatoric stress. In the context of the considered macroscopic model, in plane strain configuration, the hydrostatic pressure is defined as:

$$\bar{p}^{hydro} := -\frac{1}{3}\left(\bar{\underline{\underline{\sigma}}} : \underline{\underline{1}} + \bar{\sigma}_{zz}\right) = -\frac{\bar{J}}{3}\left(\bar{\underline{\underline{\Sigma}}} : \bar{\underline{\underline{C}}} + \bar{\Sigma}_{zz}\right), \tag{2.56}$$

where $\bar{\sigma}_{zz}$ and $\bar{\Sigma}_{zz}$ denote the out-of-plane stress components, which can be computed from the in-plane variables. Then the deviatoric stress is defined as:

$$\bar{\underline{\underline{\sigma}}}^{dev} := \bar{\underline{\underline{\sigma}}} + \bar{p}^{hydro}\underline{\underline{1}}, \qquad \bar{\underline{\underline{\Sigma}}}^{dev} := \bar{\underline{\underline{\Sigma}}} + \bar{p}^{hydro}\bar{J}\bar{\underline{\underline{C}}}^{-1}, \tag{2.57}$$

based on which the von Mises stress is defined as:

$$\bar{\sigma}^{VM} := \sqrt{\frac{3}{2}\left(\bar{\underline{\underline{\sigma}}}^{dev} : \bar{\underline{\underline{\sigma}}}^{dev} + \left(\bar{\sigma}_{zz}^{dev}\right)^2\right)}, \qquad \bar{\Sigma}^{VM} := \sqrt{\frac{3}{2}\left(\bar{\underline{\underline{\Sigma}}}^{dev} : \bar{\underline{\underline{\Sigma}}}^{dev} + \left(\bar{\Sigma}_{zz}^{dev}\right)^2\right)}, \tag{2.58}$$

where $\bar{\sigma}_{zz}^{dev} := \bar{\sigma}_{zz} + p^{hydro}$ and $\bar{\Sigma}_{zz}^{dev} := \bar{\Sigma}_{zz} + p^{hydro}\bar{J}$ denote out-of-plane deviatoric stress components.

In the microscopic model, it is more convenient to define the hydrostatic pressure based on the microscopic quantities, as it allows to avoid defining macroscopic out-of-plane stress components:

$$\begin{aligned}\tilde{p}^{hydro} &:= \frac{1}{|\omega|}\left(\int_{\omega_s} \frac{\underline{\underline{\sigma_s}} : \underline{\underline{1}} + \sigma_{s,zz}}{3}\, d\omega_s + |\omega_f|\,\tilde{p}_f\right) \\ &= \frac{1}{\tilde{J}\,|\Omega_0|}\left(\int_{\Omega_{s0}} \frac{\underline{\underline{\Sigma_s}} : \underline{\underline{C}} + \Sigma_{s,zz}}{3}\, d\Omega_{s0} + \left(\tilde{J}\,|\Omega_0| - \int_{\Omega_{s0}} J\, d\Omega_{s0}\right)\tilde{p}_f\right).\end{aligned} \tag{2.59}$$

2.2.4 Numerical resolution and implementation

The macro-model, i.e., Equation (2.21), is here only solved in 0D, i.e., at a single material point, and thus only leads to systems of nonlinear algebraic equations, which we solve using the symbolic computation library SymPy [Meurer et al., 2017]. The micro-model, i.e., Problem (4.2.13), corresponds to a coupled system of nonlinear partial differential and algebraic equations, which we solve using the finite element method. It has been implemented in an open-source finite element code [Genet et al., 2023b] based on the FEniCS library [Logg et al., 2012, Alnæs et al., 2015], and is currently freely available online at `https://gitlab.inria.fr/mgenet/dolfin_mech`. The micro-structure generator is also open-source [Manoochehrtayebi and Genet, 2023b], and is currently freely available online at `https://github.com/ManoochTayebi/micro_poro_structure_generator`. We also provide the code to reproduce the results of this paper under the form of jupyter notebooks [Manoochehrtayebi and Genet, 2023a]: static versions are given in the appendix of the paper while interactive versions are currently available online at `https://mgenet.gitlabpages.inria.fr/micro-macro-poro-paper-demos/index.html`.

2.3 Results & Discussion

We now comparatively analyse the macro- and micro-poro-mechanical models introduced in Sections 2.2.1 and 2.2.2, along with their linearized versions. More precisely, we first explore the homogenized linear response of the microscopic model with respect to geometry and porosity. Based on these homogenized parameters, the macroscopic model parameters

are chosen so that the behaviors of both models match for small strains. Then, the macro- and microscopic model responses are compared at large strains and for various values of geometrical and material parameters. A focus on hydrostatic pressure and stress distribution within the microstructure is proposed, which clearly distinguishes the microscopic model from the macroscopic one. In addition, the coupling between applied strain and pressure is investigated using the Terzaghi stress, and the coupling between deviatoric and volumetric strains by using the hydrostatic pressure and von Mises equivalent stress. For visual consistency, in all Figures red is used for the results related to the macroscopic model and blue for the results related to the microscopic model.

2.3.1 Linearized response

The linearized response of the microscopic model depends on the microstructure, namely its shape and porosity. In [Patte et al., 2022b], the macroscopic material parameters were supposed to depend linearly on porosity; this assumption can be explored using the microscopic model introduced here. In Figure 2.5, the homogenized material parameters $\tilde{k}$ and $\tilde{\mu}$ (normalized with respect to solid material parameters k_s and μ_s) are plotted as a function to porosity for three geometries (cf. Figure 2.2): (i) circular inclusions with 60° rotational symmetry, (ii) hexagonal inclusions with 60° rotational symmetry, and (iii) random Voronoi tessellation. It is clear that the influence of the geometry on the resulting homogenized parameters is limited, and that porosity is the dominant factor.

In Figure 2.5, the homogenized parameters resulting from the linearized microscopic model are confronted with two analytical upscaling schemes extracted from [Dormieux et al., 2006], namely the dilute scheme and the differential scheme. In the dilute scheme, only a single spherical pore embedded in an infinite matrix is considered, where the matrix simply has the mechanical properties of the solid constituent of the mixture, hence basically neglecting the interactions between pores. In the differential scheme, the properties of the matrix are successively (until convergence) modified to take into account the presence of the pores. As a result, the dilute scheme is only valid for small porosities (where the interaction between pores is indeed negligible), while the differential scheme behaves correctly for all porosities.

It is worth noting that the circular and hexagonal microstructures induce an isotropic macroscopic behavior in the infinitesimal strain setting, due to the 60° rotational symmetry in plane [Ptashnyk and Seguin, 2016]; this will not be the case in the finite strain setting, because of strain-induced anisotropy. As for the polygonal microstructure, it only induces a quasi-isotropic behavior due to the random distribution of the polygonal elements, which tends to exact isotropy when increasing the number of elements. Nevertheless, beside strain-induced anisotropy which will naturally be present in the finite strain micro-poro-mechanical model, anisotropic microstructures could be straightforwardly used, inducing anisotropic behavior already at the infinitesimal strain level, which would not be as straightforward with analytical upscaling schemes.

2.3.2 Nonlinear response

For consistency, all the results regarding the microscopic model are computed using the hexagonal microstructure and an arbitrary porosity $\Phi_{f0} = 70\%$, with the solid mechanical properties of Young modulus $E_s = 1\ kPa$ and Poisson ratio $\nu_s = 0.2$ for compressible and $\nu_s = 0.499$ for quasi-incompressible solids.

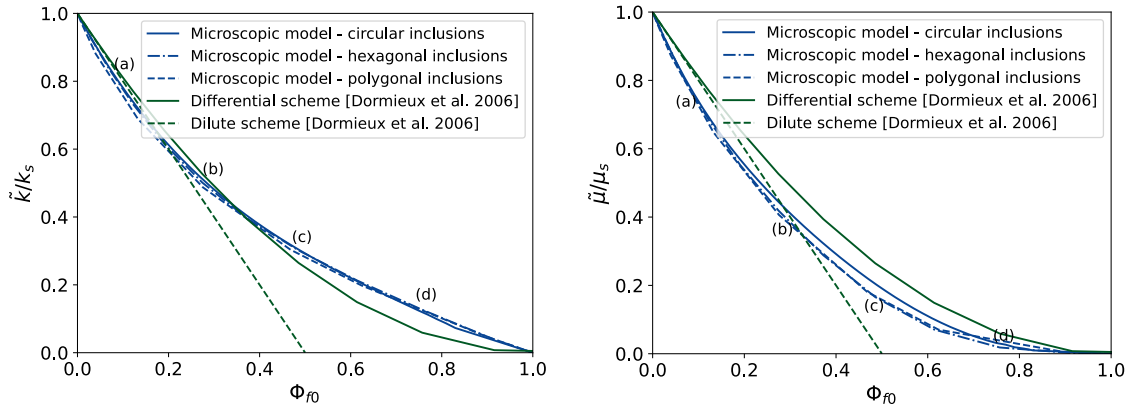

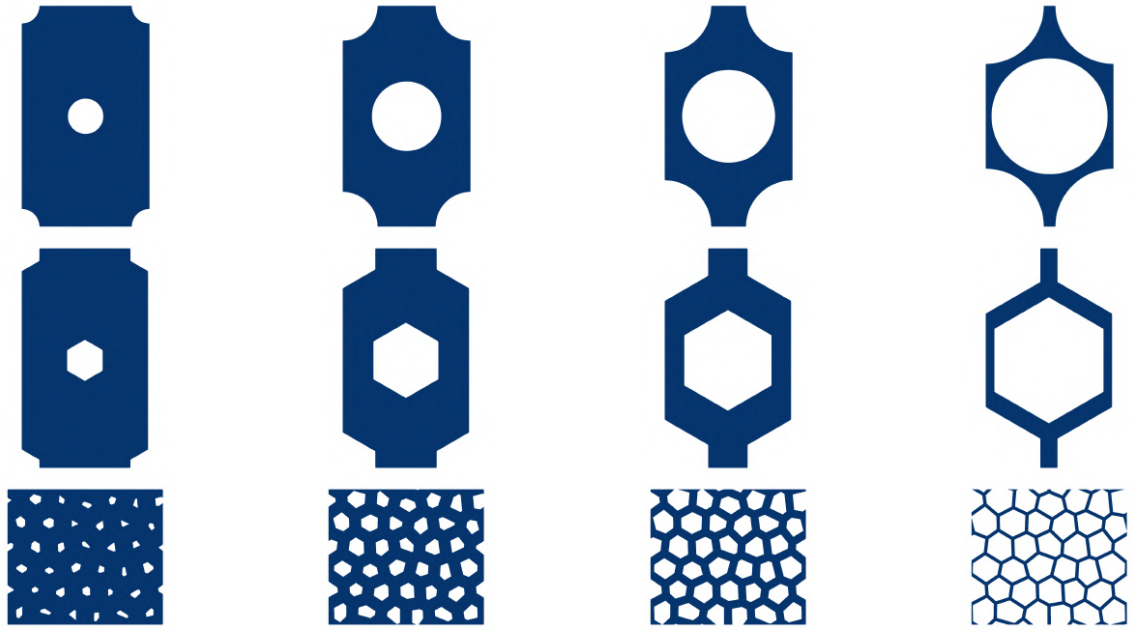

(a) $\Phi_{f0} = 8\%$ (b) $\Phi_{f0} = 27\%$ (c) $\Phi_{f0} = 46\%$ (d) $\Phi_{f0} = 75\%$

Figure 2.5: Homogenized material parameters (namely bulk modulus $\tilde{k}$ and shear modulus $\tilde{\mu}$) obtained with (i) the micro-model introduced in this paper based on various microstructures, as well as (ii) the dilute and (iii) differential schemes proposed in [Dormieux et al., 2006], as a function of porosity. The homogenized parameters are normalized with respect to the solid material parameters, which are taken here as $E_s = 1\ kPa$ and $\nu_s = 0.2$ for the sake of illustration. We can see that the impact of the type of microstructure is limited, and the main factor is simply the porosity itself; moreover, the dilute homogenization scheme is only valid for small porosities whereas the differential scheme remains valid for all porosities.

2.3.2.1 Stress-strain-pressure-porosity response

As described before, though the micro- and macroscopic models are equivalent in the infinitesimal strains and incompressible/quasi-incompressible solid limits, they differ at large strains. Figure 2.6a displays the response (in terms of Cauchy stress $\bar{\underline{\underline{\sigma}}}$ and macroscopic Cauchy stress $\tilde{\underline{\underline{\sigma}}}$) of both models, along with their linearized version, to the action of equibiaxial plane strain (imposing zero fluid pressure). The parameters of the macroscopic model were chosen such that its initial response matches the one of the microscopic model. Because of the specific constitutive choice made here, the nonlinear responses are globally softer than the linearized one. In addition, Figure 2.6b shows the response of both models to the action of internal fluid pressure (imposing zero macroscopic strain). Because of the quasi-incompressible solid assumption, both models show the same response to this loading.

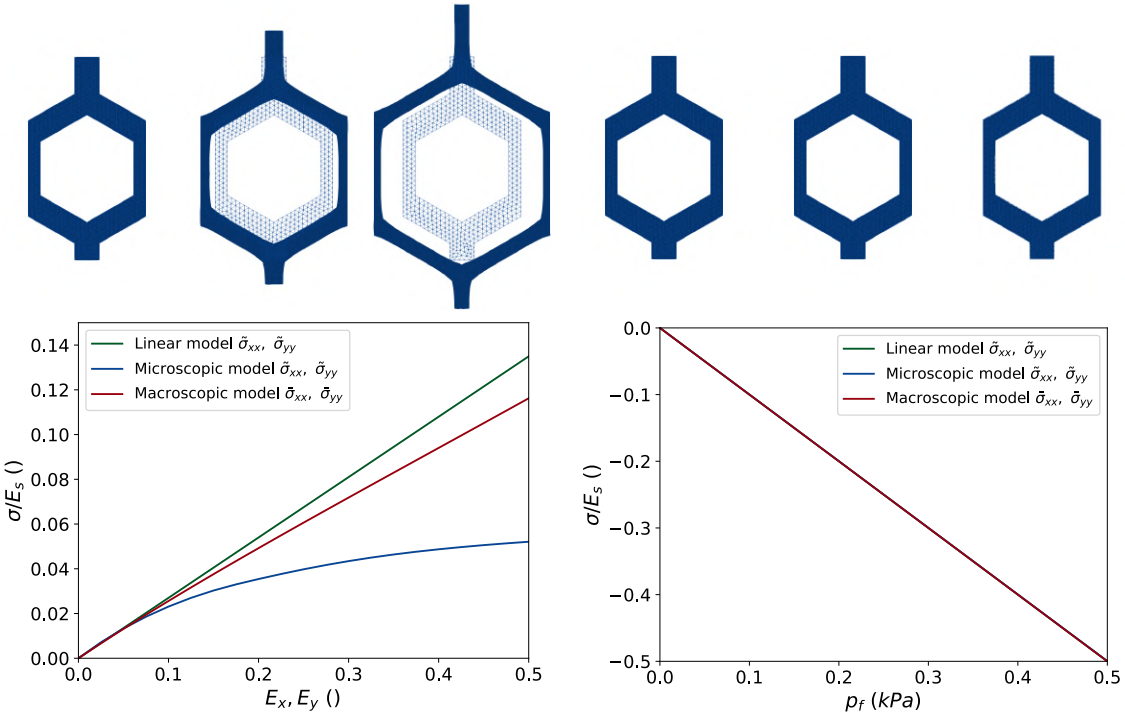

(a) Macroscopic stress-macroscopic strain relationship (with imposed zero fluid pressure).

(b) Macroscopic stress-fluid pressure relationship (with imposed zero macroscopic strain).

Figure 2.6: Normalized (with respect to E_s) Cauchy stress response of the macro- and microscopic models (with quasi-incompressible solid), in the case of equibiaxial strain loading (left) and fluid pressure loading (right). For illustration purposes, deformed RVE are provided for 0%, 25% and 50% applied strain (left), and for 0, 0.25 and 0.50 kPa applied pressure (right).

The evolution of the solid volume fraction, pulled backed into the reference configuration, with respect to the macroscopic strain and the fluid pressure, is represented in Figure 2.7, for the microscopic model with compressible and quasi-incompressible solid and the macroscopic model. As previously explained, in our formulation, the macroscopic model response to fluid pressure is only valid for incompressible or quasi-incompressible solids, which yields a constant volume fraction of solid for any level of fluid pressure or macroscopic strain. In contrast, in the microscopic model with a compressible solid, the volume fraction of the solid increases with respect to the strain, arising from the capability of the solid to deform, as shown in Figure 2.7a. Similarly, in Figure 2.7b, the volume fraction of the solid decreases with respect to pressure for the microscopic model with

compressible solid, assuming zero macroscopic strain.

In Figures 2.7c and 2.7d, the demonstrated RVE is subjected to macroscopic strain with compressible and quasi-incompressible solids, respectively. In the case of a quasi-incompressible solid, even though the RVE deforms, the volume of the solid remains constant, which explains the volume fraction of the solid being constant in Figure 2.7a. Moreover, the compressibility of the solid in Figure 2.7c is responsible for the increase of the solid volume and, consequently, of the solid volume fraction. Figures 2.7e and 2.7f display the deformed RVE under the fluid pressure loading with the macroscopic strain being equal to zero. Similarly, in the case of quasi-incompressible solid, the solid volume fraction does not change. In contrast, in the case of compressible solid, the decrease in the volume of the solid due to the fluid pressure explains the decrease in the volume fraction of the solid in Figure 2.7b.

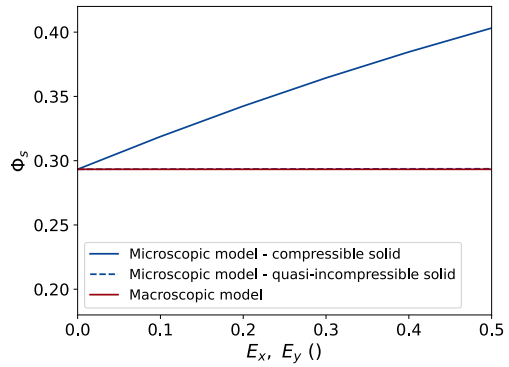

(a) Volume fraction of solid with respect to macroscopic strain, for zero fluid pressure.

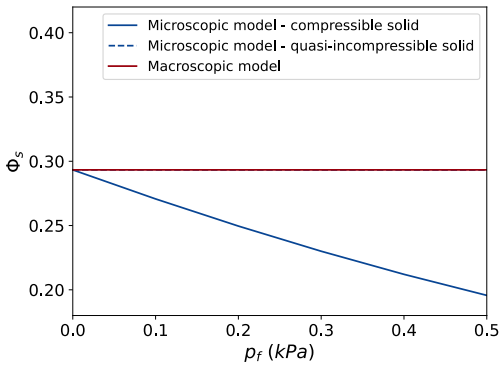

(b) Volume fraction of solid with respect to fluid pressure, for zero macroscopic strain.

(c) Equibiaxial strain loading ($E_x = E_y = 0.5, p_f = 0\ kPa$), Compressible solid.

(d) Equibiaxial strain loading ($E_x = E_y = 0.5, p_f = 0\ kPa$), Quasi-incompressible solid.

(e) Fluid pressure loading ($E_x = E_y = 0, p_f = 0.5\ kPa$), Compressible solid.

(f) Fluid pressure loading ($E_x = E_y = 0, p_f = 0.5\ kPa$), Quasi-incompressible solid.

Figure 2.7: Solid volume fraction response of the macro- (with an incompressible solid) and microscopic (with both a compressible and quasi-incompressible solid) models, in the case of equibiaxial strain loading (left) and fluid pressure loading (right). The deformed RVE is illustrated for both loadings and both compressibilities.

2.3.2.2 Influence of the solid constitutive parameters

The mechanical response of both macro- and microscopic models depends strongly on the solid constitutive behavior. Figure 2.8 illustrates the impact of the solid Young modulus and Poisson ratio on the stress-strain response of both models. It is worth noting that for each set of material parameters, the macroscopic model parameters are chosen based on

the linear homogenized behavior of the microscopic model, such that for all parameters the initial slopes of both models match.

The stress-strain response is more sensitive to the solid Young modulus as a factor of stiffness, while it is less sensitive to the solid Poisson ratio, as the Poisson ratio mainly defines how the solid reshapes under a particular loading rather than dependency of the stress magnitude to the strain.

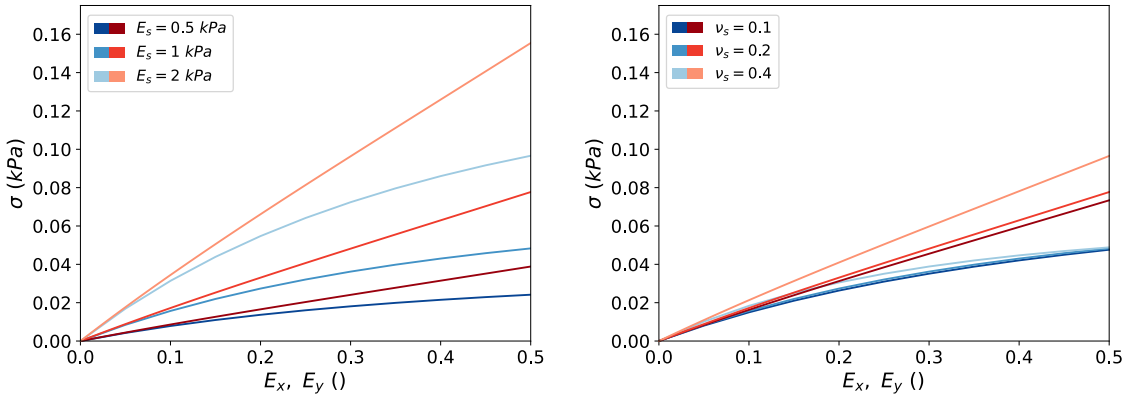

(a) Impact of E_s ($\nu_s = 0.2$).

(b) Impact of ν_s ($E_s = 1\ kPa$).

Figure 2.8: Stress-strain response for different values of solid constitutive parameters. Red color variants relate to the macroscopic model, while blue color variants relate to the microscopic model.

2.3.2.3 Pressure-strain coupling

As discussed in Section 2.2.1.2, in the macroscopic model we additively decomposed the contributions of the strain and of the solid volume fraction to the mixture free energy density, which leads to a strong decoupling between fluid pressure and skeleton strain in the response of the model. In short, as a consequence of this choice the macroscopic model verifies the Terzaghi principle, i.e., the Terzaghi stress depends only on the skeleton strain, not on the fluid pressure (see [Coussy, 2004, Coussy, 2010, Chapelle and Moireau, 2014] for more details). In the microscopic model, the coupling between strain and pressure is intrinsic to the model, and can be studied by computing the averaged Terzaghi stress, as discussed in Section 2.2.3.2. In Figure 2.9, we plot the Terzaghi stress-strain response for various fluid pressure levels, for both the macro- (in red) and micro- (in blue) -scopic models, for a quasi-incompressible (left) and a compressible (right) solid. In the case of a quasi-incompressible solid, there is no coupling between strain and pressure; conversely, in the case of a compressible solid, there is a coupling between strain and pressure, which is properly represented in the microscopic model formulated here.

This result illustrates multiple important points. First, in the incompressible solid limit, a simple macroscopic model like the one described here, with additive decomposition of the contributions of the skeleton strain and fluid pressure to the mixture free energy, is perfectly relevant as there is no coupling between strain and pressure. However, in the compressible solid case, the coupling is significant. The macroscopic model could be extended to take such coupling into account; however, formulating such a coupled strain energy potential is not straightforward. Thus, the advantage of using a microscopic model like the one introduced in this paper is clear, as it naturally describes the such coupling. Actually, in an upscaling strategy, the microscopic model could be used to derive a strain energy potential for a macroscopic model with proper coupling between strain and pressure.

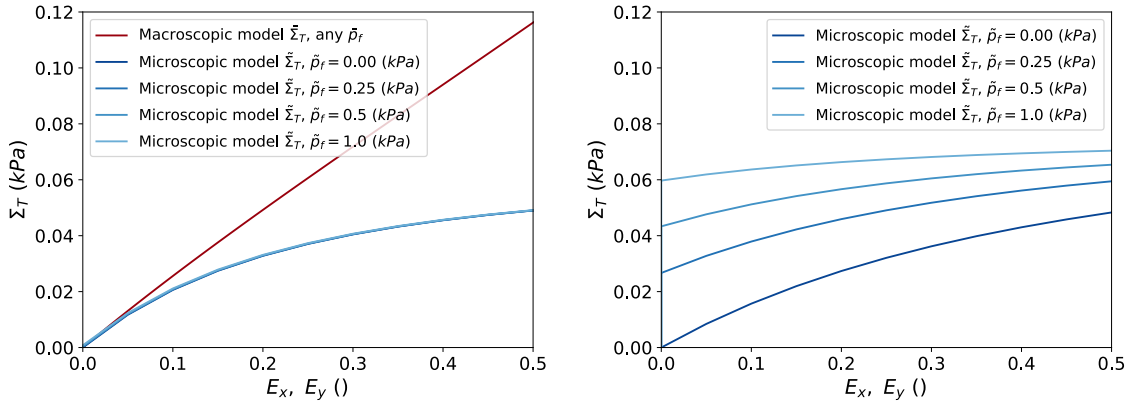

(a) Quasi-incompressible solid.

(b) Compressible solid.

Figure 2.9: Terzaghi effective stress-strain relation for various values of fluid pressure in the macro- and microscopic models.

2.3.2.4 Deviatoric-volumetric deformation coupling

It is also interesting to investigate the coupling between deviatoric and volumetric strains in the mechanical response of both models. Indeed, as discussed in Section 2.2.1.3, in the macroscopic model, we can choose a potential that strongly couples the contributions of the deviatoric and volumetric strain (e.g., $\bar{\Psi}_{skel}^{coup}$ defined in Equation (2.22)), or a potential that were both contributions are additively split, hence decoupled (e.g., $\bar{\Psi}_{skel}^{decoup}$ defined in Equation (2.23)). This is also true for the solid constitutive model of the microscopic model (see W_s^{coup} and W_s^{decoup} of Equation (2.41) in Section 4.2.1). To illustrate how these choices translate to the macroscale response, we apply the following macroscopic deviatoric strain to both the macro- and microscale models:

$$\underline{\underline{F}}^{dev} := \begin{bmatrix} \beta & 0 \\ 0 & \frac{1}{\beta} \end{bmatrix}, \tag{2.60}$$

where β is the loading parameter, and compute the macroscopic hydrostatic pressure as defined in Section 2.2.3.3. As always, for all models the parameters are adapted such that the linearized response match; as a consequence, the hydrostatic pressure resulting from the macroscopic model is expected to match the hydrostatic pressure from the microscopic model for small deformations. The results are presented in the Figure 2.10. They show that the hydrostatic pressure remains null for the macroscopic model with a "decoupled" law, which is a direct consequence of the decoupling between deviatoric and volumetric strains. Conversely, the "coupled" macroscopic law gives an evolution of the hydrostatic pressure, which is also present in the microscopic model, for which the difference between the "coupled" and "decoupled" variants give only little difference.

The coupling allowed by a coupled formulation of the skeleton is second-order compared to the structural coupling inherent to the microscopic model. Consequently, even a decoupled formulation of the skeleton results in a globally coupled behavior at the macroscopic scale. This means that the macroscopic model should rather be formulated with coupled potentials that reproduce much better what the microstructure yields as a global behavior. And as in the previous Section, in an upscaling strategy, the microscopic model could be used to derive a strain energy potential for a macroscopic model with a proper coupling between deviatoric and volumetric strains.

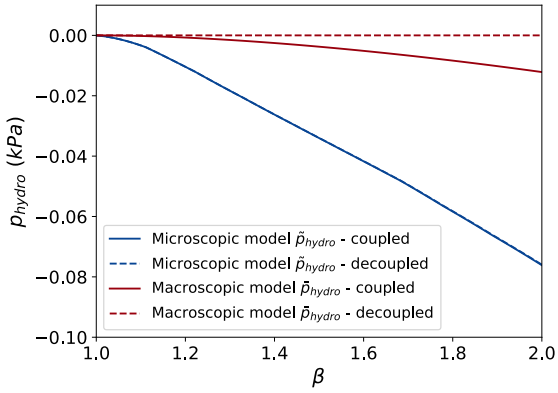

Figure 2.10: Macroscopic hydrostatic pressure p_{hydro} with respect to deviatoric deformation, for both the macro- (red) and microscopic (blue) models, for both "decoupled" (dashed lines) and "coupled" (solid lines) constitutive laws. The coupling between deviatoric and volumetric strains is naturally present in the microscopic model, but only in the "coupled" version of the macroscopic model, not the "decoupled" version.

2.3.2.5 Description of solid stresses and strains within the RVE

Another advantage of the microscopic model is that it provides the distribution of stresses and strains within the solid part of the RVE, which govern micromechanical mechanisms (micro-cracking and damage [Ladevèze et al., 1994, Genet et al., 2013], biological processed such as growth [Taber, 1995, Lee et al., 2015a], etc.). Figures 2.11 shows the spatial and frequency distributions of hydrostatic pressure and von Mises stress, respectively, in the RVE mesh elements for a given applied macroscopic deviatoric deformation defined as in Equation (2.60) (with $\beta = 1.25$), without ($p_f = 0\ kPa$, top) or with ($p_f = 0.2\ kPa$, bottom) fluid pressure. For comparison, the mixture hydrostatic pressure (Equation (2.56)) and von Mises equivalent stress (Equation (2.58)) are also provided for the macroscopic model (with "coupled" energy) submitted to the same loading.

Comparing Figure 2.11a with Figure 2.11c (left column), as well as Figure 2.11b with Figure 2.11d (right column), we can see that the hydrostatic pressure distribution is basically shifted by the applied fluid pressure, while the von Mises stress distribution is hardly affected by the fluid pressure. This is due to the fact the solid is considered here quasi-incompressible, as discussed in [Lopez-Pamies et al., 2012, Álvarez-Barrientos et al., 2021]. This also explains why the deformation is very little affected by the addition of the fluid pressure, i.e., when comparing top and bottom lines.

2.4 Conclusion

In this work, we proposed a microscopic poromechanical model based on a novel formulation of the micro-poro-mechanics problem, which involves a consistent definition of the macroscopic stress, the dual variable of the standard macroscopic strain variable. This model allows to compute the response of a periodic microstructure to any loading involving fluid pressure, macroscopic strain, and/or macroscopic stress. Outputs from the model include local stress and strain fields over the microstructure, as well as global quantities such as added fluid mass and macroscopic strain and/or stress.

The proposed micro-poro-mechanical framework provides notably a micromechanical foundation for classical poromechanics. Thus, it is clear that poromechanics is a consis-

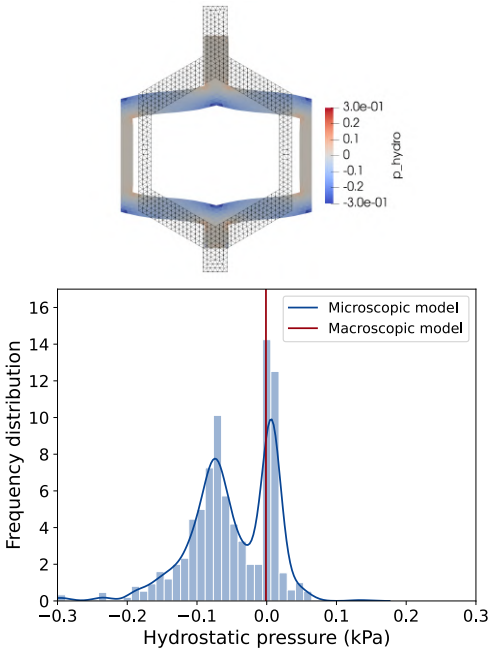

(a) Pure deviatoric deformation loading, hydrostatic pressure distribution

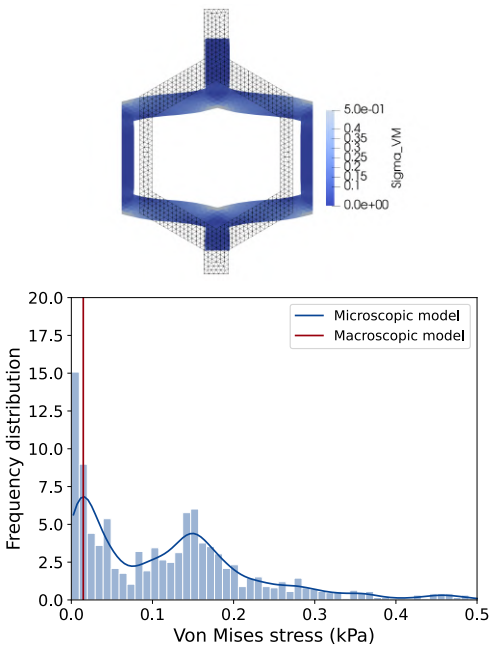

(b) Pure deviatoric deformation loading, von Mises stress distribution

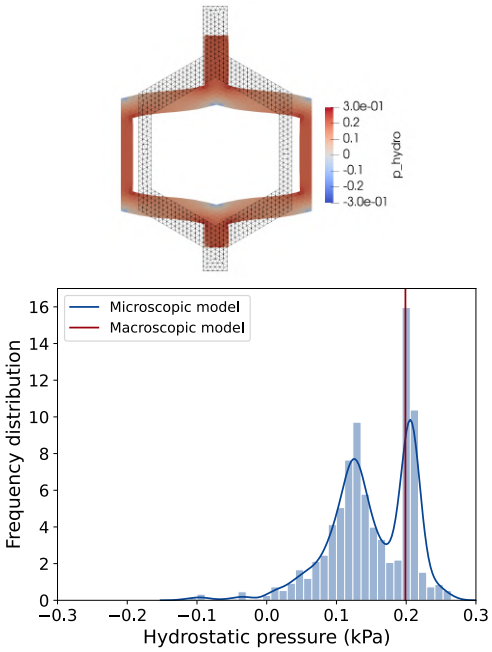

(c) Combined deviatoric deformation and fluid pressure loading, hydrostatic pressure distribution

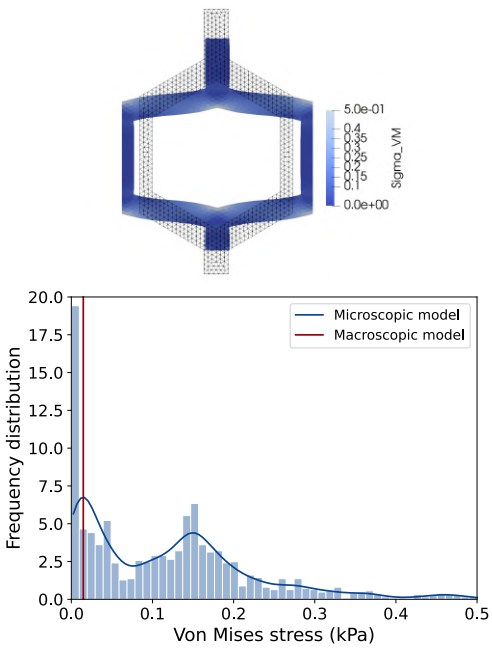

(d) Combined deviatoric deformation and fluid pressure loading, von Mises stress distribution

Figure 2.11: Frequency distribution of the hydrostatic pressure (left) and von Mises stress (right) within the RVE for a deviatoric deformation loading (no fluid pressure) (top), and a combined deviatoric deformation and fluid pressure loading (bottom). For comparison, the "solid" hydrostatic pressure and von Mises equivalent stress are also provided for the macroscopic model submitted to the same loading (red vertical line). The richness of the description of the microscopic fields provided by the microscopic model compared to the macroscopic model is evident.

tent modeling framework, and that in many cases poromechanical models can be made strictly equivalent, in terms of global stress-strain-pressure-porosity response, to micro-poromechanical models. In this paper we investigated three mechanisms that are naturally present in the micro-poromechanics framework, but not necessarily in the macro-poromechanics framework, namely solid compressibility, strain-pressure coupling and deviatoric-volumetric strain coupling. Regarding the compressibility of the solid constituent, simple poromechanical models like the one used in this paper are limited to incompressible solids (because of the additive decomposition of the free energy between strain and porosity contributions), and taking into account solid compressibility requires additional terms, as already discussed in [Coussy, 2004, Dormieux et al., 2006, Chapelle and Moireau, 2014]. And regarding the coupling between strain and pressure in the material response, it is inexistant in the case of an incompressible solid so again simple poromechanical models like the one used in this paper are relevant; however, in the case of a compressible solid, it would not be straightforward to formulate coupled energy terms to lead to the desired coupled response. Finally, regarding the coupling between deviatoric and volumetric strains in the material response, it is definitely present in the global response of the micro-model, even when using a "decoupled" law for the solid constituent, so "coupled" material laws need to be used in the macro-model, and again it is not straightforward to define energy terms that leads to a desired coupling response.

Additionally, even if macro-poromechanics remains a highly consistent modeling framework, micro-poromechanics offers many advantages. For instance, for a given material, one can derive macroscopic parameters from the microscopic model: classically, the linearized stiffness, but also parameters of nonlinear potentials like performed in this paper, or even, at least in principle, complete potentials, which would be even more useful when considering solid compressibility or proper deviatoric-volumetric coupling. Moreover, one can compute how these macroscopic parameters depend on microscopic parameters, like pore shape, porosity, material properties, etc.—analytical expressions have been obtained in the specific case of spherical pores in the linear elastic isotropic small strain setting in [Dormieux et al., 2006], but more general relations, including in the large deformation nonlinear anisotropic setting, could be derived from the framework introduced in this paper. Furthermore, the microscopic model describes all micro-variables (pore shapes, solid strains and stress, etc.) distribution within the microstructure, whereas the macroscopic model only represents averaged values.

There are many perspectives to this work. An important one will be to define a general upscaling strategy, allowing to perform structural simulations based on a material law derived from the microscopic model, either through computing macro-poromechanical potentials as mentioned above, or using general model reduction approaches [Kanouté et al., 2009, Genet et al., 2014]. In the specific context of pulmonary modeling, we also plan to make the model more physiological by defining proper solid constitutive behavior and estimating material parameters based on experimental data [Bel-Brunon et al., 2014]. We will also incorporate into the micro-model additional mechanisms, including, at the breathing time scale, gas exchanges [Kang et al., 2015] and surface tensions [Koshiyama et al., 2018], and, at longer time scales, growth and remodeling [Lee et al., 2015b].

Acknowledgements

This study was supported by the French National Research Agency (ANR) under contract number ANR19-CE45-0007. The authors would like to thank Dominique Chapelle for

fruitful discussions.

Bibliography

[Alnæs et al., 2015] Alnæs, M., Blechta, J., Hake, J., Johansson, A., Kehlet, B., Logg, A., Richardson, C., Ring, J., Rognes, M. E., and Wells, G. N. (2015). The FEniCS Project Version 1.5. Vol 3.

[Alsayednoor and Harrison, 2016] Alsayednoor, J. and Harrison, P. (2016). Evaluating the performance of microstructure generation algorithms for 2-d foam-like representative volume elements. *Mechanics of Materials*, 98:44–58.

[Álvarez-Barrientos et al., 2021] Álvarez-Barrientos, F., Hurtado, D. E., and Genet, M. (2021). Pressure-driven micro-poro-mechanics: A variational framework for modeling the response of porous materials. *International Journal of Engineering Science*, 169:103586.

[Auriault et al., 2009] Auriault, J.-L., Boutin, C., and Geindreau, C. (2009). *Homogenization of Coupled Phenomena in Heterogenous Media*.

[Bargmann et al., 2018] Bargmann, S., Klusemann, B., Markmann, J., Schnabel, J. E., Schneider, K., Soyarslan, C., and Wilmers, J. (2018). Generation of 3D representative volume elements for heterogeneous materials: A review. *Progress in Materials Science*, 96:322–384.

[Bel-Brunon et al., 2014] Bel-Brunon, A., Kehl, S., Martin, C., Uhlig, S., and Wall, W. (2014). Numerical identification method for the non-linear viscoelastic compressible behavior of soft tissue using uniaxial tensile tests and image registration – Application to rat lung parenchyma. *Journal of the Mechanical Behavior of Biomedical Materials*, 29:360–374.

[Berger et al., 2016] Berger, L., Bordas, R., Burrowes, K., Grau, V., Tavener, S., and Kay, D. (2016). A poroelastic model coupled to a fluid network with applications in lung modelling. *International Journal for Numerical Methods in Biomedical Engineering*, 32(1).

[Biot, 1941] Biot, M. A. (1941). General Theory of Three-Dimensional Consolidation. *Journal of Applied Physics*, 12(2):155–164.

[Biot and Temple, 1972] Biot, M. A. and Temple, G. (1972). Theory of Finite Deformations of Porous Solids. *Indiana University Mathematics Journal*, 21(7):597–620. Publisher: Indiana University Mathematics Department.

[Bonet and Wood, 2008] Bonet, J. and Wood, R. D. (2008). *Nonlinear Continuum Mechanics for Finite Element Analysis*. Cambridge University Press, Cambridge. 01684.

[Budiansky and Kimmel, 1987] Budiansky, B. and Kimmel, E. (1987). Elastic Moduli of Lungs. *Journal of Applied Mechanics*, 54(2):351.

[Chapelle et al., 2010] Chapelle, D., Gerbeau, J.-F., Sainte-Marie, J., and Vignon-Clementel, I. E. (2010). A poroelastic model valid in large strains with applications to perfusion in cardiac modeling. *Computational Mechanics*, 46(1):91–101.

[Chapelle and Moireau, 2014] Chapelle, D. and Moireau, P. (2014). General coupling of porous flows and hyperelastic formulations—From thermodynamics principles to energy balance and compatible time schemes. *European Journal of Mechanics - B/Fluids*, 46:82–96.

[Ciarlet and Geymonat, 1982] Ciarlet, P. G. and Geymonat, G. (1982). Sur les lois de comportement en élasticité non-linéaire compressible. *Comptes Rendus de l'Académie des Sciences Série II*, 295:423–426.

[Concha and Hurtado, 2020] Concha, F. and Hurtado, D. E. (2020). Upscaling the poroelastic behavior of the lung parenchyma: A finite-deformation micromechanical model. *Journal of the Mechanics and Physics of Solids*, 145:104147.

[Concha et al., 2018] Concha, F., Sarabia-Vallejos, M., and Hurtado, D. E. (2018). Micromechanical model of lung parenchyma hyperelasticity. *Journal of the Mechanics and Physics of Solids*, 112:126–144.

[Coussy, 2004] Coussy, O. (2004). *Poromechanics*. Wiley, Chichester, England ; Hoboken, NJ, 2nd ed edition.

[Coussy, 2010] Coussy, O. (2010). *Mechanics and Physics of Porous Solids*. John Wiley & Sons, Ltd, Chichester, UK.

[De Boer and Ehlers, 1988] De Boer, R. and Ehlers, W. (1988). A historical review of the formulation of porous media theories. *Acta Mechanica*, 74(1-4):1–8.

[Dormieux et al., 2006] Dormieux, L., Kondo, D., and Ulm, F.-J. (2006). *Microporomechanics*. John Wiley & Sons, Chichester, West Sussex, England ; Hoboken, NJ.

[Dormieux et al., 2002] Dormieux, L., Molinari, A., and Kondo, D. (2002). Micromechanical approach to the behavior of poroelastic materials. *Journal of the Mechanics and Physics of Solids*, 50(10):2203–2231.

[Genet, 2019] Genet, M. (2019). A relaxed growth modeling framework for controlling growth-induced residual stresses. *Clinical Biomechanics*, 70:270–277.

[Genet et al., 2014] Genet, M., Couégnat, G., Tomsia, A. P., and Ritchie, R. O. (2014). Scaling strength distributions in quasi-brittle materials from micro-to macro-scales: A computational approach to modeling Nature-inspired structural ceramics. 68:93–106.

[Genet et al., 2023a] Genet, M., Diaz, J., Chapelle, D., and Moireau, P. (2023a). Reduced left ventricular dynamics modeling based on a cylindrical assumption. page e3711.

[Genet et al., 2013] Genet, M., Marcin, L., and Ladevèze, P. (2013). On structural computations until fracture based on an anisotropic and unilateral damage theory. 23(4):483–506.

[Genet et al., 2023b] Genet, M., Patte, C., Manoochehrtayebi, M., and Peyraut, A. (2023b). Dolfin_mech.

[Geuzaine and Remacle, 2009] Geuzaine, C. and Remacle, J.-F. (2009). Gmsh: A 3-D finite element mesh generator with built-in pre- and post-processing facilities: THE GMSH PAPER. *International Journal for Numerical Methods in Engineering*, 79(11):1309–1331.

[Groeber, 2008] Groeber, M. (2008). A framework for automated analysis and simulation of 3D polycrystalline microstructures.Part 1: Statistical characterization. *Acta Materialia*, 56(6):1257–1273.

[Hill, 1963] Hill, R. (1963). Elastic properties of reinforced solids: Some theoretical principles. *Journal of the Mechanics and Physics of Solids*, 11(5):357–372.

[Kang et al., 2015] Kang, M.-Y., Katz, I., and Sapoval, B. (2015). A new approach to the dynamics of oxygen capture by the human lung. *Respiratory Physiology & Neurobiology*, 205:109–119. 12 citations (Crossref) [2022-04-27].

[Kanouté et al., 2009] Kanouté, P., Boso, D. P., Chaboche, J.-L., and Schrefler, B. A. (2009). Multiscale Methods for Composites: A Review. *Archives of Computational Methods in Engineering*, 16(1):31–75.

[Kantzos et al., 2018] Kantzos, C. A., Cunningham, R. W., Tari, V., and Rollett, A. D. (2018). Characterization of metal additive manufacturing surfaces using synchrotron X-ray CT and micromechanical modeling. *Computational Mechanics*, 61(5):575–580.

[Koshiyama et al., 2018] Koshiyama, K., Nishimoto, K., Ii, S., Sera, T., and Wada, S. (2018). Heterogeneous structure and surface tension effects on mechanical response in pulmonary acinus: A finite element analysis. *Clinical Biomechanics*.

[Koshiyama and Wada, 2015] Koshiyama, K. and Wada, S. (2015). Mathematical model of a heterogeneous pulmonary acinus structure. *Computers in Biology and Medicine*, 62:25–32.

[Kumar et al., 1996] Kumar, S., Kurtz, S. K., and Agarwala, V. K. (1996). Micro-stress distribution within polycrystalline aggregate. *Acta Mechanica*, 114(1-4):203–216.

[Ladevèze et al., 1994] Ladevèze, P., Gasser, A., and Allix, O. (1994). Damage mechanisms modelling for ceramic composites. 116:331–336.

[Laville et al., 2023] Laville, C., Fetita, C., Gille, T., Brillet, P.-Y., Nunes, H., Bernaudin, J.-F., and Genet, M. (2023). Comparison of optimization parametrizations for regional lung compliance estimation using personalized pulmonary poromechanical modeling. *Biomechanics and Modeling in Mechanobiology*.

[Lee et al., 2015a] Lee, L. C., Genet, M., Acevedo-Bolton, G., Ordovas, K., Guccione, J. M., and Kuhl, E. (2015a). A computational model that predicts reverse growth in response to mechanical unloading. *Biomechanics and Modeling in Mechanobiology*, 14(2):217–229. 32 citations (Crossref) [2022-04-27].

[Lee et al., 2015b] Lee, L. C., Sundnes, J., Genet, M., Wenk, J. F., and Wall, S. T. (2015b). An integrated electromechanical-growth heart model for simulating cardiac therapies. 15:791–803.

[Logg et al., 2012] Logg, A., Mardal, K.-A., and Wells, G., editors (2012). *Automated Solution of Differential Equations by the Finite Element Method: The FEniCS Book*. Number 84 in Lecture Notes in Computational Science and Engineering. Springer.

[Lopez-Pamies et al., 2012] Lopez-Pamies, O., Castañeda, P. P., and Idiart, M. I. (2012). Effects of internal pore pressure on closed-cell elastomeric foams. *International Journal of Solids and Structures*, 49(19-20):2793–2798.

[Lopez-Pamies and Ponte Castañeda, 2007] Lopez-Pamies, O. and Ponte Castañeda, P. (2007). Homogenization-based constitutive models for porous elastomers and implications for macroscopic instabilities: I—Analysis. 55(8):1677–1701.

[Lukeš and Rohan, 2022] Lukeš, V. and Rohan, E. (2022). Homogenization of large deforming fluid-saturated porous structures. *Computers & Mathematics with Applications*, 110:40–63.

[Mandel, 1972] Mandel, J. (1972). *Plasticité Classique Et Viscoplasticité: Course Held at the Department of Mechanics of Solids, September-October, 1971*. Springer.

[Manoochehrtayebi and Genet, 2023a] Manoochehrtayebi, M. and Genet, M. (2023a). Micro-macro-poro paper demos.

[Manoochehrtayebi and Genet, 2023b] Manoochehrtayebi, M. and Genet, M. (2023b). Micro_poro_structure_generator.

[Mebatsion et al., 2006] Mebatsion, H., Verboven, P., Ho, Q., Verlinden, B., Mendoza, F., Nguyen, T., and Nicolaï, B. (2006). Modeling Fruit Microstructure Using an Ellipse Tessellation Algorithm. In *13th World Congress of Food Science & Technology*, page 246, Nantes, France. EDP Sciences.

[Meurer et al., 2017] Meurer, A., Smith, C. P., Paprocki, M., Čertík, O., Kirpichev, S. B., Rocklin, M., family=Kumar, given=AmiT, g.-i., Ivanov, S., Moore, J. K., Singh, S., Rathnayake, T., Vig, S., Granger, B. E., Muller, R. P., Bonazzi, F., Gupta, H., Vats, S., Johansson, F., Pedregosa, F., Curry, M. J., Terrel, A. R., Roučka, , Saboo, A., Fernando, I., Kulal, S., Cimrman, R., and Scopatz, A. (2017). SymPy: Symbolic computing in Python. 3:e103.

[Miller and Penta, 2021] Miller, L. and Penta, R. (2021). Double poroelasticity derived from the microstructure. *Acta Mechanica*, 232(10):3801–3823.

[Ogden, 1972] Ogden, R. W. (1972). Large deformation isotropic elasticity: on the correlation of theory and experiment for compressible rubberlike solids. *Proceedings of the Royal Society of London. A. Mathematical and Physical Sciences*, 328(1575):567–583.

[Patte et al., 2022a] Patte, C., Brillet, P.-Y., Fetita, C., Bernaudin, J.-F., Gille, T., Nunes, H., Chapelle, D., and Genet, M. (2022a). Estimation of Regional Pulmonary Compliance in Idiopathic Pulmonary Fibrosis Based on Personalized Lung Poromechanical Modeling. *Journal of Biomechanical Engineering*, 144(9):091008.

[Patte et al., 2022b] Patte, C., Genet, M., and Chapelle, D. (2022b). A quasi-static poromechanical model of the lungs. *Biomechanics and Modeling in Mechanobiology*.

[Peyraut and Genet, 2023] Peyraut, A. and Genet, M. (2023). A model of mechanical loading of the lungs including gravity and a balancing heterogeneous pleural pressure.

[Ponte Castañeda, 2016] Ponte Castañeda, P. (2016). Stationary variational estimates for the effective response and field fluctuations in nonlinear composites. *Journal of the Mechanics and Physics of Solids*, 96:660–682.

[Ptashnyk and Seguin, 2016] Ptashnyk, M. and Seguin, B. (2016). Periodic Homogenization and Material Symmetry in Linear Elasticity. *Journal of Elasticity*, 124(2):225–241.

[Rausch et al., 2011] Rausch, S. M. K., Haberthür, D., Stampanoni, M., Schittny, J. C., and Wall, W. A. (2011). Local Strain Distribution in Real Three-Dimensional Alveolar Geometries. *Annals of Biomedical Engineering*, 39(11):2835–2843.

[Rohan, 2006] Rohan, E. (2006). Modeling Large-deformation-induced Microflow in Soft Biological Tissues. *Theoretical and Computational Fluid Dynamics*, 20(4):251–276.

[Sanchez-Palencia, 1980] Sanchez-Palencia, (1980). *Non-homogeneous media and vibration theory*. Number 127 in Lecture notes in physics. Springer, Berlin.

[Spyrou et al., 2019] Spyrou, L., Brisard, S., and Danas, K. (2019). Multiscale modeling of skeletal muscle tissues based on analytical and numerical homogenization. *Journal of the Mechanical Behavior of Biomedical Materials*, 92:97–117.

[Taber, 1995] Taber, L. A. (1995). Biomechanics of Growth, Remodeling, and Morphogenesis. 48(8):487.

[Terzaghi, 1943] Terzaghi, K. (1943). *Theoretical Soil Mechanics*. John Wiley & Sons, Inc., Hoboken, NJ, USA.

[Toshima et al., 2004] Toshima, M., Ohtani, Y., and Ohtani, O. (2004). Three-dimensional architecture of elastin and collagen fiber networks in the human and rat lung. *Archives of Histology and Cytology*, 67(1):31–40.

[Tueni et al., 2023] Tueni, N., Allain, J.-M., and Genet, M. (2023). On the structural origin of the anisotropy in the myocardium: Multiscale modeling and analysis. 138:105600.

[Vasilescu et al., 2012] Vasilescu, D. M., Gao, Z., Saha, P. K., Yin, L., Wang, G., Haefeli-Bleuer, B., Ochs, M., Weibel, E. R., and Hoffman, E. A. (2012). Assessment of morphometry of pulmonary acini in mouse lungs by nondestructive imaging using multiscale microcomputed tomography. *Proceedings of the National Academy of Sciences*, 109(42):17105–17110.

[Wiechert et al., 2009] Wiechert, L., Metzke, R., and Wall, W. A. (2009). Modeling the Mechanical Behavior of Lung Tissue at the Microlevel. *Journal of Engineering Mechanics*, 135(5):434–438.

[Xiao et al., 2016] Xiao, L., Sera, T., Koshiyama, K., and Wada, S. (2016). Morphological Characterization of Acinar Cluster in Mouse Lung Using a Multiscale-based Segmentation Algorithm on Synchrotron Micro-CT Images. *The Anatomical Record*, 299(10):1424–1434.

[Youssef et al., 2005] Youssef, S., Maire, E., and Gaertner, R. (2005). Finite element modelling of the actual structure of cellular materials determined by X-ray tomography. *Acta Materialia*, 53(3):719–730.

[Zhu et al., 2017] Zhu, W., Blal, N., Cunsolo, S., and Baillis, D. (2017). Micromechanical modeling of effective elastic properties of open-cell foam. *International Journal of Solids and Structures*, 115-116:61–72.

Appendix

A Invariants of Cauchy-Green dilatation tensor in plane strain

In this appendix, we derive the first invariant and first reduced invariant of the Cauchy-Green dilatation tensor in plane strain. We have the following relation between the 3D deformation gradient, denoted by $\underline{\underline{F}}^{3D}$, and the 2D (plane strain) deformation gradient, denoted by $\underline{\underline{F}}^{2D}$:

$$\underline{\underline{F}}^{3D} = \begin{bmatrix} \underline{\underline{F}}^{2D} & \begin{matrix} 0 \\ 0 \end{matrix} \\ \begin{matrix} 0 & 0 \end{matrix} & 1 \end{bmatrix}. \tag{A.1}$$

The relative change of volume in 3D and 2D are

$$J^{3D} := \mathrm{Det}\left(\underline{\underline{F}}^{3D}\right) \quad \text{and} \quad J^{2D} := \mathrm{Det}\left(\underline{\underline{F}}^{2D}\right), \tag{A.2}$$

respectively, such that

$$J^{3D} = J^{2D}. \tag{A.3}$$

Similarly, the Cauchy-Green dilatation tensor are

$$\underline{\underline{C}}^{3D} := {}^{t}\underline{\underline{F}}^{3D} \cdot \underline{\underline{F}}^{3D} \quad \text{and} \quad \underline{\underline{C}}^{2D} := {}^{t}\underline{\underline{F}}^{2D} \cdot \underline{\underline{F}}^{2D}, \tag{A.4}$$

such that

$$\underline{\underline{C}}^{3D} = \begin{bmatrix} \underline{\underline{C}}^{2D} & \begin{matrix} 0 \\ 0 \end{matrix} \\ \begin{matrix} 0 & 0 \end{matrix} & 1 \end{bmatrix}. \tag{A.5}$$

Consequently, defining the first invariants of the Cauchy-Green dilatation tensor in 3D and 2D by

$$I_1^{3D} := \mathrm{Tr}\left(\underline{\underline{C}}^{3D}\right) \quad \text{and} \quad I_1^{2D} := \mathrm{Tr}\left(\underline{\underline{C}}^{2D}\right), \tag{A.6}$$

respectively, we conclude that

$$I_1^{3D} = I_1^{2D} + 1. \tag{A.7}$$

Let us express the modified deformation gradient containing all volume-changing, i.e., dilatational, deformations:

$$\underline{\underline{F}}^{3D,\mathrm{vol}} := {J^{3D}}^{-1/3} \underline{\underline{F}}^{3D}, \tag{A.8}$$

as well as its associated modified Cauchy-Green dilatation tensor:

$$\underline{\underline{C}}^{3D,\mathrm{vol}} := {}^{t}\underline{\underline{F}}^{3D,\mathrm{vol}} \cdot \underline{\underline{F}}^{3D,\mathrm{vol}} = {J^{3D}}^{-2/3} \underline{\underline{C}}^{3D}. \tag{A.9}$$

Hence, the first reduced invariant of the Cauchy-Green dilatation tensor is given by:

$$J_1^{3D} := \mathrm{Tr}\left(\underline{\underline{C}}^{3D,\mathrm{vol}}\right) = {J^{3D}}^{-2/3} I_1^{3D} = {J^{2D}}^{-2/3} \left(I_1^{2D} + 1\right), \tag{A.10}$$

leading to the potentials used in Sections 2.2.1.3 and 4.2.1.

B Derivation of the micro-poro-mechanics problem weak formulation

In this appendix, we propose to detail the derivation of the weak formulation underlying the finite element resolution of the micro-model, i.e., Problem (4.2.13). For pedagogical purpose, we propose to first illustrate issues encountered when trying to derive such equations from a potential energy that could seem natural at first but that actually cannot be applied to any microstructure. We then show how to derive a general weak formulation from a consistent potential energy or directly from the strong equations of the problem.

B.1 Pathological formulation

Using the principle of minimum of potential energy is a classical way to obtain the weak formulation of mechanics problems when all applied loads are conservative–following pressures are in general not conservative, unless they are applied on a closed surface [Bonet and Wood, 2008], which is the case in the micro-poro-mechanics problem. Here we show how a specific potential energy that is valid for the case of known macroscopic strain leads to a pathological weak formulation in the case of unknown macroscopic strain. To simplify the presentation, we only consider the case of linearized elasticity, which already contains the pathology.

B.1.1 Preliminary: case of known macroscopic strain

We recall that the total displacement is split between affine and periodic perturbation parts (cf. Section 2.2.2.2):

$$\underline{U} = \underline{\underline{\tilde{\epsilon}}} \cdot (\underline{X} - \underline{X}_0) + \underline{\widehat{U}}, \tag{B.1}$$

where $\underline{X}_0$ is a reference point. We can define the total strain, which is the superposition of the macroscopic strain, and the strain corresponding to the perturbation:

$$\underline{\underline{\epsilon}} = \underline{\underline{\tilde{\epsilon}}} + \underline{\underline{\hat{\epsilon}}}\left(\underline{\widehat{U}}\right). \tag{B.2}$$

Let us consider the following total potential energy of the system:

$$\Pi\left(\underline{\widehat{U}}\right) := \int_{\Omega_{s0}} W_s\left(\underline{\underline{\epsilon}}\left(\underline{\widehat{U}}\right)\right) d\Omega_{s0} - \int_{\partial\Omega_{f0}} -\tilde{p}_f\ \underline{n} \cdot \underline{U}\left(\underline{\widehat{U}}\right) d\partial\Omega_{f0}. \tag{B.3}$$

which can be seen as the sum of the potential energy of "internal" and "external" forces. From the principle of minimum of potential energy, i.e., by deriving the potential energy, we obtain the following weak formulation of the problem:

$$\underline{\widehat{U}} \text{ periodic} \quad | \quad \int_{\Omega_{s0}} \underline{\underline{\sigma_s}}\left(\underline{\widehat{U}}\right) : \underline{\underline{\hat{\epsilon}}}^* d\Omega_{s0} = \int_{\partial\Omega_{f0}} -\tilde{p}_f\ \underline{n} \cdot \underline{\widehat{U}}^* d\partial\Omega_{f0} \quad \forall \underline{\widehat{U}}^* \text{ periodic}. \tag{B.4}$$

To verify that it is fully consistent, we derive the strong form of the problem, using the inverse Galerkin procedure, i.e., integrating by parts the left hand side and applying the fundamental lemma of the calculus of variations:

$$\underline{\widehat{U}} \text{ periodic} \quad | \quad \begin{cases} \underline{\mathrm{div}}\left(\underline{\underline{\sigma_s}}\right) = 0 & \text{in } \Omega_{s0} \\ {}^t\underline{\underline{\sigma_s}} = \underline{\underline{\sigma_s}} & \text{in } \Omega_{s0} \\ \underline{\underline{\sigma_s}} \cdot \underline{n} = -\tilde{p}_f\ \underline{n} & \text{on } \partial\Omega_{f0} \\ \underline{\underline{\sigma_s}} \cdot \underline{n} = 0 & \text{on } \partial\Omega_{s0} \backslash \partial\Omega_{f0} \\ \underline{\underline{\sigma_s}} = \dfrac{\partial W_s}{\partial \underline{\underline{\epsilon}}}\left(\underline{\widehat{U}}\right) & \text{in } \Omega_{s0} \end{cases}. \tag{B.5}$$

First three and fifth equations are standard equilibrium and constitutive equations for the solid; the fourth (where . denotes the jump across periodic boundaries, i.e., between left and right, top and bottom) is slightly non-standard but it is also an internal equilibrium equation for the solid, as it corresponds to the continuity of the stress vector across the periodic boundary of the representative volume element, i.e., inside the solid.

B.1.2 Case of unknown macroscopic strain

In the case where the macroscopic strain $\underline{\underline{\tilde{\epsilon}}}$ is also unknown (for instance if one wants to compute the unconstrained response to an increased pore pressure), it might be tempting to use the same expression of the potential energy, the only difference being that it is now a functional of two variables, namely the periodic perturbation and the macroscopic strain:

$$\Pi\left(\underline{\widehat{U}}, \underline{\underline{\tilde{\epsilon}}}\right) := \int_{\Omega_{s0}} W_s\left(\underline{\underline{\epsilon}}\left(\underline{\widehat{U}}, \underline{\underline{\tilde{\epsilon}}}\right)\right) d\Omega_{s0} - \int_{\partial\Omega_{f0}} -\tilde{p}_f \ \underline{n} \cdot \underline{U}\left(\underline{\widehat{U}}, \underline{\underline{\tilde{\epsilon}}}\right) d\partial\Omega_{f0}. \tag{B.6}$$

However, the weak formulation obtained by enforcing the stationarity of the potential energy with respect to both its variables, i.e.,

$$\begin{aligned} \underline{\widehat{U}} \text{ periodic}, \underline{\underline{\tilde{\epsilon}}} \quad | \quad & \int_{\Omega_{s0}} \underline{\underline{\sigma_s}}\left(\underline{\widehat{U}}, \underline{\underline{\tilde{\epsilon}}}\right) : \left(\underline{\underline{\tilde{\epsilon}}}^* + \underline{\underline{\hat{\epsilon}}}^*\right) d\Omega_{s0} \\ & = \int_{\partial\Omega_{f0}} -\tilde{p}_f \ \underline{n} \cdot \left(\underline{\underline{\tilde{\epsilon}}}^* \cdot (\underline{X} - \underline{X}_0) + \underline{\widehat{U}}^*\right) d\partial\Omega_{f0} \quad \forall \underline{\widehat{U}}^* \text{ periodic}, \underline{\underline{\tilde{\epsilon}}}^*, \end{aligned} \tag{B.7}$$

cannot be used on any microstructure, which becomes evident when writing the strong form of the (global) equation associated to the stationarity of the (global) macroscopic strain (equations associated with the stationarity of the displacement perturbation are unchanged compared to Problem (B.5)):

$$\int_{\Omega_{s0}} \underline{\underline{\sigma_s}}\left(\underline{\widehat{U}}, \underline{\underline{\tilde{\epsilon}}}\right) d\Omega_{s0} - \int_{\partial\Omega_{f0}} -\tilde{p}_f \ \underline{n} \otimes (\underline{X} - \underline{X}_0) \, d\partial\Omega_{f0} = 0. \tag{B.8}$$

Indeed, this equation seems to enforce that the macroscopic stress is null, which makes sense in an unconstrained inflation problem. And in the case of inclusions fully enclosed within the representative volume element (see, e.g., Figure B.1a), one can apply the Stokes theorem to turn Equation (B.8) into:

$$\int_{\Omega_{s0}} \underline{\underline{\sigma_s}}\left(\underline{\widehat{U}}, \underline{\underline{\tilde{\epsilon}}}\right) d\Omega_{s0} - \tilde{p}_f \, |\Omega_{f0}| \, \underline{\underline{1}} = 0, \tag{B.9}$$

which corresponds exactly to the desired zero macroscopic stress contraint. However, when considering inclusions intersecting the borders of the representative volume element (see, e.g., Figure B.1b), one cannot apply the Stokes theorem, and Equation (B.8) actually contains additional terms compared to Equation (B.9) which have no physical meaning. In other words, the potential energy (B.6) basically assumes that the Stokes theorem can be applied for the fluid volume, which is only the case if it does not intersect the borders of the representative volume element. Thus, one needs to use a more general expression of the potential energy.

B.2 Consistent formulation

B.2.1 General potential energy

A potential energy directly based on the fluid volume allows to avoid the aforementioned issue:

$$\Pi\left(\underline{\widehat{U}}, \underline{\underline{\tilde{\epsilon}}}\right) := \int_{\Omega_{s0}} W_s\left(\underline{\underline{\epsilon}}\left(\underline{\widehat{U}}, \underline{\underline{\tilde{\epsilon}}}\right)\right) d\Omega_{s0} - \tilde{p}_f \left|\omega_f\left(\underline{\widehat{U}}, \underline{\underline{\tilde{\epsilon}}}\right)\right|. \tag{B.10}$$

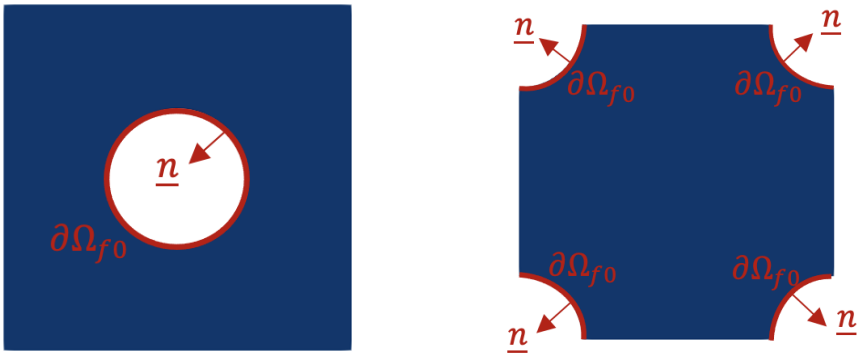

(a) Enclosed inclusion.

(b) Intersected inclusion.

Figure B.1: Two different periodic patterns (one where the inclusion is enclosed within the representative volume element, one where it intersects the border) of the same geometry (circular inclusions arranged in a square pattern).

This expression was already used in [Álvarez-Barrientos et al., 2021], but we now detail how it can allow to avoid the issue. The idea is to use an expression of the fluid volume that is completely defined by the variables of the problem, i.e.,

$$|\omega_f| = |\omega| - |\omega_s|\,, \tag{B.11}$$

with

$$\begin{cases} |\omega| = \left(1 + \mathrm{tr}\left(\underline{\underline{\tilde{\epsilon}}}\right)\right)|\Omega_0| \\ |\omega_s| = \int_{\Omega_{s0}} \left(1 + \mathrm{tr}\left(\underline{\underline{\tilde{\epsilon}}}\right) + \mathrm{tr}\left(\underline{\underline{\hat{\epsilon}}}\right)\right) d\Omega_{s0} \end{cases}. \tag{B.12}$$

The weak formulation derived from this potential energy is:

$$\widehat{\underline{U}} \text{ periodic}, \underline{\underline{\tilde{\epsilon}}} \quad | \quad \int_{\Omega_{s0}} \underline{\underline{\sigma_s}} : \underline{\underline{\hat{\epsilon}}}^* d\Omega_{s0} = \int_{\partial\Omega_{f0}} -\tilde{p}_f\ \underline{n} \cdot \widehat{\underline{U}}^* d\partial\Omega_{f0} + |\Omega_0|\,\underline{\underline{\tilde{\epsilon}}}^* : \underline{\underline{\tilde{\sigma}}}, \quad \forall \widehat{\underline{U}}^* \text{ periodic}, \underline{\underline{\tilde{\epsilon}}}^*, \tag{B.13}$$

where the macroscopic stress is defined as:

$$\underline{\underline{\tilde{\sigma}}} := \frac{1}{|\Omega_0|}\left(\int_{\Omega_{s0}} \underline{\underline{\sigma_s}}\, d\Omega_{s0} - |\Omega_{f0}|\,\tilde{p}_f \underline{\underline{1}}\right). \tag{B.14}$$

This formulation can be applied to any microstructure, including microstructures where the pores intersect the representative volume element boundary. Note that the same energy can also be used for the case of known macroscopic strain mentioned in Section B.1.1. Nevertheless, in the case of unknown macroscopic strain, it is interesting to look at the strong equations associated to the weak formulation:

$$\widehat{\underline{U}} \text{ periodic}, \underline{\underline{\tilde{\epsilon}}} \quad | \quad \begin{cases} \underline{\underline{\tilde{\sigma}}} = 0 & \\ \underline{\mathrm{div}}\left(\underline{\underline{\sigma_s}}\right) = 0 & \text{in } \Omega_{s0} \\ {}^t\underline{\underline{\sigma_s}} = \underline{\underline{\sigma_s}} & \text{in } \Omega_{s0} \\ \underline{\underline{\sigma_s}} \cdot \underline{n} = -\tilde{p}_f\ \underline{n} & \text{on } \partial\Omega_{f0} \\ \underline{\underline{\sigma_s}} \cdot \underline{n} = 0 & \text{on } \partial\Omega_{s0} \backslash \partial\Omega_{f0} \\ \underline{\underline{\sigma_s}} = \dfrac{\partial W_s}{\partial \underline{\underline{\epsilon}}}\left(\widehat{\underline{U}}, \underline{\underline{\tilde{\epsilon}}}\right) & \text{in } \Omega_{s0} \end{cases}, \tag{B.15}$$

B.2.2 Extention to component-wise strain/stress loading

In some situations (e.g., for simulating strain-driven uniaxial tension experiment), we might want to impose some components of the macroscopic strain (letting the associated macroscopic stress components free), while imposing the other components of the macroscopic stress (letting the associated macroscopic strain components free). As discussed in Section 2.2.2.5, we call IJ the set of prescribed strain components, and $\tilde{\epsilon}'_{ij}\ \forall ij \in IJ$ the prescribed values; for the prescribed stress components we use KL and $\tilde{\sigma}'_{kl}\ \forall kl \in KL$; as a consequence $\tilde{\sigma}_{ij}$ and $\tilde{\epsilon}_{kl}$ are unknown. In this case, the weak formulation becomes:

$$\begin{aligned}\widehat{\underline{U}} \text{ periodic}, \tilde{\epsilon}_{kl} \quad | \quad \int_{\Omega_{s0}} \underline{\underline{\sigma_s}} : \hat{\underline{\underline{\epsilon}}}^* d\Omega_{s0} = \int_{\partial\Omega_{f0}} -\tilde{p}_f\ \underline{n} \cdot \widehat{\underline{U}}^* d\partial\Omega_{f0} \\ + |\Omega_0| \sum_{kl} \tilde{\epsilon}^*_{kl} \cdot \left(\tilde{\sigma}_{kl} - \tilde{\sigma}'_{kl}\right), \quad \forall \widehat{\underline{U}}^* \text{ periodic}, \tilde{\underline{\underline{\epsilon}}}^*_{kl}. \end{aligned} \tag{B.16}$$

B.2.3 Extention to large deformation

In the case of finite strains, the potential energy is:

$$\Pi\left(\widehat{\underline{U}}, \tilde{\underline{\underline{\epsilon}}}\right) := \int_{\Omega_{s0}} W_s\left(\underline{\underline{E}}\left(\widehat{\underline{U}}, \tilde{\underline{\underline{\epsilon}}}\right)\right) d\Omega_{s0} - \tilde{p}_f \left|\omega_f\left(\widehat{\underline{U}}, \tilde{\underline{\underline{\epsilon}}}\right)\right|. \tag{B.17}$$

As in the infinitesimal strain setting, the fluid volume is defined as the difference between total and solid volume:

$$|\omega_f| = |\omega| - |\omega_s|, \tag{B.18}$$

where

$$\begin{cases} |\omega| = \tilde{J}\,|\Omega_0| \\ |\omega_s| = {}_{\Omega_{s0}} J\ d\Omega_{s0} \end{cases}, \tag{B.19}$$

cf. Section 2.2.2.2. This leads to the following weak formulation:

$$\begin{aligned}\widehat{\underline{U}} \text{ periodic}, \tilde{\epsilon}_{kl} \quad | \quad \int_{\Omega_{s0}} \underline{\underline{\Sigma_s}} : \delta_{\underline{U};\widehat{\underline{U}}^*} \underline{\underline{E}}\ d\Omega_{s0} = \int_{\partial\Omega_{f0}} -\tilde{p}_f\ \underline{N} \cdot \underline{\underline{F}}^{-1} \cdot \widehat{\underline{U}}^* J\ d\partial\Omega_{f0} \\ + |\omega| \sum_{kl} \tilde{\epsilon}^*_{kl} \cdot \left(\tilde{\sigma}_{kl} - \tilde{\sigma}'_{kl}\right), \quad \forall \widehat{\underline{U}}^* \text{ periodic}, \tilde{\underline{\underline{\epsilon}}}^*_{kl}, \end{aligned} \tag{B.20}$$

where the macroscopic stress is defined as:

$$\tilde{\underline{\underline{\sigma}}} := \frac{1}{|\omega|}\left(\int_{\omega_s} \underline{\underline{\sigma_s}}\ d\omega_s - |\omega_f|\,\tilde{p}_f \underline{\underline{1}}\right) \tag{B.21}$$

cf. Section 2.2.2.2.

.

CHAPTER 3

Elements of microstructural modeling

This chapter introduces an algorithm to generate Voronoi geometries in 2D based on seed distribution, in addition to defining a concept to control the irregularity of the geometry. Moreover, a meshing algorithm is introduced to generate porous microstructures based on the Voronoi geometries, being able to control porosity. In addition, a procedure to generate TetraKaiDecahedron elements is presented, which can generate porous 3D microstructures and volume elements with different porosities.

Contents

3.1 Introduction

As discussed in Chapter 1, microstructural modeling is a key element of micromechanical modeling of porous materials, such as biological tissues. A computationally low-cost method to generate the microstructure of such materials is based on *regular* or *random* geometrical elements by considering the microscopic properties of the material. For instance, TetraKaiDecahedron (TKD) is used to model the lung parenchyma [Concha et al., 2018, Roth et al., 2017, Dale et al., 1980, Wiechert et al., 2009] as a space-filling element that resembles the average shape of alveoli. On the other hand, some authors use irregular or random geometries to represent the natural structure of biological tissues more precisely. Such random geometries can be generated based on ellipse tessellation [Mebatsion et al., 2006], Voronoi [Alsayednoor and Harrison, 2016, Koshiyama and Wada, 2015] or Poisson-Voronoi tessellation [Kumar et al., 1996], using seed distribution.

This work introduces a general algorithm to generate and mesh Voronoi structures in 2D, applicable in modeling porous materials. In addition, a seed distribution approach is introduced by controlling the irregularity of the geometry, which finds application in the modeling of biological tissues, such as the lung parenchyma. Furthermore, we discuss an algorithm used to generate TetraKaiDecahedron (TKD) meshes, a widely used element to model the alveoli in 3D. Our codes are freely available (https://github.com/ManoochTayebi/Geometry-generator).

3.2 Methods

Generating a microstructure involves defining a **geometry** that is subsequently **meshed**. In the following sections, we explain the process of generating porous structures both in 2D and 3D, considering microscopic features, such as irregularity of the geometry and porosity of the structure.

3.2.1 2D geometry

The algorithm for generating 2D geometries is based on hexagonal elements. This foundational approach is expanded to generate irregular geometries encompassing polygonal elements with different shapes, sizes, and numbers of faces. Such an algorithm allows manipulating the geometry irregularity resulting from seed distribution patterns. The seeds location characterizes the polyhedron element centers; the more irregular the seeds location, the more irregular the geometry. We use **Delaunay** triangulation and **Voronoi** tessellation to nail the geometry from the seed distribution. Delaunay triangulation and Voronoi tessellation are interconnected concepts with applications in diverse fields, such as computer graphics and spatial analysis.

Delaunay tessellation The Delaunay tessellation is an approach to partition the space into non-overlapping triangles based on seeds in the space, such that no seed is placed inside the circumcircle of any triangle. Delaunay tessellation is triangulation in the plane, a tetrahedralization in 3D space. Note that the Delaunay tessellation is unique for a given set of seeds as long as no four points in the point set are co-circular.

Voronoi tessellation The Voronoi tessellation is a way to partition a space based on specific seeds such that for each seed, there is a region where all the points are closer to

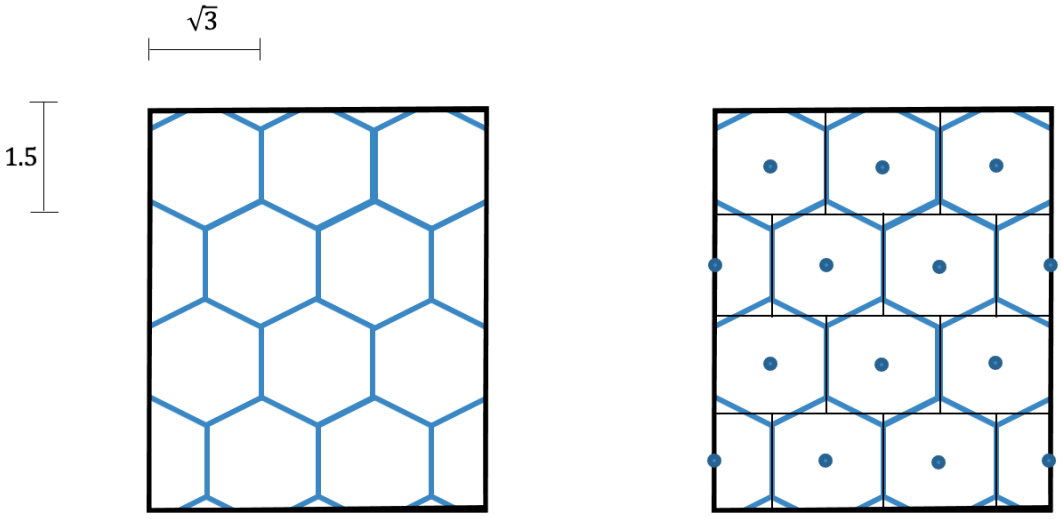

(a) Hexagonal network.

(b) Centers seeds and rectangular network.

Figure 3.2.1: Hexagonal network with center seeds and corresponding rectangular network.

that seed than any others. The Voronoi tessellation is the geometric dual of the Delaunay tessellation, such that the Voronoi vertices are the circumcenters of the Delaunay triangles.

Seed distribution

We introduce an algorithm to place the seeds based on a hexagonal network. So, the Voronoi geometry resulting from the seed distribution is supposed to be regular when the seeds are placed in the center of the hexagonal network. Then, perturbation is added to the coordinates of the regular-based seeds to nail an irregular microstructure. Note that the advantage of such an algorithm is in controlling the perturbation added to the seeds. So let us start by finding the centers of a regular hexagonal network.

Figure 3.2.1a represents a hexagonal network occupying a domain with specific dimensions. Each hexagonal element possesses a seed that represents its center. A rectangular cellular network is aligned with the hexagonal arrangement, having common centers, as shown in Figure 3.2.1b. Rectangular cells have dimensions of $2 \times \sqrt{3}$ unit, knowing the hexagonal dimension is unit.

Eliminating the hexagons leaves the rectangular cellular network and the central seeds, as shown in Figure 3.2.2a. We note that creating a Voronoi tessellation from such a seed network leads to the same hexagonal geometry. So, the arrangement of the seeds determines the configuration of its Voronoi geometry. At this point, perturbation is added to the seeds location under a constraint that allows controlling the degree of the irregularity.

The irregularity is added to the geometry by perturbing the x and y coordinates of the seeds position within the rectangular cells. However, to avoid excessively small or large polygons, we impose a constraint of minimum distance between the seeds [Spyrou et al., 2019, Koshiyama and Wada, 2015] by defining a threshold in each rectangular cell within which the seeds can be placed as shown in Figure 3.2.3b. The seeds are randomly positioned inside these thresholds, meaning that the bigger the threshold, the more irregularly the seeds are distributed and, consequently, the more irregular the geometry. We define a variable called Degree of Irregularity (DoI), based on the dimensions of the threshold and the cells, to quantify the concept of irregularity.

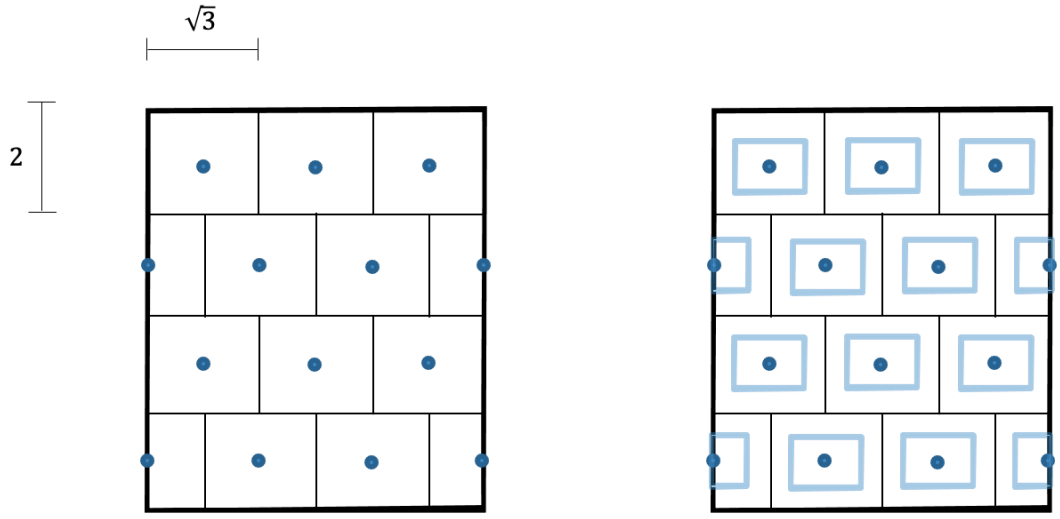

(a) Regularly distributed center seeds. (b) Threshold corresponding to each seed.

Figure 3.2.2: Voronoi polygon microstructure with six faces.

Degree of Irregularity (*DoI*) The Degree of Irregularity (DoI) specifies the dimensions of the cell threshold with respect to the cell:

$$DoI := \frac{\text{Cell threshold width}}{\text{Cell width}}. \tag{3.2.1}$$

DoI ranges from 0 to 1. $DoI = 0$ corresponds to a regular hexagonal geometry where the seeds are placed in the center of the cells, and $DoI = 1$ corresponds to the highest level of irregularity (based on this definition), where there is no minimum distance between the seeds. Figure 3.2.3 shows an example of random seed distribution with $DoI = 0.5$ where the seeds are placed within the threshold, maintaining a minimum distance of $\frac{\sqrt{3}}{2}$ unit from each other.

Generating the geometry based on Voronoi tessellation

The geometry is generated through Voronoi tessellation, involving an intermediary step of constructing a Delaunay triangulation from the seeds. This Delaunay triangulation is implemented using the Scipy library in Python. To facilitate tracking of the process, we present an algorithm for transforming the Delaunay tessellation into a Voronoi tessellation. The importance of introducing such an algorithm is in generating the mesh from the geometry in the next step.

Suppose we have the Delaunay triangulation. As an example, a triangle is represented in Figure 3.2.4a. The objective is to generate the corresponding Voronoi cells from this triangulation. Each Voronoi cell corresponds to a seed and includes the closest points of the plane to that seed. So, in a neighborhood between two seeds with arbitrary names of A and B, the points of the plane closer to seed A belong to the Voronoi cell with the center of seed A, and the ones closer to seed B belongs to the Voronoi cell with the center of seed B; meaning that two cells are separated with the vertical perpendicular of the connecting line between seeds A and B. It is important to emphasize that the proximity of two seeds is established based on a specific logic inherent to the Delaunay triangulation.

We conclude that in the Voronoi tessellation, each seed is a neighbor to the seeds with which it forms a triangle in the Delaunay triangulation. So, the intersection of the vertical

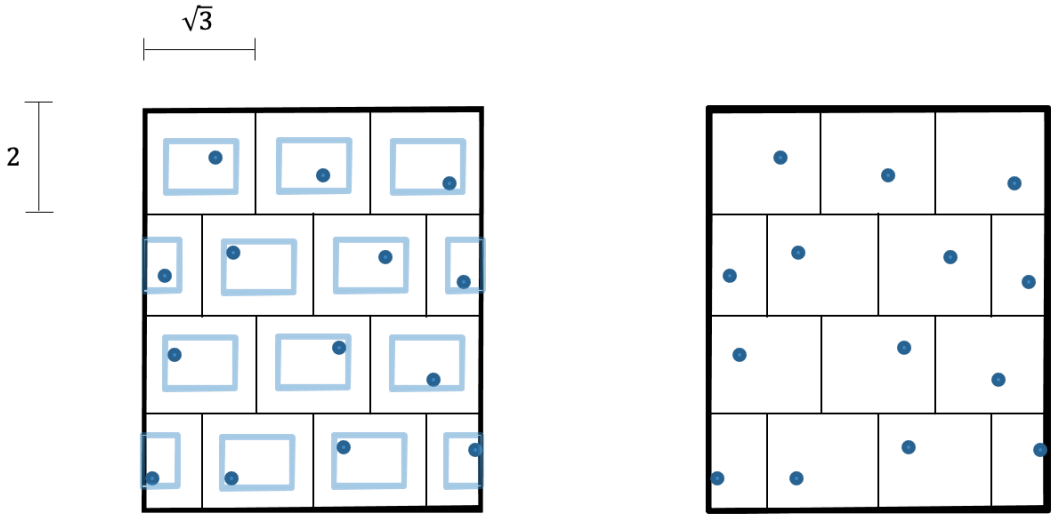

(a) Perturbed seeds within the thresholds.

(b) Perturbed seeds within the cells.

Figure 3.2.3: Center seeds distribution with perturbation.

perpendiculars of each triangle is the corner of each Voronoi cell. Notably, vertical perpendiculars of a triangle intersect at only one point, as demonstrated in Figure 3.2.4b. Finally, connecting the intersections of the vertical perpendiculars of the neighboring triangles results in a Voronoi tessellation. An example of such a transformation from a Delaunay triangulation to a Voronoi tessellation is shown in Figure 3.2.5.

3.2.1.1 Periodicity

We follow [Spyrou et al., 2019, Yan et al., 2011] to enforce periodic boundaries on the geometry by repeating the same pattern of seeds of *initial domain*, in the eight neighborhoods. The Voronoi tessellation is generated based on all seeds, as shown in Figure 3.2.6. In the end, the initial central domain is extracted, with periodic patterns on the boundaries.

3.2.1.2 Creating mesh for 2D geometries

With the objective of generating a porous microstructure, the elements of the Voronoi tessellation (which are the faces of the polygons) are meshed. Note that the thickness of the meshed elements controls the porosity of the microstructure. The procedure is performed by creating rectangles around the elements, the width of which shows the thickness of the cell walls. Each element has two points at the two ends, corresponding to the corner of the Voronoi cells. Thanks to the trackable algorithm implemented for generating the Voronoi tessellation, the position of the corners and, consequently, the slope of the elements, which are lines in the plane, are known. So, rectangles around the elements are created with the intersection of two parallel lines to the elements with a distance of $\frac{h}{2}$ from each other and two parallel lines perpendicular to them, passing from the corners, at the end of the elements. Figure 3.2.7 shows the generated rectangles around some elements. The rectangles are created around all the elements, become a union with *boolean operation*, and are meshed using the Open-Cascade kernel in GMSH [Geuzaine and Remacle, 2009].

This algorithm is aligned with the other algorithm to generate Voronoi tessellations, enabling it to create a meshed microstructure from a Voronoi-based geometry. In addition, it controls the thickness of the mesh, resulting in different porosity values.

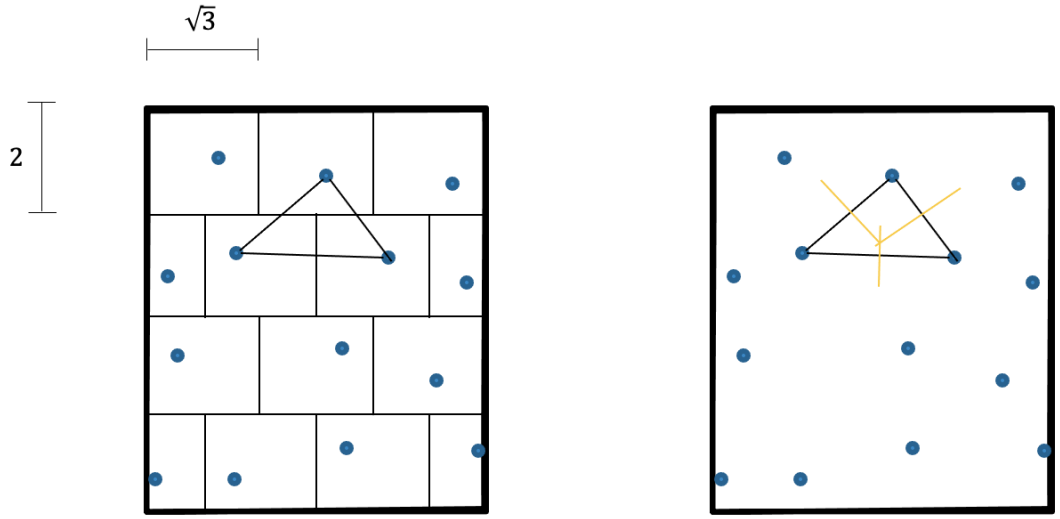

(a) Neighbor seeds creating triangles in Delaunay triangulation.

(b) Vertical perpendicular of a triangle comprised of three neighbor seeds.

Figure 3.2.4: Algorithm logic for finding polygons corners.

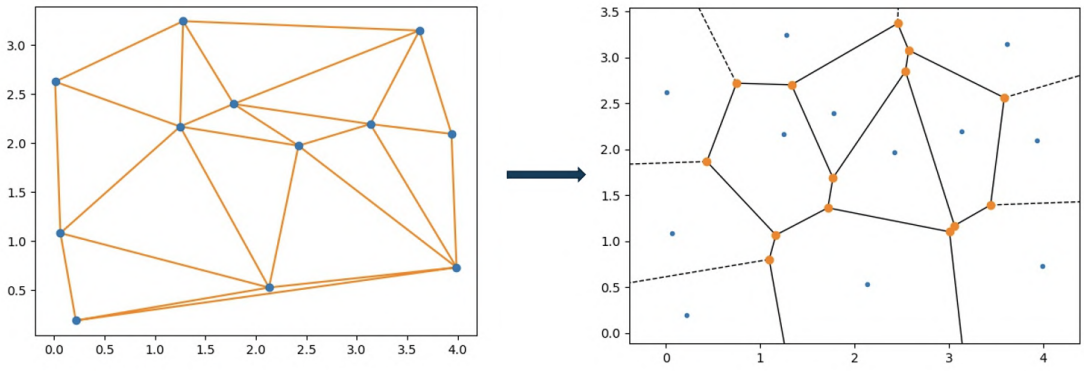

Figure 3.2.5: Connecting the intersection of vertical perpendicular of neighbor triangles, results in obtaining a Voronoi tessellation.

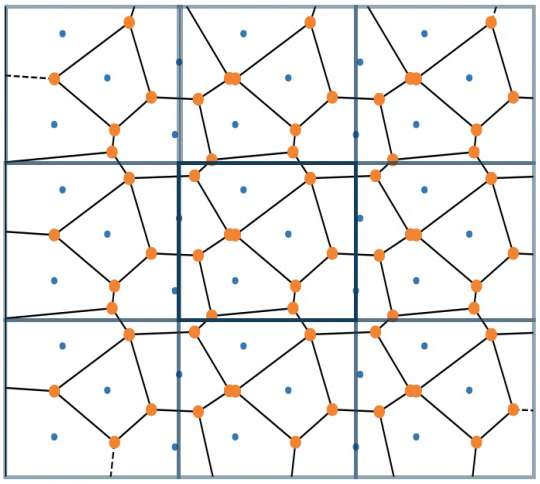

Figure 3.2.6: Creating periodicity on the boundaries by replicating the pattern of central seeds through eight neighborhoods.

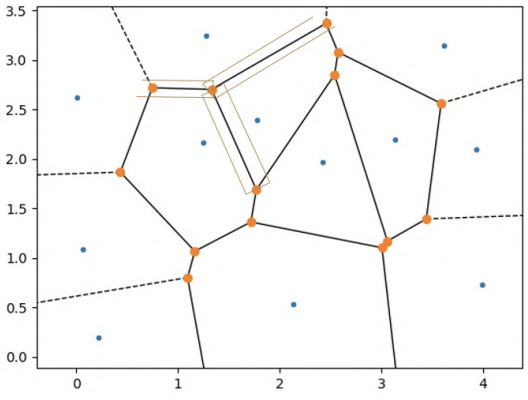

Figure 3.2.7: Creating rectangles around the walls for generating the mesh.

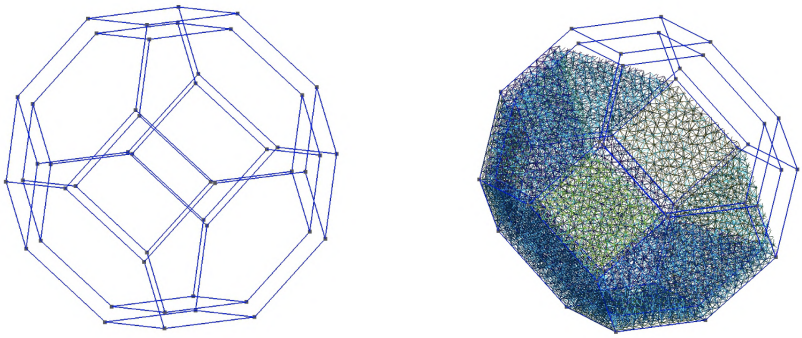

(a) Two TKD elements with different dimensions.

(b) Meshed TKD element, considering the wall thickness (using GMSH).

Figure 3.2.8: TetraKaiDecahedron (TKD) element, meshed, considering a specific thickness (or porosity).

3.2.2 3D geometry

The 3D microstructure is generated using TetraKaiDecahedron (TKD) geometry, space-filling elements with 14 faces. The geometry is generated by directly meshing an octahedron in GMSH and cutting it with a cube using *boolean operation*. Noting that the cube and octahedron ratio should be chosen such that the resulting TKD from the boolean operation maintains faces with regular hexagons and rectangles. Similarly, another TKD is generated with smaller dimensions, as shown in Figure 3.2.8a. The latter TKD is cut from the first one using *boolean operation*, while the difference between the dimensions characterizes the mesh area (cf. Figure 3.2.8b). So, the porosity of the microstructure can be tuned by the aspect ratio of the two TKDs.

An array of TKD elements are combined with boolean operations to create a microstructure as shown in Figure 3.2.9a. A Representative Volume Element (RVE) can be considered by extracting a periodic cube from the microstructure, having specific dimensions to maintain the periodicity (cf. Figure 3.2.9b). Such an RVE with periodic boundaries is the smallest volume element that can reconstruct the whole microstructure, as shown in Figure 3.2.9c.

3.3 Illustrative results and discussion

In-plane geometries

The algorithm to generate in-plane geometries can create geometries with different degrees of **irregularity** and **porosity**. Note that *porosity* is defined as the unmeshed area/volume over the total area/volume. Figure 3.3.1 shows three different microstructures of a regular hexagon, irregular with $DoI = 0.4$, and a microstructure with completely random seed distribution. The algorithm to generate the Voronoi microstructures from seeds is generic for any seed distribution, while introducing the concept of **degree of irregularity** maintains a minimum distance between the seeds to prevent generating very small or large cells, comparably. Note that the irregular and random microstructures are not generally isotropic but tend to isotropy by increasing the number of seeds.

Another parameter that can be tuned in this algorithm is the thickness of the walls which results in different porosities, ranging from 0 to 100%. Figure 3.3.2 shows an example

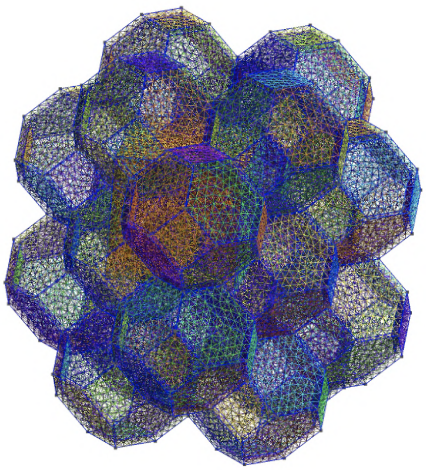

(a) A microstructure consisting of TKD elements.

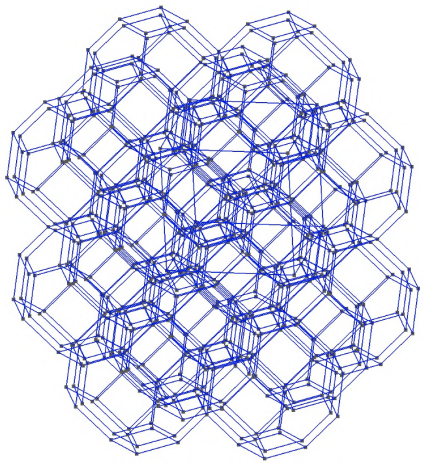

(b) Periodic RVE borders in an array of TKD elements.

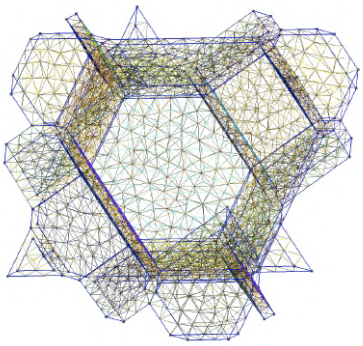

(c) TKD-based RVE with periodic boundaries.

Figure 3.2.9: A periodic RVE can be generated based on TKD elements, resembling the whole microstructure.

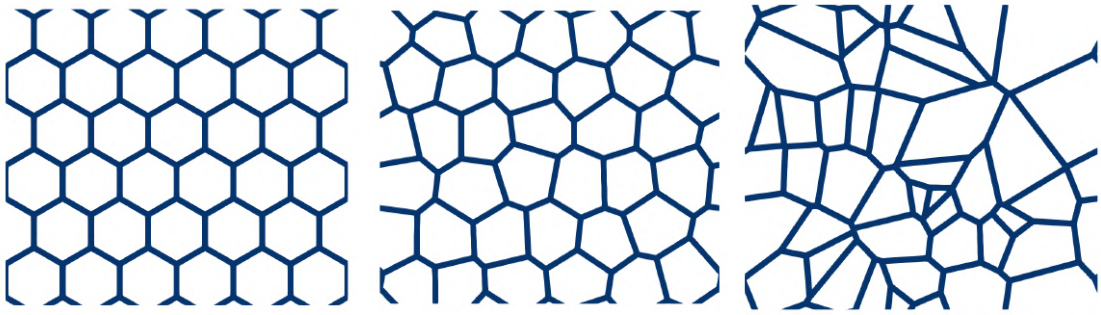

(a) Regular hexagonal microstructure.

(b) Irregular hexagonal-based microstructure ($DoI = 0.4$).

(c) Microstructure based on completely random seed distribution.

Figure 3.3.1: irregular microstructure with completely random seed distribution.

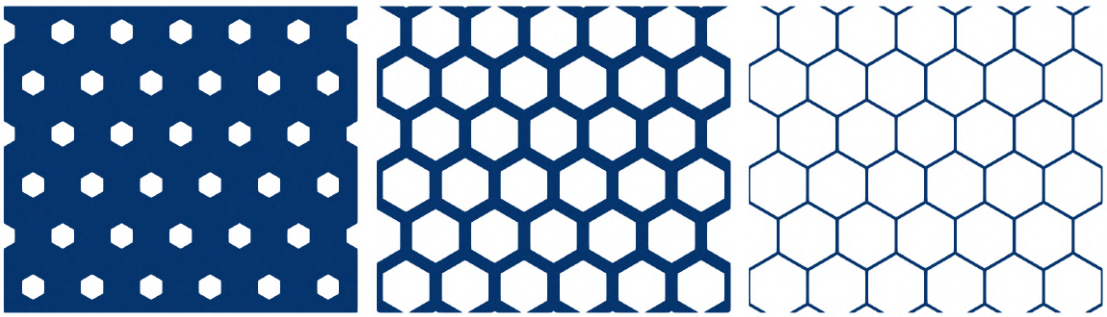

$\phi = 15\%$ $\phi = 60\%$ $\phi = 90\%$

Figure 3.3.2: Hexagonal microstructure with different values of porosity ϕ.

of geometries with different porosities. Such a characteristic of the algorithm, aligned with the ability to create irregular cells in a similar range of sizes and shapes, makes it applicable in the microstructural modeling of biological tissues. An example of such an application is modeling the lung parenchyma, where the alveoli have different shapes, sizes, and numbers of faces, and the alveolar wall thickness defines the regional porosity.

3D geometries

The 3D algorithm can generate TKD-based microstructure with different porosities, as shown in Figure 3.3.3. Similarly to in-plane microstructures, such a 3D microstructure is used in microstructural modeling of the alveoli as it is a space-filling element that looks like the average shape of the alveoli. Such an ability of the algorithm to generate microstructure with different wall thicknesses is an asset to simulate the lung parenchyma in different diseases, such as interstitial lung disease, where the tissue of the alveolar wall gets thicker at some regions [Patte et al., 2022].

3.4 Conclusions and perspectives

We introduced an algorithm to generate parameterized microstructures with different degrees of irregularities and porosities in 2D and TKD-based microstructures in 3D. Such parametrization is applicable to manipulate structural parameters, especially with the objective of microstructure modeling of the biological tissues, where the cells have different shapes, sizes, and numbers of faces. In addition, the meshing algorithm is general and is

$\phi = 60\%$ $\phi = 70\%$ $\phi = 85\%$

Figure 3.3.3: TKD microstructure with different values of porosity ϕ.

able to create Voronoi tessellation for any seed distribution. On the other hand, the new concept of controlling irregularity prevents excessively small and large cells and keeps the microstructure more homogeneous in the sense of cell size. Such a characteristic resembles more closely to the biological tissues.

The algorithm in 3D aims to generate regular TKD elements, while the irregularity concept to create Voronoi tessellation can be generalized in 3D. Moreover, with the objective of alveoli modeling, some additional features can be added, such as creating the airways by eliminating the walls.

Bibliography

[Alsayednoor and Harrison, 2016] Alsayednoor, J. and Harrison, P. (2016). Evaluating the performance of microstructure generation algorithms for 2-d foam-like representative volume elements. *Mechanics of Materials*, 98:44–58.

[Concha et al., 2018] Concha, F., Sarabia-Vallejos, M., and Hurtado, D. E. (2018). Micromechanical model of lung parenchyma hyperelasticity. *Journal of the Mechanics and Physics of Solids*, 112:126–144.

[Dale et al., 1980] Dale, P., Matthews, F. L., and Schroter, R. C. (1980). Finite element analysis of lung alveolus. *Journal of Biomechanics*, 13(10):865–873.

[Geuzaine and Remacle, 2009] Geuzaine, C. and Remacle, J.-F. (2009). Gmsh: A 3-D finite element mesh generator with built-in pre- and post-processing facilities: THE GMSH PAPER. *International Journal for Numerical Methods in Engineering*, 79(11):1309–1331.

[Koshiyama and Wada, 2015] Koshiyama, K. and Wada, S. (2015). Mathematical model of a heterogeneous pulmonary acinus structure. *Computers in Biology and Medicine*, 62:25–32.

[Kumar et al., 1996] Kumar, S., Kurtz, S. K., and Agarwala, V. K. (1996). Micro-stress distribution within polycrystalline aggregate. *Acta Mechanica*, 114(1-4):203–216.

[Mebatsion et al., 2006] Mebatsion, H., Verboven, P., Ho, Q., Verlinden, B., Mendoza, F., Nguyen, T., and Nicolaï, B. (2006). Modeling Fruit Microstructure Using an Ellipse Tessellation Algorithm. In *13th World Congress of Food Science & Technology*, page 246, Nantes, France. EDP Sciences.

[Patte et al., 2022] Patte, C., Genet, M., and Chapelle, D. (2022). A quasi-static poromechanical model of the lungs. *Biomechanics and Modeling in Mechanobiology*.

[Roth et al., 2017] Roth, C. J., Yoshihara, L., and Wall, W. A. (2017). A simplified parametrised model for lung microstructures capable of mimicking realistic geometrical and mechanical properties. *Computers in Biology and Medicine*, 89:104–114.

[Spyrou et al., 2019] Spyrou, L., Brisard, S., and Danas, K. (2019). Multiscale modeling of skeletal muscle tissues based on analytical and numerical homogenization. *Journal of the Mechanical Behavior of Biomedical Materials*, 92:97–117.

[Wiechert et al., 2009] Wiechert, L., Metzke, R., and Wall, W. A. (2009). Modeling the Mechanical Behavior of Lung Tissue at the Microlevel. *Journal of Engineering Mechanics*, 135(5):434–438.

[Yan et al., 2011] Yan, D.-M., Wang, K., Levy, B., and Alonso, L. (2011). Computing 2D Periodic Centroidal Voronoi Tessellation. In *2011 Eighth International Symposium on Voronoi Diagrams in Science and Engineering*, pages 177–184, Qing Dao, China. IEEE.

CHAPTER 4

Toward a physiological micro-model: incorporating surface tension and fitting to experiments

This chapter is an extension to Chapter 2, where the microscopic poromechanical model is extended to the lung behavior modeling. An enriched constitutive law is introduced for the solid behavior, including an exponential term, reproducing the strain-induced stiffening behavior of the lung in distortion. In addition, surface tension, as a microscopic physiological feature of the lung, is modeled based on two distinct laws in inflation and deflation. Finally, the parameters of the constitutive potential, the size of the alveoli, and the surface tension model parameters are identified by comparing them to existing experimental data, such that the response of the model matches the experiments. Considering that the existing experiments mostly report the volume of the lung with respect to its maximum capacity, we use an approach in which the maximum capacity of the model is defined where the fluid volume is asymptotic with respect to the increase of fluid pressure.

Contents

4.1 Introduction

We extend upon the work of Chapter 2, where a micro-poro-mechanical model is introduced in the finite strain domain and bridged to the macroscopic scale. Such a model permits computing the response of a specified RVE to any loading of macroscopic stress, macroscopic strain, and/or fluid pressure. The micro-poro-mechanical model can be applied to various porous materials, including the lung parenchyma, considering the interstitium tissue as the solid and the air as the fluid. To adapt the response of the micromechanical model to the behavior of the lung, we need to enrich it different aspects. Overviewing the existing experiments on the lung [Gibson and Pride, 1976, Arora et al., 2021, Bel-Brunon et al., 2014, Birzle and Wall, 2019], the constitutive potential can be chosen to produce a strain-induced stiffening behavior. Moreover, knowing that the micromechanical model allows us to represent explicitly microscopic phenomena, we can incorporate surface tension as a physiological mechanism of the lung parenchyma [Schürch et al., 1976, Bachofen and Schürch, 2001, Otis et al., 1994, Kowe et al., 1986]. Based on such modifications, the overall response of the model can be compared to the existing experiments in order to identify the parameters of the model [Bel-Brunon et al., 2014, Maksym and Bates, 1997, Patte et al., 2022a, Laville et al., 2023]

In this work, we introduce the surface tension into the model, aligned with an enriched skeleton potential, considering an exponential term based on the proposition by [Patte et al., 2022b]. Such a hyperelastic potential detains a strain-induced stiffening, with an adequate number of parameters that can be identified based on the existing experiments. First, we describe the new formulation of the micromechanical model, where surface tension is introduced; then, we review some experiments from the literature to which we compare the response of our model to identify its parameters.

4.2 Methods

4.2.1 Micro-poromechanical modeling

The micromechanical framework and the geometry are the same as introduced in Chapter 2. In addition, we propose a new constitutive potential for the solid, and the surface force resulting from the surface tension, which is introduced in the weak formulation of the problem.

Solid constitutive law. We assume that the solid obeys a standard elastic law, such that its stress-strain relation derives from its free energy potential:

$$\underline{\underline{\Sigma_s}} = \frac{\partial \Psi_s}{\partial \underline{\underline{E}}}. \tag{4.2.1}$$

Because here the solid is considered a standard continuum, its free energy has only one contribution, namely the elastic energy: $\Psi_s = W_s$. We propose the following constitutive behavior for the solid, considering Neohookean and Ogden-Ciarlet-Geymonat [Ogden, 1972, Ciarlet and Geymonat, 1982] laws, and including an exponential term that captures the stiffening behavior in finite strains [Patte et al., 2022b], defined in plane strain:

$$W_s = \frac{\beta_1}{2\beta_2\alpha}\left(\exp\beta_2\left(I_1 - 2 - 2\ln J\right)^\alpha - 1\right) + \beta_3\left(I_1 - 2 - 2\ln J\right) + \kappa\left(J^2 - 1 - 2\ln J\right), \tag{4.2.2}$$

where β_1, β_2, β_3, and α are the model parameters and κ is chosen to be large to be aligned with the assumption of incompressible lung parenchyma tissue [Concha et al., 2018, Wiechert et al., 2009, Berger et al., 2016]. Such a constitutive choice results in zero stress in the reference configuration.

Solid equilibrium equations and the surface force. We recall the internal equilibrium of the solid expressed in the deformed configuration as follows:

$$\begin{cases} \underline{\mathrm{div}}\left(\underline{\underline{\sigma_s}}\right) = 0 & \text{in } \omega_s \\ {}^t\underline{\underline{\sigma_s}} = \underline{\underline{\sigma_s}} & \text{in } \omega_s \\ [\![\ \underline{\underline{\sigma_s}} \cdot \underline{n}\ ]\!] = 0 & \text{on } \partial\omega_s \backslash \partial\omega_f \end{cases} \tag{4.2.3}$$

The first equation represents the balance of linear momentum, the second the balance of angular momentum, and the third the continuity of the traction vector at the periodic interfaces, $\underline{n}$ being the outward normal to the solid. We also have the external equilibrium of the solid, i.e., the equilibrium between the solid, fluid, and surface tension:

$$\underline{\underline{\sigma_s}} \cdot \underline{n} = -\tilde{p}_f\ \underline{n} + \underline{f_s} \quad \text{on } \partial\omega_f, \tag{4.2.4}$$

where $\underline{f_s}$ is the force density applied on the solid-fluid interface, corresponding to surface tension.

4.2.1.1 Surface tension

We use [Koshiyama et al., 2018]'s formulation of surface tension which is briefly recalled here. Based on this formulation, the force density

$$\underline{f_s} = \underline{\mathrm{div}_s} \cdot \left(\underline{\underline{\tau_s}}\right), \tag{4.2.5}$$

with $\underline{\mathrm{div}_s}$ the surface divergence [Barthès-Biesel and Rallison, 1981]:

$$\underline{\mathrm{div}_s} = \underline{\underline{P}} \cdot \underline{\mathrm{div}}, \tag{4.2.6}$$

where $\underline{\underline{P}}$ the surface projection tensor [Lay et al., 2016]:

$$\underline{\underline{P}} = \underline{\underline{I}} - \underline{n} \otimes \underline{n}, \tag{4.2.7}$$

with the normal vector in the deformed configuration

$$\underline{n} = \frac{{}^t\underline{\underline{F}}^{-1} \cdot \underline{N}}{||{}^t\underline{\underline{F}}^{-1} \cdot \underline{N}||}. \tag{4.2.8}$$

In addition, $\underline{\underline{\tau_s}}$ is the in-plane surface tension tensor. Considering isotropic surface tension γ (cf. Appendix A.2)

$$\underline{\underline{\tau_s}} = \gamma \underline{\underline{P}}, \tag{4.2.9}$$

In this study, surface tension γ can be a constant or a surface-dependent coefficient. In the case of surface-dependent behavior for surface tension, we propose the increase of surface tension to be asymptotic with respect to the surface area near its maximum value [Denny and Schroter, 2000, Wiechert et al., 2009], such that

$$\gamma\left(S\right) = \gamma_{max}\left(\frac{c_1}{1 + \left(\frac{J_s}{c_2}\right)^{c_3}}\right), \tag{4.2.10}$$

where c_1, c_2, and c_3 are the parameters of the model and γ_{max} is the maximum surface tension, reached when lung is inflated at Total Lung Capacity (TLC), and J_s the relative surface area defined as

$$J_s := \frac{d\partial\omega_f}{d\partial\Omega_{f0}}. \tag{4.2.11}$$

4.2.1.2 Problem formulation and resolution

We propose to solve the micro-poro-mechanical model using the finite element modeling. We consider two experimental data of tensile test and pressure-volume one. To perform these two test, the model is formulated such that the stress and pressure are known and the strain is computed.

Weak formulation. The weak formulation is derived by writing the strong form of the micro-poro-mechanics problem in finite strains, in the reference configuration (i.e., Lagrangian form) to find $\left(\underline{\underline{\tilde{\epsilon}}}, \underline{\widehat{U}}\ periodic\right)$ such that

$$\begin{cases} \underline{\mathrm{Div}}\left(\underline{\underline{F}} \cdot \underline{\underline{\Sigma}}\left(\underline{U}\right)\right) = 0 & \text{in } \Omega_{s0} \\ {}^t\underline{\underline{\Sigma}} = \underline{\underline{\Sigma}} & \text{in } \Omega_{s0} \\ \underline{\underline{F}} \cdot \underline{\underline{\Sigma}}\left(\underline{U}\right) \cdot \underline{N} = -\tilde{p}_f J\ {}^t\underline{\underline{F}}^{-1} \cdot \underline{N} + \underline{f_s} J || {}^t\underline{\underline{F}}^{-1} \cdot \underline{N} || & \text{on } \partial\Omega_{f0}\ . \\ [|\underline{\underline{\Sigma}} \cdot \underline{N}\ |] = 0 & \text{on } \partial\Omega_{s0} \backslash \partial\Omega_{f0} \\ \underline{\underline{\tilde{\sigma}}}\left(\underline{U}\right) = \underline{\underline{\tilde{\sigma}}}' \end{cases} \tag{4.2.12}$$

The process of deriving the weak formulation is similar to the one detailed in [Manoochehrtayebi et al., 2024] with the additional terms related to surface tension and detailed in Appendix A.4. So, we only recall here the final formulation:

$$\begin{aligned} \text{Given } \left(\underline{\underline{\tilde{\sigma}}}', \tilde{p}\right), \text{ find } \left(\underline{\underline{\tilde{\epsilon}}}, \underline{\widehat{U}} \text{ periodic}\right) \text{ such that, for all } \left(\underline{\underline{\tilde{\epsilon}}}^*, \underline{\widehat{U}}^* \text{ periodic}\right), \\ \int_{\partial\Omega_{s0}} \underline{\underline{\underline{\underline{\Sigma_s}}}} \cdot \delta_{\underline{U};\underline{\widehat{U}}^*} \underline{\underline{E}}\ d\partial\Omega_{s0} - \int_{\partial\Omega_{f0}} -p_f \cdot \underline{N} \cdot \underline{\underline{F}}^{-1} \cdot \underline{\widehat{U}}^* J d\partial\Omega_{f0} \\ + \int_{\partial\Omega_{f0}} \underline{\underline{\underline{\tau_s}}} : \underline{\mathrm{div}_s}\left(\underline{\underline{\tilde{\epsilon}}}^* \cdot \left(\underline{X} - \underline{X_0}\right) + \underline{\widehat{U}^*}\right) J || {}^t\underline{\underline{F}}^{-1} \cdot \underline{N} || d\partial\Omega_{f0} \\ - |\omega| \underline{\underline{\tilde{\epsilon}}}^* : \left(\underline{\underline{\tilde{\sigma}}}\left(\underline{U}\right) - \underline{\underline{\tilde{\sigma}}}'\right) = 0 \end{aligned} \tag{4.2.13}$$

where $\delta_{\underline{U};\underline{\widehat{U}}^*} \underline{\underline{E}} = \left({}^t\underline{\underline{F}} \cdot \underline{\mathrm{Grad}}\left(\underline{\widehat{U}}^*\right)\right)_{sym} = \frac{1}{2}\left({}^t\underline{\underline{F}} \cdot \underline{\mathrm{Grad}}\left(\underline{\widehat{U}}^*\right) + {}^t\underline{\mathrm{Grad}}\left(\underline{\widehat{U}}^*\right) \cdot \underline{\underline{F}}\right)$ is the differential of the Green-Lagrange strain tensor with respect to the displacement perturbation vector. Note that due to the periodicity conditions on the perturbation field $\underline{\widehat{U}}$, the rigid body rotations are blocked. However, the rigid body translations, which are indeed periodic, are not naturally blocked, so we block them by imposing zero perturbation at an arbitrary mesh node.

4.2.1.3 Numerical resolution and implementation

Problem (4.2.13), corresponds to a coupled system of nonlinear partial differential and algebraic equations, which we solve using the finite element method. It has been implemented in an open-source finite element code [Genet et al., 2023] based on the FEniCS library [Logg et al., 2012, Alnæs et al., 2015], and is currently freely available online at `https://gitlab.inria.fr/mgenet/dolfin_mech`. The micro-structure generator

is also open-source [Manoochehrtayebi and Genet, 2023b], and is currently freely available online at `https://github.com/ManoochTayebi/micro_poro_structure_generator`. We also provide the code to reproduce the results of this paper under the form of jupyter notebooks [Manoochehrtayebi and Genet, 2023a]: static versions are given in the appendix of the paper while interactive versions are currently available online at `https://github.com/ManoochTayebi/Lung-micro-poro-paper-demos`.

4.2.2 Preview of experimental data

In this work, we aim to apply our micromechanical modeling framework to the lung, so to find the model parameters yielding a macroscopic behaviour comparable to the one observed in experiments. Therefore we start by reviewing the relevant literature to this aim.

4.2.2.1 Morphological data

The morphological parameters which we can tune in our micro-mechanical model include the lung parenchyma porosity and the size of the alveoli, which both vary from species to species. [Gehr et al., 1978] reported the human lung porosity to be around 86.5% when ventilated at $20-30\ cmH_2O$, and similarly [Kampschulte et al., 2013] found the porosity to be equal to 83%, being ventilated 35 cmH_2O. The alveoli diameter, as another morphological parameter, is differently reported in the literature ranged from $50-500\ \mu m$ [Weibel, 2017]. For example, [Tenney and Remmers, 1966] measured the diameter of the alveoli of pig and sheep around 70 μm while ventilated at 20 cmH_2O; the rabbits alveoli diameter ranges between 50 and 100 μm when the lung is inflated at 20 cmH_2O [Kovar et al., 2002]; [Denny and Schroter, 1997] reported the alveoli diameter of the human around 200 μm when the lung is fully inflated.

4.2.2.2 Mechanical behaviour data

To distinguish the mechanical contribution of the skeleton and the surfactant and identify their constitutive parameters respectively, we base our work on two different experimental data; pressure volume experiments by [Smith and Stamenovic, 1986] and tensile test by [Jorba et al., 2019].

[Smith and Stamenovic, 1986] conduct quasi-static experiments on liquid-filled and air-filled rabbit excised lungs with two different approaches: (i) lung filled with liquids with constant liquid-liquid interfacial surface tension, resulting in a constant surface tension during inflation and deflation; (ii) air-filled lung with air-liquid surface tension, where the surface tension resulting from the air and tissue interface depends on the surface area and also the kinetic of inflation or deflation. Both fluid-filled and air-filled lungs were inflated step-by-step, up to 100% of total lung capacity (TLC). Such an experimental protocol leads to a reference library of pressure-volume relationships for different surface tensions. For the sake of illustration, in Figure 4.2.1, we display the pressure-volume curves from [Smith and Stamenovic, 1986] in deflation for different surface tensions, as well as the air-filled inflation-deflation curves.

The tensile test by [Jorba et al., 2019] is performed on a strip of $7\times2\times2\ mm$ cut from the decellularized lung parenchyma of adult Sprague-Dawley rats. One end of the strip was fixed to a hook attached to the lever arm of a displacement actuator. The other end of the strip was glued to a hook attached to a force transducer to measure the force applied to the strip. tissue strip subjected to a tensile force and the stretched length is measured.

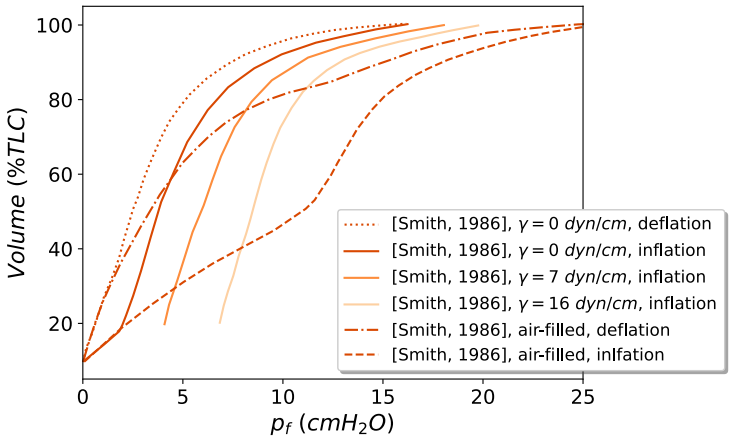

Figure 4.2.1: Comparing pressure-volume behavior of the lung in deflation, for fluid-filled with different values of surface tension and air-filled, reported by [Smith and Stamenovic, 1986].

4.2.3 Identifying the model parameters

Let us recall the micromechanical model features which parameters can be tuned to reproduce the physiological behaviour of lung parenchyma: 1. microstructure geometry, namely the alveolar size and the porosity (2 parameters); 2. the alveolar wall behaviour (4 parameters); 3. the surface tension behaviour (3 parameters in inflation, 3 parameters in deflation). First, we need to define a framework based on which we can compare the response of the model to the experimental data from the literature, where the volume is reported with respect to TLC. Then, two observations can be made: first, there is a strong coupling between porosity and alveolar wall stiffness in the mechanical response of the tissue, so we chose to set the porosity to a predefined value of 63% at end-deflation, according to literature. Second, the model response depends on the alveolar size only in the presence of surface tension. So we defined a sequential identification strategy: it consists in identifying the hyperelastic parameters of the alveolar walls based on null surface tension experiments, then the alveolar diameter based on constant surface tension experiments, then the surface tension based on surface-dependent surface tension.

4.2.3.1 Defining total lung capacity (TLC) in the model

The pressure-volume experimental data in the literature mostly define the volume of the lung with respect to the total lung capacity (TLC), which is the maximum capacity of the lung to be inflated with air. It can be noted that the pressure at 100% TLC varies between experiments, which may result from different experimental protocols. By nature, there is no maximum capacity in the model, the RVE can theoretically infinitely deform. So, we need to introduce a formal definition of the model TLC, which depends on the model parameters.

The total lung capacity corresponds to a state at which the lung exhibits increased - infinite - rigidity, preventing further inflation. At this state, the (fluid) volume increase with respect to pressure becomes negligible. It is observed both in-vivo and ex-vivo so it is not only due to the rib cage resistance but also to the lung tissue stiffening. We can use such a concept to define a criterion corresponding to TLC in our model. The exponential choice with the power parameter α for the skeleton constitutive law results in a strain-induced stiffening, and as a consequence, it leads to an asymptotic volume increase with respect to pressure.

We can plot the pressure-volume response of the model knowing the model TLC which is obtained at a specific pressure. So, the (fluid) volume is compared at different pressures as a percentage of model TLC. To obtain the model TLC we set a criterion for the slope of the pressure-volume curve of $10^{-1}|\Omega_{f0}|$ (cmH_2O^{-1}), beyond which we consider the fluid volume has reached its maximum and set it to be equal to 100% TLC.

4.2.3.2 Hyperelastic potential parameters identification

The identification of the alveolar wall hyperelastic parameters is based on the experiments from [Smith and Stamenovic, 1986] with null surface tension. We can observe on Figure 4.2.1 that this experiment exhibits a small hysteresis which cannot be obtained with our model in which the alveolar wall behaviour is elastic. So we chose to find constitutive parameters minimizing the gap between the model response and both the inflation and deflation curves, yielding an average hyperelastic response in the absence of surface tension.

Considering the parameters of the model as $\underline{\vartheta} = [\beta_1, \beta_2, \beta_3, \alpha]$ as in [Tueni, 2021, Tueni et al., 2023], we introduce the non-dimensional parameter $\underline{\bar{\vartheta}} = [\bar{\beta}_1, \bar{\beta}_2, \bar{\beta}_3, \bar{\alpha}]$ such that

$$\underline{\bar{\vartheta}} = \left(\underline{\vartheta} - \underline{\vartheta_0}\right) \oslash \underline{\vartheta_0}, \tag{4.2.14}$$

where $\underline{\vartheta_0}$ is a reference value of the parameters and $\oslash$ the Hadamard division.

So, the cost function to minimize for the pressure volume test, is defined as

$$J_{cost}\left(\underline{\bar{\vartheta}}\right) = \frac{1}{n}\sum_{i}^{n} \frac{\left(|\omega_f|_i\left(\underline{\bar{\vartheta}}\right) - |\omega_f|_i^{exp}\right)^2}{\left(|\omega_f|_i^{exp}\right)^2}, \tag{4.2.15}$$

where $|\omega_f|_i^{exp}$ is the ith experimental value of the volume with respect to TLC and $|\omega_f|_i\left(\underline{\bar{\vartheta}}\right)$ is the computed volume from the model for the corresponding pressure, with respect to the model TLC and for the dimensionless set of parameters $\underline{\bar{\vartheta}}$.

The model parameters $\underline{\bar{\vartheta}}$ are identified by minimizing the cost function J_{cost}, considering the experimental pressure-volume curves. Note that for each iteration of this minimization, the constitutive parameters change and theferore, the model TLC needs to be updated as well. The cost function is minimized using the Truncated Newton method [Dembo and Steihaug, 1983], also known as Hessian-free optimization, which is a first-order optimization method that employs the conjugate gradient. In this method, for each set of parameters, the cost function is computed multiple times. So, to lower the cost of computations, we load the RVE only once for each set of parameters and compute $|\omega_f|_i^{micro}\left(\underline{\bar{\vartheta}}\right)$ using interpolation on the computed values from the model solver in different time steps. The identifiability of the parameters is studied using the Hessian matrix of the cost function near the solution.

Similarly, the cost function to minimize for the tensile test, is defined as

$$J_{cost}\left(\underline{\bar{\vartheta}}\right) = \frac{1}{n}\sum_{i}^{n} \frac{\left(\bar{\epsilon}_{xi}\left(\underline{\bar{\vartheta}}\right) - \bar{\epsilon}_{x_i}^{exp}\right)^2}{\left(\bar{\epsilon}_{x_i}^{exp}\right)^2}, \tag{4.2.16}$$

where $\bar{\epsilon}_{x_i}^{exp}$ is the ith experimental value of the strain and $\bar{\epsilon}_{xi}$ is the macroscopic strain obtained from the model for the corresponding stress.

Hessian Matrix We compute the eigenvalues and eigenvectors of the Hessian matrix of the cost function around the solution to show the sensitivity of the cost function with

respect to the optimized dimensionless parameters. The Hessian matrix is defined as

$$\underline{\underline{\bar{H}}} = \begin{bmatrix} \frac{\partial^2 J_{cost}}{\partial \bar{\beta}_1^2} & \frac{\partial^2 J_{cost}}{\partial \bar{\beta}_1 \partial \bar{\beta}_2} & \frac{\partial^2 J_{cost}}{\partial \bar{\beta}_1 \partial \bar{\beta}_3} & \frac{\partial^2 J_{cost}}{\partial \bar{\beta}_1 \partial \bar{\alpha}} \\ \frac{\partial^2 J_{cost}}{\partial \bar{\beta}_2 \partial \bar{\beta}_1} & \frac{\partial^2 J_{cost}}{\partial \bar{\beta}_2^2} & \frac{\partial^2 J_{cost}}{\partial \bar{\beta}_2 \partial \bar{\beta}_3} & \frac{\partial^2 J_{cost}}{\partial \bar{\beta}_2 \partial \bar{\alpha}} \\ \frac{\partial^2 J_{cost}}{\partial \bar{\beta}_3 \partial \bar{\beta}_1} & \frac{\partial^2 J_{cost}}{\partial \bar{\beta}_3 \partial \bar{\beta}_2} & \frac{\partial^2 J_{cost}}{\partial \bar{\beta}_3^2} & \frac{\partial^2 J_{cost}}{\partial \bar{\beta}_3 \partial \bar{\alpha}} \\ \frac{\partial^2 J_{cost}}{\partial \bar{\alpha} \partial \bar{\beta}_1} & \frac{\partial^2 J_{cost}}{\partial \bar{\alpha} \partial \bar{\beta}_2} & \frac{\partial^2 J_{cost}}{\partial \bar{\alpha} \partial \bar{\beta}_3} & \frac{\partial^2 J_{cost}}{\partial \bar{\alpha}^2} \end{bmatrix}, \tag{4.2.17}$$

in which the second gradient of the cost function is computed using finite differences:

$$\frac{\partial^2 J_{cost}}{\partial \bar{\beta}_i^2} = \frac{J_{cost}\left(\bar{\beta}_i + h, ...\right) - 2J_{cost} + J_{cost}\left(\bar{\beta}_i - h, ...\right)}{h^2}, \tag{4.2.18}$$

$$\begin{aligned} \frac{\partial^2 J_{cost}}{\partial \bar{\beta}_i \partial \bar{\beta}_j} = & \frac{J_{cost}\left(\bar{\beta}_i + \frac{h}{2}, \bar{\beta}_j + \frac{h}{2}, ...\right) - J_{cost}\left(\bar{\beta}_i + \frac{h}{2}, \bar{\beta}_j - \frac{h}{2}, ...\right)}{h^2} \\ & + \frac{-J_{cost}\left(\bar{\beta}_i - \frac{h}{2}, \bar{\beta}_j + \frac{h}{2}, ...\right) + J_{cost}\left(\beta_i - \frac{h}{2}, \bar{\beta}_j - \frac{h}{2}, ...\right)}{h^2}, \end{aligned} \tag{4.2.19}$$

with h as the infinitesimal step size; in practice $h = 10^{-6}$.

4.2.3.3 Alveoli diameter identification

As pointed out in the section 4.2.2.1, there is no unique value proposed for the alveoli diameter, neither do [Smith and Stamenovic, 1986] declared the alveoli diameter of their samples. So we identify a size for the RVE from the experimental data and compare it to the range proposed for similar animals.

Considering the porosity and alveolar wall constitutive parameters are defined, the alveolar diameter can be adjusted. Indeed, the surface force generated by the presence of surface tension, contributes to the pressure-volume response, and from the definition, it is the integration of the surface tension over the surface area. This means that applying a constant pressure and a surface tension on alveoli of different diameters, leads to various deformed configuration with various volumes with respect to %TLC.

To identify the alveolar diameter, we use the pressure-volume experiments with constant surface tension from [Smith and Stamenovic, 1986]. For a specific pressure and a specific constant surface tension, we can adapt the alveolar diameter (cf. Figure 4.2.2) such that the volume computed from the model matches the one from the experiments.

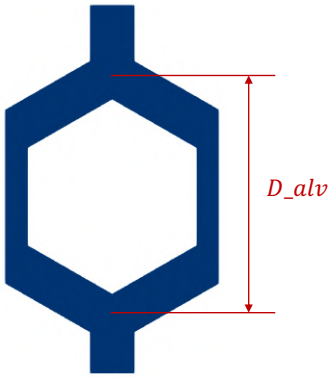

Figure 4.2.2: The diameter of the hexagon in the RVE which corresponds to the average alveoli diameter.

4.2.3.4 Surface tension model parameters

A behavior for the surface tension which depends on the surface area can be identified from the air-filled pressure-volume experiments from [Smith and Stamenovic, 1986]. To obtain the parameters of the surface tension constitutive behavior defined by Equation 4.2.10, we first track the intersection of the pressure-volume response of the model for various values of *constant* surface tension, with the air-filled experiment, both in inflation and deflation. At each intersection point, we retrieve from the model the surface tension and the interfacial surface area. We note that the intersect points lay in between the computed points, so we need to use an interpolation between the computed points to find the area at the intersect points. The normalized surface tension is defined as

$$\gamma^* := \frac{\gamma}{\gamma_{max}}, \tag{4.2.20}$$

where γ_{max} is the surface tension which makes the volume equal to 100% TLC when the lung is inflated to the maximum pressure (25 cmH_2O). The surface area is also normalized: $S^* = \frac{S}{S_0}$. This results in two sets of $(\gamma^*;S^*)$ data points, one in inflation and the other in deflation, from which the surface-dependent surface tension models parameters can be identified.

4.3 Results

We present here the results of the sequential identification method for the microstructure, constitutive law for the alveolar wall and constitutive law for the surfactant, along with some comments on the model behaviour in general. For consistency, in all the figures, blue and orange colors are used to show the response of the model and the experiments respectively.

4.3.1 Hyperelastic parameters identification

Minimizing the cost function described in Equation 4.2.15 for the pressure-volume test based on [Smith and Stamenovic, 1986], yields $\beta_1 = 0.0943\ kPa$, $\beta_2 = 0.0169\ kPa$, $\beta_3 = 0.619\ kPa$, $\alpha = 3.154$, see Figure 4.3.1. In addition, minimizing the cost function described in Equation 4.2.16, based on the experiment by [Jorba et al., 2019], results in $\beta_1 = 8.382\ kPa$, $\beta_2 = 0.305\ kPa$, $\beta_3 = 0.903\ kPa$, $\alpha = 2.055$, as in shown in Figure 4.3.2.

We remark that the asymptotic volume, which is considered in the pressure-volume test, depends on the parameters of the model. Noting that in the identification process based on a specific experimental data, the parameters change on each iteration. An infinitesimal change of the parameters in the neighborhood of the asymptotic criterion may lead to a significant gap in the cost function between those sets of parameters. As such, non-consistency is observed in some neighborhoods in the cost function, which is plotted with respect to parameters in the neighborhood of solution in Appendix B. Nonetheless, the identification is robust enough to find a local minimum of the cost function. We note that the solution of minimization of the cost function may not be unique, as the model contains four parameters, and there is only one pressure-volume response, which mainly deals with bulk deformation. The eigenvalues of the Hessian matrix of the cost function around the solution obtained by comparing the model to the pressure-volume experiment by [Smith and Stamenovic, 1986] yield $\lambda_1 = 1.219e5$, $\lambda_2 = 3.254e1$, $\lambda_3 = 7.905e2$, and $\lambda_4 = 2.829e3$. Even though the eigenvalues are not in the same range, their positivity indicates the uniqueness of the solution in the solution neighborhood.

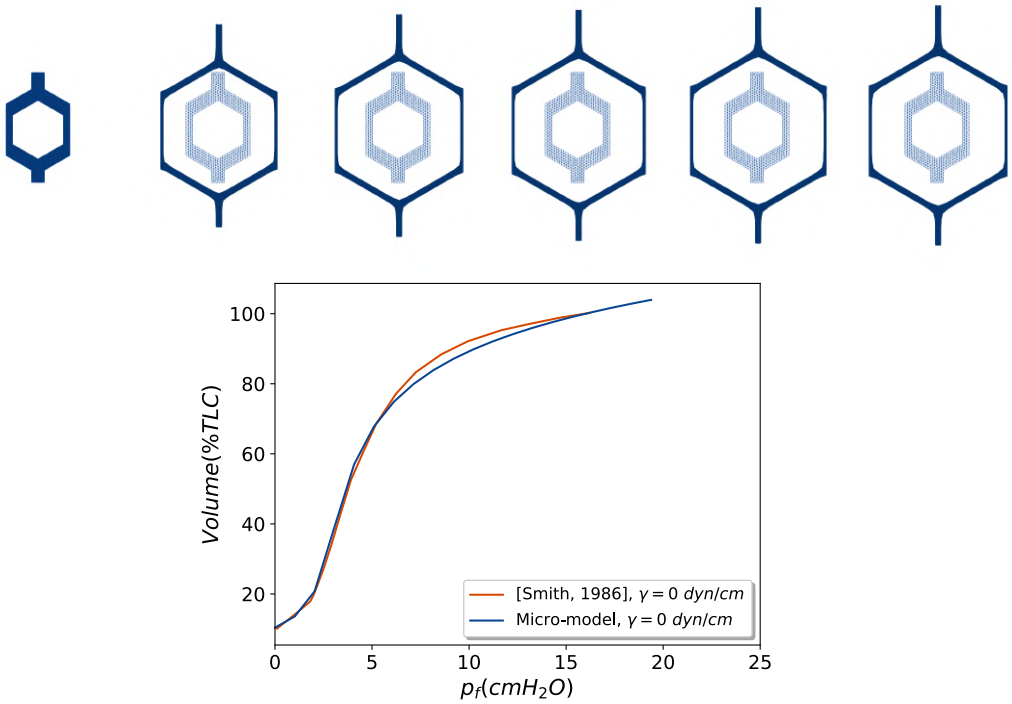

Figure 4.3.1: Model response in the absence of surface tension, with the parameters identified for the hyperelastic behaviour of the alveolar wall, for the pressure-volume test.

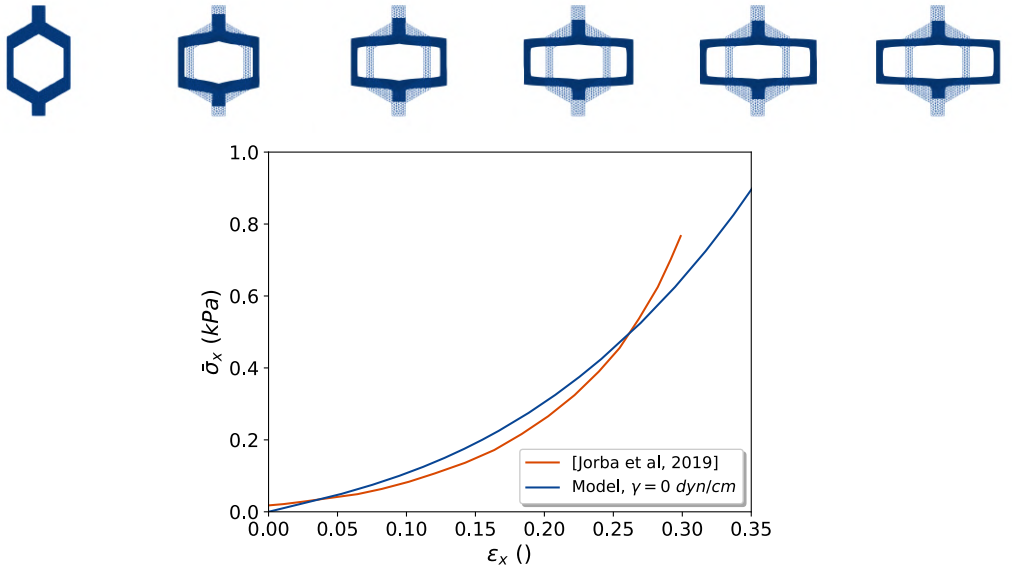

Figure 4.3.2: Model response in the absence of surface tension, with the parameters identified for the hyperelastic behaviour of the alveolar wall, for the tensile test.

Based on the identified hyperelastic parameters, we illustrate the effect of porosity on the pressure-volume response, recalling that it was set to $\Phi_{f0} = 63\%$ before the hyperelastic identification. Note that this initial porosity corresponds to $\Phi_f = 91.52\%$ at 25 cmH_2O, falling in the range of porosities experimentally observed. Figure 4.3.3 shows the pressure-volume behavior of the model for three different porosities, which values are computed in the undeformed configuration. As discussed before, the fluid volume is computed with respect to TLC, which itself varies with respect to porosity. As expected, lower porosity yields a stiffer behaviour.

4.3.2 Alveoli size identification

The hyperelastic parameters were identified in the absence of surface tension. We can now compare the model and the experiments in the presence of surface tension and investigate the effect of the alveolar size on the model response. We note that without the surface tension, the model is independent of the alveolar size. This is the reason that we use the experiments, considering surface tension to identify the size of the alveoli, while the hyperelastic parameters.

Figure 4.3.4 shows the pressure-volume response of the model in the presence of constant surface tension in the model for RVEs with two different alveoli sizes, one arbitrary chosen ($D_{alv} = 80\ \mu m$) and one manually adjusted to match the experimental curve at $\gamma = 7 dyn/cm$ ($D_{alv} = 54\ \mu m$). The latter yields $D_{alv} = 173\ \mu m$ when inflated to 20 cmH_2O, which is above the size reported for rabbits in [Kovar et al., 2002] but in the range of human alveolar size [Denny and Schroter, 1997]. Note that the diameter in the deformed configuration depends on the hyperelastic parameters for a specific pressure value.

As expected, the model response in the absence of surface tension is the same $D_{alv} = 80\ \mu m$ and $D_{alv} = 54\ \mu m$. Besides, surface tension in the model acts as a contradictory force to pressure, resulting in an increase of pressure for reaching the same volume compared to the absence of surface tension.

4.3.3 Surface tension model parameter identification

The model response with $\Phi_{f0} = 63\%$, $D_{alv} = 54\ \mu m$ and the identified hyperelastic alveolar wall behaviour reasonnably matches the experimental behavior with constant surface tension. We can now identify the parameters of the surface-dependent surface tension model, which corresponds to the air-filled lung. Figure 4.3.5 shows the pressure-volume response of the model for different surface tension values, compared to experimental air-filled lung behavior which exhibits a large difference in inflation and deflation. Let us underline that the model fails to compute the response at low pressure for high values of surface tension, which explains why some curves are incomplete. This may result from the buckling of such a periodic structure. [Smith and Stamenovic, 1986] observed some instability in the alveolar structure for a similar range of behavior. Addressing this issue in the model is beyond the scope of this work (see [López Jiménez and Triantafyllidis, 2013] for more details). We remark that the increase in the surface tension results not only in a decrease in total volume but also a decrease in the surface area by making the sharp corners smoother, see Figure 4.3.5.

To generate the data from which the surface-dependent surface tension law can be identified, we compute the intersection of the air-filled experiments with the pressure-volume curves for different surface tension values. At each point, we know the pressure and surface tension and we can compute the normalized surface area and normalized surface tension. Note that in the model, the volume is more than 100% TLC when γ is small. Based on the computations, the maximum surface tension is $\gamma_{max} = 30\ mN/m$. The

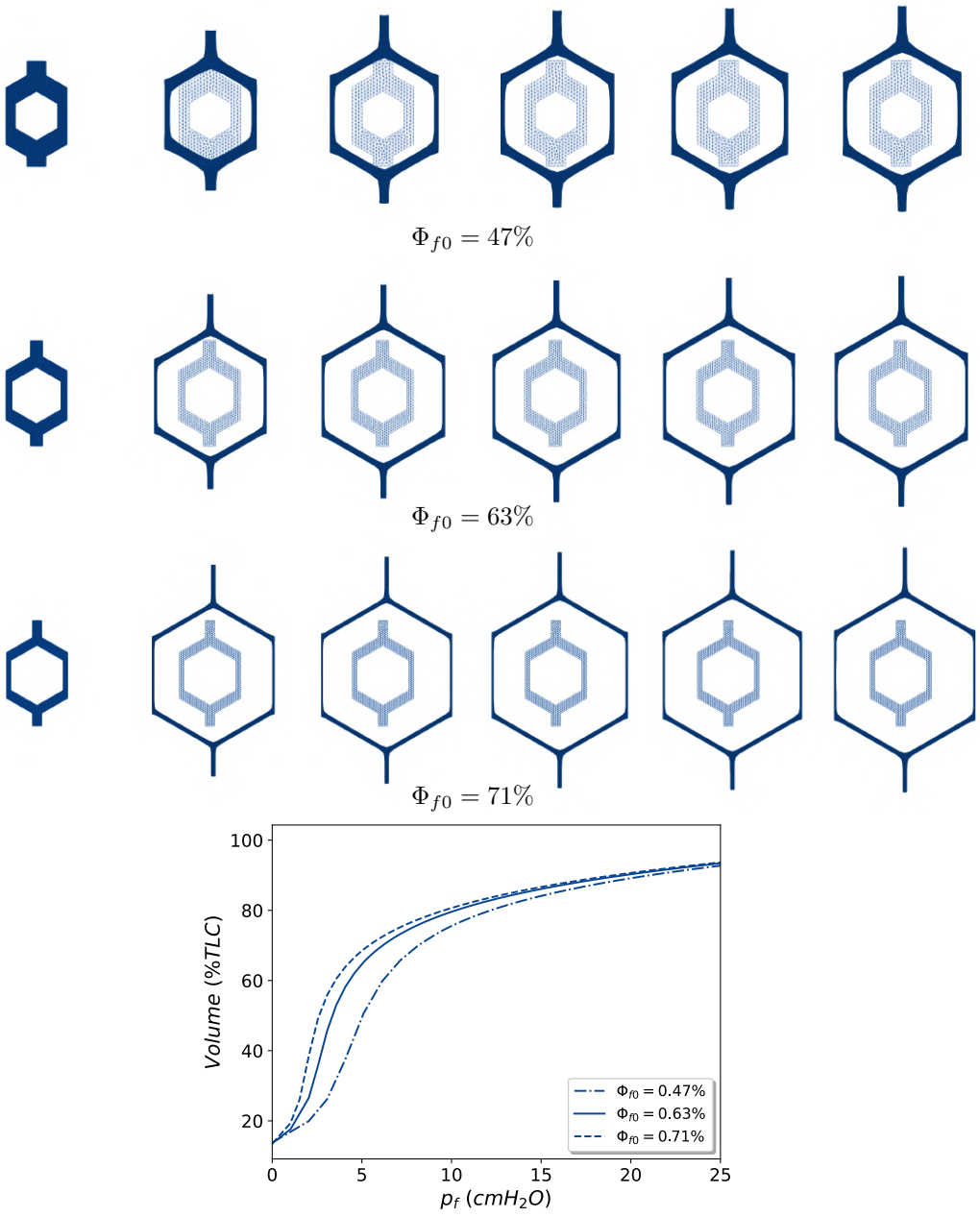

Figure 4.3.3: Pressure-volume response of the model, depending on the porosity.

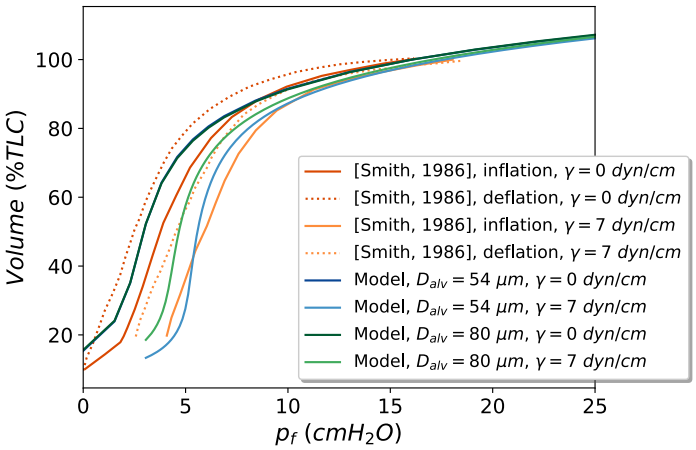

Figure 4.3.4: Pressure-volume response of the model with constant surface tension, depending on the alveolar size, compared to experimental data from [Smith and Stamenovic, 1986].

surface-dependant surface tension law described in the Equation 4.2.10, is fitted to the intersected points separately in inflation and deflation resulting in the following parameters: $c_1^{inf} = 1.042$, $c_2^{inf} = 1.970$, and $c_3^{inf} = 7.642$ in inflation, $c_1^{def} = 1.68e{-}2$, $c_2^{def} = 1.298e{-}4$, and $c_3^{def} = 3.276$ in deflation. Note that these parameters are obtained for a specific set of material parameters, alveolar size and porosity.

We can now incorporate the surface-dependent surface tension in our model to compare it to the pressure-volume experiments. The result in Figure 4.3.8 show that the model response, including surface tension, reasonnably matches the experimental air-filled curve.

4.4 Discussion

The present work aimed at proposing a robust framework for the micromechanical modeling of a porous medium in large strains and in the presence of surface tension. This framework is adaptable to any microstructure, skeleton strain energy potential and surface tension behaviour; the response of the structure can be computed for a loading in pressure, strain, stress or a combination of those. The scope of this paper was to define realistic values for the parameters of this model so it can represent fairly well the behaviour of a lung submitted to internal pressure. This is a first step towards a thorough sensitivity analysis.

The choice of experiments by [Smith and Stamenovic, 1986] in this work to identify the parameters of the model relates to the specificity of these experiments. They indeed conducted pressure-volume experiments with constant surface tension. This unique feature allows us to have a reference to compare the response of our model in the presence of constant surface tension. As mentioned before, the alveolar size plays a significant role in the model response, particularly in the presence of surface tension. Therefore, having an experimental reference allowed us to adjust the alveolar size and qualitatively match the model response to the experimental behavior.

The average diameter of alveoli depends on the specimen and varies from species to species. In the literature, there is a wide range of values reported for the morphological parameters of the same species, for instance, humans, which may result from differences in the measurement protocols [Weibel, 1963]. In our reference experiment [Smith and Stamenovic, 1986], there is no mention of morphological parameters. Considering that [Smith and Stamenovic, 1986] performed the experiments on rabbit lungs, we can compare the identified alveolar size to experiments that have reported rabbit

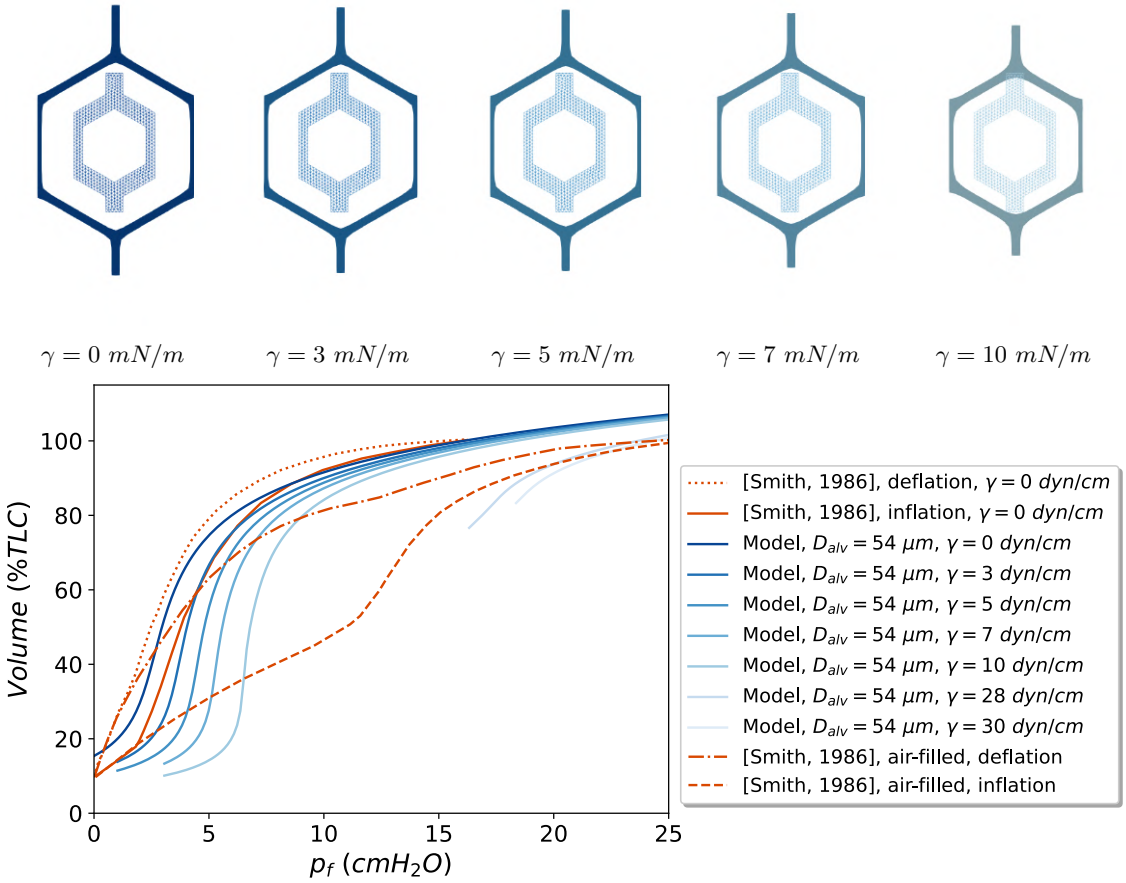

Figure 4.3.5: Comparing pressure-volume response with different values of constant surface tension to the air-filled experimental data by [Smith and Stamenovic, 1986], in the inflation and deflation. The microstructure is shown in the pressure $p_f = 7\ cmH_2O$.

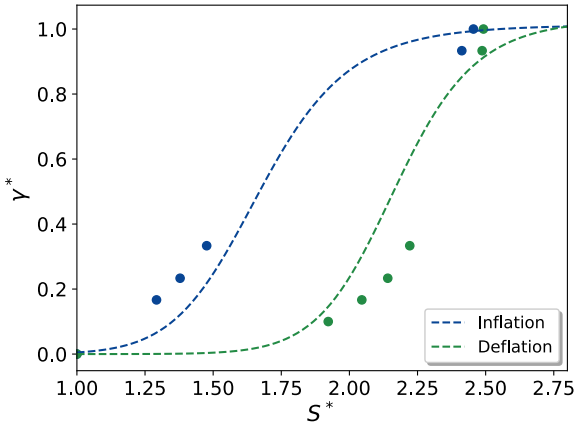

Figure 4.3.6: Fitting a curve to the intersection data points between describing the relation between γ^* and S^*.

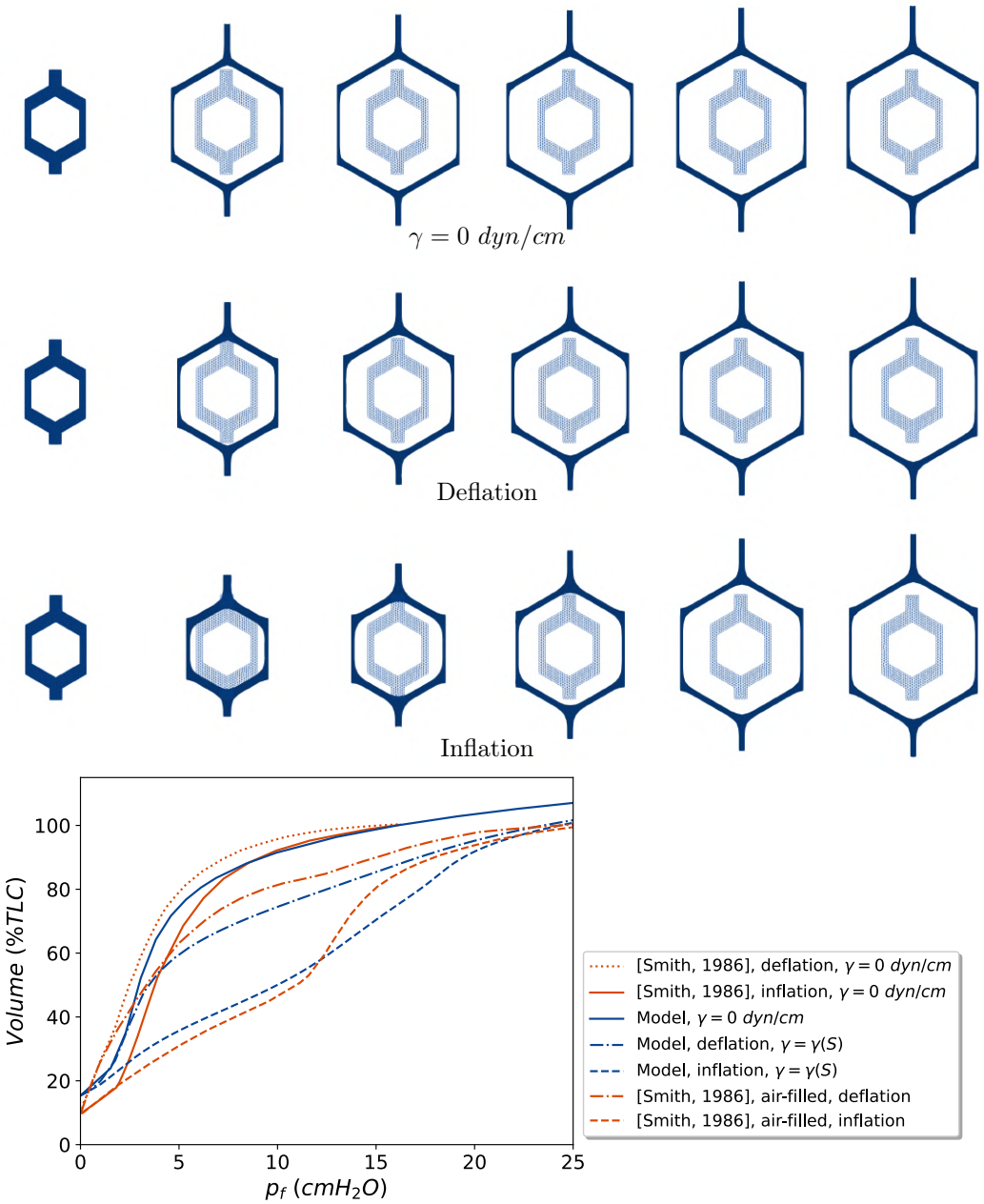

Figure 4.3.7: Comparing the pressure-volume response of the model to the experimental data by [Smith and Stamenovic, 1986], in the absence and presence of surface-dependent surface tension, inflation, and deflation.

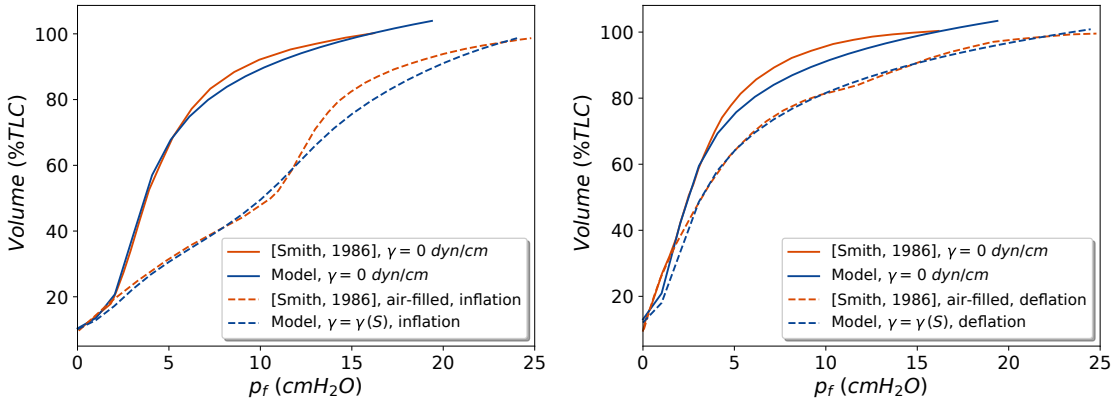

(a) Inflation.

(b) Deflation.

Figure 4.3.8: Comparing the pressure-volume response of the model to the experimental data by [Smith and Stamenovic, 1986], in the absence and presence of surface-dependent surface tension, inflation, and deflation.

lung morphometry, or even animals similar in size to rabbits, to obtain approximate values for alveolar size and porosity.

Pressure-volume experiments in the literature are conducted on different species and protocols. Nonetheless, lung volumes in these experiments are most commonly reported with respect to Total Lung Capacity, regardless of the actual volume, which may vary by species. This common measurement allows us to compare the model response to different experiments, regardless of the protocol. On the other hand, the total capacity is not defined in the model. More precisely, the model is not limited in inflation, as the exponential constitutive behavior cannot reproduce pure stiffening behavior. Therefore, we had to define a criterion based on which we attribute the total lung capacity to our model.

By comparing the model response to the experiments by [Smith and Stamenovic, 1986] and [Jorba et al., 2019], we identified the model hyperelastic parameters. We note that the experiments were performed on different species, so we expect differences between the identified parameters. However, the parameters fall within the same range. it is remarkable that in the experiments by [Smith and Stamenovic, 1986], the pressure-volume curves exhibit slightly different responses in inflation and deflation. We chose to identify one set of parameters for the model that provides the best trade-off between the inflation and deflation curves. The identification of the four hyperelastic parameters is performed based on one set of data, thus there may be more than one solution to the identification problem. The uniqueness of the parameters is not discussed in this work, while the identified parameters minimize the cost function in the local neighborhood. We note that the cost function is shown in Appendix B with respect to the model parameters with the ±10% range.

Surface tension is modeled in this work based on a single constitutive behavior, dependent on surface area, but different in inflation and deflation due to different parameters. Several works in the literature propose different constitutive behaviors of surface tension in inflation and deflation [Kowe et al., 1986]. Other authors propose a surface tension behavior that not only depends on surface area but also on its rate of change [Otis et al., 1994, Denny and Schroter, 2000, Wiechert et al., 2009]. In such models, surface tension has multiple phases, including Langmuir kinetics at some points. Such behavior has been observed experimentally, where the loading frequency impacts the behavior [Ingenito et al., 1999]. As far as our model is quasi-static, we are not able to incorporate

a surface tension model which depends on the surface area rate of change. Incorporating such a surface tension model would require to model the dynamics of inflation and deflation, also requiring a viscoelastic model for the alveolar wall [Bel-Brunon et al., 2014] which causes hysteresis in inflation-deflation cycle. This is beyond the scope of the present work.

Overall, the identification procedure described here is not meant to provide the unique set of parameters that matches the data. Though rich, the experiments from [Smith and Stamenovic, 1986] lack some information, notably the morphological ones, to be fully confident in the values that were identified in this work. Reproducing these experiments and coupling them to the imaging capabilities of today could generate sets of experimental data to further validate our model. Besides, now that a first set of parameters has been defined, a sensitivity analysis is required to determine how each of them impacts the model response. It could then be evaluated whether this micromechanical model associated to relevant microstructural alteration, is able to reproduce pathological phenomena, such as fibrosis or emphysema.

4.5 Conclusion

In this Chapter, we extend the micro-poromechanical approach proposed in Chapter 2 to simulate the mechanical behavior of the lung. The constitutive law for the alveolar wall reproduces the physiological stiffening observed on lungs. Surface tension in the lung has been modeled, where the surface tension can be either constant or dependent on the interfacial surface area. Moreover, to be able to compare the model response to the behavior reported by the experiments, a definition has been introduced in the model to show the air volume as a percentage of the Total Lung Capacity. Finally, by comparing the model response to the experiments, the parameters of the hyperelastic and geometrical parameters of the model have been identified.

In terms of perspectives, general upscaling strategy can be defined to facilitate structural simulations based on the model response, utilizing finite element methods or a general model reduction approach [Kanouté et al., 2009, Genet et al., 2014]. Besides, the current formulation of the model supports 3D computations, employing an alternative periodic 3D geometry. However, computations in 3D take significantly more time compared to 2D, which may necessitate optimization of computational costs.

Experimental investigations, associated to imaging techniques, are now required at various scales, to evaluate whether the bridge between the microscopic and macroscopic scales computed by the model accurately reproduces the physiological and pathological reality.

Bibliography

[Alnæs et al., 2015] Alnæs, M., Blechta, J., Hake, J., Johansson, A., Kehlet, B., Logg, A., Richardson, C., Ring, J., Rognes, M. E., and Wells, G. N. (2015). The FEniCS Project Version 1.5. Vol 3.

[Arora et al., 2021] Arora, H., Mitchell, R., Johnston, R., Manolesos, M., Howells, D., Sherwood, J., Bodey, A., and Wanelik, K. (2021). Correlating Local Volumetric Tissue Strains with Global Lung Mechanics Measurements. *Materials*, 14(2):439.

[Bachofen and Schürch, 2001] Bachofen, H. and Schürch, S. (2001). Alveolar surface forces and lung architecture. *Comparative Biochemistry and Physiology Part A: Molecular & Integrative Physiology*, 129(1):183–193.

[Barthès-Biesel and Rallison, 1981] Barthès-Biesel, D. and Rallison, J. M. (1981). The time-dependent deformation of a capsule freely suspended in a linear shear flow. *Journal of Fluid Mechanics*, 113(-1):251.

[Bel-Brunon et al., 2014] Bel-Brunon, A., Kehl, S., Martin, C., Uhlig, S., and Wall, W. (2014). Numerical identification method for the non-linear viscoelastic compressible behavior of soft tissue using uniaxial tensile tests and image registration – Application to rat lung parenchyma. *Journal of the Mechanical Behavior of Biomedical Materials*, 29:360–374.

[Berger et al., 2016] Berger, L., Bordas, R., Burrowes, K., Grau, V., Tavener, S., and Kay, D. (2016). A poroelastic model coupled to a fluid network with applications in lung modelling. *International Journal for Numerical Methods in Biomedical Engineering*, 32(1).

[Birzle and Wall, 2019] Birzle, A. M. and Wall, W. A. (2019). A viscoelastic nonlinear compressible material model of lung parenchyma – Experiments and numerical identification. *Journal of the Mechanical Behavior of Biomedical Materials*, 94:164–175.

[Ciarlet and Geymonat, 1982] Ciarlet, P. G. and Geymonat, G. (1982). Sur les lois de comportement en élasticité non-linéaire compressible. *Comptes Rendus de l'Académie des Sciences Série II*, 295:423–426.

[Concha et al., 2018] Concha, F., Sarabia-Vallejos, M., and Hurtado, D. E. (2018). Micromechanical model of lung parenchyma hyperelasticity. *Journal of the Mechanics and Physics of Solids*, 112:126–144.

[Dembo and Steihaug, 1983] Dembo, R. S. and Steihaug, T. (1983). Truncated-Newton algorithms for large-scale unconstrained optimization. *Mathematical Programming*, 26(2):190–212.

[Denny and Schroter, 1997] Denny, E. and Schroter, R. C. (1997). Relationships Between Alveolar Size and Fibre Distribution in a Mammalian Lung Alveolar Duct Model. *Journal of Biomechanical Engineering*, 119(3):289–297.

[Denny and Schroter, 2000] Denny, E. and Schroter, R. C. (2000). Viscoelastic Behavior of a Lung Alveolar Duct Model. *Journal of Biomechanical Engineering*, 122(2):143–151.

[Gehr et al., 1978] Gehr, P., Bachofen, M., and Weibel, E. R. (1978). The normal human lung: ultrastructure and morphometric estimation of diffusion capacity. *Respiration Physiology*, 32(2):121–140.

[Genet et al., 2014] Genet, M., Couégnat, G., Tomsia, A. P., and Ritchie, R. O. (2014). Scaling strength distributions in quasi-brittle materials from micro-to macro-scales: A computational approach to modeling Nature-inspired structural ceramics. 68:93–106.

[Genet et al., 2023] Genet, M., Patte, C., Manoochehrtayebi, M., and Peyraut, A. (2023). Dolfin_mech.

[Gibson and Pride, 1976] Gibson, G. and Pride, N. (1976). Lung distensibility. The static pressure-volume curve of the lungs and its use in clinical assessment. *British Journal of Diseases of the Chest*, 70:143–184.

[Ingenito et al., 1999] Ingenito, E. P., Mark, L., Morris, J., Espinosa, F. F., Kamm, R. D., and Johnson, M. (1999). Biophysical characterization and modeling of lung surfactant components. *Journal of Applied Physiology*, 86(5):1702–1714.

[Jorba et al., 2019] Jorba, I., Beltrán, G., Falcones, B., Suki, B., Farré, R., García-Aznar, J. M., and Navajas, D. (2019). Nonlinear elasticity of the lung extracellular microenvironment is regulated by macroscale tissue strain. *Acta Biomaterialia*, 92:265–276.

[Kampschulte et al., 2013] Kampschulte, M., Schneider, C., Litzlbauer, H., Tscholl, D., Schneider, C., Zeiner, C., Krombach, G., Ritman, E., Bohle, R., and Langheinirch, A. (2013). Quantitative 3D Micro-CT Imaging of Human Lung Tissue. *RöFo - Fortschritte auf dem Gebiet der Röntgenstrahlen und der bildgebenden Verfahren*, 185(09):869–876.

[Kanouté et al., 2009] Kanouté, P., Boso, D. P., Chaboche, J.-L., and Schrefler, B. A. (2009). Multiscale Methods for Composites: A Review. *Archives of Computational Methods in Engineering*, 16(1):31–75.

[Koshiyama et al., 2018] Koshiyama, K., Nishimoto, K., Ii, S., Sera, T., and Wada, S. (2018). Heterogeneous structure and surface tension effects on mechanical response in pulmonary acinus: A finite element analysis. *Clinical Biomechanics*.

[Kovar et al., 2002] Kovar, J., Sly, P. D., and Willet, K. E. (2002). Postnatal alveolar development of the rabbit. *Journal of Applied Physiology*, 93(2):629–635.

[Kowe et al., 1986] Kowe, R., Schroter, R., Matthews, F., and Hitchings, D. (1986). Analysis of elastic and surface tension effects in the lung alveolus using finite element methods. *Journal of Biomechanics*, 19(7):541–549.

[Laville et al., 2023] Laville, C., Fetita, C., Gille, T., Brillet, P.-Y., Nunes, H., Bernaudin, J.-F., and Genet, M. (2023). Comparison of optimization parametrizations for regional lung compliance estimation using personalized pulmonary poromechanical modeling. *Biomechanics and Modeling in Mechanobiology*.

[Lay et al., 2016] Lay, D. C., Lay, S. R., and McDonald, J. (2016). *Linear algebra and its applications*. Pearson, Boston, fifth edition edition.

[Logg et al., 2012] Logg, A., Mardal, K.-A., and Wells, G., editors (2012). *Automated Solution of Differential Equations by the Finite Element Method: The FEniCS Book*. Number 84 in Lecture Notes in Computational Science and Engineering. Springer.

[López Jiménez and Triantafyllidis, 2013] López Jiménez, F. and Triantafyllidis, N. (2013). Buckling of rectangular and hexagonal honeycomb under combined axial compression and transverse shear. *International Journal of Solids and Structures*, 50(24):3934–3946.

[Maksym and Bates, 1997] Maksym, G. N. and Bates, J. H. T. (1997). A distributed nonlinear model of lung tissue elasticity. *Journal of Applied Physiology*, 82(1):32–41.

[Manoochehrtayebi et al., 2024] Manoochehrtayebi, M., Bel-Brunon, A., and Genet, M. (2024). Finite strain micro-poro-mechanics: formulation and compared analysis with macro-poro-mechanics.

[Manoochehrtayebi and Genet, 2023a] Manoochehrtayebi, M. and Genet, M. (2023a). Micro-macro-poro paper demos.

[Manoochehrtayebi and Genet, 2023b] Manoochehrtayebi, M. and Genet, M. (2023b). Micro_poro_structure_generator.

[Ogden, 1972] Ogden, R. W. (1972). Large deformation isotropic elasticity: on the correlation of theory and experiment for compressible rubberlike solids. *Proceedings of the Royal Society of London. A. Mathematical and Physical Sciences*, 328(1575):567–583.

[Otis et al., 1994] Otis, D. R., Ingenito, E. P., Kamm, R. D., and Johnson, M. (1994). Dynamic surface tension of surfactant TA: experiments and theory. *Journal of Applied Physiology*, 77(6):2681–2688.

[Patte et al., 2022a] Patte, C., Brillet, P.-Y., Fetita, C., Bernaudin, J.-F., Gille, T., Nunes, H., Chapelle, D., and Genet, M. (2022a). Estimation of Regional Pulmonary Compliance in Idiopathic Pulmonary Fibrosis Based on Personalized Lung Poromechanical Modeling. *Journal of Biomechanical Engineering*, 144(9):091008.

[Patte et al., 2022b] Patte, C., Genet, M., and Chapelle, D. (2022b). A quasi-static poromechanical model of the lungs. *Biomechanics and Modeling in Mechanobiology*.

[Pozrikidis, 2001] Pozrikidis, C. (2001). Effect of membrane bending stiffness on the deformation of capsules in simple shear flow. *Journal of Fluid Mechanics*, 440:269–291.

[Pozrikidis, 2003] Pozrikidis, C., editor (2003). *Modeling and simulation of capsules and biological cells*. Number v. 2 in Chapman & Hall/CRC mathematical biology & medicine series. Chapman & Hall/CRC, Boca Raton, FL.

[Schürch et al., 1976] Schürch, S., Goerke, J., and Clements, J. A. (1976). Direct determination of surface tension in the lung. *Proceedings of the National Academy of Sciences*, 73(12):4698–4702.

[Smith and Stamenovic, 1986] Smith, J. C. and Stamenovic, D. (1986). Surface forces in lungs. I. Alveolar surface tension-lung volume relationships. *Journal of Applied Physiology*, 60(4):1341–1350.

[Tenney and Remmers, 1966] Tenney, S. M. and Remmers, J. E. (1966). Alveolar dimensions in the lungs of animals raised at high altitude. *Journal of Applied Physiology*, 21(4):1328–1330.

[Tueni, 2021] Tueni, N. (2021). Multiscale experimental and theoretical investigation of the structure-property relationships in the myocardium.

[Tueni et al., 2023] Tueni, N., Allain, J.-M., and Genet, M. (2023). On the structural origin of the anisotropy in the myocardium: Multiscale modeling and analysis. *Journal of the Mechanical Behavior of Biomedical Materials*, 138:105600. 3 citations (Crossref) [2023-12-18].

[Weibel, 1963] Weibel, E. R. (1963). Morphometry of the Human Lung.

[Weibel, 2017] Weibel, E. R. (2017). Lung morphometry: the link between structure and function. *Cell and Tissue Research*, 367(3):413–426.

[Wiechert et al., 2009] Wiechert, L., Metzke, R., and Wall, W. A. (2009). Modeling the Mechanical Behavior of Lung Tissue at the Microlevel. *Journal of Engineering Mechanics*, 135(5):434–438.

Appendix

A Mechanics of membrane

In this section we explain the foundation of the surface tension formulation by [Koshiyama et al., 2018] based on the mechanics of membrane discussed in [Pozrikidis, 2003].

A.1 Tangential projection oprator

We write an arbitrary vector $\underline{u}$ in curvilinear coordinate (cf. Figure A.1) such that

$$\underline{u} = u_t \underline{t} + u_n \underline{n} = (\underline{u} \cdot \underline{t}) \cdot \underline{t} + (\underline{u} \cdot \underline{n}) \cdot \underline{n}. \tag{A.1}$$

We conclude that the tangential component of the vector $\underline{u}$ is equal to

$$\underline{u_t} = \underline{u} - (\underline{u} \cdot \underline{n}) \cdot \underline{n} = \underline{\underline{P}}\ \underline{u}. \tag{A.2}$$

In the above equation, $\underline{\underline{P}} = \left(\underline{\underline{I}} - \underline{n} \otimes \underline{n}\right)$ defines tangential projection operator.

A.2 Interfacial tension

We follow [Pozrikidis, 2001] to define the in-plane tensions in the global Cartesian formulation (cf. Figure A.1). The surface tension developed in the membrane is denoted by $\underline{\underline{\tau}}$. To ensure that the surface tension lies in the tangential plane, we require that $\underline{\underline{\tau}} \cdot \underline{n} = \underline{n} \cdot \underline{\underline{\tau}} = 0$. The transverse shear tension described in Cartesian coordinates is denoted by $\underline{q}$. The transverse shear tension in the direction of the normal vector, imposed on the cross-section of the membrane that is normal to the tangential unit vector $\underline{b}$ is given by $\underline{b} \cdot \underline{q}$. Note that in 3D, it requires that $\underline{n} \cdot \underline{q} = 0$. We conclude that the total interface tension tensor would be

$$\underline{\underline{T}} = \underline{\underline{\tau}} + \underline{q} \otimes \underline{n}. \tag{A.3}$$

If the membrane shows isotropic surface tension γ, the in-plane tension exerted on a cross-section of the membrane $\underline{\underline{\tau}} = \gamma \underline{\underline{P}}$.

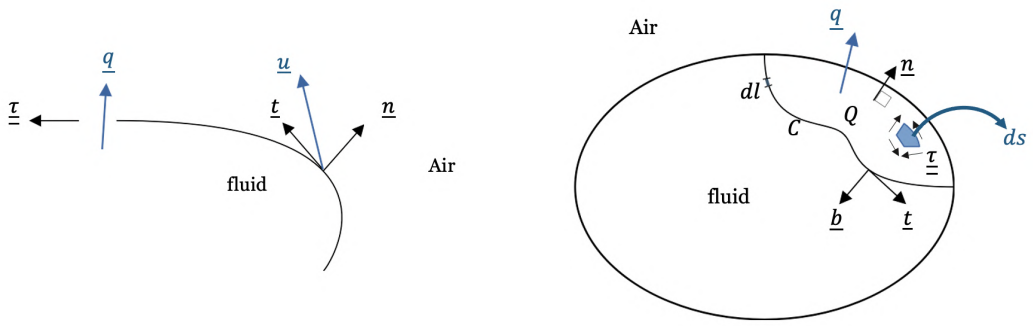

(a) Membrane in 2D

(b) Membrane in 3D

Figure A.1: Free diagram of schematic membrane in 2D and 3D.

A.3 Balance in Cartesian coordinate

Suppose we have a *patch* with a contour of Γ. The balance of force over the patch, by assuming negligible mass and for the membrane with infinitesimal thickness, reads [Pozrikidis, 2003]:

$$\int_{patch} \underline{\underline{\sigma_s}} \cdot \underline{n}\, dS + \int_{\Gamma} \underline{b} \cdot \left(\underline{\underline{\tau}} + \underline{q} \otimes \underline{n}\right) dl = 0, \tag{A.4}$$

where $\underline{\underline{\sigma_s}}$ is the hydrostatic stress tensor applied on the patch, and dS and dl are infinitesimal elements of the *patch* and its contour, respectively. Moreover, $\underline{b} = \underline{t} \otimes \underline{n}$ is the unit vector tangential to the membrane and lies in a plane that is normal to the contour C (cf. Figure A.1).

Consider a tensor function of position $\underline{\underline{L}}$, defined in three-dimensional space. The Gauss divergence theorem provides [Pozrikidis, 2001]

$$\int_{patch} \left(\underline{\underline{P}} \cdot \nabla\right) \cdot \left(\underline{\underline{P}} \cdot \underline{\underline{L}}\right) dS = \int_{\Gamma} \left(\underline{t} \otimes \underline{n}\right) \cdot \underline{\underline{L}}\, dl. \tag{A.5}$$

By comparing Equations A.4 and A.5, neglecting transverse shear tension, and remarking $\underline{t} \otimes \underline{n} = \underline{b}$ we conclude that:

$$\underline{f_s} = \underline{\underline{\sigma_s}} \cdot \underline{n} = -\underline{\underline{P}} \cdot \underline{\nabla} \cdot \underline{\underline{\tau_s}}, \tag{A.6}$$

where $\underline{f_s}$ is the force density applied on the membrane, and $\underline{\underline{P}} \cdot \underline{\nabla}$ is known as surface gradient $\underline{\nabla_s}$ [Barthès-Biesel and Rallison, 1981].

A.4 Contribution to the surface force

Based on the definition of [Koshiyama et al., 2018], the virtual work of the surface force is:

$$\int_{\partial\omega_f} \underline{f_s} \cdot \underline{U^*} = \int_{\partial\omega_f} \left(\nabla_s \cdot \left(\underline{\underline{\tau_s}} \cdot \underline{U^*}\right) - \underline{\underline{\tau_s}} : \nabla_s \underline{U^*}\right) d\partial\omega_f. \tag{A.7}$$

Converting the first term to a boundary integration results in

$$\int_{\partial\omega_f} \underline{f_s} \cdot \underline{U^*} = \int_{\partial\partial\omega_f} \underline{q} \cdot \underline{U^*} \partial\partial\omega_f - \int_{\partial\omega_f} \underline{\underline{\tau_s}} : \nabla_s \underline{U^*} d\partial\omega_f, \tag{A.8}$$

where $\underline{q}$ is the edge traction on $\partial\partial\Omega_{f0}$ which is imposed to be zero, as the edge traction is assumed to be free, considering the continuity of the air-liquid interface [Koshiyama et al., 2018]. So, Equation A.7 can be rewritten as:

$$\begin{aligned} \int_{\partial\omega_f} \underline{f_s} \cdot \underline{U^*} d\partial\omega_f = \\ \int_{\partial\Omega_{f0}} \underline{f_s} \cdot \left(\underline{\tilde{\epsilon}}^* \cdot \left(\underline{X} - \underline{X_0}\right)\right) J||{}^t\underline{\underline{F}}^{-1} \cdot \underline{N}||d\partial\Omega_{f0} + \int_{\partial\Omega_{f0}} \underline{f_s} \cdot \underline{\widehat{U}}^* J||{}^t\underline{\underline{F}}^{-1} \cdot \underline{N}||d\partial\Omega_{f0} = \\ - \int_{\partial\Omega_{f0}} \underline{\underline{\tau_s}} : \underline{\tilde{\epsilon}}^* J||{}^t\underline{\underline{F}}^{-1} \cdot \underline{N}||d\partial\Omega_{f0} - \int_{\partial\Omega_{f0}} \underline{\underline{\tau_s}} : \nabla_s \underline{\widehat{U}}^* J||{}^t\underline{\underline{F}}^{-1} \cdot \underline{N}||d\partial\Omega_{f0} \end{aligned} \tag{A.9}$$

B Optimization results

Figure B.1 shows the cost function with respect to the dimensionless parameters in the neighborhood of the solution, which minimizes the cost function (for the pressure-volume test) with respect to the parameters, with eigenvalues $\lambda_1 = 1.219e5$, $\lambda_2 = 3.267e1$, $\lambda_3 = 7.905e2$, and $\lambda_4 = 2.829e3$, and eigenvectors of $v_1 = [-0.00717,\ 0.362,\ -0.929,\ -0.0731]$, $v_2 = [0.105,\ 0.918,\ 0.344,\ 0.168]$, $v_3 = [-0.658,\ -0.0364,\ -0.0681,\ 0.749]$, $v_4 = [0.746,\ -0.157,\ -0.117,\ 0.636]$. We remark that the eigenvalues and eigenvectors are computed using finite differences with the infinitesimal step size $h = 10^{-6}$.

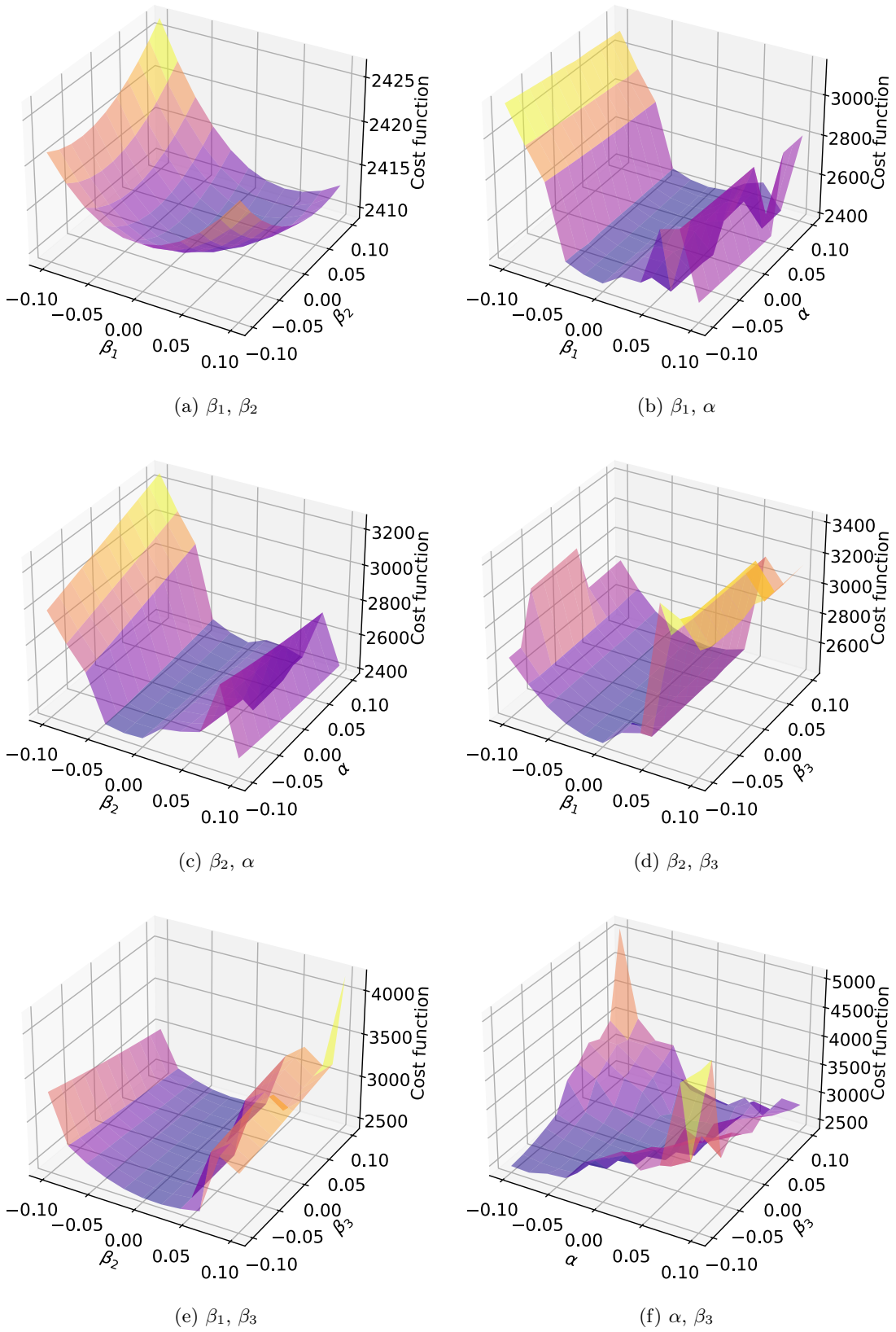

(a) β_1, β_2

(b) β_1, α

(c) β_2, α

(d) β_2, β_3

(e) β_1, β_3

(f) α, β_3

Figure B.1: Cost function with respect to dimensionless identified parameters.

Conclusions and perspectives

Summary of work

This work models the lung parenchyma behavior through a multi-scale approach. At the microscopic scale, the lung is modeled through a micromechanical approach, considering the microscopic physiological and morphological characteristics of the lung parenchyma via a variational framework. The global behavior of such a model is then studied and is compared to the macroscopic modeling approaches previously developed in the MΞDISIM team, upon the work of [Chapelle and Moireau, 2014, Patte et al., 2022] to investigate the relevance of the macroscopic approach in capturing microscopic phenomena. In addition, we benefit from the microscopic approach by adding the surface tension as a microscopic phenomenon at the alveoli scale and tuning the parameters of the model so that the model response follows different experimental behaviors.

The main achievement of this work is summarized in what follows:

- We reviewed the elements of modeling that are linked to the physiology of the lung. Elements of physiology and the breathing mechanism were discussed. We overviewed the mechanical models proposed in the literature, from the alveoli scale to the tissue scale, and discussed the elements of modeling at each scale, considering the characteristics of the lung parenchyma. In addition, we reviewed different experimental protocols conducted on the lung to capture its behavior in distortion, based on which the parameters of the models are identified.

- We established a microscopic poromechanical model based on a novel formulation where we introduce a proper definition for macroscopic stress. Such a model can compute the response of any periodic representative volume element in finite strains. Moreover, it represents the micro-scale distribution of the strain and stress with respect to any loading, including fluid pressure, macroscopic stress, or macroscopic strain. Such a microscopic model is capable of deriving macroscopic parameters based on microscopic features, such as pore shapes, porosity, and material properties. In addition, we enriched the microscopic model to simulate the behavior of the lung parenchyma by two means: First, we proposed a constitutive behavior for solid, considering an exponential term, such that the behavior of the model simulated the strain-induced stiffening behavior of the lung parenchyma in distortion; secondly, the surface tension was introduced within the micromechanical model as a counteractive force on tissue-air interface, tending to minimize the surface area with distinct laws in inflation and deflation.

- We discussed the algorithm employed to produce the geometrical microstructure in 2D and 3D as an element of micromechanical modeling. The main goal of microstructural modeling is to present geometries that resemble the geometry of the lung parenchyma. In 3D, we explained how to mesh porous TetraKaiDecahedron (TKD) elements, which are widely used as an element to simulate the average shape of alveoli [Concha et al., 2018, Dale et al., 1980], retaining periodic boundaries. In 2D, we introduced a definition that allows generating polygonal geometries with different degrees of irregularities retrieved from the random shapes of alveoli. Such a definition is based on seed distribution. In parallel, an algorithm was introduced to generate Voronoi tessellation based on any seed distribution with varying porosities.

- We took advantage of the microscopic model by comparing it to the (macroscopic) poromechanical model upon the work of [Patte et al., 2022]. Such a comparison

showed the equivalence of the poromechanical models in terms of stress-strain-pressure-porosity response in small strains, as the parameters of the poromechanical models were fed based on the homogenized behavior of the micro-mechanic model. In terms of coupling, based on the current choice of the poromechanical model, the free energy is additively decomposed between the strain and porosity contributions, which limits the model to incompressible solids unless more complexity is added to the formulation. On the other hand, the microscopic model was simply adapted to compressible and incompressible solids. Such flexibility in the microscopic model permits investigating the coupling between the strain and pressure for compressible solids. Moreover, the models were compared to capture the coupling between the deviatoric and volumetric deformation. Such a coupling in the poromechanical model is limited to the choice of constitutive law, while the microscopic model showed such a coupling exists even for the decoupled solid constitutive behavior.

- The parameters of the micromechanical model were identified such that the response of the model matched the behavior of the lung parenchyma reported from the experiments. Parameter identification concerns not only the constitutive potential parameters but also the microscopic parameters, such as RVE size and porosity. In addition, to compare the response of the micromechanical model to the ones of the experiments, we used a generic approach. Most of the experimental volumetric behaviors reported in the literature are based on Total Lung Capacity (TLC), which is different from sample to sample, and no maximum capacity is defined for the RVE in the micromechanical model. To compare the experimental data to the model behavior, we defined the volume in RVE based on its total capacity, which resulted from the strain-induced stiffening of the model. Finally, thanks to the rich constitutive behavior, in the sense of a number of parameters, we identify the parameters of the model such that it matches different behaviors reported in the literature. Moreover, the parameters of the surface tension model, introduced into the micromechanical model, were also identified by comparing the experiments that highlighted the surface tension effect.

This work presents a multi-scale approach to model the porous lung parenchyma. This approach explains the microscopic foundation, such as underlying microstructure, constitutive behavior, and microscopic mechanical features and properties and their contribution to the macroscopic scale, employing an upscaling approach. In addition, such a model is adapted to the behavior of lung parenchyma, including the surface tension as a physiological feature.

Conclusions

As the primary motivation of this work, we were looking for a model that enables us to investigate the contribution of idiopathic pulmonary diseases as a kind of interstitial lung disease, to mechanics. We recall that such diseases target the microstructure of the lung and microscopic mechanical and geometrical features, showing the importance of benefiting from a micro-mechanical model to investigate the impact of microscopic properties on macroscopic behavior. The model proposed in this work brings valuable features to address such a problem. First, the model is upgraded regarding the lung behavior and its microscopic features so that it is able to capture the physiological behavior of the lung while being general enough to follow various ranges of experimental behaviors. Secondly, such a model permits investigating stress distribution within the microstructure. Such a

characteristic of the model addresses the stress distribution within the alveoli septa, whose properties change in the case of fibrosis. Moreover, it can illustrate how the evolution of the alveolar septa affects the stress distribution on the microscopic scale. Finally, the model allows us to study the macroscopic behavior evolution with respect to microscopic mechanical and morphological features as a reference that can be compared to pulmonary fibrosis, pointing out the subsequent fibrosis tissue on the macroscopic scale behavior. In the end, it is notable that the modeling of the lung parenchyma brings a physical foundation for understanding the mechanism underneath certain pulmonary diseases and bridges the digital tools to medical applications. Nonetheless, modeling the biological tissues is complex, and many different physiological aspects need to be considered. Similarly, our model is extendable on different aspects to reach the medical applications.

Perspectives

This work is expandable in different directions:

- In this work, both microscopic and macroscopic models are illustrated in 2D and the case of plane strain; nonetheless, this model is capable of being generalized in 3D. To generalize the problem in 3D, the formulation of the problem remains the same; the constitutive potential needs to be generalized, and the geometry needs to be defined in 3D. An example of a 3D geometry is introduced in Chapter 3 with TetraKaiDecahedron (TKD) elements, which, similar to the hexagonal element in 2D, show isotropic behavior in space. Notably, the cost of the computations in 3D is significantly higher than in 2D.

- In the present work, we use simplified geometrical microstructure as the representative volume element to lower the complexity in construction and also the cost of computations. On the other hand, the microstructure can be reconstructed based on the geometry of the alveoli obtained from CT images in two different ways. The most common way to do that is using segmentation algorithms, which are complex by themselves, or more straightforwardly, only need to find the centers of the alveoli and benefit from the algorithm proposed in Chapter 3. This way, the geometry of the acinus can be constructed based on these center seeds via Voronoi tessellation. In addition, the airways inside acini can be reconstructed by removing the recognized walls between particular alveoli.

- In this work, we use a quasi-static model for the lung parenchyma, while, in fact, the lung parenchyma shows a visco-elastic behavior, leading to different behaviors in the inflation and deflation [Bel-Brunon et al., 2014]. This results from not only the visco-elasticity of the interstitium tissue but also the viscous behavior of the surface tension. So, a dynamic model can be introduced for the lung where the dynamic airflow inside pores can be studied. Such a model paves the way for integrating a surface area-rate dependent surface tension [Ingenito et al., 1999].

- With the aim of proposing a model with a response matching the behavior of the lung, the microscopic parameters of the model, such as porosity and the RVE size, as well as the elastic parameters, are identified based on the existing experimental data. On the other hand, such existing experimental data are very discrete, leading to the identification of microscopic and elastic parameters from different experiments with different protocols. The identification can be performed more precisely if we control all the parts of the experiments, such as the imaging, protocol, specimen,

and kind of test. Fortunately, we have access to an equipped experimental set-up in INSA-Lyon/LaMCoS under the collaboration of Dr. Bel-Brunon, where we can perform different experiments and obtain demanding measurements.

- The numerical upscaling performed in the present work concerns linear elasticity, while we can benefit from the microscopic model performing structural simulations in large strain. There are multiple ways to perform such a numerical homogenization. The macroscopic potential can be computed over a mesh grid discretized over the different (strain) loading, allowing us to obtain the derivative of the potential energy with respect to strain at any point via the finite element method, which corresponds to the macroscopic stress. Another way to obtain a numerical upscaled macroscopic model is by using artificial intelligence tools such as deep learning and neural networks, where they can be trained based on different applied loadings and finally predict the stress with respect to any other macroscopic loading based on the trained data.

- The micromechanical model elements, namely the geometrical features of the microstructure, the solid hyperelastic potential, and the corresponding parameters, are tuned based on the lung experimental behavior. On the other hand, a macroscopic counterpart can be proposed for structural estimations based on micromechanical model response. The poromechanical foundation for such a macroscopic model is explained in this work, while it remains identifying an adequate potential that is able to track such behavior.

Bibliography

[Bel-Brunon et al., 2014] Bel-Brunon, A., Kehl, S., Martin, C., Uhlig, S., and Wall, W. (2014). Numerical identification method for the non-linear viscoelastic compressible behavior of soft tissue using uniaxial tensile tests and image registration – Application to rat lung parenchyma. *Journal of the Mechanical Behavior of Biomedical Materials*, 29:360–374.

[Chapelle and Moireau, 2014] Chapelle, D. and Moireau, P. (2014). General coupling of porous flows and hyperelastic formulations—From thermodynamics principles to energy balance and compatible time schemes. *European Journal of Mechanics - B/Fluids*, 46:82–96.

[Concha et al., 2018] Concha, F., Sarabia-Vallejos, M., and Hurtado, D. E. (2018). Micromechanical model of lung parenchyma hyperelasticity. *Journal of the Mechanics and Physics of Solids*, 112:126–144.

[Dale et al., 1980] Dale, P., Matthews, F. L., and Schroter, R. C. (1980). Finite element analysis of lung alveolus. *Journal of Biomechanics*, 13(10):865–873.

[Ingenito et al., 1999] Ingenito, E. P., Mark, L., Morris, J., Espinosa, F. F., Kamm, R. D., and Johnson, M. (1999). Biophysical characterization and modeling of lung surfactant components. *Journal of Applied Physiology*, 86(5):1702–1714.

[Patte et al., 2022] Patte, C., Genet, M., and Chapelle, D. (2022). A quasi-static poromechanical model of the lungs. *Biomechanics and Modeling in Mechanobiology*.

ECOLE DOCTORALE

Titre : Modélisation multi-échelle du parenchyme pulmonaire

Mots clés : Poromécanique ; Modélisation mécanique du poumon ; Méthode des éléments finis ; Identification des paramètres ; Modélisation de la microstructure

Résumé : La fibrose pulmonaire idiopathique (FPI), caractérisée comme une maladie pulmonaire interstitielle qui induit un épaississement et une rigidification de certains septa alvéolaires, reste mal comprise, diagnostiquée et traitée. La FPI cible la structure du parenchyme pulmonaire telle qu'elle est observée sur les images tomodensitométriques et certaines caractéristiques microscopiques. L'évolution des propriétés microscopiques du parenchyme pulmonaire due à une telle maladie est étroitement liée au comportement du poumon à l'échelle de l'organe. La compréhension de ce lien peut être abordée par la modélisation mécanique, qui peut quantifier les données cliniques primaires, à savoir les tomodensitogrammes, et fournir un diagnostic relativement rapide. Dans ce travail, nous avons proposé une modélisation multi-échelle du parenchyme pulmonaire par le biais d'une approche mécanique. Un modèle général micro-poro-mécanique est proposé pour simuler le comportement des matériaux poreux compressibles et incompressibles à l'échelle microscopique et relier les caractéristiques mécaniques et morphologiques microscopiques au comportement à l'échelle macroscopique. Un tel modèle est défini sur la base d'une microstructure périodique avec différents choix qui subissent des déformations finies. En outre, le modèle micro-poro-mécanique peut montrer non seulement la distribution des contraintes et des déformations microscopiques sous diverses charges telles que les contraintes macroscopiques, les déformations macroscopiques et la pression du fluide, mais aussi leurs manifestations moyennes à l'échelle macroscopique. Ce modèle est d'abord comparé à la macro-poromécanique, afin d'étudier la pertinence de l'approche macroscopique par rapport aux approches microscopiques. Deuxièmement, le modèle est mis à jour pour reproduire le comportement expérimental du parenchyme pulmonaire. La tension superficielle, en tant que phénomène physiologique microscopique sur les parois alvéolaires, qui est une réponse pour maintenir la stabilité et le parenchyme pulmonaire en présence d'une pression de fluide, est prise en compte dans le modèle. En outre, les paramètres du modèle sont identifiés sur la base de certaines données expérimentales existantes.

Title : Multi-scale modeling of the lung parenchyma

Keywords : Poromechanics; Lung mechanical modeling; Finite element method; Parameter identification; Microstructure modeling

Abstract : Idiopathic Pulmonary Fibrosis (IPF), characterized as an interstitial lung disease that induces thickening and stiffening of certain alveolar septa, remains poorly understood, diagnosed, and treated. IPF targets the structure of the lung parenchyma as observed in CT images and some microscopic features. The evolution of microscopic properties within the lung parenchyma due to such a disease is intricately connected to the organ-scale behavior of the lung. Understanding such a connection can be addressed through mechanical modeling, which can quantify the primary clinical data, namely CT scans, and return a relatively quick diagnosis. In this work, we have proposed a multi-scale modeling of the lung parenchyma through a mechanical approach. A general micro-poro-mechanical model is proposed to simulate the behavior of the compressible and incompressible porous materials at the microscopic scale and link the microscopic mechanical and morphological features to the macroscopic scale behavior. Such a model is defined based on a periodic microstructure with different choices that undergo finite strains. Moreover, the micro-poro-mechanical model can show not only the microscopic stress and strain distribution under various loadings such as macroscopic stress, macroscopic strain, and fluid pressure but also their average manifestations at the macroscopic scale. This model is first compared to the macro-poromechanics, to investigate the relevance of the macroscopic approach to the microscopic ones. Second, the model is updated to reproduce the experimental behavior of the lung parenchyma. Surface tension, as a microscopic physiological phenomenon on the alveolar walls, which is a response for maintaining stability and lung parenchyma in the presence of fluid pressure, is encountered in the model. Moreover, the parameters of the model are identified based on some existing experimental data.

Institut Polytechnique de Paris
91120 Palaiseau, France